Alma Mater Studiorum – Università di Bologna

DOTTORATO DI RICERCA IN

Scienze della Terra, della Vita e dell'Ambiente

Ciclo XXIX

Settore Concorsuale di afferenza: 04/A3

Settore Scientifico disciplinare: GEO/05

TITOLO TESI

Study of the evolution of active earthflows through field monitoring and geophysical investigations

Presentata da: Lara Bertello

Coordinatore Dottorato — **Barbara Mantovani**

Relatore — **Matteo Berti**

Esame finale anno 2017

1. INTRODUCTION

2. METHODS

3. MANUSCRIPTS

Paper 1 - *Rheological properties of clayey soils originating from flow-like landslides*
(Carrière S.R., Jongmans D., Chambon G., Bièvre G., Lanson B., **Bertello L**., Berti M., Chambers J.E., Jaboyedoff M., Malet J-P.) – submitted to **Journal of Geophysical Research: Earth Surface** in June 2016

Paper 2 – *Field monitoring of surface-wave velocity and displacement rate in an active earthflow* (**Bertello L.**, Berti M., Castellaro S.) – submitted to **Journal of Geophysical Research: Earth Surface** in January 2017

Paper 3 – *Unsteady sediment discharge in earth flows: Mount Pizzuto earth flow, southern Italy* (Guerriero L., **Bertello L.**, Cardozo N., Berti M., Grelle G., Revellino P.) **–** submitted to **Geomorphology** in September 2016

Paper 4 – *A surface seismic approach to liquefaction*
(Castellaro S., Panzeri R., Mesiti F., **Bertello L.**) **–** published in **Soil Dynamics and Earthquake Engineering** in 2015

4. CONCLUSIONS

REFERENCES

1. INTRODUCTION

The three year research project has involved a detailed study of the evolution and kinematic of earthflows. Varnes (1978) classification included earthflows which were divided into rapid and slow flows. Rapid flows occur in fine-grained silt, clay and clayey sand and form a complete gradation with slides involving failure by lateral spreading, retrogressive failure, and liquefaction of the entire slide mass. Slow earthflows are drier then rapid flows and involve plastic earth resulting from a combination of clay, clay bearing, rocks, moderate slopes and adequate moisture. Generally, the slip surface within the moving masses are not visible or are very short-lived and the boundary between the moving mass and the in-place material may be a sharp surface of differentiated movement or a zone of distributed shear. Hutchinson (1988) used the term “mudslide” to describe Varnes’s (1978) earthflows. He described these landslides as slow-moving, lobate or elongated, masses of accumulated debris in a softened clayey matrix, which advance chiefly by sliding on discrete shear surfaces. He underlined that mudslide movement is frequently highly seasonal (e.g. Hutchinson, 1971) with undrained loading in the upper part of the mudslide tending to contribute to their forward movement. This is particularly common where the slope inclination of the slide is low. Cruden and Varnes (1996) described an earthflow as a spatially continuous movement in which surfaces of shear are short-lived, closely spaced and usually not preserved, and the distribution of velocity in the displacing mass resembles to that in a viscous liquid. They specified that the boundary of the displaced mass may be a surface along which appreciable differential movement has occurred or a thick zone of distributed shear. Hungr (2001) used the term “earth flow” to describe an intermitted flow-like movement of plastic, clayey earth, that may accumulate on the slope in a tongue-like form. He specified that this type of flow is typical of over-consolidated clays and continued movement may be maintained for long periods of time and over long distances by intermittent plastic deformation combined with internal creep, aided by pore-pressure fluctuations. Hungr et al. (2014) maintaining the previous definition of earthflow (Hungr, 2001), specified that “movement is facilitated by a combination of sliding along multiple discrete shear-surfaces, and internal shear strains” and that “long periods of relative dormancy alternate with more rapid surges”.

An earthflow consists basically of a movement in a pre-existing and more or less defined channel and usually occurs in many hilly and mountainous areas and are pervasive in many rapidly eroding landscapes (Mackey et al., 2009). Earthflow dominated landscapes are characterized by crescent-shaped or basin-shaped scars, loaf-shaped bulging toes, and long narrow tongue- or teardrop-shaped transport zones (D’Elia, 1975; Keefer and Johnson, 1983; Bovis and Jones, 1992; Booth et al., 2013) (Fig 1).

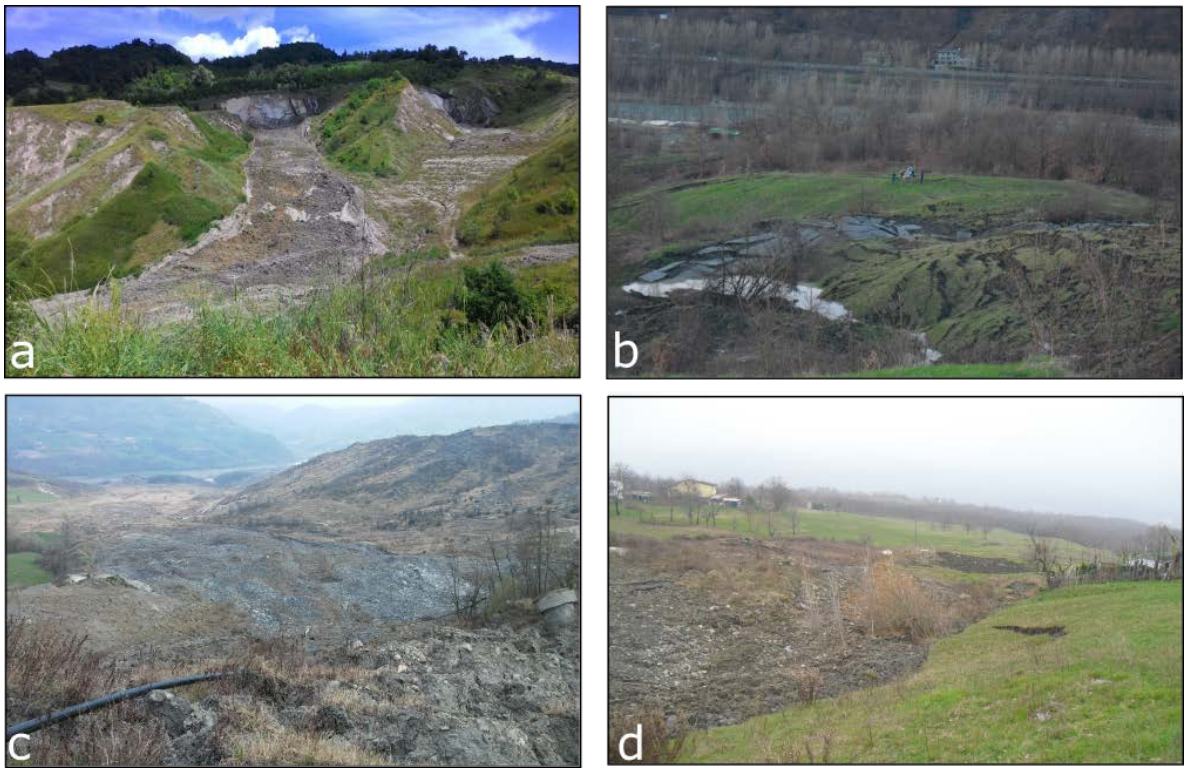

Fig. 1- Examples of active earthflows in the Emilia-Romagna region, Northern Apennines. a) The Montevecchio landslide, near the city of Cesena. The main scarp is completely exposed and the bedding of the layers is dip slope; b) The picture show the deposit/toe of the Boceto landslide (near the city of Parma), where there are a lot of cracks; c) The Calita landslide (near the city of Modena) present an huge channel body with a maximum width of almost 200m. d) The Silla landslide (near the city of Bologna) is classified as a complex landslide and reactivated in 2014.

Basically, these landslides have a source area that are generally characterized by the terrace of the slide that originates the earthflow, a track (or more than one) and an accumulation area (Picarelli et al., 2005). However, there are cases in which a real channel does not exist and the earthflow spreads over a flat slope. Guida et al., (1993) proposed a model regarding the evolution of earthflows divided in four differentiated phases on the basis of the morphological characteristic elements, recognizable by the macroscopic evidence of movement (Fig.2). In the phase A, the main scarp is evident and the detached materials move downslope at first with an high velocity (>0.3 m/day; Varnes, 1978), then with a velocity of 1.5 m/month. The landslide surface is highly softened and very irregular. The duration of this phase is usually seasonal. During the B phase, the material has a medium to low velocity (> 1.5 m/year; Varnes, 1978) and the accumulation area starts to enlarge as a lobate toe. In the C phase, the geometry of the landslide is characterized by a lower steepness of the shape and the velocity of the movement is low to very low (> 0.06 m/anno; Varnes, 1978). The phase D is characterized by the considerable morphological evolution of the main scarp, while the landslide body is not easily recognizable on the slope. There are no macroscopic evidences of deformation in the channel and in the toe (dormant phase).

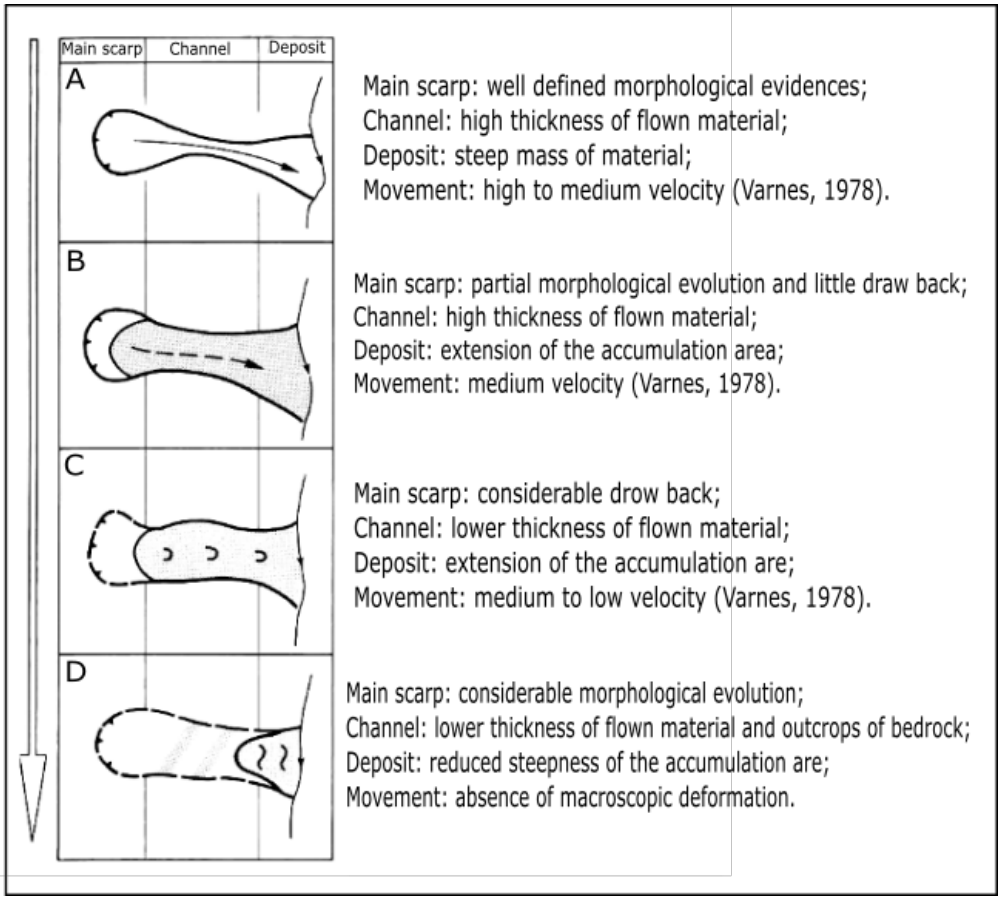

Fig. 2- Evolution scheme of earthflows. The different phases represent how usually earthflow move downslope and the kinematics over time. In the first phases, the main scarp is well defined and the material is accumulated in the channel. In the lasts phases the main scarp draw back, the accumulation area reduces its steepness and basically there are no evidences of deformation. Modified from D'Elia, 1975.

Active earthflows commonly exhibit seasonal movements controlled by rainfall, snowmelt, and in some cases atmospheric tides (e.g. Coe et al. 2009; Schulz et al. 2009) and in particular conditions, some earthflows can remain active for several centuries and move over very long distances (Coe et al., 2009). Earthflow response to rainfall or snowmelt is often delayed, and in several cases, long periods of cumulated precipitation are required to trigger activation (Kelsey 1978; Iverson 1986; Iverson and Major 1987). Velocity profiles generally show the existence of well-defined basal and lateral shear-surfaces normally associated with sliding movement (e.g. Hutchinson, 1971). In spite of their flow-like morphology, the dominant mechanism of the earth-flow movement is sliding at residual strength (Keefer and Johnson, 1983; Baum, 2003; Schulz et al., 2009). Continued movement may be maintained over long distances and periods of time with intermittent plastic deformation combined with internal creep controlled by pore-pressure fluctuations (e.g. Iverson, 2000; Baum, 2003). Slow movement could persists for days, months, or years (e.g. Varnes and Savage, 1996; Coe et al., 2009). In others cases, earthflows move intermittently; this character of motion is especially pronounced in arid climates (Hungr et al., 2014). Surges in movement are less common and earth flows capable of surging move in a slow persistent manner most of the time (Keefer and Johnson, 1983; Hungr et al., 2014). Observations of earthflow velocities (Keefer and Johnson, 1983) reveal three distinct patterns of variation: the first is characterized by period of

constant velocity lasting for several days, interrupted by short lived accelerations and decelerations; the second movement pattern is characterized by relatively slow velocity with few millimeters or centimeters movement surges. A third movement pattern is characterized by major surges causing abrupt advancements of several meters. (Keefer and Johnson, 1983).
Movement and activity of the earthflows are controlled by the water content of the involved materials (Baum et al., 2003). A pore-water pressure rise decreases the effective stress, thus the shear strength of the soil. Pore-pressure fluctuations, driven by rainfall and/or atmospheric tides, in combination with soil properties and shear-surface roughness, directly influence the rate of earthflow movement (Hutchinson and Bhandari, 1971; Keefer and Johnson, 1983; Iverson and Major, 1987). Moreover, changes in pore-water pressure near the basal slip surface, induced by earthflow material deformation, may play a role in damping acceleration (Iverson, 2000; Coe et al., 2009; Schulz et al., 2009). It indicate that earthflow velocity is generally positively correlated with groundwater pore pressure near the center of the landslide, and inversely correlated with pore-water pressure along the margin of the landslide (Schulz et al., 2008). The inverse correlation along the margin may be due to a pore-pressure feedback mechanism (Schulz et al., 2008) wherein landslide material dilates during acceleration, causing pore pressures to decrease and the landslide to decelerate. Baum and Johnson (1993) proposed that the deformation of earth-flow material moving on an irregular slip-surface induces a forced circulation of water that occurs as secondary flow of pore water.
The presence of clay layers causes the landslide to retain water, thus to react quickly to precipitation and snowmelt events. Shear strength of the clay layers tend to be significantly lower than both the landslide materials and the adjacent ground, helping to perpetuate movement on relatively gentle slopes. In some cases, the clay layers are pre-existing features, such as buried soil horizons or stratigraphic layers, while, in other cases they appear to have formed by redistribution or mechanical enrichment of existing clay as a by-product of earth-flow movement (Baum et al., 2003).

The aim of this work is to study the evolution of active earthflows. At first, we focused our attention on the solid-to-fluid transition of the material involved in earthflows, and we analyzed this aspect through laboratory tests, field monitoring and geophysical investigations (ReMi-MASW surveys and continuous ReMi measurements) (paper 1 and 2). On the second hand, we studied the distribution of surface structures to characterize the short-term behavior of an active earthflow in southern Italy, and we reconstructed the 3D geometry (using HVSR acquisitions and ReMi-MASW surveys) of the earthflow in order to compute sediment discharge at the transition of kinematic zones (paper 3). Finally, we used HVSR and ReMi-MASW acquisitions in order to study the seismic liquefaction effect on soils and to understand how the seismic wave velocity is influenced by the different liquefaction potential.
One way of characterizing the solid-to-fluid transition is to carry out rheometric tests on clayey soil samples in order to assess the evolution of the viscosity with the shear stress. We perform rheometric tests on clay soil collected in six landslides defined as earthflows (see paper 1). One of these is located in the Emilia Romagna region (Northern Apennines of Italy), and is referred to as the Montevecchio landslide. The primary objective of the study is to assess if these clayey soils exhibit similar rheological properties at the solid-fluid transition, in particular in terms of critical shear stress and viscosity bifurcation. The second objective is to investigate whether the rheological properties of these clayey soils can be related to (and possibly predicted by) their geotechnical

characteristics. These six landslides were chosen because they locally and temporally evolved to mud flows or debris-flows during heavy rainfalls. The three mechanical properties of the clayey soils (critical shear stress τ_c, critical shear strain rate γ_c and shear modulus G) for different water contents are determined from rheometric tests. Finally, the influence of the geotechnical properties on the rheological behavior is studied in order to identify the main parameters controlling the clay fluidization. The results shown that the Montevecchio landslide appears to exhibit a very strong fluidization (the highest values of shear strain rate). In order to confirm the partial or total fluidization of the soil involved and to understand the evolution of the movements, we decided to carry out a field monitoring activity and geophysical investigations. In particular, we studied the variations of the Rayleigh wave velocity over time with an experimental monitoring system using the Refraction Microtremors technique (ReMi) (Louie, 2001) (paper 2) and we performed periodic ReMi-MASW acquisitions. This allow us to study the variation of the surface seismic velocity (V_r) with the different evolutional phases of the landslide and to find a relationship between the V_r and the displacement rate.

From a geomorphological point of view, we used data from 17 GPS surveys, boreholes, seismic profiles, ambient seismic noise acquisition (HVSR), T-LiDAR surveys with the purpose of mapping the distribution of deformational structures on the Monte Pizzuto earthflow, located in Southern Italy (paper 3). We also performed a strain analysis, a mechanical model and an estimation of sediment discharge along the earthflow transport zone. This allows us to understand i) the characteristics of flow movement, ii) the control exerted by the basal slip surface on flow velocity, iii) changes and distribution of flow velocity, and iv) characteristics of sediment transport along the flow and cascade effects during both ordinary and extraordinary (i.e. surge) movements.

In the first three papers, we used geophysical investigations (ReMi-MASW and HVSR) in order to define different rheological state of the material ("fluid state" and "plastic state"), and to find the depth of the basal slip surface. In this work, we also aimed at deepening the knowledge of the seismic liquefaction phenomena including the possibility to define a priori which soils were potentially subject to liquefaction. In the paper 4, we explore the performance of geophysical methods (ReMi-MASW surveys (Park et al., 1999) and HVSR analysis (Nakamura, 1989)) in assessing the susceptibility of soils to seismic liquefaction, after the Emilia Romagna earthquake in 2012. We grouped the 84 surveys sites in four classes: Class A and B sites include shallow (<8 meters) sandy soils with liquefaction potential. In sites labeled A, liquefaction occurred during the 2012 earthquake while at sites B there was no surface evidence of liquefaction. Class C are those where sand is present at a depth major that 8 meters and did not exhibit liquefaction. Instead, Class D represents the clayey and silty soils with no liquefaction potential. At last step, we applied the state-of-the art Critical Stress Ratio – Shear wave velocity (CSR–Vs) method (Kayen et al., 2013) to assess the liquefaction potential of sandy deposits.

This three years research is the result of a collaboration of the University of Bologna (Department of Biology, Earth and Environmental Sciences) with:

1. The Institut des Sciences de la Terre (IsTerre, in Grenoble, France), which made available to us laboratory data collected in several landslides and allowed us to carry out laboratory tests on clay samples collected in the Montevecchio earthflow (Forlì-Cesena Province, Northern Apennines).

2. The University of Sannio, Department of Sciences and Technologies (Prof. Guadagno Research Group), which made available geomorphology and monitoring data regarding the Mount Pizzuto earth flow in Southern Italy (Campania Region).

2. METHODS

Rheology is the study of flow and deformation of materials under applied forces which is routinely measured using a rheometer. In practice, rheology is principally concerned with extending the relatively straightforward disciplines of elasticity and Newtonian fluid mechanics to more complicated and realistic materials developing fundamental relations, called constitutive relations, between force and deformation (Malkin and Isayev, 2012).

The measurement of rheological properties is applicable to all materials – from fluids such as diluted solutions of polymers and surfactants through to concentrated protein formulations, to semi-solids such as pastes and creams, to molten or solid polymers as well as asphalt (Barnes et al.,1989 (pp. 9)). Rheological properties can be measured from bulk sample deformation using a mechanical rheometer, or at a micro-scale by using a microcapillary viscometer or an optical technique such as microrheology. We used a Bohlin CVOR rheometer at the Isterre laboratory (paper 1) in order to study the solid-to-fluid transition on clayey samples from six different earthflows.

A partial or total fluidization of the mass has been widely reported in the literature for earthflow kinematic, and it is now considered a fundamental mechanism of earthflow dynamics (Picarelli et al., 2005; van Asch et al., 2007; Pastor et al., 2009; Daehne et al., 2010; Pastor et al., 2010; Jongmans et al., 2015). Despite its importance, the process of solid-fluid transition and the consequent transformation of a slide into a flow is extremely difficult to measure in the field.

In the last decades, shallow geophysics has considerably evolved with the emergence of 2D and 3D spatial imaging, and now 4D time and space imaging (Jongmans and Garambois, 2007).

The advantages of surface geophysical techniques are that (1) they are flexible, relatively quickly deployable on slopes, (2) they are non-invasive and give information on the internal structure of the soil or rock mass, and (3) they allow a large volume to be investigated. On the other hand, their main drawbacks are: (1) the decreasing resolution with depth, (2) the non-uniqueness of the solution for a set of data and the resulting need for calibration and (3) the indirect information they yield (physical parameters instead of geological or geotechnical properties).

Recently, Mainsant et al., (2012) successfully used the variation of shear wave velocity (V_s) as an indicator of fluidization in active landslides, and they detect a significantly decreases of V_s well before the reactivation of their monitored landslide (a first 2% drop about one month before the failure, and a second 7% drop four days before the failure).

In this research, we replicated the Mainsant et al. (2012) experiment and we used the Refraction Microtremor (ReMi) technique (Louie, 2001) for monitoring an active earthflow in the Emilia Romagna region (paper 2).

2.1 Rheometric tests

We used a Bohlin CVOR rheometer with a 60 mm parallel-plates geometry (Fig. 3) to carry out laboratory tests on clayey samples collected in six different earthflows. The specific characteristics of the Bohlin CVOR are listed in the following Table 1.

Specification	Value
Torque range	0.1μNm to 150μNm
Torque resolution	Better than 1nNm

Position resolution	50nrad
Frequency range	1μHz to 150Hz
Measurable speed range	10nrad s^{-1} to600 rad s^{-1}
Temperatur range	-150°C to 550°C

Tab. 1- A view of all the main characteristics of the Bohlin rheometer.

The clayey soils were placed between the two parallel-plates (Fig. 3c) following a specific procedure. At first you have to install the upper tool, inserting the 5mm diameter shaft on the top of the tool into the collet on the air bearing. In the display on the right of the rheometer (Fig. 3a) it is possible to observe the normal force meter that indicate the amount of normal thrust that you are placing on the air bearing. It is important to monitor this thrust so as not to overload the air bearing. Once the instrument has stabilized at the desired test temperature, you must zero the gap between the top and bottom plates or between the cone and the plate. Once the gap is properly zeroed, the instrument will correctly read sample thickness relative to this zero value. After that it is possible to set the intended gap (in this case 3600 μm for all the tests). To load the sample, it is first necessary to use the up and down arrows (on the right side of the rheometer), and raise the upper plate, then you have to proceed as follows: 1) separate the two plates until there is enough space to insert your sample; 2) insert your sample; 3) lower the upper plate using the knob on the top or press the down arrow on the test station front and hold for about one second to instruct the instrument to electronically lower the upper tool to the intended gap.

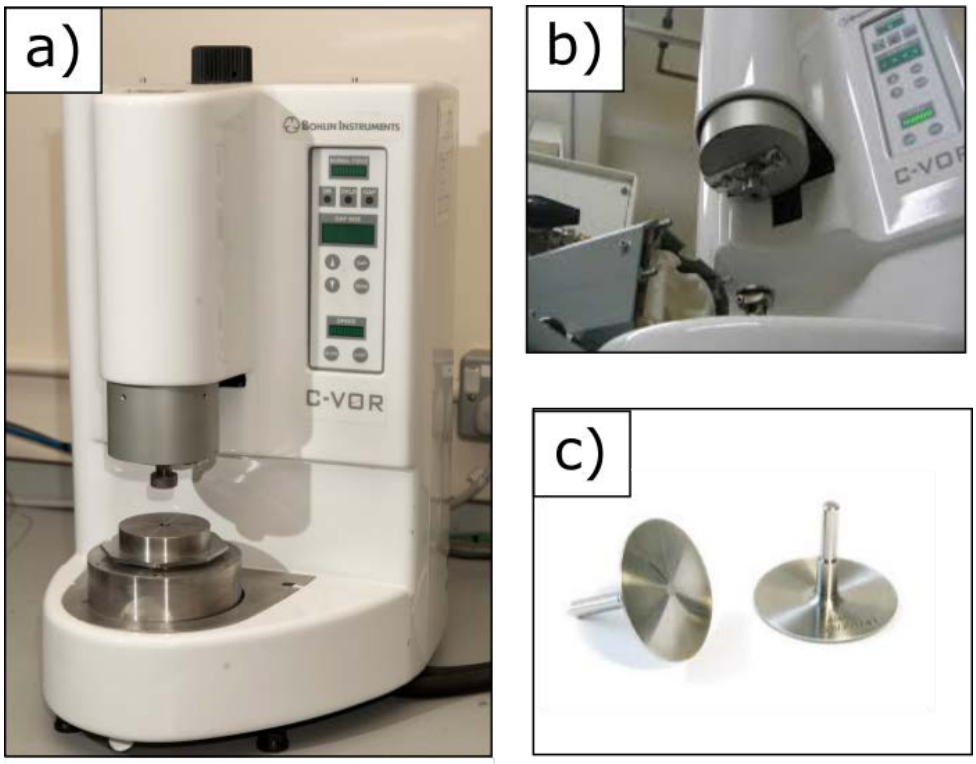

Fig. 3. a) The Bohlin CVOR rheometer. On the right, it is possible to see the display in which you can set the parameter of the test (e.g. the parallel-plats gap, the duration of the test). b) View of the sliding lock and assembly that hold upper tool. c) The parallel-plats that rotate during the tests and apply the shear strain to the samples.

In our tests the gap between the plates was kept constant at 3600 μm. This value, approximately ten times larger than the maximum grain size in the samples, enabled the consideration of a continuous material at the scale of the rheometer. The tests were carried out in an air-conditioned room, and the temperature of the samples was maintained constant at 21°C during the experiments. Before each test, the samples were pre-sheared at a strain rate of 50 s-1 for 20 s and then left at rest for 10 s to ensure a reproducible initial state. The samples at different water contents were prepared by mixing the dried soil with distilled water in a blender. All tests were carried out on six soils for 4 to 6 gravimetric water contents (w) above the liquid limit LL.
It is important to bear in mind that:

if $F_{external} < F_{internal}$ the material does not flow

if $F_{external} > F_{internal}$ the material starts to flow

Flow curves for plastic liquids run on the ordinate axis until the yield point is reached, then they converge from the ordinate. The flow curves can be expressed mathematically using a number of equations, depending on the actual material.

$\tau = f_B + \eta_B \times \gamma$ f_B is the yield point according to Bingham (1922); $\gamma =$ shear rate

$\sqrt{\tau} = \sqrt{f_c} + \sqrt{\eta_c \times \gamma}$ f_c is the yield point according to Casson (1959);

$\tau = f_H + m \times \gamma^P$ f_H is the yield point according to Herschel and Bulkley (Mitsoulis, 2007) and where $p < 1$ for pseudoplastic and $p > 1$ for dilatant materials.

Two types of rheometric protocols were applied in this research. First, standard creep (SCr) tests were used to determine the critical shear stress (τc) and critical strain rate (γc) of the clayey soil at the solid-fluid transition. Secondly, oscillatory creep (OCr) tests were used to capture the associated drop in elastic shear modulus.
Creep testing is a very useful technique that can be performed on a controlled-stress rheometer. The test entails applying a very small constant shear stress (τ) onto a sample and observing the resulting elastic deformation and/or viscous flow. The test has two particular uses: 1) to obtain a high quality zero-shear viscosity measurement - by the sustained application of a shear stress that is significantly within the linear viscoelastic limit for the material under test; 2) to simulate situations and explore product behavior where low stresses are maintained for a period of time, for example in draining, sedimentation, sagging or leveling scenarios.
With the SCr measuring method, the rotational speed (n) is preset at the rheometer, and the shear rate is calculated based on the gap (h) and the rotational speed. The flow resistant moment M (or the shear force F) of the braking, tough material under investigation is measured. This torque M is converted into the rheological parameter of shear stress using the shear area A of the measuring system. The dynamic viscosity η is calculated from the shear stress τ and the shear rate γ (Fig. 4).

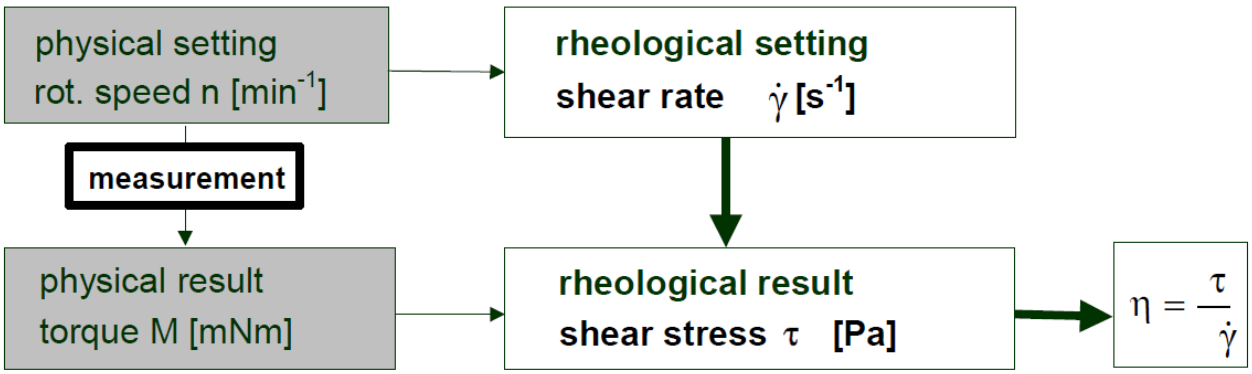

Fig. 4. A schematic view of a standard creep test (from the techinical manual of rheotec, Introduction to rheology)

Instead, the basic principle of an oscillatory test is to induce a sinusoidal shear deformation in the sample and to measure the resultant stress response; the time scale probed is determined by the frequency of oscillation (ω) of the shear deformation. During the test, while the top plate remains stationary, a motor rotates the bottom plate, thereby imposing a time dependent strain $\gamma(t)=\gamma \cdot \sin(\omega t)$ on the sample. Simultaneously, the time dependent stress $\sigma(t)$ is quantified by measuring the torque that the sample imposes on the top plate. Measuring this time dependent stress response at a single frequency immediately reveals key differences between materials. If the material is an ideal elastic solid, the sample stress is proportional to the strain deformation, and the proportionality constant is the shear modulus of the material. The stress is always exactly in phase with the applied sinusoidal strain deformation. In contrast, if the material is a purely viscous fluid, the stress in the sample is proportional to the rate of strain deformation, where the proportionality constant is the viscosity of the fluid. The applied strain and the measured stress are out of phase, with a phase angle $\delta=\pi/2$. Viscoelastic materials show a response that contains both in-phase and out-of-phase contributions, and these contributions reveal the extents of the solid-like and liquid-like behaviors. As a consequence, the total stress response shows a phase shift (δ) with respect to the applied strain deformation that lies between that of solids and liquids, $0<\delta$ (Weitz et al., 2007).

All the clayey tested samples shown a thixotropic behavior (Mainsant et al., 2012b) (paper 1).
By definition, the viscosity of a thixotropic material does not reach a steady value for some time upon application of stress, or shear rate. This steady state is dependent on the stabilization of internal network structures that can be broken down by shearing, and require time to rebuild (Fig. 5) (Coussot et al., 2002). A steady state plateau in viscosity is reached if an equilibrium has been established between structure breakdown and rebuilding. Upon ceasing the shear rate which caused the breakdown, the material reforms its internal network, and the viscosity recovers. In studying such materials it can be beneficial to destroy the network structure entirely by shearing the material, giving a clean-slate for examination of the path by which the viscosity rebuilds. The viscosity of thixotropic materials does not follow the same path on structure breakdown and recovery. In most cases, when the shear rate is slowed, the stress path lags forming a hysteresis loop, which then returns to a point lower than the initial critical shear stress. The area within the hysteresis loop represents the energy consumed in structure breakdown (Khaldoun et., 2009).

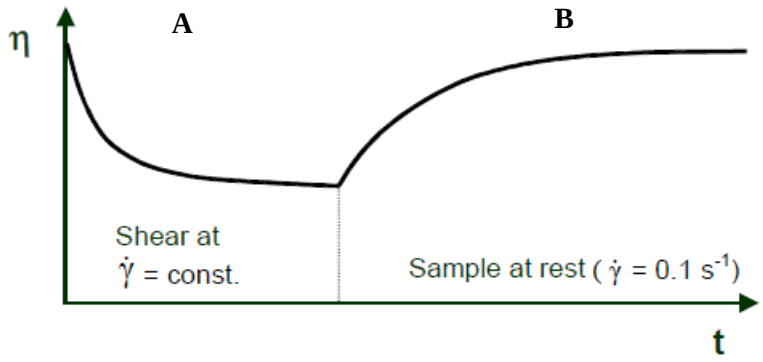

Fig. 5- Viscosity-time curve of a thixotropic material. Two transitional areas can be defined. A) a gel is quickly trasformed into a sol (colloidal solution) at a constant shear force. B) during a period of rest the material-specific network structures are re-established, i.e the soil turn back in a gel. Modified from the techinical manual of rheotec, Introduction to rheology.

2.2 Refraction Microtremor technique

Jhon Louie (2001) introduced the Refraction Microtremor (ReMi) method with the aim to evaluate the dispersion curve and to analyze the ambient seismic noise vibrations. He suggested to use a linear array of geophones and to apply the ω-p analysis of the seismic signal. Because the seismic waves are not continuously harmonic but arrive in groups, the ReMi analysis needs not just two seismograms, but more Pullammanappallil et al., (2003). This method is also called NASW (Noise Analysis Surface Waves) (Mucciarelli et al., 2003). The ReMi method is most often performed with 8 Hz resonant frequency geophones due to their low cost. However, the depth of interest of the shear wave profile should be the deciding factor in ReMi geophones selection. For greater depths, 4.5 Hz and 1 Hz geophones are recommended for more near surface detail (Beekman, 2008). Also, according to Pullammanappallil et al., (2003), geophone calibration for amplitude or frequency response is unnecessary because ReMi in its analysis uses only phase information. As long as the array is linear along 95% of its length and there are not major deviations in elevation along the array, the accuracy of the method is unaffected according to Pullammanappallil et al., (2003). The linear array calculates phase velocities as if the energy is propagating from one end of the array to the other (Beekman, 2008). The algorithm which is the basis of the ω-p analysis was proposed by McMechan and Yedlin (1981), with the aim of studying the surface waves present in active seismic acquisitions. The procedure consists of two linear transforms of the signal: 1) τ-p or slant-stack transform and 2) the Fourier transform (Fig.6).

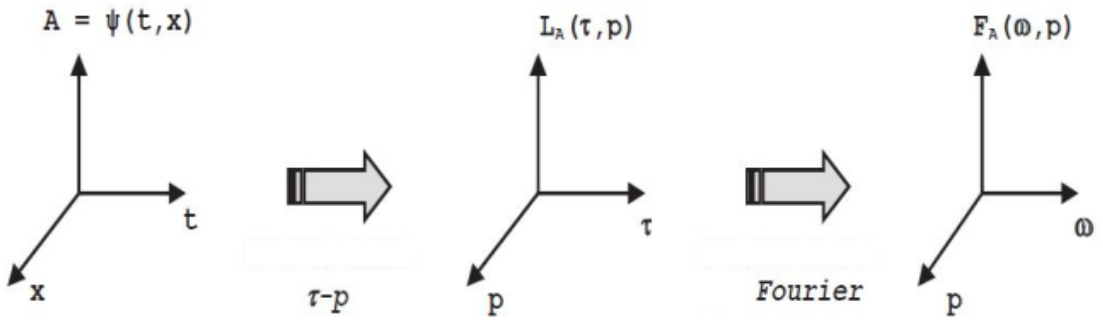

Fig. 6: The procedure in order to transform the signal in the ω-p domain. At first step is the τ-p transform and the second one is the Fourier transform (picture from Baliva, 2006).

The first transform consist to apply an integral in the time-space domain (1)

$$L_a(p,\tau) = \int_{-\infty}^{+\infty} \int_{-\infty}^{+\infty} \varphi(x,t) \cdot \delta(t + px - \tau) \cdot dx \cdot dt \qquad (1)$$

$$d(q) = 1 \; if \; q = 0; \; \delta(q) = 0 \; if \; q \neq 0$$

in order to obtain the intercept time (τ)-phase slowness (p) domain. In this domain it is possible to distinguish the surface wave from the volume wave (Foti, 2000). The slant - stack is a special case of the Radon transform, which performs a line integral of a function with two-dimensional domain, bringing it back to a new domain defined by parameters that specify the generic curve in which the integration is performed (Thorson and Claerbout, 1985). From the practical point of view, it performs the beam-forming for each time interception and for all values of phase slowness between a minimum and a maximum (Baliva, 2006).
The Fourier transform (2)

$$F_A(p,\omega) = \int L_A(p,\tau) \cdot e^{-i\omega\tau} \cdot d\tau \qquad (2)$$

allows to switch in the plan ω-p, in which is possible the direct determination of the dispersion curve of the surface waves. It is showed, in fact, that in the ω-p domain or, similar, in the frequency – phase velocity $f = \frac{\omega}{2\pi}$; $v = \frac{1}{p}$ domain, the image of the surface waves tends theoretically an infinite number of values (McMechan and Yedlin,1981). The dispersion curve is identified in the ω-p plan by the characteristic alignments of the maximum values that correspond to a compatible position of the Rayleigh waves. To complete the analysis, Louie (2001) proposed the calculation of the power spectrum.
The double transformation of the wave field is a reversible process: you can return to the original domain without losing any information. Practical difficulties are then, however, linked to the finite and discrete sampling of the signal, both in space and in time (Baliva, 2006).
An important element of ambiguity of the method is linked to the use of the ReMi linear array of sensors. When the direction of the horizontal propagation of the waves is unknown, it is still possible to have velocity values, associated to the apparent slowness phase, lower than the real one or, in the opposite, a velocity that refers to values of apparent velocity, higher than the true one. The relationship between the true phase velocity and the apparent one is a function of the cosine of the angle (α) between the direction of the propagation of the wave, the frequency (ω), and the direction of the array (3) (Louie, 2001):

$$V_a = \frac{1}{p_a} = v \cdot cos(\alpha) \, , \alpha = cos^{-1}(v \cdot p_a) = cos^{-1}\left(\frac{v}{v_a}\right) \qquad (3)$$

2.3 Continuous measurement of surface wave velocity

In order to experiment the ReMi method, a seismograph should be deployed in the field for automatic long-term measurements. However, conventional seismographers used in geophysical applications are not suited to monitor active landslides because they are generally heavy, expensive, and power demanding. Therefore, a cost-effective monitoring system was designed to include these

features (fig. 7a): 1) easy to install in the field and quick to remove; 2) low maintenance; 3) light enough to be carried by hand; 4) resistant to harsh field conditions (intense rainfall events, large ground displacements); 5) minimal energy consumption; 6) compatibility with geotechnical sensors. A number of laboratory and field tests were conducted to find the optimal configuration. We tested different combinations of sampling rate (50 to 300 Hz), number of geophones (2 to 6) and duration of the acquisition session (from 30 sec to 5 min) in order to balance the desired signal accuracy with the capabilities of the data logger and the power requirement. This appeared to be a suitable configuration for our needs: i) Campbell CR1000 datalogger with CFM100 Compact Flash Module (2GB); ii) 4 vertical geophones at 4.5Hz with 4 signal amplifiers (gain=500); iii) power supplied by a 12 V 7 Ah battery recharged by a 20 W solar panel. Good results were obtained by reading the four geophones at 300 Hz for 2 minutes every 1 hour, thus simulating the execution of 24 ReMi surveys every day (paper 2).

In Figure 7 b) 1) the CR1000 datalogger, which consists of a measurement, a control module and a wiring panel. This datalogger uses an external keyboard/display and power supply. Low power consumption allows the CR1000 to operate for extended time periods on a battery recharged with a solar panel (eliminating the need for AC power). The CR1000 stops working when the primary power drops below 9.6 V, reducing the risk of inaccurate measurements. Some of the specifications are listed in Table 2.

b) 2) illustrates the GSM/GPRS communication system with a preconfigured COM110A modem that allows data to be collected from a remote datalogger across the GSM cellphone network. The COM110 modem has very low power consumption which allows it to be left on over a long time in many applications, and allows therefore also incoming calls to be received all the time. For very low power applications, it can be switched off at certain times of the day using the power switch built into the data logger. Some of the specifications are listed in Table 3.

b) 3) illustrates the Flash Memory Drive SC115. The SC115 consists of electronics protected in a custom molded package. It has a USB 2.0 compatible connector for plugging it to the PC's USB port, and a CS I/O 9-pin connector for plugging it to a datalogger's CS I/O port. The SC115 may be connected directly to a PC or data logger, or connected through the supplied extension cables. The SC115 is typically used as an external data storage device, but may also be used as a USB-to-CS I/O synchronous device communications (SDC) adapter. Some of the specifications are listed in Table 4.

Specification	Value
Maximum Scan Rate	100 Hz
Pulse Counters	2
Analog Inputs	16 single-ended or 8 differential (individually configured)
Switched Excitation Channels	3 voltage
A/D Bits	13
Power Requirements	9.6 to 16 Vdc
Switched 12 Volt	1

Tab.2 Specifications of the CR1000 data logger (Cambpell Scientific).

Specification	Value
Input Power Supply Requirements	5-32V DC at an average maximum current of 400mA
System Power Consumption	typical: 5 mA in `standby' mode (GSM)
Communication	Data Rate: Up 9600 baud

Tab.3 Specifications of the GSM/GPRS communication system (Cambpell Scientific).

Specification	Value
Storage Capacity	2GB
Power Requirements	12 V
Typical Current Drain	35 mA (active)

Tab.4 Specifications of the Flash Memory Drive SC115 (Cambpell Scientific).

The monitoring system has also a rain gauge, a solar panel 20 W, a rechargeable Battery 12 V 7 Ah, one pressure sensor buried into the ground and a charge regulator Steca Solsum 8.8 (Fig. 4 b.4). The latter is used to monitor the state of charge of the battery bank, the charging process, and the connection/disconnection of loads. This optimizes the battery use and significantly extends its service life.

Moreover, in order to increase the power of the signal, four homemade amplifiers were connected to the geophones (Fig. 7c). The electronic components used in the amplifiers are: 1) two small signal diodes 200mA 100V; 2) two electronic resistance at 340 K-Ohm; 3) one amplifier AD623ANZ; 4) one electronic resistance at 3 K-Ohm; 5) a LM385Z transistor at 1.2V; 6) one resistance with an amplification factor of 1 K-Ohm; 7) a 2950ACZ3.3 voltage regulator; 8) three 0.1μF capacitors; 9) two 10μF capacitors; 10) one electrical resistance at 88.7 K-Ohm; 11) one electrical resistance at 316 K-Ohm; 12) a 0.01μF capacitor; 13) a 0.047μF capacitor; 14) one electrical resistance at 34.8 K-Ohm; 15) one electrical resistance at 162 K-Ohm and 16) an operational amplifier LM385N. We built up these amplifiers following the amplifier model of Richard Laursen.

All the seismic files were stored in the Flash Memory Drive SC115 and were converted in an appropriate format for the Grilla software (MoHo s.r.l.) (i.e. an ASCII matrix file with no heading and a column for each channel).

This system configuration proved its effectiveness but the accuracy of the method can be improved. Several modifications could be done to get best results: 1) combine active and passive mode acquisition in order to improve the dispersion curve at high frequency ranges, for example using an automatic hammer controlled by the datalogger; 2) use a large number of geophones to ensure an adequate data redundancy (Tokimatsu, 1997); 3) use a longer measurement session because short-period range are dominated the higher-mode Rayleigh wave (Tokimatsu et al., 1992). A powerful datalogger that combines fast acquisition, large memory capability, and relays control is required to this purpose.

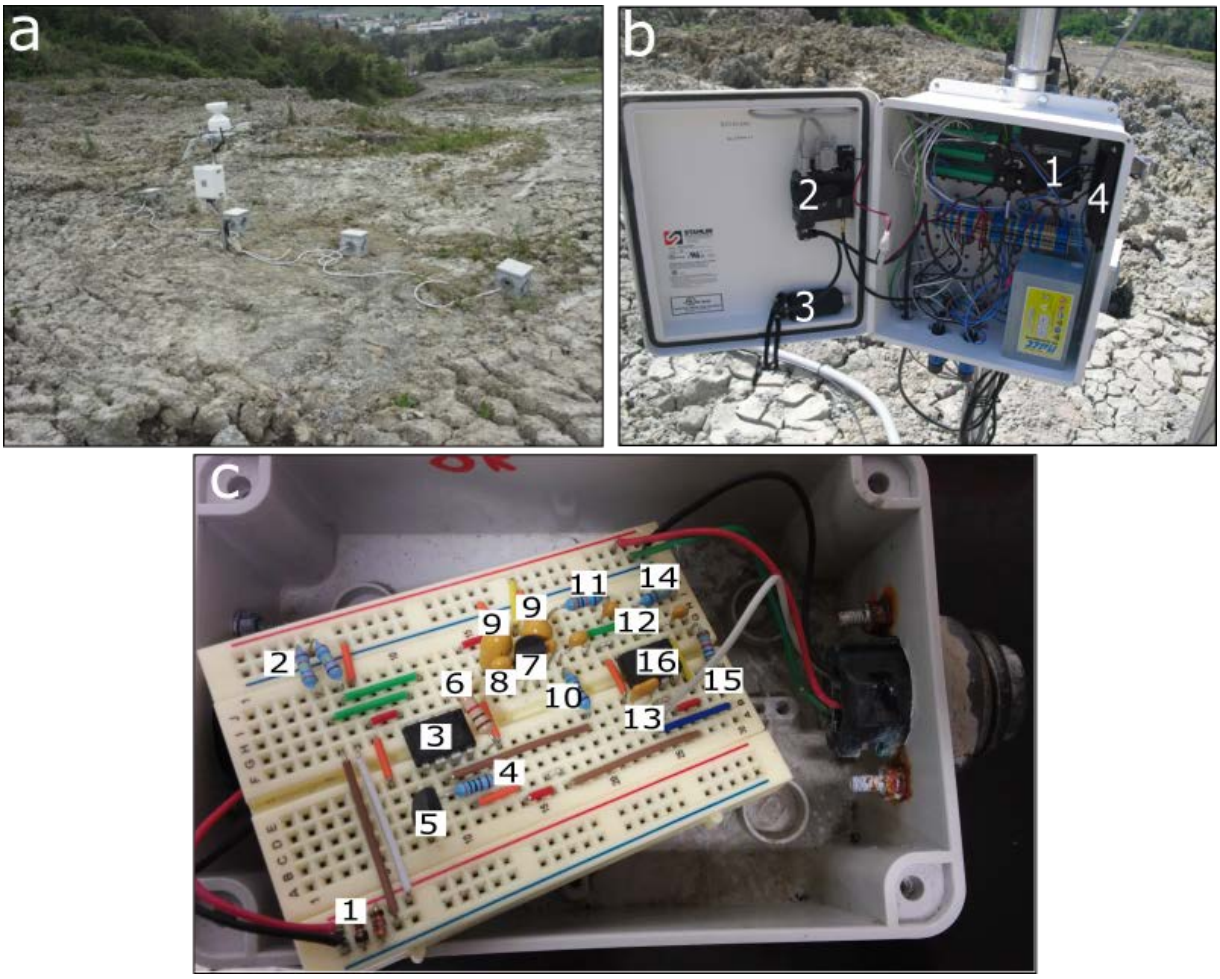

Fig. 7- a) shows the monitoring system with four geophones at 4.5Hz (buried at a depth of 30 cm in order to avoid atmospheric thermal effect), the rain gauge and the solar panel. In b) the details of the acquisition system are presented. 1) is the CR1000 data logger produced by the Campbell Scientific; 2) the GSM/GPRS communication system; 3) the Flash Memory Drive SC115 and 4) the charge regulator Steca Solsum 8.8. c) The homemade amplifier and all the electrical components (see full text for details).

3. MANUSCRIPT

This work is divided in four different papers. The first two focus on the study of the solid-to-fluid transition occurred in the material involved in earthflow kinematics. The third one regard a study about the geomorphological characteristics of an earthflow located in the South of Italy, and the last one represent an attempt to use geophysical methods in the study of the liquefaction phenomenon.

For earthflows occurring in fine grained soils during or after rainfalls, the most often proposed triggering mechanism is the partial or total liquefaction of the mass, resulting from an increase in pore water pressure (Picarelli et al., 2005; van Asch et al., 2007). As the shear wave velocity (V_s) in a fluid tends to 0 (Reynolds, 1997), the bulk shear wave velocity should dramatically decrease in the vicinity of liquefied zones (Mainsant et al., 2012a). Moreover, it has been recently observed that, in a clay-rich landslide, V_s also significantly decreases with the extent of damage in the material (Renalier et al., 2010). This suggests that continuous V_s measurements could be valuable for monitoring clay slope degradation and would constitute an alternative to the classical prediction methods. However the transient mechanisms involved in the solid-fluid transition are still poorly understood (Carriere et al., 2016, in review). One way is to carry out rheometric tests on clay samples (paper 1). These type of tests allow to identify the variation of the elastic shear modulus (G) with time, using the oscillatory creep test and the shear strain rate (γ) with time, and using the standard creep test. The latter test makes possible to individualize the critical shear stress (τc), that is defined as the stress level for which the solid-to-fluid transition occurs.

In order to verify the possibility to detect this transition in the field, we decided to install a monitoring system in one of the six landslides investigated in the previous paper. We configured a low cost and reliable monitoring system composed of four geophones at 4.5 Hz distributed in a linear array (2m spacing and a total length of 6m) (see paper 2 for details). The system was placed in the main track of the channel with the purpose of studying the section through which the hugest quantity of material passes. We also installed a time-lapse video in order to calculate the rate of the displacements. During the monitoring activity (2 years), the landslide reactivated three times and this allow us to detect clear data of a ‘steady’ condition, in which the earthflow moved downslope with a velocity in a range of cm/month, and also of a paroxysmal phase, in which the velocity reached the range of several meters/hours.

Concerning the geomorphology of the this type of landslides, recent researches have revealed that large earthflows can be composed of several distinct kinematic zones operating in unison to transmit sediment pulses along the length of the flow (e.g. Guerriero et al., 2014, 2016). A kinematic zone (Guerriero et al., 2014) is formed by major paired driving and resisting earth flow elements and can be considered as a sector of the earth flow with a specific kinematic behavior (e.g. Guerriero et al., 2016c). It comprises an area of extension with one or more normal faults at its head (driving elements), and an area of shortening with one or more back-tilted surfaces and/or thrusts at its toe (resisting elements). Under these conditions, a large earth flow can be considered as a chain of kinematic zones, and the transition between two consecutive kinematic zones is the area between the compressive structures of the upper kinematic zone and the extensional structures of the lower kinematic zone. We study the Monte Pizzuto earthflow (Campania Region, South of Italy) in order to understand kinematic and geomorphological characteristic of this landslide.

After field investigations and observations, we think that it is not always correct to consider the earth flow sediment discharge as constant. This assumption should be framed in the context of the activity state of the flow and considering that during surging events, the earthflow material behaves

as a incompressible fluid. Moreover, during surging events, the earth flow behavior might be simulated using macro-viscous models without oversimplifying the problem, and the distribution of structures at the surface of an earth flow provide information about the geometry of the basal slip surface and the velocity profile of the earth flow.

In the second paper, we used the ReMi technique in order monitor the slope in continuous and to find a relationship between the surface wave velocity and the displacement rate. In the same paper, we used periodic ReMi-MASW surveys to obtain reliable data of surface wave velocity over time. In the third paper, we used HVSR and ReMi-MASW acquisitions to reconstruct the depth and the geometry of the basal slip surface. Instead, in the last paper (4) we used similar geophysical approach to verify the liquefaction susceptibility of soils. Our dataset was built on the technical information coming from the May 20 and 29, 2012 earth- quakes (ML=5.9 and ML=5.8, respectively) (Castellaro et al., 2015) that occurred in the Po Plain area (Emilia Romagna region, Northern Italy), which caused a large number of liquefaction phenomena (Bertolini and Fioroni, 2012; Di Manna et al., 2012; Papathanassiou et al., 2012; Emergeo Working Group, 2013) to a distance of up to 30 km from the epicenters. We performed 84 surveys in the study area using twelve 4.5 Hz polarized geophones set at intervals of 2.5 m each, connected to a Soilspy Rosina acquisition system (MoHo s.r.l). All the data were processed by using the Grilla software. The results shown that is it impossible to distinguish liquefied from not liquefied soils, due to the fact that these geophysical approaches do not have sufficient sensitivity to be used as predictors of liquefaction in the classic frame of seismic demand versus soil capacity scheme.

PAPER 1

Rheological properties of clayey soils originating from flow-like landslides

Carrière S.R., Jongmans D., Chambon G., Bièvre G., Lanson B., Bertello L., Berti M., Chambers J.E., Jaboyedoff M., Malet J-P.

*submitted to **Journal of Geophysical Research: Earth Surface,** June 2016

Rheological properties of clayey soils originating from flow-like landslides

S.R. Carrière[1], D. Jongmans[1], G. Chambon[2], G. Bièvre[1], B. Lanson[1], L. Bertello[3], M. Berti[3], J.E. Chambers[6], M. Jaboyedoff[4], J-P. Malet[5]

[1] Université Grenoble Alpes, CNRS, ISTerre, F-38000 Grenoble

[2] Université Grenoble Alpes, IRSTEA, UR ETGR Grenoble, France

[3] Universita' di Bologna, Dipartimento di Scienze Biologiche, Geologiche e Ambientali, 40127, Bologna, Italy.

[4] Université de Lausanne, Géopolis, Switzerland

[5] Institut de Physique du Globe de Strasbourg, CNRS UMR 7516 / Université de Strasbourg, 5 rue Descartes, F-67084 Strasbourg Cedex, France

[6] British Geological Survey, Keyworth, U.K

Corresponding authors:

- Simon Carrière simon.carriere@hotmail.fr
- Denis Jongmans denis.jongmans@univ-grenoble-alpes.fr

Key Points:

- Clayey soils producing flow-like landslides exhibit a yield stress fluid behavior and a viscosity bifurcation when ongoing fluidization
- Relationships between the rheological and geotechnical parameters of the soils are investigated
- The water content deviation from the Atterberg liquid limit controls the mechanical behavior of clay soils at the solid-fluid transition

Abstract

Flow-like landslides in clayey soils represent serious threats for populations and infrastructures and have been the subject of numerous studies in the past decade. However, despite the rising need for landslide mitigation with growing urbanization, the transient mechanisms involved in the solid-fluid transition are still poorly understood. One way of characterizing the solid-fluid transition is to carry out rheometrical tests on clayey soil samples to assess the evolution of viscosity with the shear stress. In this study, we carried out geotechnical and rheometrical tests on clayey samples collected from 6 flow-like landslides in order to assess if these clayey soils exhibit similar characteristics when they fluidize (solid-fluid transition). The results show that: 1) all tested soils except one clearly exhibit a yield-stress fluid behavior associated with a bifurcation in viscosity (described by the critical shear rate $\dot{\gamma}_c$) and in shear modulus G; 2) the larger the amplitude of the viscosity bifurcation, the larger the associated drop in G; 3) the water content (w) deviation from the Atterberg liquid limit (LL) is a key parameter controlling a common mechanical behavior of these soils at the solid-fluid transition. We propose exponential laws describing the evolution of the critical shear stress τ_c, the critical shear rate $\dot{\gamma}_c$ and the shear modulus G as a function of the deviation w-LL.

Keywords: clay - solid-fluid transition – rheology - viscosity bifurcation - Atterberg limits

1. Introduction

Landslides in clay-rich soils are very common and exhibit a large variety of sizes, morphologies and kinematics [*Maquaire et al., 2003; Mackey et al., 2009; Picarelli et al., 2005, Chambers et al., 2011; Bièvre et al., 2011*]. Particularly intriguing are the complex processes through which initially rigid slides can transform into flow-type movements like mud flows or debris flows [*Van Asch et al., 2009; Mainsant et al., 2012a*]. Slow-moving earthflows, with typical velocities of meters per year ($m.yr^{-1}$), can suddenly accelerate and acquire velocities ranging from meters per hour ($m.h^{-1}$) to meters per second ($m.s^{-1}$) [*Hungr et al., 2014]*. These apparently unpredictable acceleration and fluidization events constitute a serious threat to local populations and infrastructures. Although the triggering mechanisms always appear to involve a rapid increase in soil water content, generally caused by heavy and/or long-lasting rainfalls, the current ability to forecast and model these events is still limited. In geotechnics, the mechanical behaviour of cohesive soils is classically characterized by two experimentally-determined water contents, the Atterberg plastic and liquid limits PL and LL [*Mitchell, 1993*]. A fair assumption is then to consider that fluidization of the moving mass, and slide-to-flow transition, occur when the water content w reaches the liquid limit LL [e.g., *Hungr et al., 2014*]. However, this interpretation disregards the stress state within the material, which constitutes the driving force of the instability. One of the main challenges therefore lies in the characterization of the mechanical behavior (stress – strain – shear rate relations) of these clayey landslides in the vicinity of the apparent solid-fluid transition.

From a mechanical point of view, two main approaches coexist to describe the generation of mud and debris flows from landslides. The *two-phase* approach posits that solid-fluid transition is caused by an increase in interstitial pore pressure, i.e. by a decrease in effective normal stresses in the soil [e.g., *Iverson et al., 1997 2005, 2016; Picarelli et al., 2004*]. The rheological approach, on the other hand, assumes that the material can be described by an effective single-

phase constitutive law, and that fluidization occurs when a critical stress threshold is exceeded [*Ancey 2007; Mainsant et al., 2015*]. While the former approach is well-suited to frictional materials, whose strength is intrinsically pressure-dependent, the latter better applies to cohesive materials with high water content ($w \approx LL$), for which strength can be regarded, at least as a first approximation, as an intrinsic rheological property [*Coussot and Piau, 1994; Coussot and Ancey, 1999*]. The present study takes place within the rheological framework, and investigates the possibility to describe solid-fluid transition in clayey landslides in terms of a few characteristic rheological parameters. Following the most recent landslide classification proposed by *Hungr et al.* [*2014*], we consider here clay soils as soils with a plasticity index $PI = LL\text{-}PL$ larger than 5%. The cohesive character of these soils arises from the relatively large proportion of fine particles (diameter less than 10 - 40 μm, typically, among which mineralogical clays) that develop colloidal interactions. When the water content approaches the liquid limit *LL*, these soils typically turn into muddy slurries, although large, non-colloidal debris can also be present.

Rheological measurements on various types of colloidal suspensions and pastes show that these materials generally obey, in steady-state, a viscoplastic-type constitutive law [e.g., *Coussot, 2005*]. They behave as soft solids when the applied stress lies below a critical stress threshold (or yield stress) τ_c, and flow as viscous fluids above this threshold. Although only few studies attempted to directly characterize the rheological behavior of clay soils and muds originating from landslides [e.g., *Coussot et al., 1998; Picarelli et al., 2004; Malet et al., 2003, 2005*], existing ones show that these natural materials can also be described by viscoplastic laws for sufficiently high water contents. The evolution of critical shear stress τ_c with water content and particle properties (e.g., size distribution, mineralogy, etc.), however, remains poorly understood. For fine-grained sediments, a few authors [*Locat and Demers, 1988; Locat, 1997; Jeong et al., 2010*] proposed empirical relations between τ_c and the geotechnical parameter $LI = (w–PL)/PI$ (liquidity index). Water salinity and ionic content were also shown to have an influence on the critical stress [*Locat. 1997; Jeong et al., 2010, 2012; Maio and Scaringi, 2016*]. For debris flows, the critical shear stress τ_c was shown to be highly sensitive to the type of clays (in particular, swelling clays) present in the material [*Bardou et al., 2007*]. More fundamental studies indicated that, in general, the influence of fine and coarse particle fractions should be distinguished [*Coussot and Piau, 1994; Ancey and Jorrot, 2001*]. The critical stress τ_c is reported to increase exponentially with the concentration in fine colloidal particles [*Coussot and Piau, 1994; Coussot, 1995; Ancey and Jorrot, 2001*]. An increase in τ_c with the addition of coarse, non-colloidal, particles is also observed, but at a smaller rate [*Ancey and Jorrot, 2001; Ovarlez et al., 2015; Dagois-Bohy et al., 2015*]. A primary objective of this study was then to investigate how the critical shear stress τ_c of clay landslides vary, and how these variations can be rationalized in terms of geotechnical parameters of the material.

In addition to viscoplasticity, colloidal materials are also frequently characterized by thixotropy, i.e. time / history dependence of the critical shear stress τ_c, and by the existence of a critical shear rate $\dot{\gamma}_c$ below which the material cannot flow [*Coussot et al., 2002a, b; Coussot, 2005*]. This critical shear rate is associated to an abrupt viscosity drop (or bifurcation) at the solid-fluid transition, potentially leading to catastrophic fluidization phenomena [*Coussot, 2005; Huynh et al., 2005, Khaldoun et al., 2009*]. Recently, rheometrical tests performed on natural clay samples originating from the Trièves area (a French Alps region affected by numerous landslides) also revealed a thixotropic behaviour with a highly pronounced viscosity bifurcation [*Mainsant et al.,*

2012b; Mainsant et al., 2015]. In addition, this bifurcation was accompanied by a severe drop in elastic shear modulus *G*, suggesting that this parameter (or, alternatively, the shear wave velocity $Vs = (G/\rho)^{1/2}$, where ρ is the bulk density of the soil), which characterizes the rigidity of the soil, could actually constitute a proxy for the solid-fluid transition. A second objective of this study was therefore to investigate whether these complex rheological trends are also observed with other clay landslides and, more generally, to assess whether soils coming from clayey landslides exhibit similar rheological properties at the solid-fluid transition.

This paper thus reports on a detailed geotechnical and rheometrical characterization of soil samples coming from six different clayey landslides across Europe. These landslides were chosen because they gave rise to mud or debris flows in the past and appear prone to slide-to-flow transitions. The main morphological features of the landslides and the experimental methods used to characterize the soil samples are first briefly described. We then summarize the geotechnical and rheological properties of the samples, with a particular focus on critical shear stress τ_c, critical shear rate $\dot{\gamma}_c$, and shear modulus G (as well as the corresponding shear wave velocity V_s). Finally, the existence of relations between these different properties is investigated, and the possible implications of our laboratory results at field scale are discussed.

2. Site description

Clayey soils were sampled at six landslide sites having experienced flow-like motions: Harmalière (HA), Super-Sauze (SU), and Char d'Osset (CO) in the French Alps, Hollin-Hill (HO - England), Montevecchio (MO – Northern Apennines, Italy) and Pont-Bourquin (PO - Switzerland). The location of the landslides and their geometry are shown in *Figure 1*. Pictures of the landslides are shown in *Figure 2* and their main characteristics are given in *Table 1*. The landslides have developed in geological formations of various ages (from Callovo-Oxfordian to Quaternary) and exhibit a large variety in shape, surface and volume (from approximately 35 10^3 m^3 for PO to 25 10^6 m^3 for HA) (*Table 1*). Only one landslide affects the in-situ geological bedrock itself (quaternary glaciolacustrine deposits at HA). In all other sites, the moving mass is made of weathered clay sliding on the parent rock. In terms of slope angles, the HA, HO and MO landslides exhibit gentle slopes ranging from 9 to 12°. In contrast, the PO, SU and CO landslides have a more abrupt morphology with slope angles between 25 and 33°. Three landslides are channelized in thalwegs (SU, CO and MO), with a high length/width ratio ranging from 6 to 23 (*Figures 1 and 2*). The Harmalière landslide is channelized in its lower part only, and exhibits a length/width ratio of 1.8. In contrast, the HO landslide exhibits a length/width ratio lower than 1, while the PO landslide is elongated.

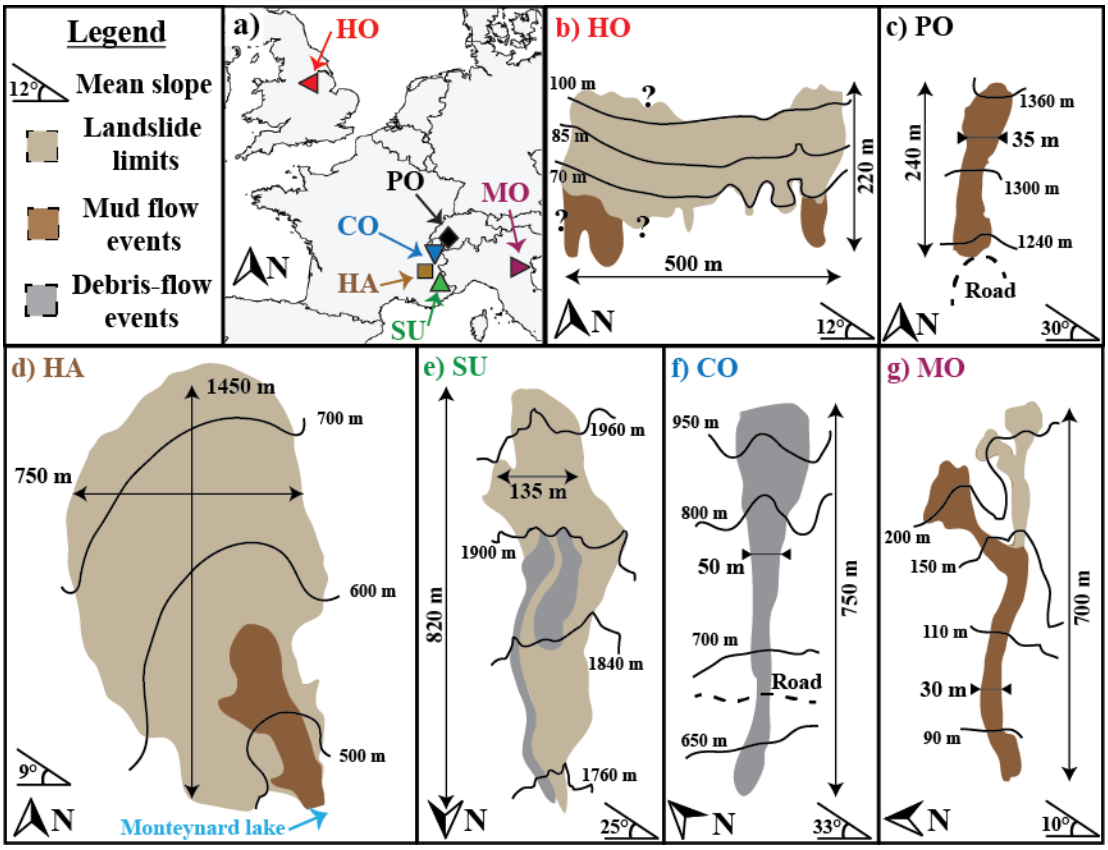

Figure 1: Location (a) and simplified morphological maps of the six landslides: b) HO: Hollin-Hill, c) PO: Pont-Bourquin, d) HA: Harmalière, e) SU: Super-Sauze, f) CO: Char d'Osset, and g) MO: Montevecchio. The mud flow and debris flow events are differentiated by their brownish and grey color, respectively. As the CO landslide only evolves sporadically to a debris flow, the site is shown in grey with the limits of the last debris flow of 2011. The western part of the HO landslide is covered by trees, making it difficult to assess the exact limits of the earthflow.

The maximum measured displacement rates range from 0.01 m.yr^{-1} at HO to more than 50 m.yr^{-1} at SU. According to *Hungr et al., [2014]*, these landslides can therefore be described as very slow to moderately slow earthflows. The CO landslide is dormant at the present time. Information about recorded mud flow and debris flow events is also given in *Table 1*, including the volume of the flows, their velocity (when known) and their mobility coefficient (or Heim coefficient: ratio height/length, H/L). The CO and SU sites are characterized by clayey soils having a high content of rocks or debris, while the other 4 sites are characterized by clayey soils with low content of rocks or debris. Size distribution measurements made on the 6 sites show that the complete material passes through the 400 µm sieve, except for Pont-Bourquin and Super-Sauze soils. Although no size distribution measurements could be made on the soil of Char d'Osset, field observations indicate that the fraction of grains passing through the 400 µm should be less than 50 %. To highlight the different grain-size compositions, we call "debris flows" (DF) the flow-like landslides originated in clayey soils enriched with debris (CO and PO SU sites) and "mud flows" those generated in clayey soils with low debris content (HA, MO, HO sites). The volume and velocity of these flow events can vary significantly among the sites. For example, at SU, several debris flows were reported with volumes of a few thousand m^3 and velocities as high as 4 m.s^{-1}, while the MO landslide experienced mud flows of about 90 10^3 m^3

flowing at approximately 5 m.day^{-1}. The *H/L* coefficient of these flow events, which varies inversely with the mobility, also exhibits a large range of values with low values of 0.16 and 0.17 for the HO, HA, and MO landslides (showing high mobility), and higher values of 0.3 and 0.45 (hence lower mobility) for SU and PO. More detailed geomorphological and geological information about the 6 landslides can be found in the supporting information of this paper.

	Site	Hollin-Hill	Pont-Bourquin	Harmalière	Super-Sauze	Char d'Osset	Monte-vecchio
Geology and morphology	Geology	Lias, Whitby Mudstone	Aalenian black shales and flysch	Quaternary glaciolacustrine clays	Callovo-Oxfordian black marls	Eocene clayey flyschs	Holocene clayey and silty marl
	Sliding Material	Weathered	Weathered	Parent	Weathered	Weathered	Weathered
	Length (m)	220	240	1450	820	400	700
	Width (m)	> 500	30-60	750	50-150	30-100	30-50
	Thickness (m)	2-5 10^3	5-10 10^3	10-50 10^3	8-30 10^3	5-10 10^3	8-10 10^3
	Surface (m²)	100 10^3	8 10^3	10^6	170 10^3	24 10^3	28 10^3
	Volume (m^3)	≈ 500 10^3	≈ 35 10^3	≈ 25 10^6	≈ 750 10^3	≈ 100 10^3	≈ 350 10^3
	Slope (°)	12°	30°	9°	25°	33°	10°
	Maximum surface velocity (m.yr^{-1})	0.01-2	3-6	0.1-7	50-100	0	0.1
	Channelized	No	Yes	Yes, in lower part	Yes	Yes	Yes
	% of fraction below 400 µm	100	65	100	50	?	100
Debris flows and mud flows	Flow type	MF	DF	MF	DF	DF	MF
	Volume	100-200 10^3	1 – 5 10^3	100 10^3	2 - 8 10^3	10^3	90 10^3
	Velocity	Unknown	Unknown	Unknown	3 – 4 m.s^{-1}	Unknown	5m.day^{-1}
	Mobility H/L (Height/Length)	0.16	> 0.5	> 0.16	0.3	0.45	0.17

Table 1: Geological, morphological and kinematic characteristics of the Hollin-Hill (HO), Pont-Bourquin (PO), Harmalière (HA), Super-Sauze (SU), Char d'Osset (CO) and Montevecchio (MO) landslides. The characteristics of the earthflows, as well as those of the known mud flow (MF) and debris flow (DF) events, are given.

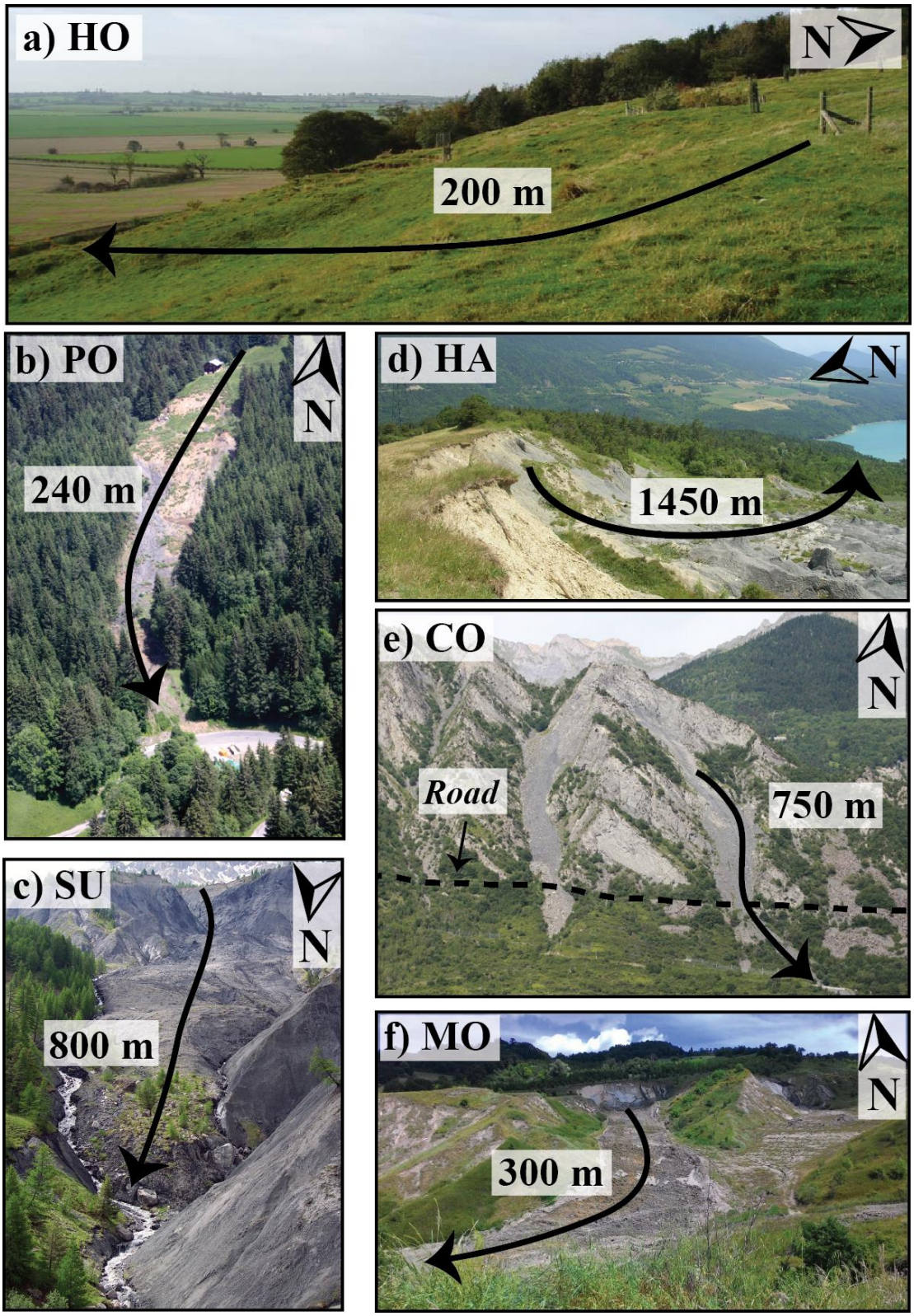

Figure 2: Pictures of the six landslides. a) Hollin-Hill (HO), b) Pont-Bourquin (PO), c) Super-Sauze (SU), d) Harmalière (HA), e) Char d'Osset (CO) and f) Montevecchio (MO) landslides. The arrows show the movement direction and gives an order of magnitude of the distance.

192 ## 3. Methods

193 ### 3.1 Geotechnical and mineralogical characterization

194 The clay soils were collected at a depth of approximately 0.3 m on the six landslides. All
195 samples were sieved and particles with a size lower than 400 µm were retained. Resulting
196 particle size distributions were measured using a laser analyzer (Malvern Mastersizer 2000).
197 Identification of crystalline materials in the samples was performed through X-ray diffraction
198 (XRD) using a Bruker D8 diffractometer. XRD patterns were recorded from randomly oriented
199 powders. No attempt was made at quantifying amorphous materials that are possibly present in
200 the samples.
201 The Atterberg limits of the 400-µm sieved soil samples were measured using the cup apparatus
202 for the liquid limit (*LL*) and the rolling test method for the plastic limit (*PL*), applying European
203 norm CEN/ISO/TS 17892-12. The gravimetric water content w (in %) was measured as M_w/M_s,
204 where M_w is the mass of water in the sample and M_s is the mass of dried soil. The plasticity index
205 $PI=LL-PL$ and liquidity index $LI = (w-PL)/PI$ were derived from these measurements.
206 Methylene Blue (*MB*) absorption tests were conducted to determine the specific surface area S_s
207 of the clay particles [*Santamarina et al., 2002*] according to the European norm EN 933-9. The
208 Cation Exchange Capacity (*CEC*, expressed in milliequivalents (meq) per 100 g of dry solid*)*
209 was measured through exchange with cobaltihexamine and dosing of its residual concentration in
210 the equilibrium solution using a UV-visible spectrophotometer and cobaltihexamine ion
211 absorption band at 472 nm.

212 ### 3.2 Rheometrical characterization

213 Rheometrical tests were performed using a Bohlin-CVOR instrument with a 60 mm parallel-
214 plate tools (see *Figure 3a*). With this geometry, relatively thick samples can be tested (as
215 required to consider the tested mixtures as continuum materials) while the shear stress and shear
216 rate within the samples can still be determined accurately [*Coussot, 2005*]. The gap between the
217 plates (sample thickness) was kept constant at 3600 µm for all tests. This value, approximately
218 ten times larger than the maximum grain size in the samples, was found to be a good
219 compromise to minimize end effects that develop with thicker samples. Two sets of tools, in
220 PVC and stainless steel respectively, both roughened to prevent wall slip, were used to check for
221 repeatability of the results. The tests were carried out in an air-conditioned room, and the
222 temperature of the samples was maintained constant at 21 °C during the experiments. Before
223 each test, the samples were pre-sheared at a shear rate of 50 s^{-1} for 20 s and then left at rest for 10
224 s to ensure a reproducible initial state. Samples at different water contents were prepared by
225 mixing the dried soils with distilled water in a blender. It was only possible to test samples with a
226 gravimetric water content w above the liquid limit *LL*. For $w < LL$, cracking and heterogeneous
227 deformation were observed.
228
229 Two types of rheometrical protocols were applied to investigate the behavior of the clay soils in
230 the vicinity of the solid-fluid transition. First, standard creep (SCr) tests, which consist in
231 imposing a constant shear stress τ and monitoring the resulting shear rate, were used to determine
232 the critical shear stress τ_c and critical shear rate $\dot{\gamma}_c$ of the samples. Four typical SCr tests obtained
233 for PO soils at a water content w = 87.4 % (LI = 3.66) are shown in *Figure 3b*. At low imposed
234 stress (τ = 30 Pa), the shear rate regularly decreases to reach values lower than 10^{-4} s^{-1} at the end
235 of the test. In turn, the apparent viscosity, defined as the ratio of shear stress over shear rate,

tends towards very high values (above 10^7 Pa.s), which corresponds to a solid behavior. Conversely, at high stress (τ = 60 Pa), the shear rate tends towards a constant value that increases with the imposed stress level, as for a viscous fluid. These observations are consistent with a viscoplastic behavior of the material. The critical shear stress, here $\tau_c \approx 53$ Pa, can be defined as the stress level for which the transition between these two regimes occurs. To obtain a good accuracy, multiple tests with stress increments of 1 to 5 Pa were performed in the vicinity of the solid-fluid transition. In some cases, however, it was difficult to determine whether the sample is effectively in solid or fluid regime within a range of a few Pa. In practice, the value of τ_c is thus taken as the average between the lowest stress value for which the sample is surely in fluid regime, and the highest stress value for which it is surely in solid regime. Depending on the suddenness of the transition and the repeatability of the results, which varies among the samples, the corresponding uncertainty on τ_c ranges between 5 % and 15 %. In the example of *Figure 3b*, the solid-fluid transition is also characterized by a marked jump in shear rate, which discontinuously passes from zero in solid regime to a finite value when the stress is just above the critical stress. This behavior is characteristic of a viscosity bifurcation, with the existence of a critical shear rate $\dot{\gamma}_c$ below which no steady flow is possible. In practice, due to the above-mentioned difficulties sometimes encountered in the determination of τ_c, we chose to define $\dot{\gamma}_c$ as the shear rate measured for $\tau = \tau_c + \Delta\tau$, where $\Delta\tau$ is a small stress increment above the transition taken equal to 5 Pa. This definition proved to be more robust, while still representative of the jump in shear rate observed at the transition. Hence, for PO sample at w=87.4 % (*Figure 3b*), $\dot{\gamma}_c$ is taken at 2.5 10^{-2} s^{-1}, which corresponds to the asymptotic shear rate value reached in the test at 58 Pa.

Second, oscillatory creep (OCr) tests were used to capture the associated drop in elastic shear modulus at the solid-fluid transition. These tests consist in superimposing small stress oscillations to a constant average shear stress level τ (see *Figure 3a*). The resulting strain is monitored and corrected for any linear trend associated to the average stress level. The complex viscoelastic modulus G^* is defined as the ratio between the stress and the detrended strain in the Fourier domain [*Bird et al., 1987*]. The amplitude of the stress oscillations was chosen to be roughly 1/10 of the critical stress τ_c in order to remain in the linear regime. The frequency of the oscillations was fixed at 5 Hz in order to be in a regime where the storage modulus (i.e. the real part of G^*) is independent of the frequency and can be identified to the elastic shear modulus G of the clayey soil [*Mainsant et al., 2012b*]. Four typical examples of OCr tests for PO soil at w = 87.4 % are shown in *Figure 3c.* A clear decrease in elastic shear modulus is observed when the soil fluidizes, with G dropping from values above 10,000 Pa when τ is just below τ_c (solid state), to values of about 1000-3000 Pa just above τ_c (fluid state). The shear elastic modulus then continues to rapidly decrease when the stress level is further increased, reaching very low values (100 Pa in the example shown) in the fully fluidized regime. We characterize the amplitude of the drop in G at the transition by the ratio of G_s/G_{tf}, where G_s and G_{tf} correspond to the values of G in the solid and fluid states, respectively. As for $\dot{\gamma}_c$, the value of G_{tf} is determined for $\tau = \tau_c + \Delta\tau$.

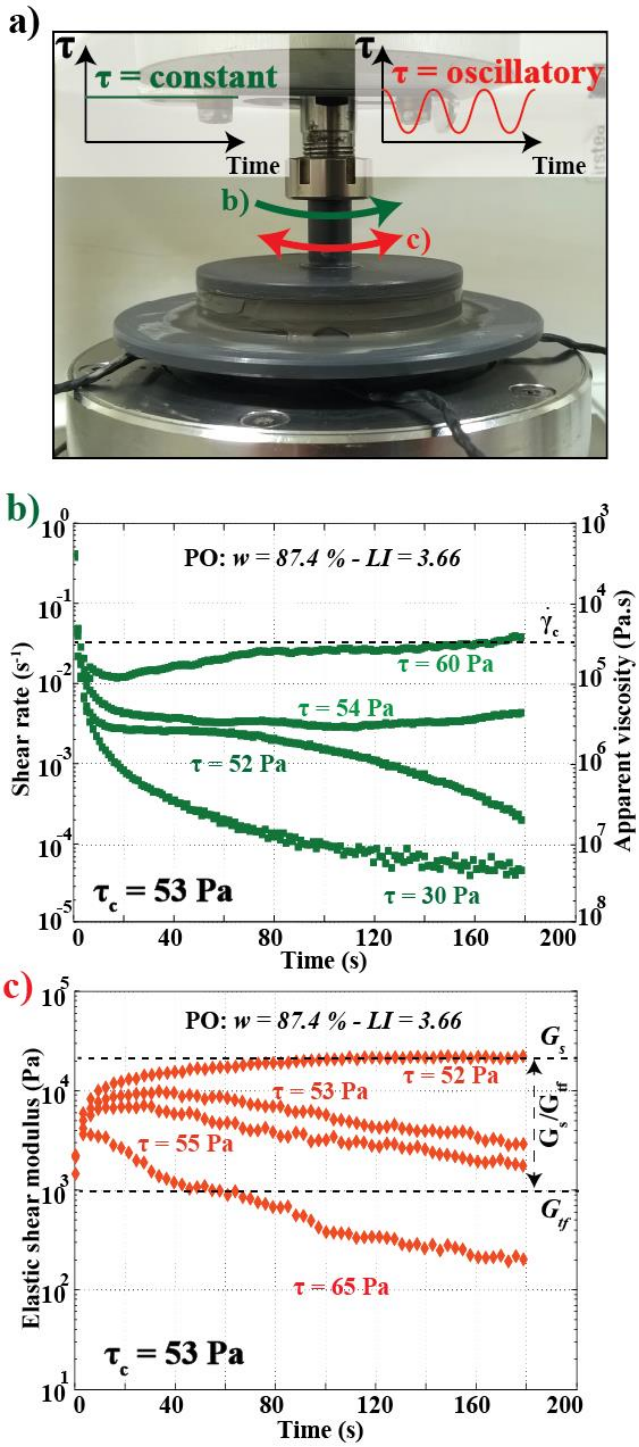

Figure 3: Illustration of the rheometrical tests. a) Picture of the Bohlin CVOR rheometer used to perform the standard creep tests SCr (constant stress with time – in green) and the oscillatory creep tests OCr (oscillatory stress with time – in red). b) Four SCr tests performed at stress levels τ = 30, 52, 54 and 60 Pa on PO (Pont-Bourquin) soil with a water content w = 87.4 % (LI = 3.66). The increase in shear rate (or decrease in apparent viscosity) at the critical shear stress τ_c =53 Pa is indicative of the transition from solid to fluid state. c) Four OCr tests performed below (52 Pa and 53 Pa) and above (55 Pa and 65 Pa) the critical shear stress τ_c for the same sample.

4. Geotechnical results

The grain size distributions of the six 400 μm-sieved soils are shown in *Figure 4a*.The values of D_{40} and D_2 (soil fractions below 40 and 2 μm, respectively), of the uniformity coefficient $C_u = d_{60}/d_{10}$, and of the curvature coefficient $C_c = (d_{30})^2/(d_{60}\ d_{10})$ are given in *Table 2*. (The diameter d_X correspond to the particle size for which X% of the particles are finer.) All samples exhibit C_u values higher than 6 and C_c values around 1, indicating wide particle size distributions with unimodal shapes. CO and PO samples stand out as coarser than the others, as shown by their grain size distributions and their lower D_{40} values (48 % and 60 %, respectively).

As shown in *Figure 4b*, the Atterberg limits show large variations among the different soils. Liquid limit *LL* ranges from very low (26.7 %) for CO to high (73.3 %) for HO. Plasticity index *PI* varies between 9.9 % (CO) and 25.6 % (HO and MO). According to the Unified Soil Classification System (USCS), four samples are described as low to medium plasticity clay soils (CO, SU, PO and HA), while the other two are high plasticity clay soils (MO and HO). In addition, two of the soils are classified as organic (HO and PO). Blue methylene and *CEC* tests also highlight wide variations in clay properties among the samples. HO soil exhibits the highest values with a specific surface area S_s of 80.1 $m^2.g,^{-1}$ and a *CEC* of 28.6 $meq.100g^{-1}$. In contrast, the CO sample is characterized by a low *CEC* (3.5 $meq.100g^{-1}$) and extremely low specific surface area S_s (5.7 $m^2.g^{-1}$). In terms of mineralogical composition (*Table 2*), most of the soils contain a significant amount of quartz and micas, from 19.6 % (MO) to 54.8 % (PO), with a fraction of clay minerals (all phyllosilicate but di-octahedral micas) varying between 4.3 % (SU) and 45.6 % (HO). Expendable 2:1 swelling clays, considered in this paper as smectites, have been detected in HO (33.8 %), MO (15.3%) and HA (9.4 %).

In summary, the soils collected at the six landslide sites exhibit strong differences in terms of geotechnical properties and mineralogical composition. HO and MO are the soils with the highest swelling potential, as shown by their large values of smectite content, *CEC*, and S_s. They also exhibit the highest values of *PI* and *LL*, indicating a high plastic potential. In contrast, the HA soil shows *PI* and *LL* values lower than those of MO and HO. This last sample contains nevertheless a significant amount of smectite (9.4 %), resulting in relatively high *CEC* and S_s values. SU and PO are described by intermediate *CEC*, S_s, *PI* and *LL* values and no smectite. Finally, CO has the lowest *CEC*, S_s, *PI* and *LL* values.

As previously attempted by several authors [i.e. *Farrar and Coleman, 1967; Yukselen and Kaya, 2006*], we looked for potential relations between these different geotechnical parameters of the samples. In particular, *Yukselen and Kaya. [2006]* proposed simple correlations between *CEC*, Atterberg limits, organic matter content, fine fraction and specific surface area. As shown in *Figures 4c-e*, the clay fraction D_2, the percentage of smectites, the Atterberg parameters *PL*, *LL* and *PI*, and the specific surface area S_s all appear to be positively correlated to the *CEC*. The highest determination coefficients are obtained between the specific surface area and the CEC (0.95) and between the percentage of smectite and CEC (0.93). Conversely, the determination coefficient between D_2 and CEC is weak (0.33), and the determination coefficients between *PL*, *LL*, *PI* and *CEC* are moderate (0.65, 0.86, and 0.86 respectively). It must be stressed out that these results have been obtained for six samples only, and therefore cannot provide generic trends. They appear however in good agreement with the conclusions of *Farrar and Coleman. [1967]* and *Yukselen and Kaya. [2006]*, which were based on more complete soil datasets. In

particular, *Yukselen and Kaya. [2006]* also reported a low determination coefficient between D_2 vs *CEC* (R^2 = 0.37), whereas they found better correlations between *CEC* and S_s (R^2=0.82), and between *CEC* and *LL* (R^2 = 0.6).

	Hollin-Hill	Pont-Bourquin	Harmalière	Super-Sauze	Char d'Osset	Monte-Vecchio
$D_{40} - D_2$ (%)	90 -16	60 – 6	98 – 20	88 – 15	48 – 3	83 – 29
C_u	6.7	14.3	6.7	8.7	11	11.4
C_c	1.1	0.7	0.8	0.9	1.5	0.9
Liquid limit *LL* (%)	73.3 +/- 0.8	47.7 +/- 0.7	39.0 +/- 0.2	33.3 +/- 0.9	26.7 +/- 0.4	51.7 +/- 0.5
Plasticity index *PI*	25.6 +/- 1	14.9 +/- 0.9	16.9 +/- 0.2	11.9 +/- 0.8	9.9 +/- 1	25.6 +/- 0.8
USCS classification	OH	OL	CL	CL	CL	CH
Specific surface area S_s ($m^2.g^{-1}$)	80.1 +/- 4.2	29.2 +/- 0.3	45.1 +/- 0.3	29.6 +/- 1	5.7 +/- 0.5	61.6 +/- 0.4
C.E.C ($meq.100g^{-1}$)	28.6	9.9	17.0	6.2	3.5	18.7
XRD (%)						
Quartz	21.8	16.5	18.9	23.9	20.9	15.5
Dioct. micas	20.1	54.8	28.9	37.3	33.4	19.6
Clay minerals	45.6	9.9	16.3	4.3	15.2	41
Expandable 2:1 clay	33.8	Ø	9.4	Ø	Ø	15.3

Table 2: Geotechnical and mineralogical characteristics of the 6 soil samples. D_{40} and D_2 represent the soil fraction below 40 and 2 μm respectively. $C_u = d_{60}/d_{10}$, where d_{60} and d_{10} are the diameters for which 60 % and 10 % of the particles are finer. $C_c = (d_{30})^2/(d_{60}\ d_{10})$. USCS classification: CL stands for inorganic silty clays of low to medium plasticity – OL: organic clays of low plasticity – CH: inorganic clays of medium to high plasticity - OH: organic clays of medium to high plasticity. The complete XRD results are presented in Appendix A of this paper.

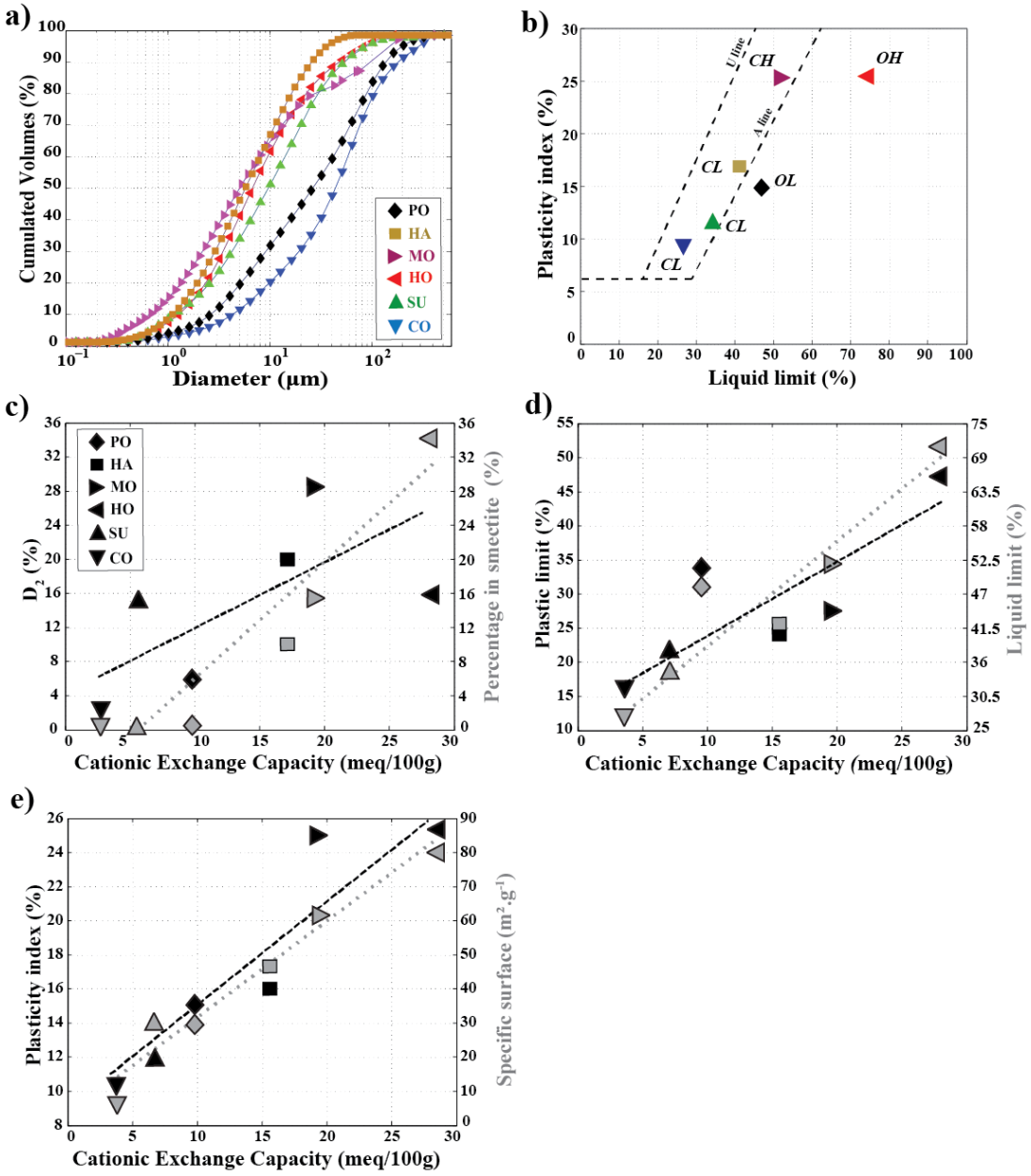

Figure 4: a) Grain size distribution of the six landslide samples sieved at 400 µm. b) Casagrande's chart with the U and A lines [*Mitchell, 1993*]*. According to the USCS classification, HA, SU and CO samples are inorganic clayey soils of low to medium plasticity (CL). PO and HO are classified as organic clayey soils of low plasticity (OL) and high plasticity (OH), respectively. MO is defined as an inorganic clayey soil of high plasticity (CH). c, d and e) Relationships between geotechnical, geochemical and mineralogical parameters for the six clay samples. In all cases, measurement errors are smaller than marker sizes. c) D_2 (soil fraction below 2µm, in black dashed line) and percentage of smectite (in grey dotted line) versus CEC. Linear regressions on D_2 vs CEC data (black dashed line) and percentage of smectite vs CEC data (grey dotted line) yield determination coefficients R^2 = 0.33 and 0.93, respectively. d) Atterberg limits PL and LL versus CEC. The determination coefficients obtained by linear regression are R^2 = 0.65 and R^2 = 0.86 for PL-CEC data (black dashed line) and LL-CEC data (grey dotted line), respectively. e) Plasticity Index and Specific surface area versus CEC. Determination coefficients are 0.86 and 0.95 for PI-CEC and S_s-CEC data, respectively.*

5. Rheometrical results

Standard Creep (SCr) and oscillatory creep (OCr) tests were carried out on the six soils for 4 to 6 values of gravimetric water content w above the liquid limit LL. In *Figures 5 and 6*, representative results are shown for two values of w that differ between the samples but always correspond to liquidity index LI approximately equal to 2 and 3, respectively.

In SCr tests at low water content ($LI \approx 2$, left column of *Figure 5*), all samples exhibit a solid-fluid transition occurring for critical shear stress values ranging from 43 to 166 Pa. The CO sample displays the lowest critical stress, while the largest values correspond to MO and SU soils. The solid-fluid transition is marked by clear viscosity bifurcations for HO and MO samples, with critical shear rate values of the order of 10^{-1} s^{-1}. SU and CO soils display less pronounced viscosity bifurcations, with $\dot{\gamma}_c$ of the order of 10^{-2} s^{-1}, and the solid-fluid transition appears almost continuous for the PO and HA samples. If existent, $\dot{\gamma}_c$ values in these latter cases are very small, at most of the order of 10^{-2} s^{-1}. At a higher water content ($LI \approx 3$, right column of *Figure 5*) solid-fluid transitions are still observed for all samples, except for the CO soil for which the fluid regime seems reached even for the lowest shear stress values tested. Generally, the critical shear stress τ_c is observed to decrease when water content w increases. Conversely, the critical shear rate $\dot{\gamma}_c$ tends to increase with w. These trends are particularly marked for the HO sample, with a critical stress dropping from 127 to 40 Pa between $LI = 2$ and 3, respectively, and a concurrent spectacular increase in $\dot{\gamma}_c$ from $2\ 10^{-1}$ to more than 10 s^{-1}. PO and HA samples, for which a viscosity bifurcation was hardly observed at $LI = 2$, are characterized by values of $\dot{\gamma}_c = 10^{-2}$ s^{-1} and $4\ 10^{-2}$ s^{-1} at $LI = 3$, respectively.

OCr tests in *Figure 6* show the evolution of the elastic shear modulus G at the solid-fluid transition. Consistently with the results of [*Mainsant et al., 2012b*], the solid-fluid transition appears to be systematically accompanied, for all tested samples, by a decrease in G. We carefully ascertained that this decrease occurs for critical shear stress values which are identical, within experimental uncertainties, to the critical shear stress values determined in SCr tests. Values of G in the solid regime (G_s) are observed to decrease with the water content: they vary in the range $10^4 - 4\ 10^4$ Pa for $LI = 2$, and in the range $5\ 10^3$ - $2\ 10^4$ for $LI = 3$. The drop in G at the transition, characterized by the ratio G_s/G_{tf}, appears to be variable among the samples. It is highly pronounced for HO and MO soils, in particular for $LI = 3$, where G drops by several orders of magnitude when increasing the stress level by only a few Pa beyond the critical stress. On the contrary, the drop in G at the transition is much smaller for HA, SU and PO soils for $LI = 2$, and the decrease in elastic modulus between the solid and fluid regimes appears more progressive in these cases. Generally, it is observed that, the larger the amplitude of the viscosity bifurcation observed in SCr tests, the larger the associated drop in G at the solid-fluid transition. The elastic modulus then continues to decrease when the stress level is further increased beyond τ_c, and all samples are eventually characterized, in the "fully-fluidized" regime, by G values that are at least one order of magnitude smaller than G_s.

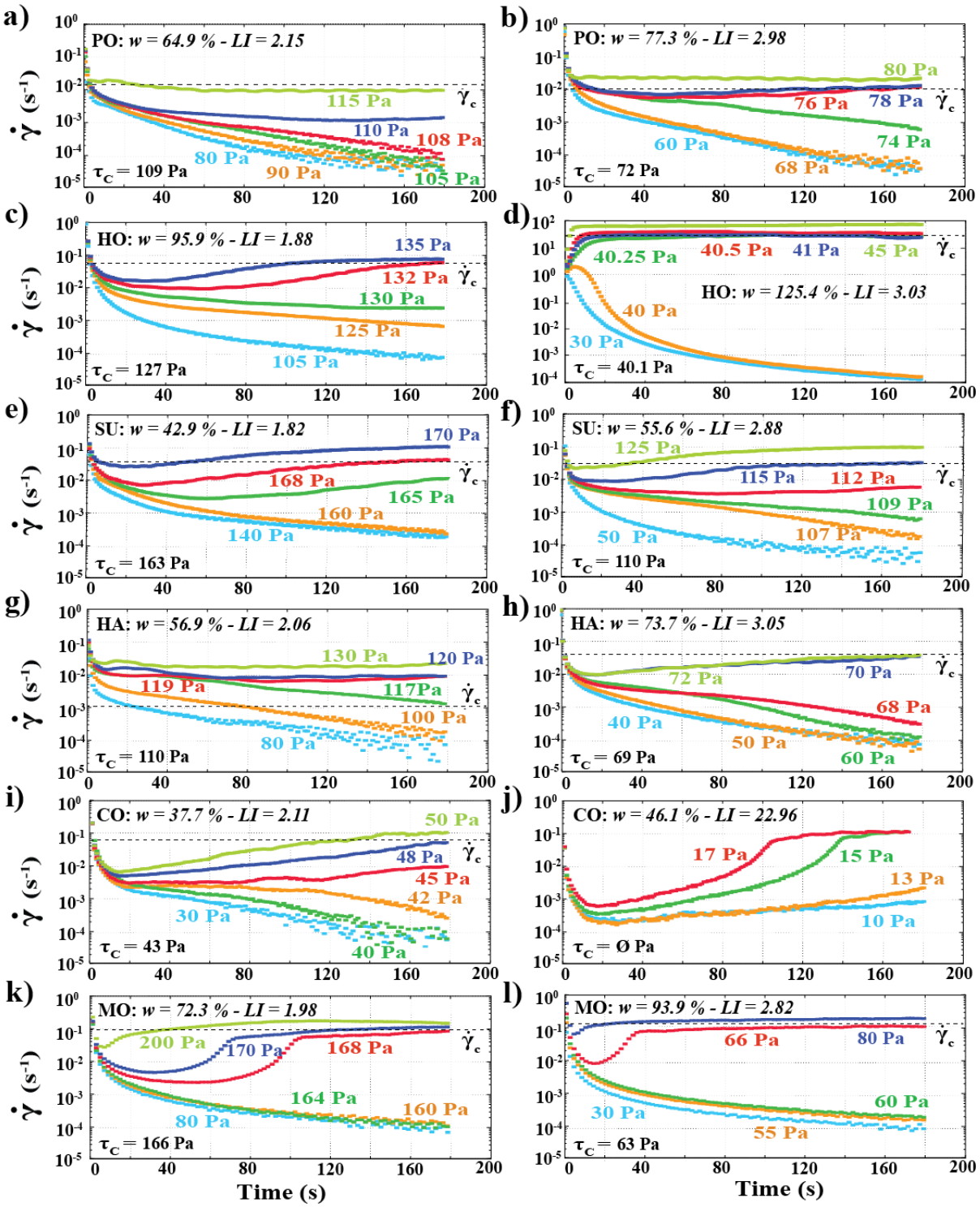

Figure 5: Shear rate $\dot{\gamma}_c$ vs time curves measured during Standard Creep tests (SCr) conducted on Pont-Bourquin (PO, a-b), Hollin-Hill (HO, c-d), Super-Sauze (SU, e-f), Harmalière (HA, g-h), Char d'Osset (CO, i-j) and Montevecchio (MO, k-l) samples for two values of liquidity index approximately equal to 2 (left column) and 3 (right column). Corresponding water contents w are indicated in legend. The critical shear stress τ_c and critical shear rate $\dot{\gamma}_c$ inferred from the tests (see Methods section) are indicated for each sample.

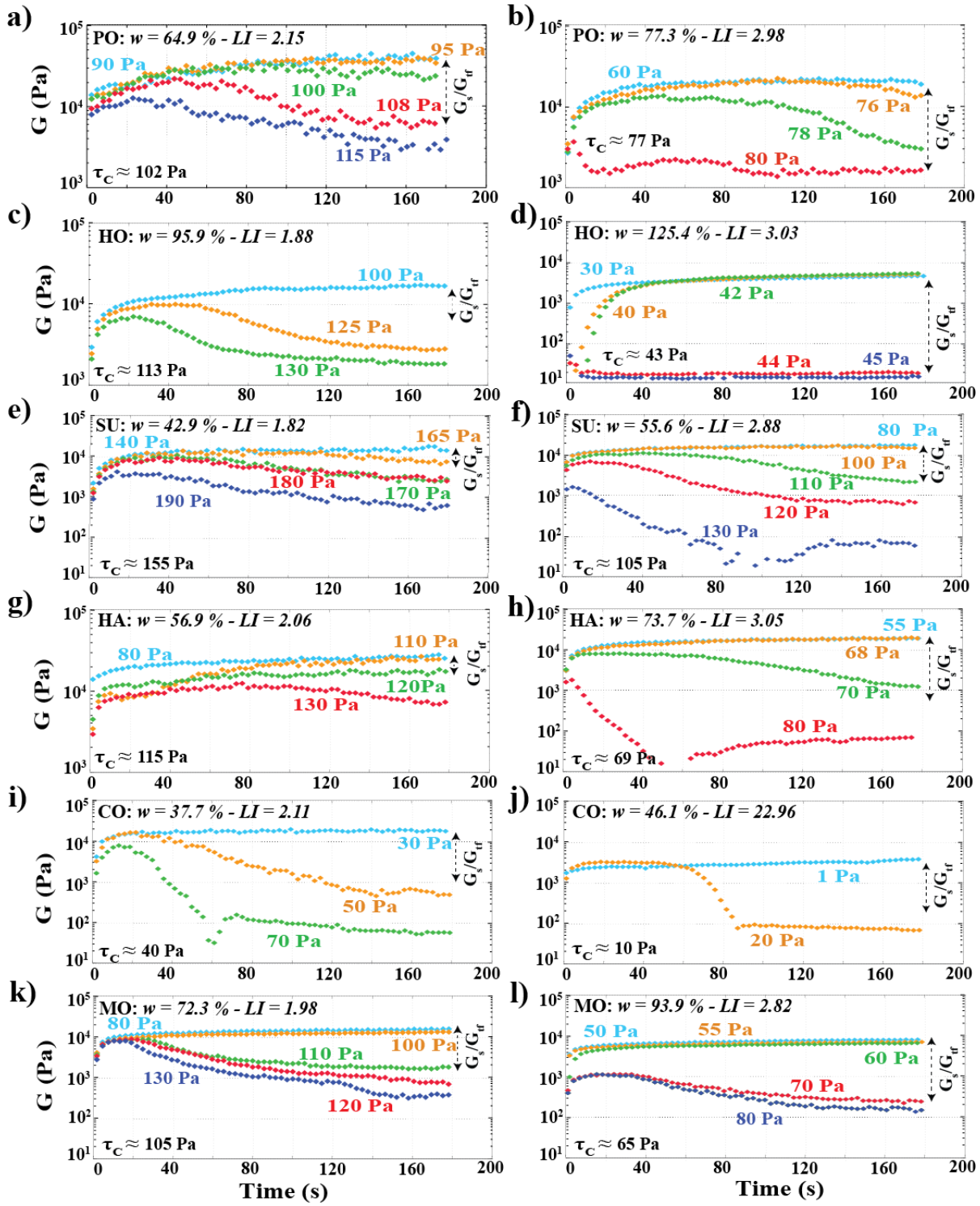

Figure 6: Elastic shear modulus G vs time measured during Oscillatory Creep tests (OCr) on Pont-Bourquin (PO, a-b), Hollin-Hill (HO, c-d), Super-Sauze (SU, e-f), Harmalière (HA, g-h), Char d'Osset (CO, i-j) and Montevecchio (MO, k-l) samples for two values of liquidity index approximately equal to 2 (left column) and 3 (right column). The values of the critical shear stress τ_c obtained in SCr tests are recalled. The ratio between G_s and G_{tf} (see Méthodes section) is used to quantify the drop in G at the solid-fluid transition.

6. Discussion

The occurrence, in fixed-volume rheometrical tests, of a solid-fluid transition for a well-defined value of critical shear stress τ_c, is a clear hallmark of a viscoplastic rheological behavior. Frictional materials, on the contrary, do not display any yield stress in such a configuration [*Boyer et al., 2011; Trulsson et al., 2015*]. Hence, all soil samples tested in this study effectively exhibit a viscoplastic behavior, except for CO soil at high water content for which no critical stress could be measured. This latter soil is also characterized by the lowest plasticity index *PI*, the lowest *CEC* and S_s values, and the lowest amount of fine particles. According to these characteristics, we may assume that CO soil actually presents a rheological behavior that is more of the frictional-type, particularly when the water content is high. This soil will not be taken into account in the upcoming analyses, in which only samples exhibiting a clear viscoplastic behavior will be considered.

6.1 Evolution of the critical shear stress

Our results for the five soils exhibiting a viscoplastic behavior show a clear increase in the critical shear stress τ_c when the water content w decreases (*Figure 7a*), i.e. when the solid fraction Φ increases ($\Phi = 1/(1 + w.\rho_s)$ where ρ_s is the dry density, taken equal to 2.7 g.cm^{-3}) since all samples are saturated. However, values of τ_c may vary by almost a factor of 2 among the different soils for a given solid fraction (*Figure 7a*), and no generic trend is apparent among the samples. This indicates that other parameters beyond the volume fraction also have an influence on the critical stress. In particular, it is known that fine (colloidal) and coarse (non-colloidal) particles contribute differently to the critical shear stress [*Coussot and Piau, 1994; Ancey and Jorrot 2005; Ovarlez et al., 2015*], and that the critical shear stress is therefore also sensitive to the grain size distribution of the samples. In our study, large differences in D_{40} (see *Table 2*), and therefore in the relative proportions of fine and coarse particles, can be noted between the different clay soils. This is likely to partly explain the specific evolutions of τ_c as a function of the solid fraction (or water content) observed for each soil. We thus examined whether the variations of τ_c could be rationalized in terms of the geotechnical characteristics of the samples.

In an early study on sensitive clays, *Locat and Demers [1988]* proposed relations between the critical shear stress τ_c and the liquidity index *LI*. The parameter *LI*, in which the water content w is scaled by Atterberg's limits *PL* and *LL*, indirectly accounts for fine content and clay surface properties (through the existence of relations between D_2, *PI*, *LL*, *CEC* and S_s, as shown in *Figure 4*) [*Locat and Demers, 1988*]. These authors showed that τ_c values, obtained in their case through a fit of flow curves measured with a laboratory rheometer, could be bounded by the two following relations:

$$\tau_c = \left(\frac{12.05}{LI}\right)^{3.13} \quad (1)$$

for high pore salinity (30 g.L^{-1}), and

$$\tau_c = \left(\frac{5.81}{LI}\right)^{4.55} \quad (2)$$

453
454 for low pore salinity (0 $g.L^{-1}$).
455
456 Subsequently, *Locat [1997]* showed that these two bounding relations remain valid for different
457 clay soils, mostly of glaciomarine origin, over a wide range of *w* and plasticity values. Values of
458 τ_c versus *LI* corresponding to our samples are displayed in *Figure 7b*, along with the two curves
459 corresponding to equations (1) and (2). It appears that all τ_c measurements are gathered around
460 the high-salinity curve for low *LI*-values, while some of the data tend to exceed this curve for
461 high *LI*-values. It must be stressed out that none of the soils studied here contain salts. The
462 relative agreement between the high-salinity curve and our data may therefore be coincidental. In
463 addition, *Locat and Demers [1988]* and *Locat [1997]* determined τ_c through a fit of the flow
464 curves (using a Bingham model) while, in our study, τ_c values were obtained directly from creep
465 tests (without any underlying model). τ_c values measured in these two different ways can show
466 significant discrepancies [*Bonn et al., 2015*]. Similarly, *Locat and Demers [1988]* used the cone
467 penetration method for determining *LL*, while we applied the percussion technique, and it has
468 been shown that liquid limits measured by the two methods are not necessarily identical
469 [*Sridharan and Prakash, 2000*]. Given these differences, further quantitative comparisons
470 between our results and those of *Locat and Demers [1988]* are not appropriate. A notable feature
471 of *Figure 7b*, however, is that the different soils follow specific trends according to *LI*. Hence
472 HO and SU samples, which show similar τ_c values for *LI* = 2.5, strongly diverge when *LI*
473 increases such that the value τ_c = 55 Pa is reached for *LI* = 3 with the HO soil, and for *LI* = 4.4
474 with the SU soil. Correspondingly, the SU soil is characterized by a much lower liquid limit *LL*
475 than the HO soil (33.3 and 73.3 respectively, see *Table 1*).
476
477 Detailed examination of *Figure 7b* led us to change the scaling of *w* and plot τ_c directly versus
478 the quantity *w-LL*. As shown in *Figure 7c*, this representation leads to a spectacular gathering of
479 all the data on a common linear trend (in log-linear coordinates). The data can be fitted by the
480 following exponential law with a determination coefficient R^2 = 0.91:
481
482 $$\tau_c = 246.7 \exp(-0.034(w\text{-}LL)) \qquad (3)$$
483
484 with τ_c in Pa, *w* and *LL* in %. The quantity *w-LL* thus appears as a major control parameter for the
485 critical shear stress values measured in this study. This parameter includes the effect of solid
486 fraction Φ as well as, through the Atterberg liquid limit, the effects of fine content and clay
487 properties. Nevertheless, the fact that such a simple measure of the deviation of *w* from *LL* is
488 sufficient to account for critical shear stress values measured in a variety of different clay soils
489 can seem surprising. It can be argued, however, that the existence of a relation between *LL* and
490 the shear strength (measured here by the critical shear stress) of the soil is not entirely
491 unexpected. In the percussion method used to determine *LL* (with Casagrande cup), the soil mass
492 flows on both sides of the cup due to impacts on the base. According to *Sridharan and Praklash*
493 *[2000]*, this flow is viscous and controlled by the shear strength of the soil. Along the same line,
494 *Haigh [2012]* recently found that *LL* is a function of the ratio between the undrained shear
495 strength and the density of the material. These former studies provide some support to our
496 results, showing that the parameter *w-LL* may be used to predict the critical shear stress τ_c,
497 disregarding the nature of the clay soil.

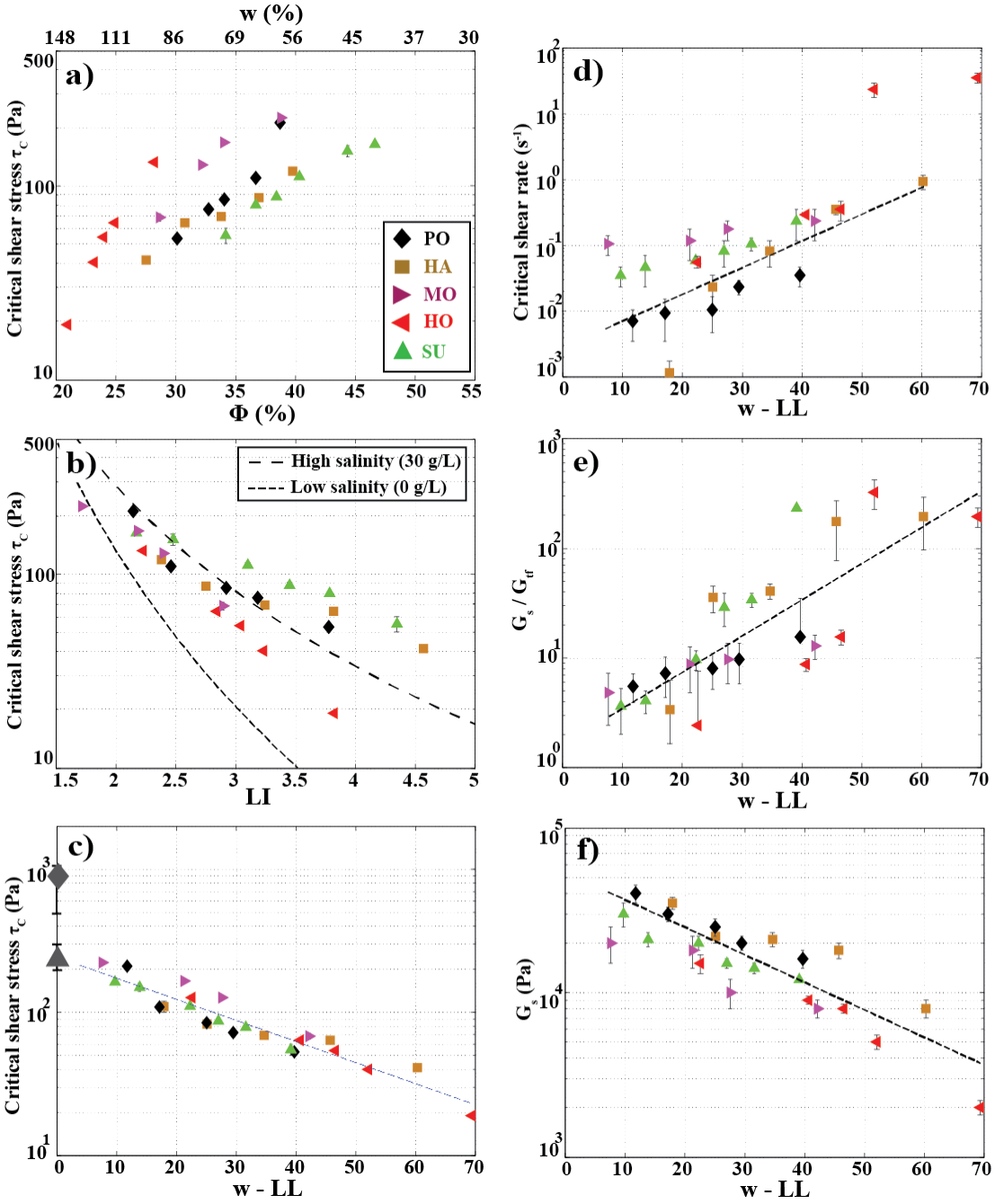

Figure 7: a, b and c) Variation of the critical shear stress τ_c measured during rheometric creep tests with a) solid fraction Φ and gravimetric water content w, b) liquidity index LI and c) the deviation of w from the Atterberg liquid limit, w-LL . In b), the power laws describing the evolution of τ_c with LI for high and low salinity [Locat, 1997] are plotted. In c), the exponential law τ_c = 246.7 exp(-0.034(w-LL)) fits the data with a determination coefficient of 0.91. Grey markers in c) correspond to yield stress values back-calculated from real debris flow events of PO and SU sites (see section 6.3). d, e and f) Variation of critical shear rate $\dot{\gamma}_c$, ratio of elastic shear modulus between solid and fluid regimes G_s/G_{tf}, and elastic shear modulus in solid regime G_s. with the deviation w-LL. Error bars are systematically plotted (when not visible, they are smaller than marker size). In c) to f), dashed curves correspond to exponential fits of the data (see text).

6.2 Evolution of viscosity and elastic bifurcations

The critical shear rate $\dot{\gamma}_c$ characterizing the amplitude of the viscosity bifurcation at solid-fluid transition for the different soils tested, is plotted against the deviation *w-LL* in *Figure 7d.* As already noted, for each soil, $\dot{\gamma}_c$ shows a clear increase with the water content *w*. Furthermore, it is observed that the data here also roughly collapse on a single relation of *w-LL*. Fitting an exponential law of the form *a.exp(b.(w-LL))* yields the following coefficients: $a = 6.9\ 10^{-3}$ s^{-1}; $b = -0.0712$, and a determination coefficient $R^2 = 0.56$. This latter value shows that the dispersion around this mean trend is significantly larger than in the case of the critical shear stress τ_c. For similar values of *w–LL*, differences as large as one order of magnitude are observed between the critical shear rates $\dot{\gamma}_c$ measured for the different samples (*Figure 7d*). As already pointed out, for some of the samples, the existence of a viscosity bifurcation can even be questioned (typically, when the reported values of $\dot{\gamma}_c$ are less than10^{-2} s^{-1}). Hence, even if the deviation *w–LL* appears again to be an important control parameter, this parameter is not sufficient to fully account for the existence and magnitude of the viscosity bifurcations in the different studied clay soils. The presence of smectite, in particular, seems to also play a significant role, as the two soils exhibiting the highest values of $\dot{\gamma}_c$ (HO and MO) are also those with the highest proportion of swelling clays (see *Table 1*). It can also be noted that HO soil, for which the fraction of smectite is the largest (33.8 %), presents a peculiar behavior at high water content. Above *w-LL* = 50 %, the magnitude of the viscosity bifurcation abruptly increases with a value of $\dot{\gamma}_c$ jumping from 0.2 s^{-1} to 20 s^{-1}. (Note that the values of $\dot{\gamma}_c$ measured for HO samples above the jump were not taken into account in the exponential trend presented above.)

Similarly, the ratio G_s/G_{tf}, which characterizes the amplitude of the drop in elastic shear modulus at the solid-fluid transition, is shown as a function of *w-LL* in *Figure 7e*. In *Figure 7f,* we also show the evolution of the solid state elastic shear modulus G_s versus *w-LL*. Since the elastic modulus of the samples systematically reaches very low values (compared to G_s) in the fluid regime, the value of G_s can be considered as representative of the total drop in elastic shear modulus between the solid and fluid regimes. For all soil samples, the ratio G_s/G_{tf} increases, while on the contrary the value of G_s decreases with the water content. Here again, simple relations with the deviation *w-LL* appear to reasonably capture the main trends of these parameters. Fitting exponential laws of the form *a.exp(b.(w-LL))* yields the following coefficients: $a = 1.85$, $b = 0.074$ and a determination coefficient $R^2 = 0.64$ for the ratio G_s/G_{tf}, and $a = 4.5\ 10^4$ Pa, $b = -0.036$ and $R^2 = 0.72$ for G_s. We also note that MO and HO samples, which are characterized by the highest smectite content, stand out by showing the lowest G_s values and, for HO, a jump in G_s/G_{tf} for *w-LL* > 50 %.

Finally, it can be concluded that the first-order trends shown by the different mechanical properties of the clay soils at the solid-fluid transition (τ_c, $\dot{\gamma}_c$, G_s/G_{tf}, G_s), are all explained by exponential relations with the deviation *w-LL*. However, claiming that this parameter completely controls the rheological behavior of the studied soils would be abusive. Even if the liquid limit already partly accounts for the physico-chemical properties of the materials, other parameters, and in particular the presence of swelling clay, also seem to have a significant influence on the viscosity and elastic bifurcations observed at the solid-fluid transition. To go further, it could be

553 relevant to investigate second-order dependencies between the coefficients *a* and *b*
554 characterizing the evolutions of $\dot{\gamma}_c$, G_s/G_{tf} and G_s versus *w-LL* for each soil sample, and
555 geotechnical properties such as *PI*, *CEC* or smectite content. However, with the limited available
556 data, no consistent relations could be found at this stage.
557

558 ### 6.3 Extrapolation to field scale

559 To finish, we discuss the potential implications of our results for the prediction and
560 understanding of slide-to-flow transition in clay landslides. A first striking feature is the
561 existence of a marked viscosity bifurcation for some of the tested soils. As shown by *Coussot et*
562 *al. [2005]*, we can expect materials exhibiting such characteristic to be particularly prone to
563 catastrophic fluidization events, and to give rise to high-velocity mud or debris flows. On the
564 contrary, soils without this property, or characterized by low values of $\dot{\gamma}_c$, are expected to transit
565 more progressively from solid to fluid regimes, and thus to produce less catastrophic flow events.
566 In this respect, the three landslides showing the highest values of $\dot{\gamma}_c$ in the experiments, at low
567 and high water contents, – namely HO, HA, and MO (*Figure 7d*) – are also those for which the
568 highest mobility flows have been observed (*Table 1*).
569
570 Also of particular interest is the excellent correlation observed between τ_c and *w-LL* [*Eq.(3)*] for
571 the different tested soils. This result suggests that the critical shear stress of a landslide, i.e. the
572 stress level at which solid-fluid transition occurs, might be evaluated and monitored directly
573 from measurements of the water content *w*, provided the liquid limit *LL* is known. Following
574 *Hungr et al. [2014]*, who indicate that debris flows are likely to be triggered when materials are
575 close to their liquid limit, our results could even imply that a unique critical stress value, on the
576 order of 200-300 Pa (extrapolation of relation (3) to *w-LL* = 0, see *Figure 7c*), could be used to
577 predict the occurrence of such flow events. Care should nevertheless be taken concerning the
578 representativeness of the critical stress values measured in our rheometrical tests, since these
579 tests were not performed on the in-situ soils, but on samples sieved at 400 μm. In fact, clay soils
580 collected at MO, HA and HO sites contain essentially no particles larger than 400 μm (see
581 section 2). In these cases the tested samples can thus effectively be considered as representative
582 of the complete materials. On the contrary, CH, SU and PO landslides contain significant
583 amounts of particles larger than 400 μm. According to existing studies on model materials
584 [*Ancey and Jorrot, 2001, Ovarlez et al., 2015, Dagois-Bohy et al., 2015*], we can expect the
585 value of τ_c to increase with the addition of coarse grains. Yet, interestingly, *Malet and al. [2004]*
586 back-analyzed the run-out and thickness of past debris flow deposits at SU site using the flow
587 code Bing *[Imran et al., 2001]*, and reported a critical stress value of τ_c = 250 +/- 50 Pa that is
588 well within the range arising from our experimental results. We performed a similar back-
589 analysis on a debris flow event that took place at PO site (see Appendix B). In this case, the
590 analysis yields a critical stress of τ_c = 900 +/- 400 Pa, larger than our experimentally-derived
591 values but still within the same order of magnitude. These two back-calculated critical stress
592 values have been represented in *Figure 7c* at *w-LL = 0*. Although additional field cases would be
593 needed to strengthen these results, the good agreement between the back-analyzed and
594 laboratory-derived values tends to indicate that relation (3) can effectively be used to obtain at
595 least first estimates of the critical stress of clay landslides at field scale, and this even when a
596 coarse fraction > 400 μm is present in the material.

Finally, we turn to the measurements of elastic shear modulus G, and the systematic drop in G of at least one order of magnitude observed in all tested soils at the solid-fluid transition. This systematic drop, followed by a further decrease in G as the material fully fluidizes, is consistent with the decrease in seismic shear velocity V_s reported before the occurrence of flow events both in laboratory flume experiments [*Mainsant et al., 2015*] and in the field [*Mainsant et al., 2012a*]. This indicates that a loss of rigidity at the solid-fluid transition can be considered as a generic feature of clay soils, and confirms that V_s variations constitute a good indicator for monitoring clay landslides. It shall be emphasized, however, that the values of G inferred from our OCr tests appear relatively low compared to typical field values. When converted into shear wave velocities through the simple relation $V_s = (G/\rho)^{1/2}$, our laboratory measurements correspond to V_s values ranging between 3 and 5 $m.s^{-1}$ in solid regime, and less than 1 $m.s^{-1}$ in fluid regime. As a comparison, typical values of V_s inferred from seismic noise measurements at the base of the PO landslide varied between 400 and 200 $m.s^{-1}$ typically, during the preparation of a flow event [*Mainsant et al., 2012a*]. We interpret this quantitative discrepancy as resulting from the strong sensitivity of V_s, and thus of G, to the water content when the sample is below its liquid limit LL. Experiments performed by *Mainsant et al. [2012b]* on HA soil showed values of V_s as low as 10 $m.s^{-1}$ for samples at the liquid limit, consistent with our measurements, but values of V_s of more than 100 $m.s^{-1}$ for $w\text{-}LL$ = -10 %. A strong decrease in G and V_s with porosity, resulting from clay deconsolidation, was also reported by *Renalier et al. [2010]* both from laboratory tests and field data. To complement our results, measurements of G at the solid-fluid transition for samples presenting water contents more representative of those typically found in the field, i.e. below LL, would thus be useful. Designing well-controlled experimental tests to monitor solid-fluid transition in such strongly plastic samples represents an interesting perspective for future work.

7. Conclusion

The solid-fluid transition in clay soil samples collected from six landslides producing flow-like events was studied in laboratory rheometrical tests. Creep and oscillation tests were performed to measure the critical shear stress τ_c, the critical shear rate $\dot{\gamma}_c$, and the elastic shear modulus G at the solid-fluid transition, as a function of the water content w. All soils, except for Char d'Osset landslide, exhibit a clear viscoplastic rheological behavior. The critical shear stress triggering solid-fluid transition varies among the samples and decreases with the water content. The particular behavior of Char d'Osset clay soil has been linked to its low specific surface and cation exchange capacity. The five other clay soils are also characterized by bifurcations in viscosity and marked losses of rigidity at the solid-fluid transition. The existence and amplitude of the viscosity bifurcation, as well as the amplitude of the concurrent drop in elastic shear modulus, are influenced by the water content as well as by the presence of swelling clays in the samples.

An important result of our study is that all the viscoplastic soils, which come from landslides characterized by very different geomorphological features, obey a common exponential law relating τ_c and the deviation $w\text{-}LL$. This relation is further strengthened by the back-analyses of real flow events at PO and SU sites, which lead to critical stress values that are consistent with the extrapolation of the laboratory-derived exponential law for $w = LL$. Similar simple

642 exponential laws with *w-LL* were also proposed for the critical shear rate and the drop in shear
643 modulus, albeit with lower correlation coefficients. These results reveal that the deviation *w-LL*
644 is a key parameter controlling the mechanical behavior of these clay soils at the solid-fluid
645 transition. This parameter captures the first-order effects of both water content and solid fraction
646 properties (grain size distribution, physico-chemical characteristics, etc.). Our study can be
647 regarded as a first attempt at linking the rheological behavior of clay landslides with simple
648 geotechnical characterizations. It opens up promising prospects for landslide monitoring and
649 suggests that *w* measurements could be used to assess the conditions for which a clay soil of
650 known liquid limit *LL* can fluidize. Alternatively, these results highlight the potential value of
651 geophysical monitoring (electrical resistivity and shear wave velocity) on landslides to gain
652 insight in the rheological change in clay soils during slide-to-flow transition.
653
654

655 **Acknowledgments and Data**

656 The authors thank Frédéric Ousset and Hervé Bellot from IRSTEA (rheometrical tests), and
657 Martine Lanson and Nathaniel Findling from ISTerre (geochemical and mineralogical analyses)
658 for their assistance. The authors acknowledge financial support from the French VOR federative
659 structure, the ARC project from the Rhônes-Alpes region (France) and the CNRS through the
660 INSU-TS-aléas program.

661

References

Ancey, C. (2007), 'Plasticity and geophysical flows: A review', *Journal of Non-Newtonian Fluid Mechanics* **142**(13), 4-35.

Ancey, C. & Jorrot, H. (2001), 'Yield stress for particle suspensions within a clay dispersion', *Journal of Rheology* **45**(2), 297-319.

van Asch, T. W. J. & Malet, J.-P. (2009), 'Flow-type failures in fine-grained soils: an important aspect in landslide hazard analysis', *Natural Hazards and Earth System Sciences* **9**(5), 1703-1711.

Bardou, E.; Bowen, P.; Boivin, P. & Banfill, P. (2007), 'Impact of small amounts of swelling clays on the physical properties of debris-flow-like granular materials. Implications for the study of alpine debris flow', *Earth Surface Processes and Landforms* **32**(5), 698-710.

Bièvre, G.; Jongmans, D.; Winiarski, T. & Zumbo, V. (2011), 'Application of geophysical measurements for assessing the role of fissures in water infiltration within a clay landslide (Trièves area, French Alps)', *Hydrological Processes* **26**(14), 2128-2142.

Bird, R. B.; Armstrong, R. C. & Hassager, O. (1987), *Dynamics of polymeric liquids, vol. 1*, John Wiley and Sons, New York, USA.

Bonn, D.; Paredes, J.; Denn, M. M.; Berthier, L.; Divoux, T. & Manneville, S. (2015), 'Yield Stress Materials in Soft Condensed Matter', *Reviews of Modern Physics*.

Boyer, F.; Guazzelli, E. & Pouliquen, O (2011). Unifying syspension and granular rheology, *Physical Review Letters*, 107, 188301.

Chambers, J. E.; Wilkinson, P. B.; Kuras, O.; Ford, J. R.; Gunn, D. A.; Meldrum, P. I.; Pennington, C. V. L.; Weller, A. L.; Hobbs, P. R. N. & Ogilvy, R. D. (2011), 'Three-dimensional geophysical anatomy of an active landslide in Lias Group mudrocks, Cleveland Basin, UK', *Geomorphology* **125**(4), 472-484.

Coussot, P. (1995), 'Structural Similarity and Transition from Newtonian to Non-Newtonian Behavior for Clay-Water Suspensions', *Physical Review Letters* **74**, 3971-3974.

Coussot, P. (2005), *Rheometry of pastes, suspensions, and granular materials*, Wiley Online Library.

Coussot, P. & Ancey, C. (1999), 'Rheophysical classification of concentrated suspensions and granular pastes', *Physical Review E.* **59**, 4445-4457.

Coussot, P.; Laigle, D.; Arattano, M.; Deganutti, A. & Marchi, L. (1998), 'Direct Determination of Rheological Characteristics of Debris Flow', *Journal of Hydraulic Engineering* **124**(8), 865-868.

Coussot, P.; Nguyen, Q. D.; Huynh, H. T. & Bonn, D. (2002), 'Viscosity bifurcation in thixotropic, yielding fluids', *Journal of Rheology* **46**(3), 573-589.

Coussot, P.; Nguyen, Q. D.; Huynh, H. T. & Bonn, D. (2002), 'Avalanche Behavior in Yield Stress Fluids', *Physical Review Letters* **88 - Number 17 - 5501**, 4p.

Coussot, P. & Piau, J. M. (1994), 'On the behavior of fine mud suspensions', *Rheologica Acta* **33**(3), 175-184.

Dagois-Bohy, S.; Hormozi, S.; Guazzelli, E. & Pouliquen, O. (2015), 'Rheology of dense suspensions of non-colloidal spheres in yield-stress fluids', *Journal of Fluid Mechanics* **776**.

Farrar, D. M. & Coleman, J. D. (1967), 'The correlation of surface area with other properties of nineteen British clay soil', *Journal of Soil Science* **18**(1), 118-124.

Haigh, S. K. (2012), 'Mechanics of the Casagrande liquid limit test', *Canadian Geotechnical Journal* **49**(9), 1015-1023.

Hungr, O.; Leroueil, S. & Picarelli, L. (2014), 'The Varnes classification of landslide types, an update', *Landslides* **11**(2), 167--194.

Huynh, H. T.; Roussel, N. & Coussot, P (2005). Aging and free surface flow of a thixotropic fluid, *Physics of Fluids*, 17, 033101.

Imran, J.; Harff, P. & Parker, G. (2001), 'A numerical model of submarine debris flow with graphical user interface ', *Computers & Geosciences* **27**(6), 717 - 729.

Iverson, R. M. (2005), 'Regulation of landslide motion by dilatancy and pore pressure feedback', *Journal of Geophysical Research: Earth Surface* **110**(F2).

Iverson, R. M. (1997), 'The physics of debris flows', *Reviews of Geophysics* **35**(3), 245-296.

Iverson, R. M. & George, D. L. (2016), 'Modelling landslide liquefaction, mobility bifurcation and the dynamics of the 2014 Oso disaster', *Géotechnique* **66**(3), 175-187.

Jaboyedoff, M.; Pedrazzini, A.; Loye, A.; Oppikofer, T.; i Pons, M. G. & Locat, J.Malet, J.-P.; Remaitre, A. & Bogaard, T., ed. (2009), *Earth flow in a complex geological environment: the example of Pont Bourquin, Les Diablerets (Western Switzerland)*, Landslide Processes, From Geomorphologic Mapping to Dynamic Modelling.

Jeong, S. W.; Locat, J.; Leroueil, S. & Malet, J.-P. (2010), 'Rheological properties of fine-grained sediment: the roles of texture and mineralogy', *Canadian Geotechnical Journal* **47**(10), 1085-1100.

Jeong, S. W.; Locat, J.; Leroueil, S. & Malet, J.-P. (2012), 'The effects of salinity and shear history on the rheological characteristics of illite rich clays', *Clays and Clay Minerals* **60**, 108-

120.

Khaldoun, A.; Moller, P.; Fall, A.; Wegdam, G.; De Leeuw, B.; Méheust, Y.; Fossum, J. & Bonn, D. (2009), 'Quick Clay and Landslides of Clayey Soils', *Physical Review Letters* **103**, 188301.

Locat, J. (1997), 'Normalized rheological behavior of fine muds and their flow properties in a pseudoplastic regime', *Debris-flow hazards mitigation: mechanics prediction and assessment, Water Ressources Engineering Division, American Society of Civil Engineers*, 260-269.

Locat, J. & Demers, D. (1988), 'Viscosity, yield stress, remolded strength, and liquidity index relationships for sensitive clays', *Canadian Geotechnical Journal* **25**(4), 799-806.

Mackey, B. H.; Roering, J. J. & McKean, J. A. (2009), 'Long-term kinematics and sediment flux of an active earthflow, Eel River, California', *Geology* **37**(9), 803-806.

Mainsant, G.; Chambon, G.; Jongmans, D.; Larose, E. & Baillet, L. (2015), 'Shear-wave-velocity drop prior to clayey mass movement in laboratory flume experiments', *Engineering Geology* **192**, 26-32.

Mainsant, G.; Jongmans, D.; Chambon, G.; Larose, E. & Baillet, L. (2012), 'Shear-wave velocity as an indicator for rheological changes in clay materials: Lessons from laboratory experiments', *Geophysical Research Letters* **39**(19), 5p.

Mainsant, G.; Larose, E.; Brönnimann, C.; Jongmans, D.; Michoud, C. & Jaboyedoff, M. (2012), 'Ambient seismic noise monitoring of a clay landslide: Toward failure prediction', *Journal of Geophysical Research: Earth Surface* **117**(F1).

Maio, C. & Scaringi, G. (2016), 'Shear displacements induced by decrease in pore solution concentration on a pre-existing slip surface', *Engineering Geology* **200**, 1-9.

Malet, J.-P.; Laigle, D.; Remaître, A. & Maquaire, O. (2005), 'Triggering conditions and mobility of debris flows associated to complex earthflows ', *Geomorphology* **66**, 215-235.

Malet, J.-P.; Maquaire, O. & Remaître, A. (2004), 'Assessing debris flow hazards associated with slow moving landslides: methodology and numerical analyses', *Landslides* **1**, 83-90.

Malet, J.-P.; Remaître, A.; Maquaire, O.; Ancey, C. & Locat, J. (2003), Flow susceptibility of heterogeneous marly formations. Implications for torrent hazard control in the Barcelonnette basin (Alpes-de-Haute-Provence, France), *in* D. Rickenmann & C.-L. (Eds) Chen, ed., 'Third International Conference on Debris-Flow Hazard Mitigation: Mechanics, Prediction and Assessment', Millpress, Rotterdam, Davos, Switzerland, 351-362.

Maquaire, O.; Malet, J.-P.; Remaître, A.; Locat, J.; Klotz, S. & Guillon, J. (2003), 'Instability conditions of marly hillslopes: towards landsliding or gullying? The case of the Barcelonnette basin, South East France', *Engineering Geology* **70**(1-2), 109-130.

Mitchell, J. K. (1993), *Fundamentals of soil behavior, second edition*, John Wiley & Sons Inc.

Ovarlez, G.; Mahaut, F.; Deboeuf, S.; Lenoir, N.; Hormozi, S. & Chateau, X. (2015), 'Flows of suspensions of particles in yield stress fluids', *Journal of Rheology* **59**(6), 1449-1486.

Picarelli, L.; Urciuoli, G.; Ramondini, M. & Comegna, L. (2005), 'Main features of mudslides in tectonised highly fissured clay shales', *Landslides* **2**(1), 15-30.

Picarelli, L.; Urciuoli, G. & Russo, C. (2004), 'Effect of groundwater regime on the behaviour of clayey slopes', *Canadian Geotechnical Journal* **41**(3), 467-484.

Renalier, F.; Bièvre, G.; Jongmans, D.; Campillo, M. & Bard, P. Y.Miller, R. D.; Bradford, J. H. & Holliger, K., ed. (2010), *Clayey Landslide Investigations using Active and Passive VS Measurements*, Vol. 15, Advances in Near-Surface Seismology and Ground-Penetrating Radar, Geophysical Dev. Series.

Rickenmann, D.; Laigle, D.; McArdell, B. W. & Hubl, J (2006). Comparison of 2D debris-flow simulation models with field events, *Computational Geosciences*, 10, 241-264.

Santamarina J.C, Klein K.A, W. Y. H. & Prencke, E. (2002), 'Specific surface: determination and relevance', *Canadian Geotechnical Journal* **39**, 233-241.

Sridharan, A. & Prakash, K. (2000), 'Percussion and cone methods of determining the liquid limit of soils: controlling mechanisms', *Geotechnical Testing Journal* **23**, 236-244.

Trulsson, M.; Bouzid, M.; Kurchan, J.; Clément, E.; Claudin, P. & Andreotti, B (2015). Athermal analogue of sheared dense Brownian suspensions, *Europhysics Letters*, 111, 18001.

Yukselen, Y. & Kaya, A. (2006), 'Prediction of cation exchange capacity from soil index properties', *Clay Minerals* **41**, 827-837.

833 # APPENDIX A: MINERALOGICAL CONTENT OF THE SOIL SAMPLES

XRD (quoted as %)	Hollin-Hill	Pont-Bourquin	Harmalière	Super-Sauze	Char d'Osset	Montevecchio
Chlorite		7.4	6.9	4.3	15.2	
Kaolinite	11.8	2.5				25.7
Smectite	33.8		9.4			15.3
Di-octahedral Micas	20.1	54.8	28.9	37.3	33.4	19.6
Pyrophyllite		5.3				
Quartz	21.8	16.5	18.9	23.9	20.9	15.5
Albite	3.1		4.8	7.3	12.5	4.5
K-spars	2.4		3.3			
Calcite		5.0	22.5	20.8	15.1	16.0
Aragonite					1.2	
Ankerite		6.5	1.8	5.6	0.8	3.4
Pyrite			0.2			
Magnetite						0.2
Goethite	4.8					
Lepidocrocite	0.8					
Anatase	0.7		2.0			
Rutile		2.2		0.7	1.0	
Jarosite	0.7					
Hornblende			1.3			
Total	100	100	100	100	100	100.2

834
835
836

APPENDIX B: BACK ANALYSIS OF PONT-BOURQUIN DEBRIS FLOW EVENT

The Bing software [*Imran et al., 2001*] solves a 1D shallow-flow model relying on a viscoplastic rheology (Bingham or Herschel Bulkley) to simulate the propagation of debris flows. It has been initially developed for submarine debris flows, but can be adapted to subaerial flows by using an ambient fluid density equivalent to the air (1 $kg.m^{-3}$). The computation of the flow starts from a semi-parabolic mass defined by a length and a thickness. The flow then propagates on an altimetric profile which is provided by the user.

Similar to *Malet et al. [2004]*, we used this software to carry out a back-analysis of a debris flow event that occurred on the PO landslide in summer 2007 and was documented by *Jaboyedoff et al., [2009]*. After heavy rainfalls, a flowing volume of about 11,000 m^3 cut the road at the toe of the landslide. A detailed geomorphological analysis provided the necessary information regarding the localization and size of the initial unstable mass. Accordingly, a maximum thickness of 3 meters and a length of 100 m were used as initial conditions in Bing. Field observations after the event indicated a length of propagation of 130 to 160 m, and a front thickness of approximately 2 m on the road. In agreement with recommendations of *Imran et al., [2001],* numerical parameters were taken as follows: artificial viscosity = 10^{-4}; number of nodes in domain = 21; time step = 10^{-5} min. A Herschel-Bulkley viscoplastic law with an exponent n = 0.25 was used. In agreement with the common practice for muddy debris flows [*Coussot et al., 1998; Rickenmann et al., 2006*], the ratio τ_c/K between the critical stress τ_c and consistency K the material was considered constant, with values in the range 3-5 s^{-n}. *Figure B1* shows the evolution of flow runout as a function of the considered critical shear stress and ratio τ_c/K. All the simulated-flows shown in *Figure B1* present front thicknesses between 1 and 2 m, in agreement with field values. It is observed that the simulated runout significantly decreases with the ratio τ_c/K. Depending on the value of this ratio, values of critical shear stress τ_c lying between 550 and 1300 Pa are necessary to reproduce the runout of the 2007 event.

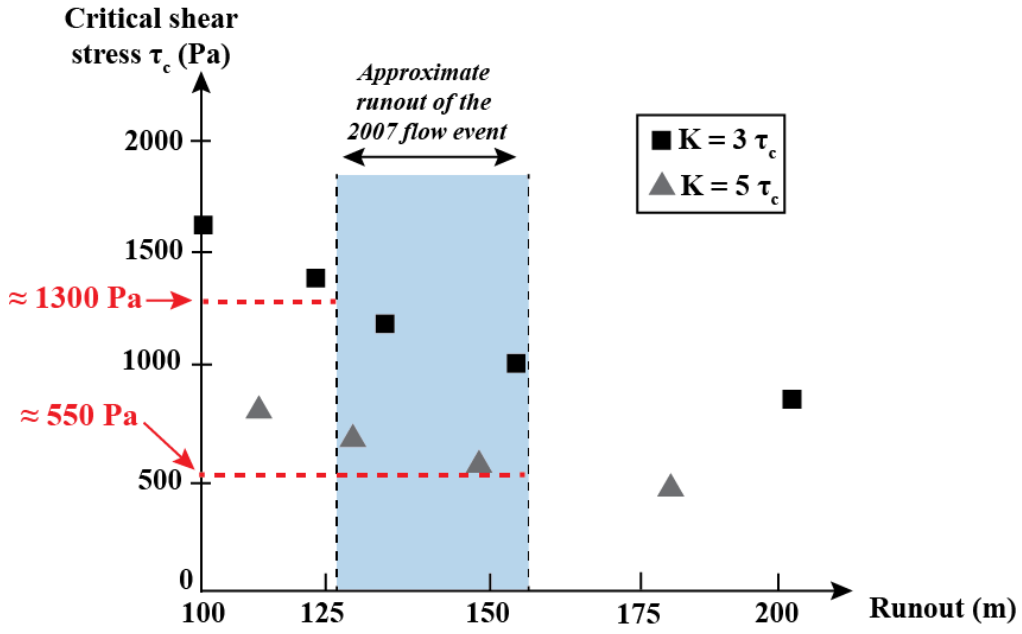

Figure B1: Back-analysis of the 2007 flow event at Pont-Bourquin (PO) landslide with Bing software using a Herschel Bulkley viscoplastic law.

PAPER 2

Field monitoring of surface-wave velocity and displacement rate in an active earthflow

Bertello L., Berti M., Castellaro S.

*submitted to **Journal of Geophysical Research: Earth Surface,** January 2017

Field monitoring of surface-wave velocity and displacement rate in an active earthflow

Lara Bertello[1], Matteo Berti[1], and Silvia Castellaro[2]

[1] Department of Biological, Geological and Environmental Sciences, University of Bologna, 40127, Bologna, Italy

[2] Department of Physics and Astronomy, University of Bologna, 40127, Bologna, Italy

Corresponding author:

- Matteo Berti matteo.berti@unibo.it

Key Points:

- There is a relationship between the displacement rate of the landslide and the surface wave velocity
- Surface wave velocity decreases as the landslide starts to move, then increases as the landslide decelerates after failure.
- The earthflow experiences significant variation of soil stiffness, void ratio, and water content during failure

Abstract

Earthflows are landslides in fine soils or clay-bearing rocks that move downslope as viscous fluid flows. Mass flow is typically accompanied by basal sliding along shear surfaces, and the relative importance between these two mechanisms is controlled by the displacement rate. During the long dormancy phase, earthflows slowly move at rate of 10^{-2} or 10^{-1} m/year along discrete shear boundaries with minor internal deformations; mass flow characterizes the paroxysmal stage of movement, when the displacement rate increases up to 10 m/day. The rapid acceleration shown by earthflows has been explained by invoking a solid-to-fluid transformation of the material. However, this process is still poorly understood and very few data are available. In this study, we present the results of periodic and continuous measurements of surface wave velocity carried out in an active earthflow located in the Northern Apennines of Italy (the Montevecchio landslide). The detected change in seismic velocity is compared with the variation of the displacement rate measured by continuous GPS monitoring and a time-lapse camera. The data clearly show a direct relationship between surface wave velocity and displacement rate, indicating that the earthflow undergoes significant change in soil stiffness during failure. This supports the evidence of a drastic change in the mechanical behavior when the earthflow reactivates.

1 Introduction

Earthflows are the most common type of failure in active slopes where fine soils are dominant [*Keefer and Johnson, 1983, Hungr et al., 2001, Picarelli et al., 2005, Guerriero et al., 2014*]. These landslides generally have an elongated or lobate shape, and show a complex style of movement in which mass flow is accompanied by basal sliding along localized shear zones [*Hutchinson, 1970; Prior and Stephens, 1972, Keefer and Johnson, 1983, Baum and Johnson, 1993, Lanzo and D'Elia, 1997, Guerriero et al., 2013*]. Earthflows undergo periodic reactivations with a strong retrogressive nature [*D'Elia et al, 1998, Schulz et al. 2009a, 2009, Giordan et al., 2013, Handwerger et al., 2013*]. The reactivation mechanism typically consists of an initial drained failure located in the crown area followed by undrained loading of the pre-existing landslide deposits [*Evans and Brooks, 1994, Giusti et al., 1996, Sassa et al., 2004, Picarelli et al, 2005, Borgatti et al., 2006*]. The undrained loading induces stress-related pore pressure changes [*Hutchinson, 1970, Van Asch, 2005, Daehne and Corsini, 2012, Lollino et al., 2014*] which can yield to a rapid acceleration of the landslide accompanied by mass fluidization [*Bovis, 1985, Malet et al., 2005, Geertsema et al., 2006, Comegna et al., 2007, Van Asch and Malet, 2009, Okada et al., 2012, Bernardi et al., 2015, Picarelli, 2015*]. A partial or total fluidization of the mass has been widely reported in the literature, and it is now considered a fundamental mechanism of earthflow dynamics [*Picarelli et al., 2005, van Asch et al., 2007, Pastor et al., 2009, Daehne et al., 2010, Pastor et al., 2010, Jongmans et al., 2015*]. Despite its importance, the process of solid-fluid transition and the consequent transformation of a slide into a flow is extremely difficult to measure in the field. Paroxysmal reactivations are in fact rare events and earthflows can continue to move slowly over a long period sliding along a basal shear

surface at residual strength [*Zhang et al. 1991, Coe et al., 2003, Giordan et al., 2013, Guerriero et al., 2013, Guerriero et al., 2014*]. Moreover, the fluidization process is unpredictable and difficult to monitor using traditional geotechnical instruments. For these reasons, very few studies documented this process. *Mainsant et al.* [*2012*] successfully used the variation of shear wave velocity (V_s) as an indicator of fluidization in active landslides. The idea behind the method is that, as the shear wave velocity in a fluid tends to zero [*Reynolds, 1997*], the bulk shear wave velocity should decrease in the proximity of liquefied areas. *Renalier et al.* [*2010*] also showed that in clay-rich landslides V_s significantly decreases with the extent of damage in the material. Therefore, the continuous measurement of S-wave velocity could be valuable for investigating the solid-fluid transition in the first stage of the reactivation process [*Mainsant et al., 2012, Mainsant et al., 2015*].

In this study, we used surface wave velocity to investigate the behavior of the Montevecchio landslide, an active earthflow located in the Northern Apennines of Italy (Savio River valley, Province of Cesena). In February 2014, the earthflow entered a period of intense activity that lasted for 17 months until June 2015. During this period, the earthflow experienced three paroxysmal reactivations characterized by the complete fluidization of the moving mass. We documented the reactivation process by periodic and continuous measurements of seismic surface wave velocities carried out using the active Multichannel Analysis of Surface Waves (MASW) [*Park et al., 1999*] and the passive Refraction Microtremors (ReMi^{TM}) techniques [*Louie, 2001*]. The data reveal a complex relationship between rainfall, displacement rate, and surface seismic velocity, providing new insight into the dynamics of active earthflows.

2 Study Area

The Montevecchio landslide is located in the Northern Apennines of Italy, approximately 16 km to the south of the city of Cesena. The landslide occupies the valley of the Ribianco Creek, a tributary of the Savio River (Fig. 1). The area is characterized by relative gentle slopes (inclination in the range of 7° to 17°) covered by grass and native brush, and ranges in elevation from 70 to 215 m a.s.l.. The upper part of the basin has typical badland morphologies characterized by small gullies, steep slopes (35° to 45°) and low vegetation coverage.

Bedrock geology consists of shallow marine deposits belonging to the Colombacci Formation [*Ricci Lucchi et al., 2002*]. This Formation deposited from the Late Miocene to the Holocene with a maximum thickness of 450 meters. In the study area, the Colombacci Formation consists of predominant marly and silty clay interbedded with thin layers of fine sandstone (sandstone/clay ratio is lower than 1/3). The clay is stiff to very stiff with a dark grey-blue color when fresh, and becomes soft and brown when weathered. The sandstone layers are loose or only weakly cemented, the color turning from grey to yellow with weathering. The Colombacci Formation is well exposed on the source areas of the earthflow (zone A-B-C; Fig. 1). In zone A the bedding planes dip with the same direction as the slope scarp at an angle of 40° with the horizontal, promoting slope instability by translational sliding and flexural buckling.

Old landslide deposits accumulated by multiple earthflow events occupy about 45% percent of the Ribianco basin (Fig. 1). These deposits consist of a clay-rich colluvium containing scattered blocks of weakly cemented sandstone of variable size. They have an average inclination of about 13° and a thickness ranging from 1 to 8 meters. In the last 50 years, the Montevecchio landslide reactivated once in 1979, when almost reached the houses and the road at the toe, then in 1997, 1999, 2002, 2005, 2006, and 2008 with partial reactivations in the upper part of the slope. During the last period of activity (February 2014 to June 2015) the earthflow underwent a new complete remobilization (see next section).

Results from geotechnical tests show that the earthflow material has medium plasticity (Liquid Limit=50%; Plastic Index=26%) and it is composed by 15% sand, 43% silt, and 42% clay. Blue methylene tests [*Chiappone et al., 1999*] provide a specific surface of the clay of 112±1 m^2/g, which is a typical value for an illite [*Hang et al., 1970*] and an activity index of the clay fraction [Acb; *Lautrin, 1989*] equal to 12.5±0.5. The unit weight is 19.5 kN/m^3 in saturated conditions and 15 kN/m^3 for the dry soil (average values of 500 g undisturbed samples taken in the first meter). Direct shear tests give a critical state friction angle ϕ'_{cs}=20° and a residual friction angle ϕ'_r=13°. The local climate is Mediterranean with two main rainy periods from autumn to early winter (October to December) and during spring (March to May). The average annual precipitation is 780 mm and the average annual snowfall is about 30 cm. The average annual temperature is 14°C and it ranges between 17° and 29° during the dry season and between 1° and 20° C during the wet season.

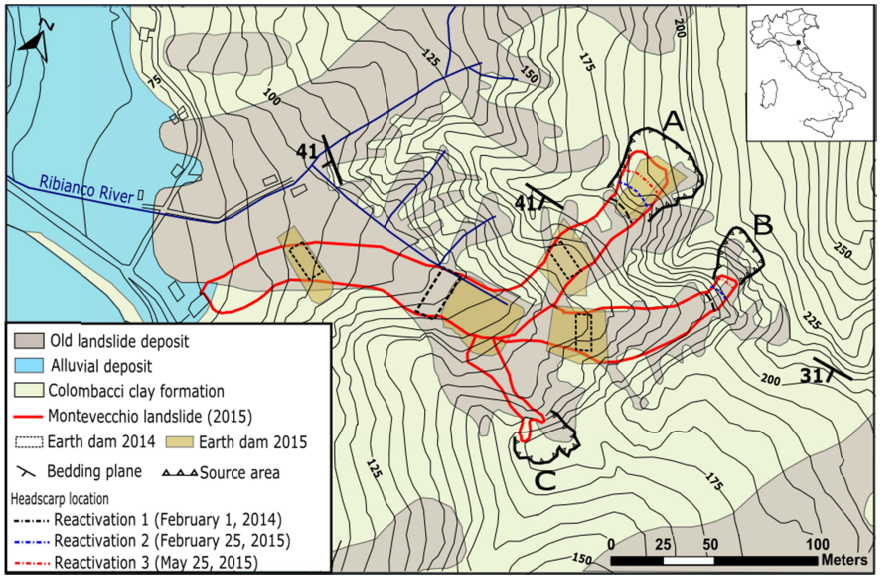

Figure 1: Geological map of the study area. The capital letters (A, B and C) indicate the source areas of the Montevecchio earthflow. The boundary of the landslide (red line) is reffered to July 2015. The colored dotted lines represent the three reactivations and the evolution of the headwall scarp in source area A and B.

3 Recent activity of the Montevecchio landslide

In February 2014, after a prolonged rainfall of 109 mm in 16 days, the Montevecchio earthflow entered into a new period of activity. The trigger rainfall was above the probabilistic rainfall threshold established for the area [*Berti et al., 2012*] and caused a large number of landslides in all the Emilia Romagna Region. The activity lasted for 17 months (until June 2015) and within this period the earthflow reactivated three times (1st reactivation: February 1, 2014; 2nd reactivation: February 25, 2015; 3rd reactivation: May 25, 2015). The term "reactivation" indicates here a paroxysmal stage of movement leading to the complete remobilization of the existing landslide deposits from the source area to the toe. In the following, we also use the term "partial reactivation" to indicate the remobilization of a small part of the landslide, and "suspended phase" to indicate the time after a reactivation when the landslide slows down [*Schadler, 2010*].

The first reactivation (February 1, 2014) started as sliding failure in the source area A (Fig. 2a) and caused a retrogression of the headscarp of about 8 m. The failure quickly propagated downslope (Fig. 2b), and in a couple of days the landslide reached the toe (Fig. 2c-d). Local authorities decided to protect the houses and the road by removing the advancing toe material, which was continuously excavated for weeks and deposited on the fluvial terrace to the other side of the road. In March and April 2014, the earthflow partially reactivated several times after heavy rain. The excavations at the toe continued and 4 earth berms were built across the landslide to stop the movement (Fig. 1). From May 2014, the earthflow entered a suspended phase that lasted about 9 months. During this period, the landslide velocity decreased gradually from m/day to cm/day, with episodes of acceleration following intense rainfall events. The suspend phase ended with the second reactivation of February 25, 2015. This time the failure involved both the source area A and B (Fig. 1) causing further retrogression of the headscarps, the complete mobilization of the earthflow, and the destruction of two earth berms. Further partial reactivations occurred in March 2015, then the landslide slowed down and almost stopped at the end of April 2015. The third and last reactivation was in May 25, 2015. Again, the landslide remobilized into a fluid, fast-moving earthflow that quickly reached the toe. Here local authorities removed the material 24 hours a day to save the houses. In June 2015, the earthflow almost stopped and significant consolidation works were carried out. Five earth berms were built across the landslide (Fig. 1) and a trench drain system was realized to stabilize the middle-upper part of the slope. The landslide remained essentially stable in the last year with some localized failures in the source area and along the north flank.

The three reactivations show a consistent behavior. The failure always starts as a sliding failure in the source area followed by undrained loading of the saturated landslide material. The undrained failure and the resulting deformations are clearly associated with an increase of void ratio and water content of the soil, which changes the state of the material from solid to "fluid" turning the initial slide into a flow. In the flow stage, the water content of the soil is apparently above the liquid limit and the earthflow moves downslope at high velocity (in the order of

several meter/hour) generating flow structures such as pressure ridges, lateral levees and tongue-shaped deposits. Movements can be so large to leave the slip surface exposed along the channel. This stage of paroxysmal activity generally lasts 2-5 days, then the earthflow decelerates. During the suspended phase the velocity decreases gradually from m/day to cm/month and the landslide moves within lateral shears with minor internal deformations. The soil becomes stiffer (at least near the ground surface) and the landslide turns back from a flow-like to a slide-like behavior. Apparently, the soil experiences two change of state (solid-to-fluid and fluid-to-solid) throughout a reactivation event.

Figure 2: Air photograph of the Montevecchio earthflow in July 2015. a) panoramic view of the source area A with the upper part of the earthflow channel; b) main reach of the earthflow channel; c-d) deposition area after the second reactivation of February 2015.

171 # 4 Field data

172 ## 4.1 Periodic measurements of surface wave velocity

173 After the first reactivation, we performed periodic measurements of seismic surface wave
174 velocity (vertical component of Rayleigh wave, V_r) by combining active (MASW) and passive
175 (ReMi) investigation techniques. Rayleigh waves in layered media travel at a velocity that
176 depends on their wavelength [*Foti et al., 2014*] and their wavelength is linked to the depth. The
177 wavelength (or frequency) vs velocity relation is named dispersion curve and is generally
178 obtained from the seismic time-series by means of correlation algorithms. Once this is obtained,
179 the velocity-depth profile is derived with forward modelling or inversion algorithms that
180 simulate the propagation of surface waves in layered media. In the standard practice, Rayleigh
181 wave velocity is used as a proxy to the more relevant (in geotechnical applications) shear wave
182 velocity, since its values is just 10-15% lower (the exact difference depends on the Poisson's
183 ratio, *Castellaro et al., 2015*).
184 At Montevecchio, periodic measurements were done every 1-2 months (Tab. 1) along 7 seismic
185 lines located both inside and outside the landslide (Fig. 3).
186

Date	Measurement section						
	A	B	C	D	E	F	G
2014/05/07	X	X	X	X	X	X	X
2014/06/06	X	X	X	X	X	X	X
2014/06/06	X	X	X	X	X	X	X
2014/07/27	X	X	X	X	X	X	X
2014/08/28		X	X	X			
2015/01/23		X	X	X			
2015/02/18			X				
2015/03/11		X	X	X			
2015/03/24		X	X	X			
2015/04/17		X	X	X			
2015/04/24	X	X	X	X			
2015/04/30			X		X	X	X
2015/05/07	X	X	X	X			
2015/05/19	X	X	X	X	X	X	X
2015/06/08	X	X	X	X			
2015/06/19		X	X	X			
2015/07/09	X	X	X	X			
2015/07/16		X	X				
2015/08/05	X	X	X	X			
2015/08/27			X				
2015/09/04	X	X	X	X			

187 *Table 1: Periodic seismic surveys carried out at Montevecchio (location of the measurement*
188 *sections in Fig.3).*
189
190

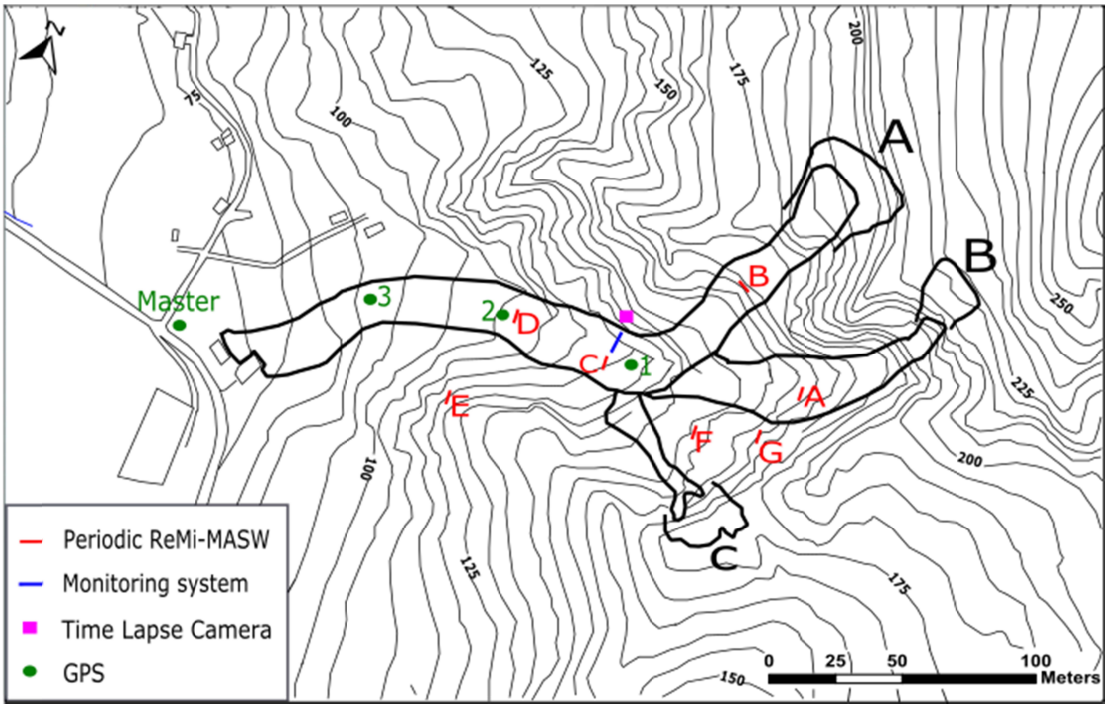

Figure 3: Map showing the location of the monitoring system and periodic seismic surveys.

The investigation used six vertically polarized 4.5 Hz geophones set at intervals of 2 m each (total length of the seismic lines 10 m). A 10 m aperture antenna can detect waves as long as 40 m (that is wavelengths as long as 4 times the array aperture, *Castellaro, 2016*), which correspond to maximum investigation depth of ~12 m (~1/3 of the maximum wavelength). The first 5 minutes of each acquisition were done in the passive mode, just acquiring the ambient seismic noise, while the last minute was in the active mode by putting a seismic source at about 5 m from the first geophone, in order to ensure as planar as possible wavefronts at the geophones. All the geophones were connected to a Soilspy Rosina acquisition system and data were processed using the software Grilla [*MoHo s.r.l.*].

Acquiring surface waves is a simple task, but the interpretation of their dispersion curves poses a number of challenges which have been extensively been discussed in *Foti et al.* [*2014*] and *Castellaro* [*2016*]. We will not therefore focus on this. The difficult field conditions provided further sources of uncertainty. During the dry season, the surface of the landslide is pervaded by desiccation cracks and open fractures (Fig. 5a-b) and a firm coupling of the geophones with the ground was difficult. Conversely, during the rainy season or after the major reactivation events (Fig. 5c) the material was fluid and most measuring points were not accessible. Both the variable ground conditions and the different location of the measuring points affected the accuracy of the results.

Figure 4 shows a typical Rayleigh-wave phase-velocity vs. frequency plot (spectrum) obtained in Montevecchio using active (a) and passive (b) methods. The dispersion curve can be traced by following the red-shaded areas of the plot phase-velocity plots. Hereinafter we will refer to the

phase-velocity spectra directly as dispersion curves for simplicity's sake. In the active mode (a) the dispersion curve is generally well defined over a wide range of frequencies and fundamental mode can easily be identified. Instead in the passive mode (b) the curve is discontinuous and the fundamental mode can be recognized only in some frequency intervals. The fact and the reasons why passive approaches are more reliable at low frequencies compared to active ones has been discussed in several papers *[Castellaro, 2016]*.

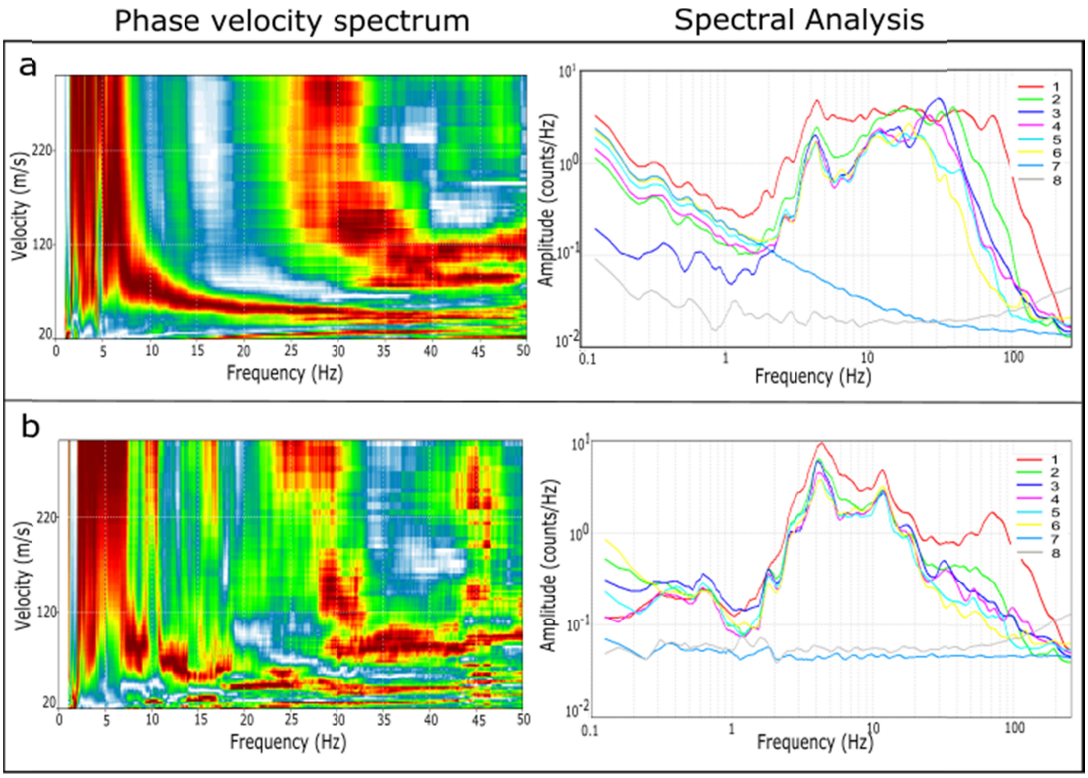

Figure 4: Rayleigh-wave phase-velocity spectra acquired on January 23th 2015 along section C (a=active survey; b=passive survey). The active survey provides clearer results above 10 Hz.

Figure 5: Pictures showing difficult ground conditions encountered during periodic seismic surveys. a-b) cracks and open fractures characterize the landslide surface during the dry period; c) water ponds and soft soil reduce the accessibility soon after a reactivation or an intense rainfall.

4.2 Continuous measurements of surface wave velocity

Periodic surveys were integrated by continuous measurements of surface wave velocity. To this aim, a cost-effective self-produced monitoring system was designed to include these features: 1) easy to install in the field and quick to remove; 2) low maintenance; 3) light enough to be carried by hand; 4) resistant to harsh field conditions (intense rainfall events, large ground displacements); 5) minimal energy consumption; 6) compatibility with geotechnical sensors. A number of preliminary laboratory and field tests were conducted to find the optimal configuration. Different combinations of sampling rate (50 to 300 Hz), number of geophones (2 to 6) and duration of the acquisition session (from 30 s to 5 min) were tested in order to balance the desired signal accuracy with the capabilities of the datalogger and the power requirement. This appeared to be a suitable configuration for our needs: i) Campbell CR1000 data logger with CFM100 Compact Flash Module (2GB); ii) 4 vertical geophones at 4.5Hz with 4 signal amplifiers (gain=500); iii) power supplied by a 12 V 7 Ah battery recharged by a 20 W solar panel. Good results were obtained by reading the four geophones at 300 Hz for 2 minutes every 1 hour, thus simulating the execution of 24 surface wave passive surveys every day.

This monitoring system was installed at Montevecchio in May 16, 2014 (Fig. 6b). The geophones were placed along the main track of the earthflow channel with a spacing of 2 m

(Fig.3, blue line) and buried at a depth of 20 cm (Fig. 6a) in order to avoid the atmospheric thermal effect and to ensure an adequate coupling with the ground [*Beekman, 2008*]. Based on direct observation during the first field tests, the main source of ambient seismic noise vibration was identified in the national road located at the toe of the landslide (about 400 m far from the monitoring system). The data collected from the datalogger were periodically downloaded and analyzed using the same software adopted for periodic surveys (Grilla).

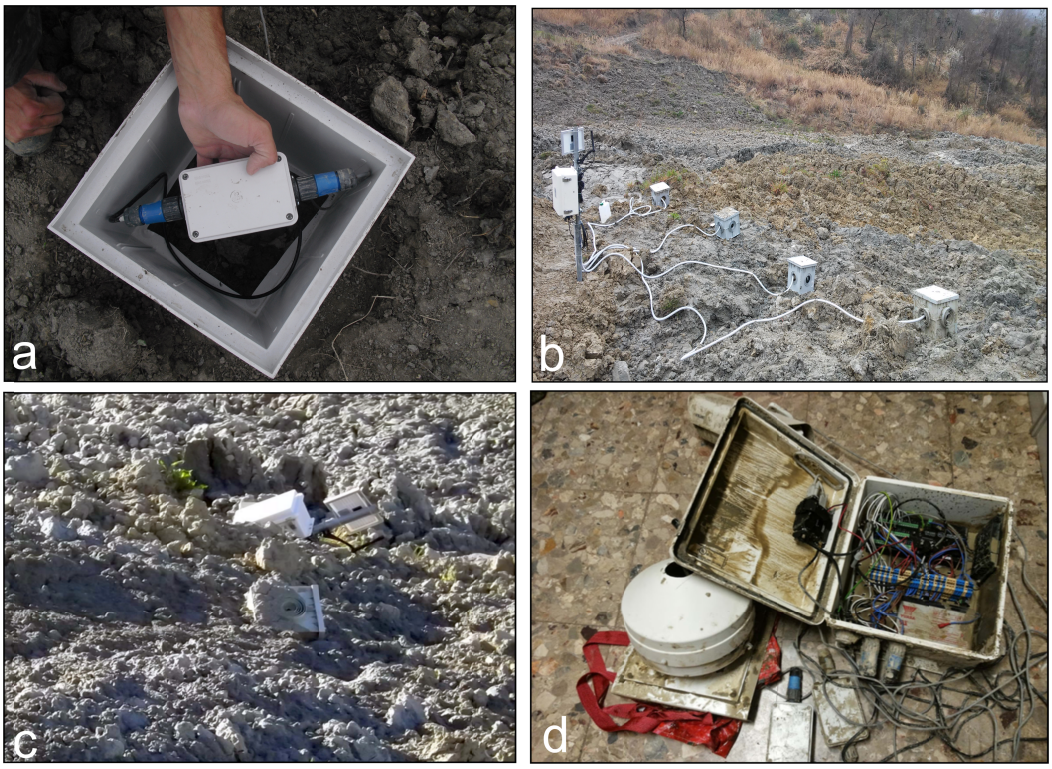

Figure 6: Pictures of the Montevecchio monitoring system. a) geophone amplifiers inserted in a waterproof box; b) continuous monitoring system installed in the main track of the earthflow channel. c-d) equipment damaged by a reactivation of the earthflow.

Also in this case, dispersion curves were sometimes difficult to interpret, thus we decided to classify each curve as "good", "fair", or "bad" according to quality of the phase velocity spectrum (Fig. 7). Figure 7a shows a dispersion curve classified as "good": here the fundamental as well as a number of higher modes can clearly be distinguished in a wide frequency interval (5-50 Hz). The case (b) shows a "fair" dispersion curve in which the fundamental mode can be recognized only at low frequencies (5-10 Hz). Case c) shows a dispersion curve classified as "bad" because the fundamental mode cannot be detected. Bad curves are generally due to electrical problems with the signal amplifiers, cable ruptures, or bad ground coupling. For the purpose of the analysis, we only considered the "good" (a) or "fair" (b) dispersion curves.

Field monitoring was difficult and sometimes risky due to the strong landslide activity. Figure 6c-d shows the monitoring system just after the reactivation of February 25, 2015: all the

equipment was moved downslope for about 100 m, several sensors were destroyed and both the geophones and the amplifiers were lost. The landslide was not accessible for almost two months, not even to retrieve the equipment. The system was rebuilt and reinstalled on May 7, 2015. Less than one month later, the earthflow reactivated again and the monitoring system was again destroyed. During the monitoring period, we reinstalled the system six times because of the continuous landslide movements.

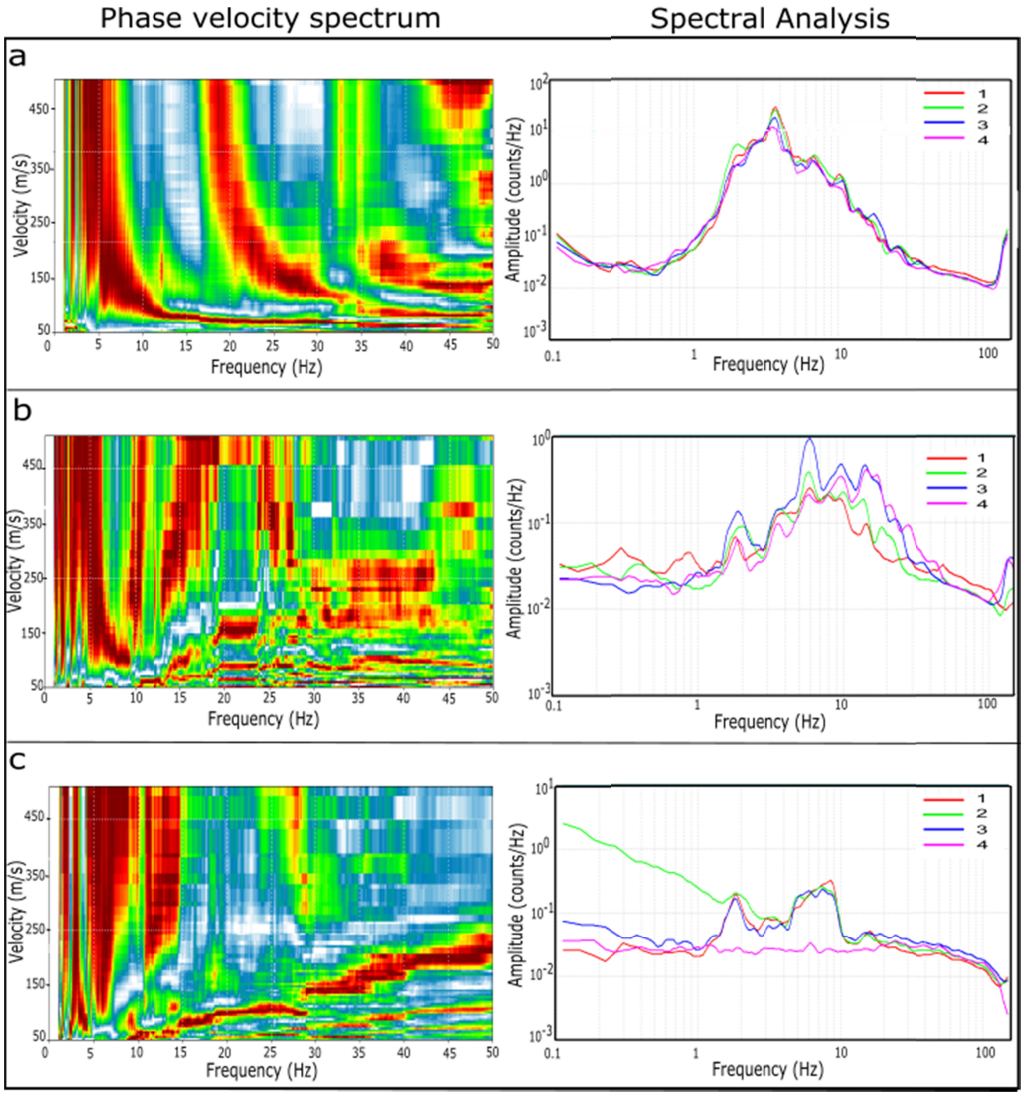

Figure 7: Example of three dispersion curves acquired by the monitoring system. These curves were classified as 'good' (a), 'fair' (b), and 'bad' (c) according to the quality of the phase velocity spectrum (see text).

4.3 Landslide displacement

Landslide movement was measured using continuous GPS monitoring and a time-lapse camera. The GPS system consists of one reference master station located in a stable area outside the landslide and three rover stations installed along the earthflow (Fig. 3). Rover GPS devices are LEICA-GMX901 antenna (single frequency; 10 Hz update; horizontal accuracy: 3 mm + 0.5 ppm; vertical accuracy: 5 mm + 0.5 ppm) powered by two batteries (12 V 14 Ah in parallel) and recharged by a 60 W solar panel. Rover stations are equipped with Wi-Fi direction antennas (model Ubiquiti Nanostation M5) for transmitting data to the Master Unit. Both the GPS receiver, the control unit, and the WiFi antenna were installed on a 2 m long pole equipped with a helicoid tip, that allowed to screw it into the ground. The master unit is a dual-frequency LEICA GMX902 antenna connected to an industrial PC. The PC run the software Leica GNSS Spider used to process the data in real time. Power to the master unit was provided via a connection to the grid at 220 V.

The time-lapse camera is a Brinno TLC200 that was placed outside the right flank of the earthflow (Fig 3) shooting the monitoring system. The camera has a focal length of 36 mm and it was set to take one picture every 30 minutes with a resolution of 640x480 pixels. An AVI video is created in the camera during recording, which results in a file of about 0.2 MB/frame stored on a 8 GB SD card. The analysis of these videos was carried out with the free software Tracker. The displacement was calculated knowing the dimension of an object in the camera view (a wood pole with red/white markings) and the distance from the camera to it. The pole was placed in the midline of the channel in order to measure the maximum velocity of the earthflow.

5 Results

5.1 Periodic acquisitions

The periodic seismic surveys were performed at Montevecchio from May 2014 to September 2015. For sake of clarity, we divide the dataset into the three periods that followed the three main reactivations.

Figure 8 illustrates the data collected after the first reactivation (May 2014-January 2015). The charts show the surface wave velocity profiles measured inside (section A, B, C, D) and outside (section E, F) the landslide in the different campaigns (location in Fig. 3). The surface wave velocity V_r is the one detected from the dispersion curve picked every 5 Hz from 50 Hz to 10 Hz and converted from frequency to depth by using the approximate relation depth $z \approx \lambda/2.5$ where λ is the wavelength [*Foti et al., 2014; Castellaro, 2016*]. The dates of the seismic surveys are reported as days elapsed since the last paroxysmal failure (in this case the partial reactivation of April 27, 2014) in order to highlight the variation of V_r with time.

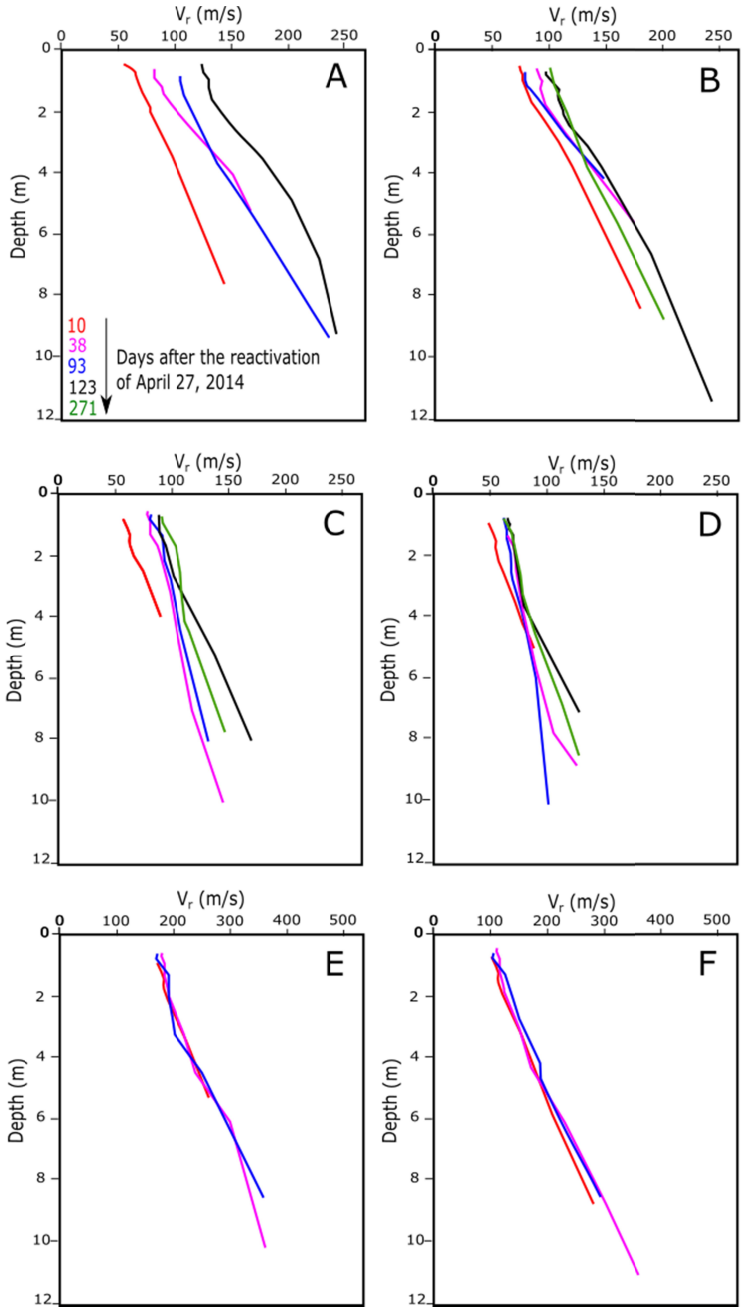

Figure 8: Surface wave velocity profiles measured after the reactivation of April 27, 2014 inside (A, B, C, D) and outside (E, F) the landslide.

As it can be seen, the surface wave velocity increases over time inside the landslide, while it remains constant outside. In particular, soon after the reactivation (10 days later) the landslide material is characterized by very low velocity values ($V_r \approx 50$ m/s) with no significant differences between the four sections. Then V_r increases as the material consolidates under its own weight. The rate of recovery along the earthflow is however different: in the source area

(section A) it is faster than in the lower part (section D), whereas sections B and C show intermediate values. For instance, in 271 days, the surface wave velocity at a depth of 5 m increases of 100, 45, 30, and 15 m/s moving from section A to D. These differences indicate that the rate of consolidation is affected by local factors such as landslide thickness or residual slope deformations. It is important to underline that some remedial works started at the toe of the landslide at the beginning of July 2014, that could influence the acquisitions in section D. In fact, during the surveys in the field, some displacements and remobilization of the material were observed in this area. In the meantime, the local authorities started to build the earth berm near the source area B (Fig. 3, black dotted rectangle), that can explain the abrupt increase of V_r in section A.

The data collected after the second failure (March to May 2015) provide similar results (Fig. 9). The first survey was done only 14 days after the reactivation of February 25, when the landslide material was still partially fluid. The data show very low velocity profiles throughout the earthflow (see sections B, C, D; section A is missing because it was not accessible) revealing a sharp drop in stiffness compared to pre-failure conditions (Fig. 8, end of the period). V_r remains low in the next two weeks due to the continuous movements of the earthflow, and gradually increase to the values shown before the failure. In this case the recovery rate is similar in the three sections. The surface wave velocity outside the landslide remains constant and equal to that measured in the first period ($V_r \approx$ 200-250 m/s).

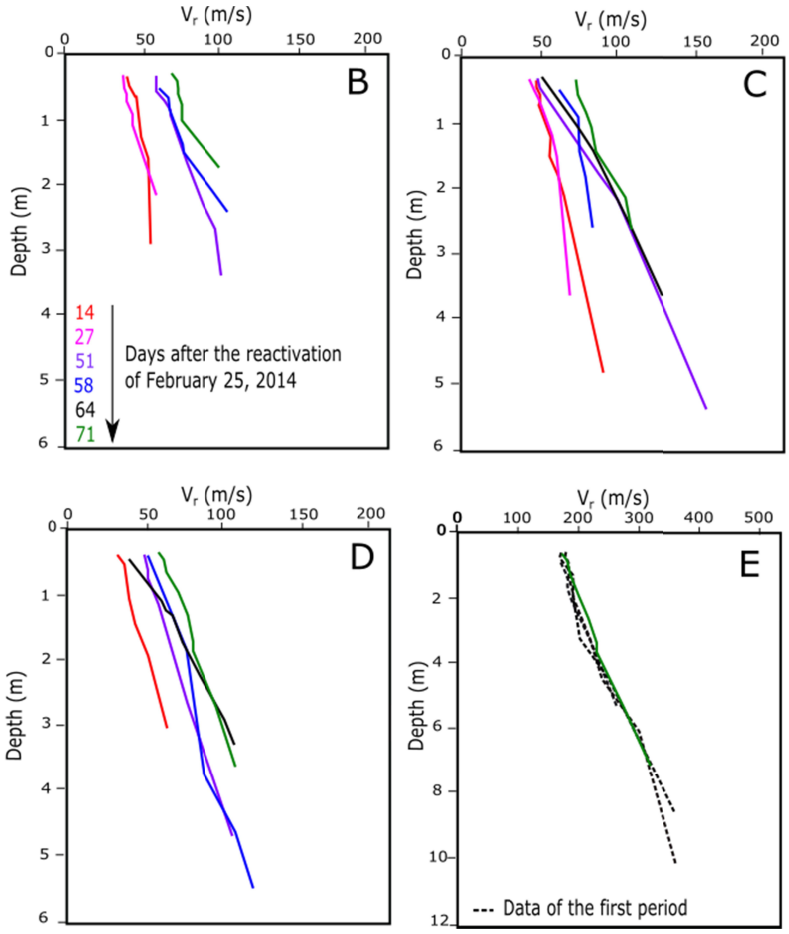

Figure 9: Surface wave velocity profiles measured after the reactivation of February 25, 2015 inside (B, C, D) and outside (E) the landslide.

The data of the third period (June to September 2015) further confirm these findings (Fig. 10). Again, the lowest values of V_r occur soon after the reactivation of May 25, 2015, then the wave velocity increases up to the pre-failure value. During this third period the variation of V_r with time is quite complex (especially in sections B and C) because of the extensive consolidation works carried out from July to September 2015, that triggered partial reactivations of the earthflow around the construction area of the earth berms. The last survey was on September 4, 2015. After that, local authorities realized a dense network of trench drains and drainage channels to stabilize the landslide, and most of the material was reworked up to a depth of 2-4 m.

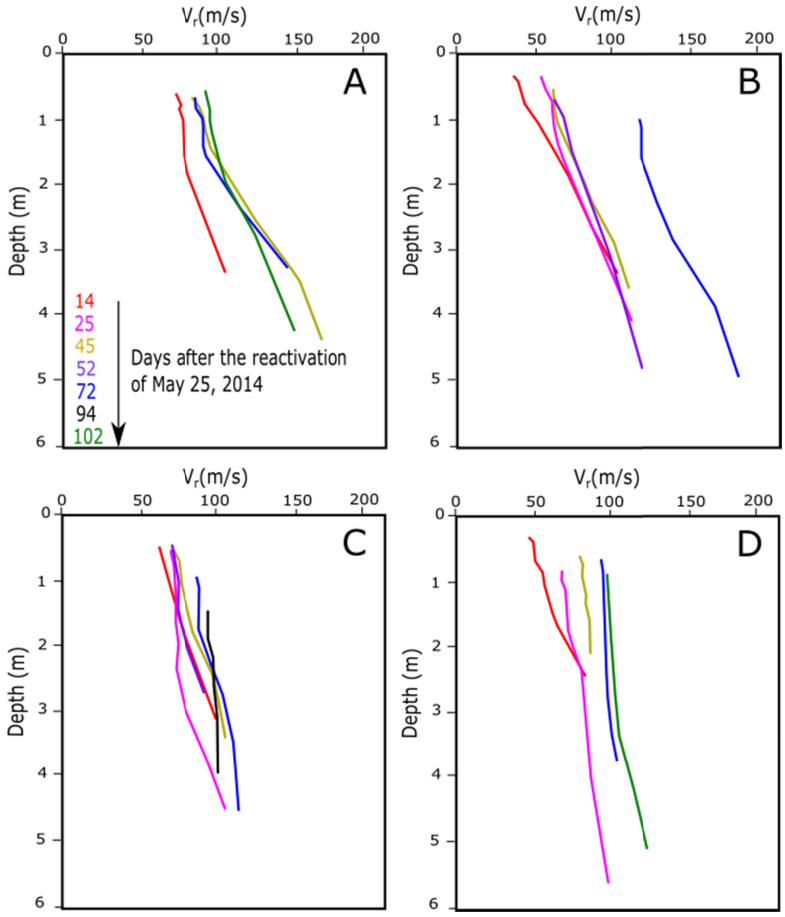

Figure 10: Surface wave velocity profiles measured in the period June 2015-September 2015 inside the landslide.

The chart in Fig. 11 summarizes the results of the seismic surveys performed inside and outside the landslide over the whole period. For this comparison, we used the surface wave velocity measured at a depth of 2 m, where the dispersion curves are well defined. Despite the difficulties posed by the harsh field conditions and the uncertainties in these geophysical measurements, a clear trend emerges from the data: the surface wave velocity drops to very low values as the earthflow reactivates, then it backs up to the initial values following a non-linear trend. This behavior is consistent with the exponential decrease of pore volume (and increase of soil stiffness) that occur with time during the consolidation of a porous material.

Of course, periodic surveys do not provide any indication on surface wave velocity during the paroxysmal stage of movement, when the earthflow seems to behave like a fluid. In that stage the landslide was not accessible and the values measured 10-15 days later ($V_r \approx 50$ m/s) were already affected by significant soil consolidation. However, such low values of V_r are typical of soft clay soils with very high porosity [*Reynolds, 1997*]. This suggests that during the paroxysmal stage of movement the surface wave velocity of the earthflow material should be extremely low, likely indicating a soil with negligible shear stiffness.

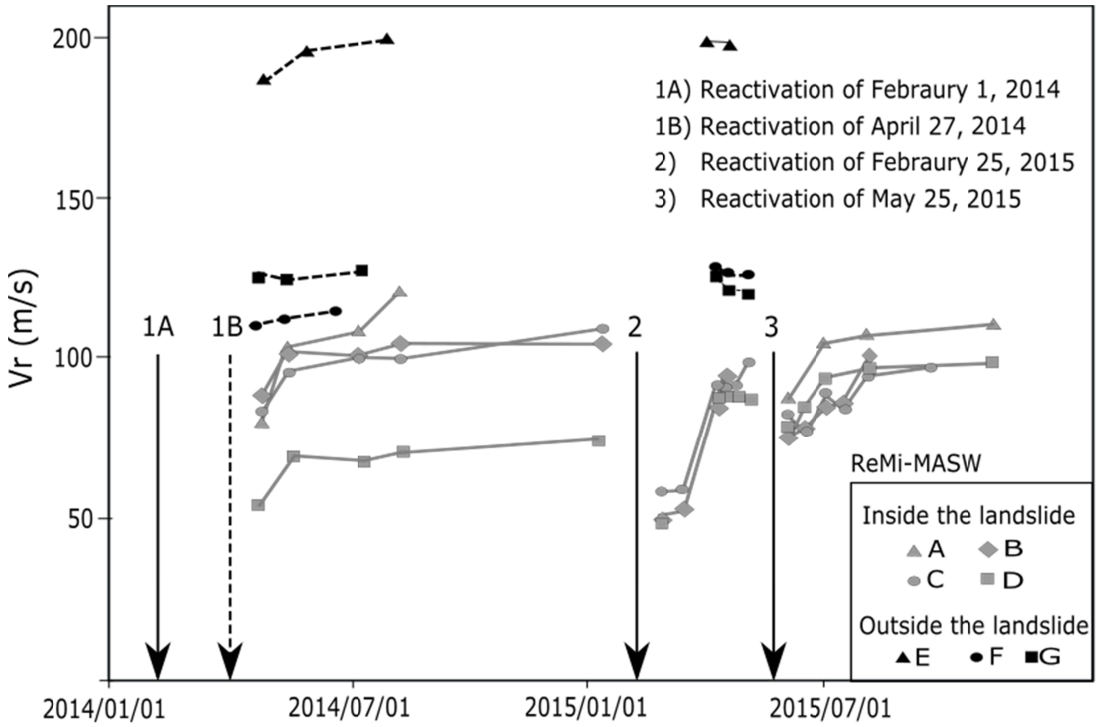

Figure 11: Variation of surface wave velocity with time during the whole period of measurement. Each point indicated the value measured at a depth of 2 m. Arrows show the main reactivations of the earthflow.

5.2 Continuous monitoring

Continuous monitoring was designed to capture the solid-fluid transition that should precede the failure. This process was first documented by *Mainsant et al.* [*2012*], that observed a significant drop of Rayleigh velocity a few days before the triggering of a landslide in the Swiss Alps. The Montevecchio monitoring system was installed in May 2014 (after the first reactivation) and recorded the second and third reactivation. The third failure of May 25, 2015 is the best documented being both the GPS and the time-lapse camera active.

Figure 12 shows the data collected one month before and after the failure (geophones data are not available during the paroxysmal stage of movement because the earthflow damaged the monitoring system). The black and gray dots indicate the surface wave velocity at 11 and 15 Hz, which correspond to an approximate depth of 1 and 2 m respectively. The pink dots are the velocities at 8 Hz (approx. 3 m). The investigation depth is here restricted to the first meters because the uncertainty increases excessively beyond 3 m. However, since the velocity profiles obtained by the periodic surveys are almost linear with depth and vary evenly over time (Fig. 10) we think that these data are representative of the general behavior of the landslide.

403 In the first three weeks of May 2015 the landslide was moving slowly at a rate of 3 cm/day. V_r
404 was almost constant and in the range 50-60 m/s, as typically measured by the monitoring system
405 during the suspended state of activity of the landslide (these values are 20-30% lower than those
406 obtained by periodic ReMi-MASW surveys for the reasons that will be discussed later). On May
407 22, it started to rain at 01:10 AM and continued until May 24 08:40 AM with 47 mm in 56 hours.
408 The landslide began to move and the surface wave velocity dropped remarkably to 30-35 m/s.
409 The velocity remained low for the whole day, then the landslide accelerated in the night of May
410 24-25, reached a peak velocity of 50 cm/hour, and then progressively decelerated in the next day.
411 The landslide was probably reaching a new equilibrium state when a second rainfall event of 24
412 mm in 3 hours occurred on May 26 05:30 PM, leading to the complete reactivation of the
413 earthflow. The paroxysmal stage of movement lasted five days with a peak velocity of 0.7
414 m/hour and a total displacement of 36 m. No data are available to assess the state of the material
415 during the failure because the geophones were buried by the landslide and most of the equipment
416 was destroyed. The monitoring system was reinstalled on June 3, 2015 and the post-failure data
417 confirm the results of periodic surveys: the surface wave velocity increases with time as the
418 landslide slows and consolidates. Three weeks after the reactivation, V_r almost returned to the
419 initial values of 50-60 m/s (Fig. 13).
420 The displacement rate continued to decline until the end of July 2015 while the surface wave
421 velocity remained essentially constant. On July 26, the local authorities started to build an earth
422 dam in the source area A (location in Fig.3) causing a local reactivation of the landslide. The
423 monitoring system recorded an increase of the displacement rate (mean velocity from 50 cm/day
424 to 80 cm/day) accompanied by a decrease in V_r of about 20% (Fig. 13). Again, V_r rises up to 50-
425 60 m/s as the earthflows decelerates.
426

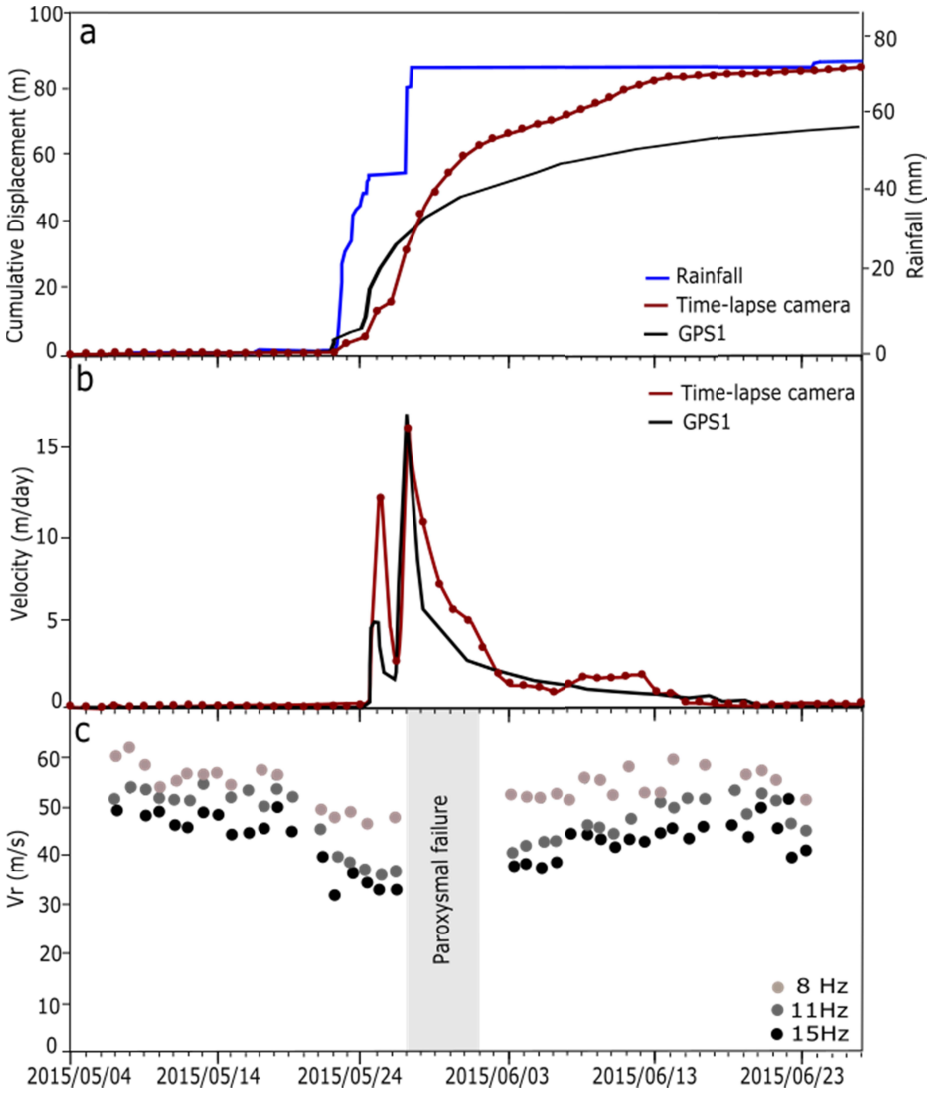

Figure 12: Comparison between rainfall (a), cumulative displacement (a), displacement rate (b) and surface wave velocity (c) measured by the monitoring system before and after the reactivation of May 25, 2015.

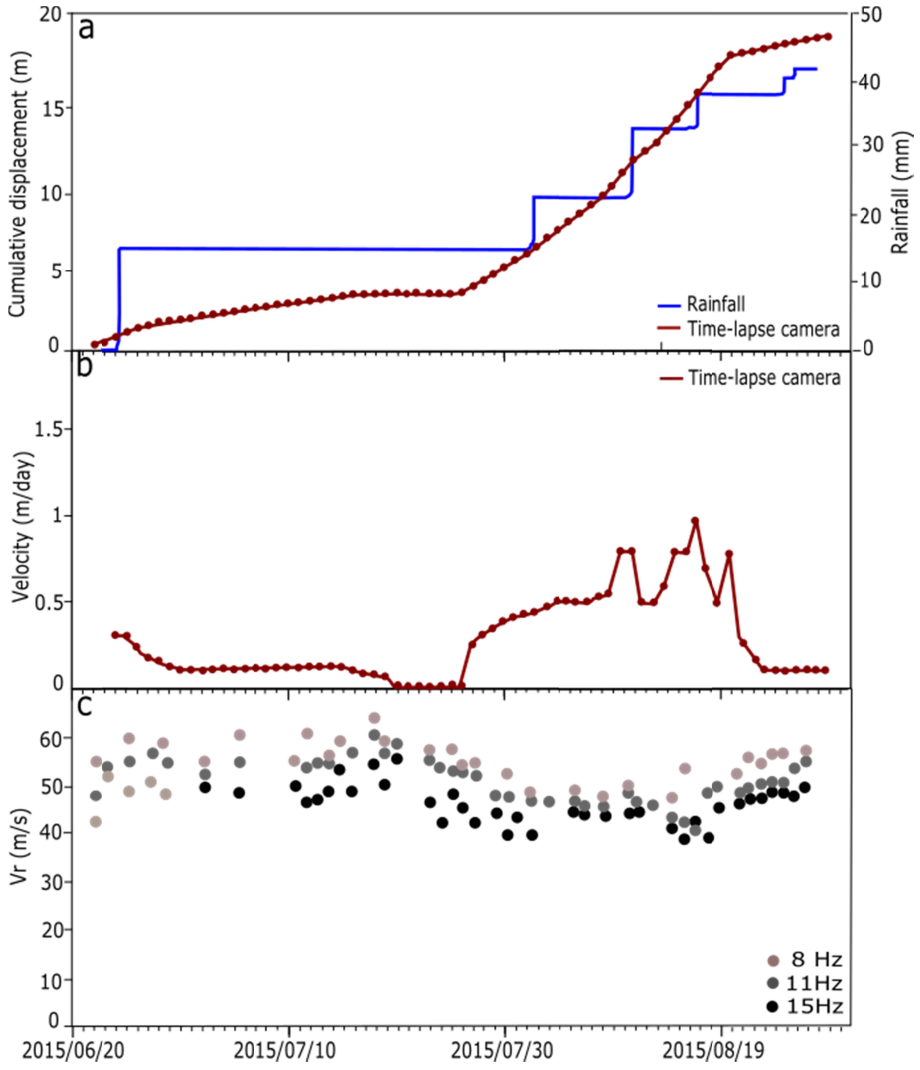

Figure 13: Comparison between rainfall (a), cumulative displacement (a), displacement rate (b) and surface wave velocity (c) measured by the monitoring system from June to August 2015.

The data collected during the second reactivation of February 25, 2015 provide similar results (Fig, 14). The landslide started to accelerate on January 29, 2015 in response to a localized failure in the source area that was triggered 9 days before by a very small rainfall (15 mm in 4 days). The surface wave velocity also began to decrease following the increase of speed. The displacement rate gradually increased to failure in the next three weeks showing two distinct episodes of increased landslide velocity. The first pulse occurred from February 3 to 6 after a rainfall of about 160 mm in 4 days combined with snowmelt. The landslide reached a peak velocity of 1.2 m/day and the monitoring system traveled about 2.5 m downslope. Despite this movement, the surface wave velocity remained essentially constant without further decline. On February 18, we reinstalled the system 5 m upslope and realigned the four geophones. The

surface wave velocity remained low and relatively constant until February 21, then it decreased to the lowest values of 30-40 m/s during the second landslide pulse, just before the paroxysmal failure of February 25. The triggering rainfall started at February 24, 05:00 PM and the landslide quickly accelerated 14 hours later. Unfortunately, we missed the time of the failure because the geophone cables were broken the day before.

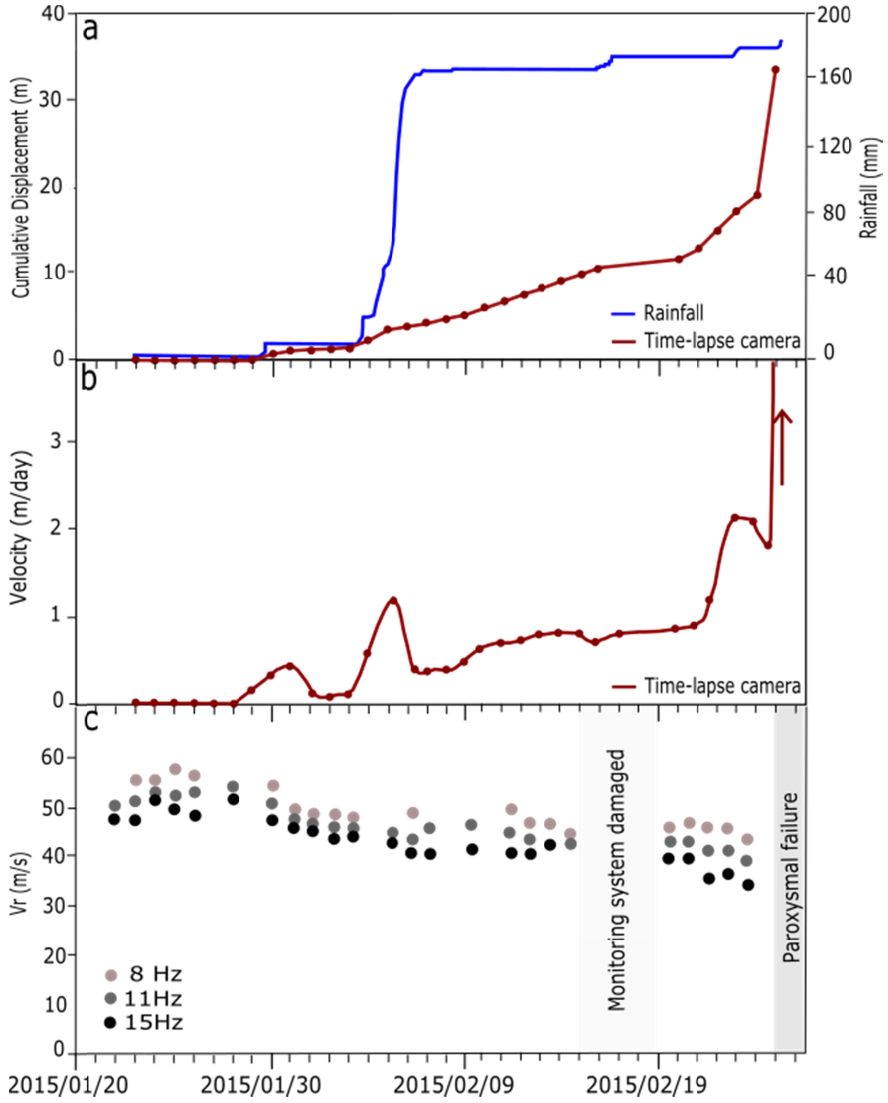

Figure 14: Comparison between rainfall (a), cumulative displacement (a), displacement rate (b) and surface wave velocity (c) measured by the monitoring system before the reactivation of February 25, 2015.

The data collected during the first phase of suspended activity (from May to December 2014; Fig. 15) prove the validity of the measurements above. In that stage the landslide was moving very slowly (less than 1 cm/day) with a general trend of decreasing velocity, and the surface wave velocity was essentially constant fluctuating around 50 m/s. The temporary accelerations exhibited by the landslide in response to rainfall events did not cause any significant decrease of

surface wave velocity probably because our measurements do not have the required accuracy to detect these small changes, or because the landslide was sliding along the basal shear surface with minor internal deformations. Anyway, the values of V_r for three considered frequencies are found to be normally distributed with a standard deviation of 2.2. Therefore, the drop in V_r measured when the landslide reactivates (in the order of 20-30 m/s) exceeds 6.7 times the standard deviation of measurements dispersion.

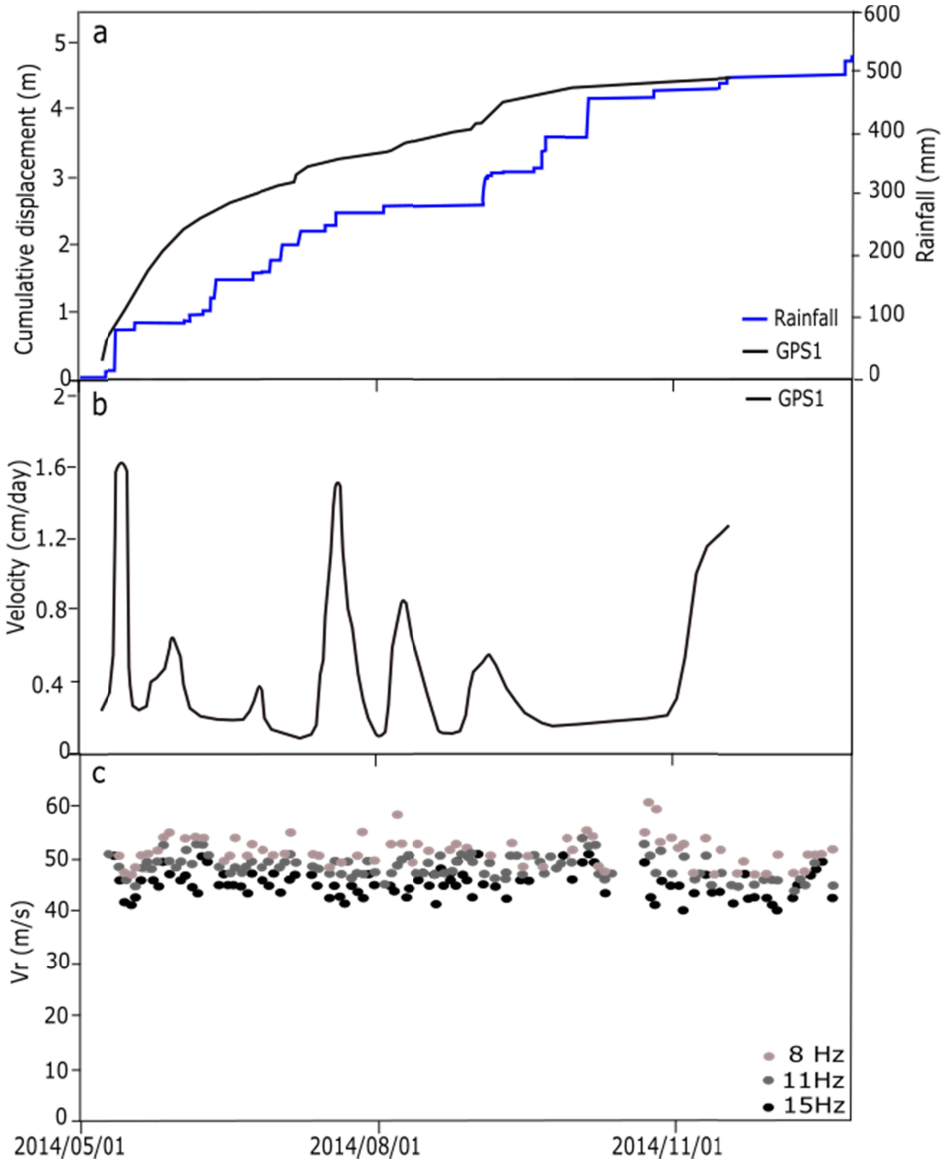

Figure 15: Comparison between rainfall (a), cumulative displacement (a), displacement rate (b) and surface wave velocity (c) measured by the monitoring system during the suspended phase from May to December 2015.

6 Discussion

The data collected at Montevecchio support the hypothesis that a relationship exists between the displacement rate of the earthflow and the dynamic soil properties. In fact, both the periodic and the continuous measurements of surface wave velocity show that V_r decreases when the landslide accelerates approaching the failure, and returns slowly to the original value as the landslide decelerates. However, the correlation is not simple and direct, and many uncertainties and ambiguities remain.

The most consistent evidence from field data is that the earthflow material is "soft" few days after the failure, and becomes progressively stiffer through time following the gradual decrease of the displacement rate. Although the absolute values of V_r may differ across the landslide, the overall trend is similar (Fig. 11). These changes are not restricted to the shallower soils but seem to affect the entire landslide depth (Fig. 8-10). The chart in Fig. 16a provides an overall view of the data collected by periodic surveys. Each point is the mean value of V_r measured at a depth of 2 m inside (sections A to D) and outside (sections E and F) the landslide. Time is reported as number of days elapsed since the last reactivation of each data series. The different trend is evident despite the scatter: inside the landslide, the surface wave velocity increases with time following a power function with an exponent of 0.13, outside the landslide it remains constant. There is a strong increase of V_r during the first 50-70 days after a reactivation, then the velocity seems to attain a constant value (though the curve is not well constrained in the long term).

Continuous monitoring provides similar results but the measured variation of surface wave velocity is less and the values of V_r are generally lower (compare sections C and D in Fig.11 with Figs. 12-15). When we first noticed the discrepancy between periodic and continuous measurements, we performed a series of direct comparison tests in the field. The tests indicate that the two systems provide exactly the same results in terms of frequency spectra and dispersion curves. The different site conditions that exist across the landslide, and where the permanent and the temporary systems are installed, can then explain the observed difference (for instance, section C is the nearest to the monitoring system but it is on the left side of the channel where the bedrock is closer to the ground surface).

A key point is to assess whether the measured variation of V_r describes a significant change of soil porosity (or gravimetric water content) that might indicate the fluid-to-solid transition of the earthflow. As an example, let us consider the surface wave velocity measured by periodic surveys soon after the reactivation ($V_r \approx 50$ m/s) and several months later ($V_r \approx 100$ m/s). Knowing that the S-wave velocity V_s is approximately 15% higher than V_r ($V_s \approx 1.15 \cdot V_r$) and that the small-strain shear modulus is $G_0 = \rho V_s^2$ (where ρ is the density of the soil that range from 1400 to 1800 kg/m^3), we obtain a shear stiffness G_0 of about 4-5 MPa and 20-25 MPa respectively. It is recognized in the literature that G_0 is significantly influenced by void ratio e, and a number

of empirical and theoretical functions between G_0 and e have been proposed [e.g., *Hardin and Black, 1969; Iwasaki and Taksuoka; 1977, Santos 1999*]. According to the relationship proposed by *Santos and Correia [2000]*, an increase of G_0 from 4-5 MPa to 20-25 MPa roughly corresponds to a decrease of void ratio from $e \approx 2$ to $e \approx 0.7$, which is a relevant change of porosity for a clay soil.

Using the same formula we can convert our V_r values (Fig. 16b) into a normalized void ratio $\hat{e} = \frac{e_{\max} - e}{e_{\max} - e_{\min}}$ (where $e_{\max} = 2$ and $e_{\min} = 0.7$ are the initial and final void ratio respectively, and e is the void ratio at a certain time estimated by V_r) to point out the change of soil porosity with time. The data exhibit a nonlinear decrease of $\hat{e}$ that basically recalls the change of volume during a consolidation process. In fact, the general trend of the experimental points well agrees with the theoretical trend computed by the one-dimensional consolidation equation [*Terzaghi, 1943*] using reasonable values of the coefficient of consolidation c_v. Moreover, since in a fully-saturated soil the void ratio is directly correlated with the gravimetric water content w ($w = e / G_s$, where $G_s = 2.7$ is the specific gravity of solids), it turns out that the landslide material has a water content $w \approx$70%-85% soon after failure and $w \approx$20%-30% several months later. Interestingly, the first values are well above the Liquid Limit of the material (LL=50%) while the latter fall around the Plastic Limit (PL=26%).

In the geotechnical literature, the Liquid Limit is the moisture content that defines where the soil changes from a plastic to a viscous fluid state [*Terzaghi and Peck, 1967*]. Based on the simple calculations above we could then conclude that the earthflow is in a "fluid state" soon after the paroxysmal stage of movement and returns into the "plastic state" as the consolidation takes place. However, our data do not allow us to draw such a conclusion with confidence. In fact: i) the existing $G_0 - e$ relationships are based on laboratory tests and may not be applicable to the field due to the presence of cracks, open fractures, and heterogeneities into the soil [*Castellaro, 2016a, Pitilakis et al., 1992*]; ii) the values of V_r vary remarkably with depth and location across the landslide; iii) the accuracy of the measurement method is limited by the factors described above (see section C); iv) it is questionable to assume that Atterberg's limits are relevant for describing the solid-fluid transition observed in the field, and for landslides the same meaning of the term "flow" is still debated in the literature *[Ancey, 2007]*. Nevertheless, we can say that the detected change of V_r likely indicates a relevant variation of void ratio and water content of the earthflow. A number of geotechnical and rheometric tests on clay samples collect at Montevecchio (and in other 5 earthflows) were conducted to assess the evolution of viscosity with the shear stress and to identify the critical shear strain rate associated with bifurcation in viscosity [*Carriere et al., submitted*]. Test results show that the water content is a key parameter controlling the solid-fluid transition of these soils.

A further point of discussion is the behavior of the landslide before the failure. *Mainsant et al.* [*2012*] detected a decrease of the relative Rayleigh wave velocity well before the reactivation of their monitored landslide (a first 2% drop about one month before the failure, and a second 7% drop four days before the failure). *Mainsant et al.,* [*2015*] carried out some laboratory experiments on artificial clay slopes at different water content and identified a drop in V_r values before the onset of the mass movements. These results suggest that field monitoring of surface wave velocity could be potentially used to predict landslides [*Mainsant et al., 2012*]. Also in this work we find a relationship between displacement rate and V_r. However, in our case the surface wave velocity decreases while the landslide starts to move and not before (see Fig. 12). A possible explanation of this different behavior is that all the data of the Montevecchio earthflow were collected after the paroxysmal failure of the February 2014, that completely remolded the existing deposits and generated a dense network of pervasive cracks and fissures into the landslide mass. In this condition, we had no chance of measuring any cracking phenomena before the subsequent reactivations. For these reasons, our data cannot prove (or disprove) the use of surface wave monitoring for early landslide detection.

The last comment deals with some technical issues related to the field monitoring of surface wave velocity. The system configuration adopted at Montevecchio (4 vertical geophones at 4.5 Hz; 2 min sessions at 300 Hz every 1 hour; passive mode) proved its effectiveness but the accuracy of the method can be improved. Quite often the dispersion curves were not clear enough to obtain a reliable value of V_r and a number of measurements were discarded. Several modifications could be done to get best results: 1) combine active and passive mode acquisition in order to improve the dispersion curve at high frequency ranges, for example using an automatic hammer controlled by the datalogger and 2) use a larger number of geophones to ensure an adequate data redundancy [*Tokimatsu, 1997*], although *Ohori,* [*2016*] showed that no benefits derive by using more that 7-8 geophones. A powerful datalogger that combines fast acquisition, large memory capability, and relays control is required to this purpose.

We are currently developing a simple down-hole probe specifically designed for long-term monitoring in order to get direct measurements of shear wave velocity inside an active landslide. The idea is to combine accurate V_s data with independent measurements of soil porosity obtained by continuous monitoring of the volumetric soil water content.

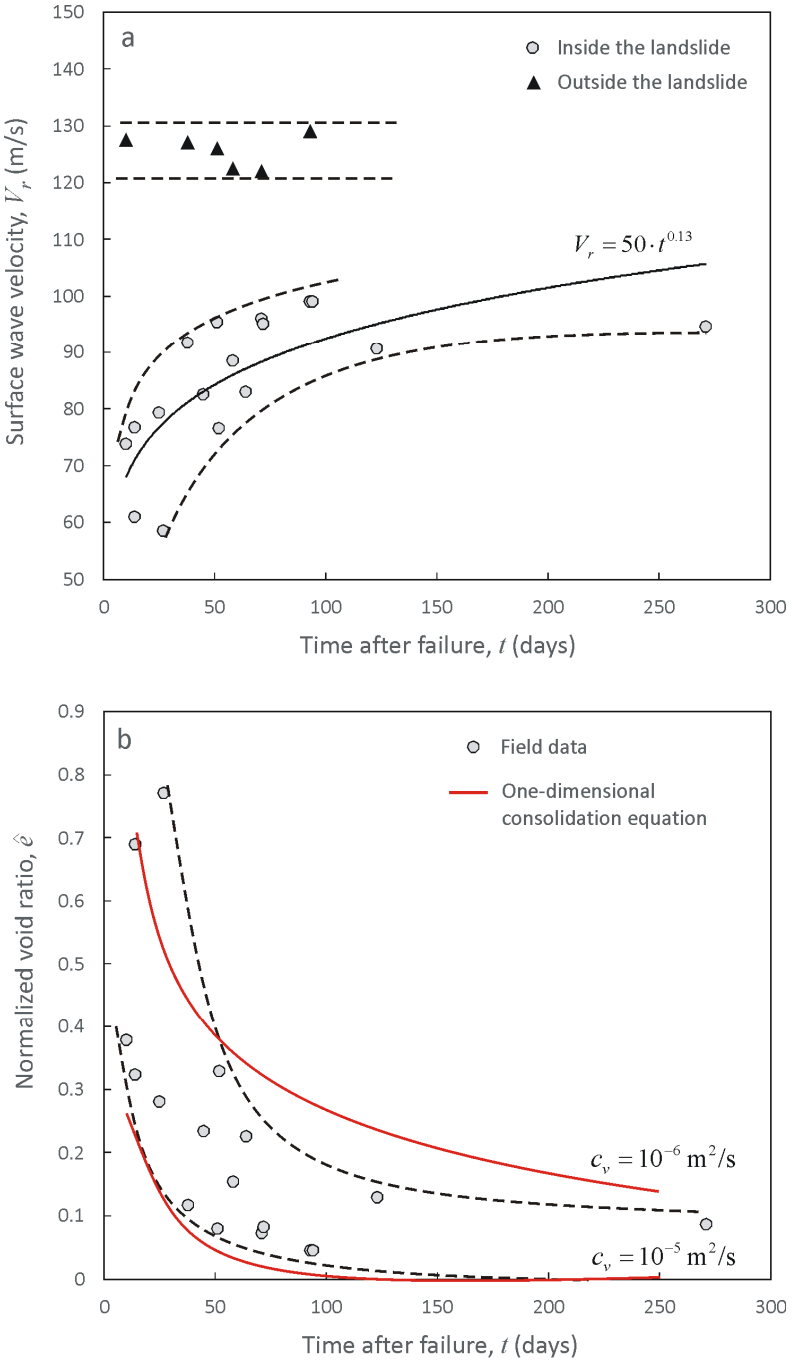

Figure 16: Charts showing the variation of surface wave velocity with time at a depth 2 m (a) and the corresponding variation of the normalized void ratio (b). Each point represents the mean value of V_r measured by periodic surveys inside (gray dots) or outside (black triangles) the landslide. Red lines in (b) indicates the theoretical trend predicted by the one-dimensional Terzaghi equation.

7 Conclusions

Ambient seismic noise monitoring proved to be an effective method to investigate the mechanical changes that occur when an earthflow reactivates. In this study, we monitored rainfall, ground displacement, and surface wave velocity of an earthflow located in the Northern Apennines of Italy during a two-years period of intense activity. Based on these data, several conclusions can be drawn:

1. There is a direct relationship between the displacement rate of the landslide and the surface wave velocity (V_r): V_r decreases when the landslide accelerates approaching the failure, and gradually increases over time as the landslide decelerates after failure; the minimum value of V_r is probably reached during the paroxysmal stage of movement (displacement rate in the order of meters/hour), although monitoring data are not available in this stage

2. The increase of surface wave velocity after failure can be explained by the progressive decrease of soil porosity associated with the consolidation of the landslide mass; this process can continue for weeks or months and may be interrupted by a new reactivation

3. At Montevecchio, the surface wave velocity starts to decrease as the landslide starts to move, not before as found by *Mainsant et al.,* [*2015*]. In our case, however, the soil was already remolded and softened by the previous failures, so we probably missed the initial cracking that affects the soil when the reactivation occurs after a long period of dormancy

4. Our measurements are not accurate enough to permit an analysis of the solid-fluid transition that turns the initial slide into a flow. However, the detected variation of surface wave velocity indicates that the landslide material undergoes significant variation of soil stiffness, void ratio, and water content supporting the hypothesis of a drastic change in mechanical behavior during failure.

Acknowledgments

This work was supported by the Civil Protection Agency of the Emilia-Romagna Region under the framework agreement “Special activities on support to the forecast and emergency planning of Civil Protection with respect to hydrogeological risk” (ASPER-RER, 2011–2015 and 2016-2021). All the data used in this paper are listed in the references or are included in the figures and tables.

References

Aki, K. (1957), Space and time spectra of stationary stochastic waves, with special reference to microtremors. *Bulletin of Earthquake Research Institute*, **35**, 415-456.

Baum, R.L. and A.M. Johnson (1993), Steady movement of landslide features in fine-grainedsoils—a model for sliding over an irregular slip surface. Chapter D of landslide processes in Utah—observation and theory. U.S. Geological Survey Bulletin 1842. *U.S. Geological Survey*, Reston, VA, D1–D28.

Beekman, A. N. (2008), A comparison of experimental ReMi measuraments with various source, array, and site condition. *Master thesis of Sciences in Civil Engineering*, University of Arkansas.

Bernardie, S., Desramaut, N., Malet, J.P., Gourlay, M., Grandjean, G., (2015), Prediction of changes in landslide rates induced by rainfall. *Landslide*, **12**, 481-494.

Berti, M., Martina, M.L.V., Franceschini, S., Pignone, S., Simoni, A., Pizziolo, M., (2012), Probabilistic rainfall thresholds for landslide occurence using a Bayesian approach. *Journal of Geophysical Reaserch*, **117**, 1-20.

Borgatti, L., Corsini, A., Barbieri, M., Sartini, G., Truffelli, G., Caputo, G., Puglisi, C., (2006), Large reactivated landslides in weak rock masses: a case study from Northern Apennines (Italy). *Landslide*, **3**,115-124.

Bovis, M.J. (1985), Earthflows in the Interior Plateau, southwest British Columbia. *Canadian Geotechnical Journal*, **22**(2), 313-334.

Castellaro, S., Panzeri, R., Mesiti, F., Bertello, L., (2015), A surface seismic approach to liquefaction. *Soil Dynamics and Earthquakes Engineering*, **77**, 35-46.

Castellaro S., (2016), The complementarity of H/V and dispersion curves. *Geophysics*, **81**, T323-T338.

Castellaro S., (2016a), Soil and structure damping from single station measurements. *Soil Dynamics and Earthquake Engineering*, **90**, 480-493.

Chiappone, A., and C. Scavia (1999), La prova di blu metilene nella caratterizzazione geotecnica: un'applicazione allo studio della stabilità dei versanti. *Rivista Italiana di Geotecnica*, **4**, 36-51.

Coe, J. A., Ellis, W. L., Godt, J.W., Savage, W.Z., Savage, J.E., Michael, J.A., Kibler, J.D., Powers, P.S., Lidke, D.J., Debray, S., (2003). Seasonal movement of the Slumgullion landslide determined from Global Positioning System survey and field instrumentation, July 1998 – March 2002. *Engineering Geology*, **68**, 67-101.

Comegna, L., Picarelli, L., Urciuoli, G., (2007), The mechanics of mudslides as a cyclic undrained-drained process. *Landslide*, **4**, 217-232.

657 Corominas, J., Moya, J., Ledesma, A., Lloret, A., Gili, J. A., (2005), Prediction of ground
658 displacement and velocities from groundwater level changes at the Vallcebre landslide (Eastern
659 Pyrenees, Spain). *Landslide*, **2**, 83-96.
660
661 Daehne, A., Corsini, A., Travelletti, J., Spickermann, A., Malet, J.-P., Van Asch, Th.W.J.,
662 Bégueria-Portuguès, S., (2010), Applications of a numerical model for slow moving landslides to
663 the Valoria landslide in the Italian Apennines, and the Super Sauze mudslide in the French
664 Alps (Mountain Risks: Bringing Science to Society - Firenze - 24-26 Novembre 2010) (Malet JP,
665 Glade T, Casagli N. - Proceedings of the International Conference "Mountain Risks: Bringing
666 Science to Society") (CERG Editions Strasbourg FRA) – 233-241
667
668 Daehne, A., and A. Corsini (2012), Kinematics of active earthflows revealed by digital image
669 correlation and DEM subtraction techniques applied to multi-temporal LiDAR data. *Earth Surf.*
670 *Process. Landforms*, **38**(6), 640-654.
671
672 D'Elia, B., Picarelli, L., Leroueil, S., (1998), Geotechnical characterization of slope movements
673 in structurally complex clay soils and stiff jointed clays. *Rivista Italiana di Geotecnica*, **33**, 5-32.
674
675 Evans, S.G., and G.R. Brooks (1994), An earthflow in sensitive Champlain Sea sediments at
676 Lemieux, Ontario, June 20, 1993, and its impact on the South Nation River. *Canadian*
677 *Geotechnical Journal*, **31**(3), 384-394.
678
679 Foti, S., Lai G. C., Rix G. J., Strobbia C., (2014), Surface wave methods for near-surface site
680 characterization. CRC Press.
681
682 Geertsema, M., Clague, J.J., Schwab, J.W., Evans, S. G., (2006), An overview of recent large
683 catastrophic landslide in northern British Columbia. *Canada. Engineering Geology*, **83**, 120-143.
684
685 Giordan, D., Allasia, P., Manconi, A., Baldo, M., Santangelo, M., Cardinali, M., Corazza, A.,
686 Albanese, V., Lollino, G., Guzzetti, F., (2013), Morphological and kinematic evolution of a large
687 earthflow: The Montaguto landslide, Southern Italy. *Geomorphology*, **187**, 61-79.
688
689 Giusti, G., Iaccarino, G., Pellegrino, A., Picarelli, L., (1996), Kinematic features of earthflows in
690 Southern Apennines. *International Symposium of landslides*, Trondheim, **1**, 457-462.
691
692 Guerriero, L., Revellino, P., Coe, J.A., Focareta, M., Grelle, G., Albanese, V., Corazza, A.,
693 Guadagno, F.M., (2013), Multi-temporal maps of the Montaguto earth flow in southern Italy
694 from 1954 to 2010. *Journal of Maps,* **9**(1), 135–145.
695
696 Guerriero, L., Coe, J.A., Revellino, P., Guadagno, F. M., (2014), Influence of slip-surface
697 geometry on earth-flow dedformation, Montaguto earthflow, southern Italy. *Geomorphology*,
698 **219**, 285-305.
699
700 Handwerger, A. L., Roering, J. J., Schmidt, D. A., (2013), Controls on the seasonal deformation
701 of slow-moving landslides. *Earth and Planetary Sciences Letters*, 377-378, 239-247.
702

703 Hang, P. T., and G.W. Brindley (1970), Methylene blue absorption by clays minerals.
704 Determination of surface areas and cation exchange capacities (clay organic studies XVIII).
705 *Clays and clay minerals*, **18**(4), 203-212.
706
707 Hardin, B.O. and Black, W.L. (1969), Closure to vibration modulus of normally consolidated
708 clays. *Journal of Soil Mechanics and Foundations Division*, ASCE, vol. **95** (6), 1531-1537.
709
710 Hungr, O., Evans, S.G., Bovis, M.J., Hutchinson, J.N., (2001), A review of the classification of
711 the flow type. *Environ. Eng. Geosci.,* **7**, 221–238.
712
713 Hutchinson, J.N., (1970), A coastal mudflow on the London clay cliffs at Beltinge, North Kent.
714 *Geotechnique*, **20**(4), 412-438.
715
716 Hutchinson, J.N. and R.K. Bhandari (1971), Undrained loading, a fundamental mechanism of
717 mudflows and other mass movements. *Geotechinique*, **21**(4), 353-383.
718
719 Iwasaki, T. and Taksuoka, F. (1977), Effects of Grain size and grading on dynamic shear moduli
720 of sands. *Soils and Foundations*, 17(3), 19-35.
721
722 Jongmans, D., and S. Garambois (2007), Geophysical investigation of landslide: a review. *Bull.*
723 *Soc. geol. Fr*, **178**(2), 101-112.
724
725 Jongmans, D., Baillet, L., Larose, E., Bottelin, P., Mainsant, G., Chambon, G., Jaboyedoff M.,
726 (2015), Application of ambient vibration techniques for monitoring the triggering of rapid
727 landslides. *Engineering Geology for Society and Territory*, **2**, 371-374.
728
729 Keefer D.K., and A.M Johnson (1983), Earthflows: morphology, mobilization and movement.
730 U.*S. Geological Survey Professional Paper*, 1264, 54.
731
732 Lanzo, G., and B. D'Elia (1997), Experiences on slope movements in clayey soils. *Rivista*
733 *Italiana di Geotecnica*, **31**, 15-27.
734
735 Lautrin, D. (1989). Utilisation pratique des parametres derives de l'essai au blue de methylene
736 dans le les projets de genie civile. *Bulletin de Liaison des laboratories des ponts et Chaussees*,
737 **160**, 29-41.
738
739 Lollino, P., Giordan, D., Allasia, P., (2014). The Montaguto earthflow: A back analysis of the
740 process of landslide propagation. *Engineering Geology*, **170**(10), 66-79.
741
742 Louie, J. N. (2001), Faster, better: shear-wave velocity to 100 meters depth from refraction
743 microtremor arrays. *Bulletin of Seismological Society of America*, **91**(2), 347-364.
744
745 Mainsant, G., Larose, E., Bronnima, C., Jongmans, D., Michoud, C., Jaboyedoff M. (2012),
746 Ambient seismic noise monitoring of a clay landslide: toward failure prediction. *Geophisical*
747 *Research Letters*, **117**, F01030.
748

Mainsant, G., Chambon, G., Jongmans, D., Larose, E., Baillet L., (2015), Shear-wave-velocity drop prior to clayey mass movement in laboratory flume experiment. *Engineering Geology*, **192**, 26-32.

Malet, J. P., Laigle, D., Remaitre, A., Maquaire, O., (2005), Triggering conditions of debris-flows associated to complex earthflows. *Geomorphology*, **66**, 215-235.

Mitaritonna, G., Amorosi, A., Cotecchia, F., (2010), Multidirectional bender element measuraments in the triaxial cell: equipment set-up and signal interpretation. Rivista Italiana di Geotecnica, 1, 50-69.

Okada, H. (2003), The microtremor survey method (K. Suto, trans.). SEG Geophysical Monograph Series No. 12.

Okada, Y., Kurokawa, U., Asano, S., (2012), Examining Fluidisation Mechanisms of Hikagemor Landslide Triggered by Iwate-Miyagi Nairiku Earthquake in 2008 by Laboratory Soil Tests. Earthquake-Induced Landslides, 431-435.

Park, C., Miller, R., Xia, J., (1999), Multi-channel analysis of surface waves. Geophysics, 64(3), 800-808.

Park, C. B., Miller, R. D., Xia, J., Ivanov, J., (2007), Multichannel analysis of surface waves (MASW) —Active and passive methods. The Leading Edge, 26(1), 60–64.

Pastor, M., Blanc, T., Pastor, M.J., (2009), A depth integrated viscoplastic model for dilatant saturated cohesive-frictional fluidized mixitures: Application to fast catastrophic landslides. Journal of non-Newtonian fluid mechanics, 158(1-3), 142-153.

Pastor, M., Manzanal, D., Fernandez Merodo, J.A., Mira, P., Blanc, T., Drempetic, V., Pastor, M.J., Haddad, B., Sanchez, M., (2010), From solids to fluidized soils: diffuse failure mechanisms in geostructureswith applications to fast catastrophic landslides. Granular Matter, 12(3), 211-228.

Picarelli, L., Urcioli, L., Ramondini, G., Comegna, L., (2005), Main features of mudslides in tectonised highly fissured clays shales. Landslides, 2(1), 15-30.

Picarelli, L. (2015). Observing, Modelling and checking slope behaviour: is there a better way to fully exploit the expertise og geologists and engineers at the same time?. Engineering Geology for Society and Territory, 2, 59.77.

Pitilakis K.D., Anastassiadis A., Raptakis D., (1992), Field and laboratory determination of dynamic properties of natural soils deposit, Earthquake Engineering, Tenth World Conference.

Prior, D.B. and N. Stephens (1972), Some movement patterns of temperate mudflows—examples from northeastern Ireland. Geol. Soc. Am. Bull., 83(8), 2533–2543.

795 Renalier, F., Bievre, G., Jongmans, D., Campillo, M., Bard, P. Y., (2010), Clayey landslide
796 invastigations using active and passive Vs measurements. Advances in near surface seismology
797 and ground penetrating radar, Geophys. Dev. Ser., 15(7), 397-414.
798
799 Reynolds, J. M. (1997), An introduction to applied and environmental geophysics, 796, Jhon
800 Wiley, Chichester, UK.
801
802 Ricci Lucchi, F., Bassetti, M.A., Manzi, V., Roveri, M., (2002), Il Messiniano trent'anni dopo:
803 eventi connessi alla crisi di salinità dell'avanfossa appenninica. Studi Geol. Camerti, 1, 127-142.
804
805 Santos, J.A. (1999), Behaviour of piles under lateral static and dynamic loading. PhD Thesis,
806 Technical University of Lisbon, Portugal.
807
808 Santos J.A and G. Correia, (2000), Shear modulus of soils under cyclic loading at small and
809 medium strain level, Proc., 12WCEE 2000, paper no.0530
810
811 Sassa, K., Fukuoka, H., Wang, G., Ishikawa N., (2004). Undrained dynamic-loading ring-shear
812 apparatus and its application to landslide dynamics. Landslide, 1, 7-19.
813
814 Satoh, T., Kawase, H., Matsushima, S., (2001), Estimation of S-wave velocity structures in and
815 around the Sendai Basin, Japan, using array records of microtremors. Bulletin of the
816 Seismological Society of America, 91(2), 206–218.
817
818 Schadler W., Slope movements of the earthflow type - engineering -geological investigation,
819 geotechnical assessment, and modelling of the source areas on the basis of case studies from the
820 Alps and Apennines. Logos verlag Berling GmbH, 2010.
821
822 Schulz, W. H., Mackenna, J. P., Kibler, J. D., Biavati, G., (2009), Relations between hydrology
823 and velocity of a continuously moving landslide – evidence of pore pressure feedback regulating
824 landslide motion? Landslides, 6, 181-190.
825
826 Schulz, W. H., Kean, J. W., Wang, G., (2009a), Landslide movement in southwestern Colorado
827 triggered by atmospheric tides. Nature Gosciences, 2(12), 863-866.
828
829 Socco, L. and D., Jongmans (2004), Special issue on seismic surface waves. Near Surface
830 Geophysics, 2(4), 163-165.
831
832 Socco, L. and C. Strobbia (2004), Surface-wave method for near-surface characterization. A
833 tutorial. Near Surface Geophysics, 2(4), 165-185.
834
835 Terzaghi K., (1943), Theoretical Soil Mechanic. Jhon Wiley and Sons., New York.
836
837 Terzaghi K. and R. B. Peck (1967), Soil mechanics in engineering practice. Second Edition: John
838 Wiley & Sons, New York.
839 Tokimatsu, K. (1997), Geotechnical site characterization using surface waves. Proc. 1st Intl.
840 Conf. Earthquake Geotechnical Engineering, 3, 1333–1368.

Van Asch, T. W. J. (2005), Modelling the hysteresis in the velocity pattern of slow-moving earth flows: the role of excess of pore pressure. Earth Surf. Process. Landforms, 30(4), 403-411.

Van Asch, T. W. J., Van Beek, T. A., Bogaard, L. P. H., (2007), Problemsin predicting the mobility of slow-moving landslides. Eng. Geol. Amsterdam, 91(1), 46-55.

Van Asch, T. W. J. and J.P. Malet (2009), Flow-type failures in fine-grained soils: an important aspect in landslide hazard analysis. *Nat. Hazards Earth Syst. Sci.,* **9**(5), 1703–1711.

Wathelet, M., Jongmans, D., Ohrnberger, M., (2004), Surface wave inversion using a direct search algorithm and its application to ambient vibration measurements. *Near Surface Geophysics*, **2**, 211–221.

Zhang, X., Phillips, C., Marden, M., (1991), Internal deformation of a fast-moving earthflow, Raukumura Peninsula, New Zealand. *Geomorphology,* **4**, 145-154.

PAPER 3

Unsteady sediment discharge in earth flows: Mount Pizzuto earth flow, southern Italy

Guerriero L., Bertello L., Cardozo N., Berti M., Grelle G., Revellino P.

*****submitted to **Geomorphology,** September 2016

Unsteady sediment discharge in earth flows: Mount Pizzuto earth flow, southern Italy

Luigi Guerriero[a]*, Lara Bertello[b], Nestor Cardozo[c], Matteo Berti[b], Gerardo Grelle[a], Paola Revellino[a]

[a]Department of Science and Technologie, University of Sannio, via Port'Arsa 11, 82100 Benevento, Italy

[b]Department of Biological, Geologic and Environmental Sciences, University of Bologna, 40127, Bologna, Italy

[c]Department of Petroleum Engineering, University of Stavanger, 4036 Stavanger, Norway

*Corresponding author: Luigi Guerriero, e-mail: luigi.guerriero@unisannio.it

Abstract

Surface mapping, GPS surveys, T-LiDAR surveys, boreholes, seismic profiles, and HVSR measurements were used to study the mechanisms of sediment transport along the Mount Pizzuto earth flow in southern Italy. The earth flow presents several kinematic zones, with transitional areas marked by a change of structural style, from compressional structures (thrusts) upslope to extensional structures (normal faults) downslope. We relate sediment discharge at the transition of the kinematic zones to internal strain. The results suggest that during surge, flow acceleration starts within the head and propagates downslope inducing a cascade effect between kinematic zones. During this event, the average sediment discharge is nearly constant along the

transport zone, and the change from slide to flow allows movement propagation towards the toe. During ordinary movement, the activity of kinematic zones is mutually independent and sediment discharge varies along the flow length. In general, the velocity profile and the dilatation style are controlled by the geometry of the basal slip surface. Moving through a kinematic zone, the earth flow volume changes in relation to the earth flow velocity. The implications of our results are: i) earth flows having a well-defined neck are more likely to surge with respect to those without, ii) sediment discharge is not constant but is a function of the earth flow activity, iii) during surge, earth flow material behaves similar to an incompressible fluid and, iv) the distribution of structures at the flow surface can provide information about the geometry of the slip surface and the velocity profile.

Keywords: earth flow, kinematics, sediment discharge, deformation, basal slip surface, mechanical modeling,

1. Introduction

Earth flows (sensu Varnes, 1978) occur in many hilly and mountainous areas and are pervasive in many rapidly eroding landscapes (Mackey et al., 2009). Earth flow dominated landscapes are characterized by crescent-shaped or basin-shaped scars, loaf-shaped bulging toes, and long narrow tongue- or teardrop-shaped transport zones (Keefer and Johnson, 1983; Bovis and Jones, 1992; Booth et al., 2011; 2013; Calista et al., 2016). Large earth flows often span from the

channel to the ridge and can persist for significant periods of time (Mackey and Roering, 2011). The evolution of large earth flows is often characterized by an alternation between long periods of slow and/or localized movement, and "surging events" (e.g. Keefer and Johnson 1983; Zhang et al. 1991; van Asch et al., 2006; van Asch and Malet, 2009; Giordan et al., 2013; Guerriero et al., 2013a; 2014; 2015; 2016a). Slow movement is driven by hydrologic forcing, and seasonal acceleration and deceleration are induced by pore-water pressure variations (e.g. Iverson and Major, 1987; Iverson 2005; Handwerger et al., 2013). Increase in pore pressure is caused by the infiltration of rainfall and springs (Iverson and Major, 1987; Guerriero et al., 2015). Decrease in pore pressure is a consequence of drainage and shear zone dilatation (e.g. Krzeminska et al., 2012; Schulz et al., 2009).

Earth flow surge is characterized by a velocity that approaches several meters per day and in some cases several meters per hour. A surge can occur when prolonged rainfalls are associated with the loss of efficient drainage pathways (Iverson 2005), and new sediments in the source area are available through retrogression of the upper boundary (Mackey and Roering, 2011; Guerriero et al., 2014; Pinto et al., 2016). In these conditions, acceleration occurs when the source area becomes unstable. As material in the upper earth flow tongue accelerates, it overrides or compresses soil masses downslope, locally generating deformational structures similar to thrust faults (e.g. van Asch et al., 2006; Guerriero et al., 2016), and increasing pore pressure through a mechanism of undrained loading (e.g. Bertolini and Pizziono, 2008; van Asch and Malet, 2009). In this way, a kinematic wave propagates through the soil mass and new material is transferred downslope until the toe advances (Hungr et al., 2014). This process might be facilitated by the

presence of a network of preferential flow pathways (i.e. extensional structures) that allow rapid infiltration of water within the earth flow (e.g. Krzeminska et al., 2012), and by the fluidization of the moving mass (van Asch et al., 2006; van Asch and Malet, 2009). In general, fluidization occurs when increasing pore pressures lead to zero effective stress in the soil mass (frictional behavior; e.g., Woods, 1990; Darve et al., 2004; van Asch et al., 2006), or when the material shear stress or strain rate approaches the critical state (non-frictional behavior; Coussot et al., 2002; Ancey, 2007). For a moving earth flow, van Asch et al. (2006) indicate that the fine-grained material can fluidize through deformation and compression of a sliding block.

Persistent-slow earth flow movement creates deformational structures along the ground surface (i.e. faults and folds; Fleming et al., 1988; Fleming and Johnson, 1989; Parise, 2003; Manconi et al., 2014) that are similar to large-scale tectonic structures (i.e. normal, thrust and strike slip faults; Gomberg et al., 1995; Savage and Wasowski, 2006; Guerriero et al., 2013; 2014; 2015; 2016). Observation of mesoscopic structures on the surface of earth flows in Utah, Colorado, and Italy (Baum and Fleming, 1991; Coe et al., 2009; Guerriero et al. 2014; 2015a) indicate that earth flow material is subject to both longitudinal extension and shortening, and the structural style is controlled by the geometry of the basal slip surface (Guerriero et al., 2014). For structurally and lithologically controlled earth flows (e.g. Pinto et al., 2016), the slip surface can be a series of steeply sloping surfaces (risers) and gently sloping surfaces (treads; e.g. Guerriero et al., 2014) along the earth flow profile (Fig. 1). Longitudinal extension (normal faulting) occurs at risers and in the transition between treads and risers, while shortening (thrusting and back-tilting) occurs at the transition between risers and treads (Fig. 1). Guerriero

et al. (2014) suggested that the slip surface geometry might be unchanged during earth flow movement for periods of tens of years. Pinto et al. (2016) showed that the slip surface of a large earth flow is directly controlled by the structural and stratigraphic setting of the region upslope from the neck (i.e. the narrowest section of the earth flow, often corresponding to the lower end of the source area), and roughly corresponds to the pre-earth flow topography (and drainage) downslope.

Recent research has revealed that large earth flows can be composed of several distinct kinematic zones (e.g. Guerriero et al., 2014, 2016). A kinematic zone (Fig. 1) is formed by major paired driving and resisting earth flow elements (Baum and Fleming, 1991), and can be considered as a sector of the earth flow with a specific kinematic behavior (e.g. Guerriero et al., 2016c). Driving elements are comprised of an area of extension with one or more normal faults at its head, and resisting elements are comprised of an area of shortening with one or more back-tilted surfaces and/or thrusts at its toe. Under these conditions, a large earth flow can be considered as a chain of kinematic zones, and the transition between two consecutive kinematic zones is the area between the compressive structures of the upper kinematic zone and the extensional structures of the lower kinematic zone (Fig. 1).

While many studies have contributed to the understanding of earth flow kinematics and dynamics (e.g. Iverson and Major, 1987; Coe et al., 2003; Shultz et al. 2009; van Asch and Malet, 2009; Daehne and Corsini, 2013; Handwerger et al., 2013; Giordan et al., 2013; Prokešová et al., 2014; Handwerger et al., 2015), and sediment flux to the river network (e.g. Mackey et al., 2009; Mackey and Roering, 2011), no account exists about the mechanisms of sediment transport along

an active, segmented earth flow, and the possible interaction between successive kinematic zones. In this paper, in order to fill this gap and provide an additional contribution to the study of earth flow kinematics, we use a combination of data from GPS surveys, boreholes, seismic profiles, ambient seismic noise acquisition, T-LiDAR surveys, and the mapped distribution of surface structures, to characterize the short-term behavior of the Mount Pizzuto earth flow in the Apennine mountains of southern Italy (Figs. 2, 3).

We use velocity data from GPS surveys completed between April 2014 and March 2016 and the reconstructed 3D geometry of the earth flow to compute sediment discharge at the transition of kinematic zones. We relate sediment discharge entering and outgoing a kinematic zone to the effects of internal strain (e.g. Baum et al., 1993) and use 2D mechanical modeling to link structure geometry to driving and resisting elements kinematics. To supplement our interpretation, we use Lidar data of the upper source area to understand sediment supply during ordinary movement. This allows us to better understand i) flow movement, ii) the control exerted by the basal slip surface on flow velocity, and iii) sediment transport along the flow during ordinary and extraordinary movement. It is important to note that the mapped distribution of surface structures used in this paper is simplified from Guerriero et al. (2016), and displacement data from two GPS surveys considered here were already used by Guerriero et al. (2016b and 2016c).

2. The Mount Pizzuto earth flow

2.1 Earth flow description

The Mount Pizzuto earth flow (Fig. 2) affects the northeastern side of the Pizzuto Mount from about 550 to about 720 m above sea level (masl), and involves an estimated volume of 300,000 m^3 of fine-grained flyschoid material (Fig. 3). The earth flow has a complex source area with two active branches, a well-defined neck, an inactive source zone downslope from the neck, a 500 m long transport zone, and a fan-shaped bulging toe (Figs. 2, 3). The earth flow is located on the footwall of a E-vergent thrust between the Argille Varicolori Formation (Cretaceous–early Miocene) in the upper part of the slope on the hanging wall, and the flysch of the San Bartolomeo Formation (late Tortonian to early Messinian) in the middle and lower part of the slope on the footwall (Fig. 3; Pescatore et al., 2000).

The Mount Pizzuto earth flow has been periodically active in the last decades and, as described by the locals, it surged early in 2006 damming the Ginestra torrent at its toe. The earth flow dam induced episodic floods that periodically damaged a segment of a local road, power, and telephone service lines. In 2008, a man-made ditch was excavated along the torrent course and a large diameter drain was installed. These mitigation structures worked until early 2011, when a flood destroyed the drain and the local road and service lines. In October 2015, two new flooding events generated by large rainfalls (e.g. Valente et al., 2016; Magliulo and Cusano, 2016) destroyed the local road and the service lines and considerably enlarged the bed of the Ginestra torrent.

2.2 Structures and segmentation

Deformational structures on the surface of the Mount Pizzuto earth flow are described using terminology and classifications from structural geology because they accurately depict the geometry and displacement of the observed structures (e.g. Guerriero et al., 2016). Structures within the earth flow consist of normal faults and tension cracks indicating extension, thrusts, flank ridges, folds and pressure ridges indicating shortening, back-tilted surfaces indicating backward rotation, and strike-slip faults bounding the earth flow moving core. Based on the distribution of structures, five kinematic zones are recognized along the earth flow: the ***head***, the ***hopper***, the ***neck***, the ***body***, and the ***toe*** (Figs. 4, 5, 6; Guerriero et al., 2016; 2016c). We use italics for the kinematic zones in order to distinguish them from the earth flow geomorphologic parts, which have the same names (e.g. the ***neck*** kinematic zone as opposed to the neck).

The ***head*** is formed by two coalescent branches (Fig. 4). The northern branch, 230 m long and 9.5 to 30 m wide, begins with a group of normal faults, 3 to 4 meters high, defining the upper bound of the main head-scarp. In this part of the flow, the moving core is laterally bounded by normal faults locally associated with sets of en echelon tension cracks, while downslope it is bounded by discontinuous strike-slip faults. Strike-slip faults, 4 to 30 m long, are arranged as left- or right-stepping en echelon arrays, with the stepping direction controlling the width of the earth flow. From 705 to 665 masl, there are three groups of normal faults indicating extension of earth flow material and a group of thrusts indicating shortening. A shallow landslide is located external to the left flank of the moving core. Downslope from the lower group of normal faults, where the slope angle ranges between 10 and 15°, a group of tension cracks around benchmark 4 indicates extension, and an association of thrusts, pressure ridges and

back-tilted surfaces indicates shortening. Back-tilted surfaces contain ponds. Similarly, the 160 m long and 7.5 to 16 m wide southern branch begins with a group of normal faults, from 2 to 4 m high. Downslope, the earth flow is bounded by strike-slip faults and several normal faults indicating extension. Upslope from benchmark 6, a thrust is associated to three back-tilted surfaces, two of which contain ponds. Downslope from benchmark 6, three groups of tension cracks indicate extension along the flow and a back-tilted surface is present near the right flank (right and left flanks are established on the basis of the orographic and movement direction). Downslope from benchmark 5, thrusts indicate shortening. In this zone, the northern and the southern branches join and the head kinematic zone ends.

Downslope from the ***head*** zone, a highly fractured area marks the beginning of the 115 m long and 32 to 45 m wide ***hopper*** kinematic zone (Fig. 4). This area is laterally bounded by inward-stepping strike-slip faults, 2 to 20 m long. The ***hopper*** can be divided into three major zones: i) an upper zone characterized by upper and lower highly fractured areas with a group of normal faults in the middle (benchmarks 9 to 13), ii) a middle zone containing a group of normal faults facing downslope in the upper part and towards the flanks in the lower part (benchmarks 13 to 16) and, iii) a lower zone characterized by thrusts associated with back-tilted surfaces containing ponds (benchmarks 16 and 17).

The ***neck*** begins around benchmark 18. This zone is 130 m long and 10 to 30 m wide (Fig. 5). It contains the narrowest section of the earth flow: the neck. Along the ***neck***, the moving core is bounded on both flanks by discontinuous strike-slip faults that step inward upslope from the neck and outward downslope. The zone begins with a highly fractured area that evolves

downslope into a cluster of downslope-facing normal faults (benchmarks 18 to 20). Near benchmark 21, thrusts dipping toward the flanks are associated with lateral ridges. The narrowest section of the flow between benchmarks 21 and 22 corresponds to an area of normal faulting. During the last surge on April 2014, this area of the ***neck*** was exposed, allowing the observation of its geometry (Fig. 7). The ***neck*** ends at 610 masl near benchmark 23 in conjunction with a group of thrusts.

Downslope from the ***neck*** is the ***body*** kinematic zone. It is 240 m long and 14 to 40 m wide (Fig. 5). Along the ***body***, strike-slip faults locally alternating with en echelon tension cracks laterally bound the earth flow. On its upper part around benchmark 24, a set of tension cracks and two groups of normal faults indicate extension. Near benchmark 25, a thrust indicates shortening. Downslope near benchmark 26, two groups of normal faults indicate extension. Outward stepping of the right-lateral strike-slip faults on the right flank at ~589 masl produces a pull-apart basin that widens the earth flow by ~5 m. This structural depression contains both extensional and compressional structures. At 590 masl, a group of upslope- and downslope-dipping normal faults accommodates material migration towards the depression. Extensional and compressional structures in this area indicate planar rotation of the material induced by the presence of the structurally controlled pull-apart basin. Downslope from benchmark 27, the presence of downslope-dipping and upslope-dipping normal faults can also be connected to the planar rotation of the sliding material. Such rotation indicates the presence of a second, larger, pull-apart basin on the right flank. Normal faults and tension cracks indicate downslope extension towards this basin. Within the structural depression at 580 masl, a longitudinal thrust

and a fold are present. Downslope, a 30 m longitudinal thrust and several thrust segments mark the suture line between the material remobilized on April 2014 and the material outgoing from the structural basin. On the hanging wall of this thrust, a group of normal faults oblique to the thrust accommodates extension. Along the right flank, a third larger pull-apart basin is present at ~570 masl. Thrusts, folds and strike-slip faults delineate this basin. Upslope, extension of earth flow material towards this basin is accommodated by upslope and downslope facing normal faults. Material outgoing from the basin is affected by tension cracks. Thrusts in this part of the earth flow mark the end of the ***body*** kinematic zone.

At 570 masl, a group of normal faults around benchmark 28 delineates the beginning of the 200 m long and 60 to 150 m wide ***toe*** kinematic zone (Fig. 6). It consists of a smaller, upper extensional zone with a group of normal faults near benchmark 28, and a larger compressional zone with large thrusts associated to back-tilted surfaces from benchmark 29 to the Ginestra torrent. Its lower end forms the right flank (hydrographic direction) of the course of the Ginestra torrent. Most of these back-tilted surfaces contain ponds. Downslope of benchmark 35, normal faults delimit grabens. Shallow landslides affect the distal part of the toe and transfer earth flow material towards the Ginestra torrent.

2.3 Hydrographic network

The earth flow hydrographic network begins with a spring along the northern branch of the ***head*** (Fig. 4). In this part of the flow, the creek is a V-shaped channel connecting downstream with the largest pond of the lower sector of the ***head***. The presence and persistence

of this pond is probably caused by the inflow in the back-tilted surface and the absence of an outflow channel (e.g. Coe et al., 2009). In the southern part of the ***head*** and on the right flank, a spring associated with a thrust feeds the earth flow creek. This V-shaped creek is located along the right flank of the flow in the upper part of the ***hopper*** and tends to develop along the longitudinal axis of the flow downslope, until the earth flow neck (Figs. 4, 5). Around benchmark 19 (Fig. 5), a second creek fed by a pond located downslope from a thrust near benchmark 18 contributes water to the channel. Downslope from the ***neck*** in the ***body*** area, the earth flow creek is located along the right flank following the steps in the earth flow lateral boundaries and the pull-apart depressions. Downslope from the lowest structural basin and in the upper part of the ***toe***, the creek migrates towards the north, feeding a pond located within a back-tilted surface on the left flank (Fig. 6). Downslope from this pond, the creek develops toward the northeast reaching the Ginestra torrent. At 570 masl, along the right flank, a spring feeds another creek that follows the right flank of the earth flow reaching the Ginestra torrent. Field observations conducted in 2014 showed that water within the earth flow creeks was also persistent in the summer.

3. Methods

We use GPS surveys, terrestrial LiDAR, and subsurface data (boreholes and shallow seismic) to characterize the earth flow. In addition, we analyze these data for strain, mechanics, and sediment discharge.

3.1 GPS surveys

We installed 35 monitoring points inside the earth flow on April 2014 (grey points 1-35, Fig. 8). Each point consists of a 70 cm long wooden-rebar equipped on its head with a red hat. The rebars were inserted completely into the earth flow material using a sledgehammer and only the red hat was visible after installation. Monitoring points were distributed along the longitudinal axis or following two approximately parallel lines (i.e. along the hopper and at the toe). In each kinematic zone, we installed 4 to 9 points.

On May 2015, 63 complementary monitoring points (black points, Fig. 8) and a new monitoring point (point 0) were installed. The complementary monitoring points were positioned to form polygonal arrays (e.g. quadrilaterals) with the existing monitoring points (e.g. Baum et al., 1988). In order to determine the size and shape of the new polygons, we used the mapped distribution of structures (Figs. 4, 5, 6). Each polygon was designed such that it encompassed an area characterized by a similar style of deformation. It is important to note that in the ***hopper*** and ***toe***, monitoring points were already positioned to form polygonal arrays (Figs. 4, 6, 8). Thus, the installation of the complementary points reduced the area of the polygons, increasing the spatial resolution of the monitoring system, and also allows us to extend the analysis from the ***hopper*** and ***toe*** to most of the earth flow.

The monitoring points placed with a clear view to the sky were surveyed using real time kinematic GPS techniques (RTK-GPS; Gili et al., 2000). The points were surveyed using a 1.8 m high tripod during 17 GPS campaigns of 1 day over a period of 694 days (Table 1). After some surveys, points 16 and 24 were covered by earth flow material and we had to install new points

on similar locations, thus compromising monitoring continuity for these points. The first survey was on April 8, 2014 and the last on March 2, 2016. The time interval between two survey campaigns ranges from 12 to 83 days. We used a Leica rover equipped with a dual-frequency antenna for survey 1 and surveys 12 to 17, and a Geomax rover for surveys 2 to 11 (Table 1). Each survey campaign started at the toe of the flow when a RTK fixed solution was reached and each point position was averaged over a 30 seconds surveying sub-session. Real-time correction for high-accuracy measurements was broadcasted simultaneously by at least two stations of the "Regione Campania" network. Table 1 reports the associated errors in each campaign as minimum, maximum and average horizontal (h) and 3D root-mean-square (RMS) errors. When the earth flow displacement was below the surveys associated error, we assumed no movement. The Leica device is more accurate than the Geomax device. Minimum and maximum horizontal errors for the Leica device are 7 and 19 mm, while for the Geomax device they are 20 and 130 mm.

3.2 T-LiDAR surveys

We evaluated the short-term topographic evolution of the earth flow source area using DEMs of difference (DoD; e.g., James et al., 2012) generated from T-LiDAR data. We created 2 incremental DoDs using 3 DEMs from LiDAR point clouds acquired using a Riegl long range TLS device on September 10, 2014, February 3, 2015 and March 2, 2016. All point clouds were acquired from the same position using a tripod, and the range of acquisition varied between 1200 and 1420 m. The position of the TLS device and of a set of 3 to 5 reflectors was measured using RTK-GPS techniques and the Leica device (9 < h RMS < 18 mm). Real time corrections for high

accuracy measurements were obtained through the "Regione Campania" network. The point clouds were processed in order to delete points representing vegetation, and then they were co-registered following a two steps procedure: i) coarse manual alignment of a stable portion of the slope, ii) iterative automated procedure to align the point clouds (alignment h RMS < 0.15 m). All DEMs used for the analyses have a 0.5 × 0.5 m cell size.

3.3 Subsurface exploration

We used 2 boreholes, 7 Refraction Microtremor and Multi-channel Analysis of Surface Waves (ReMi-MASW) surveys, 23 ambient seismic noise acquisitions (i.e. HVSR), and 4 shallow seismic tomographic profiles to determine the depth to the basal slip surface (Fig. 8). The boreholes (S1-S2, Fig. 8), completed during two field campaigns, one in December 2014 and another in May 2015, were hand-excavated using a helicoidal auger and the basal slip surface was identified based on the depth of sheared and/or in-place material and buried soils observed in the extracted material.

Shallow-seismic profiles combining the active seismic exploration approach of MASW (Park et al., 1999) and the passive approach of ReMi (Louie, 2001; Ohori et al., 2002; Mulargia and Castellaro, 2013), were completed during a field campaign on May 21, 2015 (purple lines a-g, Fig. 8). The MASW approach relies on mid-to-high frequency artificial sources and usually provides better results in the high frequency domain, i.e. low depth. The ReMi analysis relies on ambient noise, which is ubiquitous and spans a wider frequency range, potentially working better in the mid-to low frequency domain, i.e. mid-to-high depths. This kind of survey is based

on the dispersion of surface waves with different wavelengths and velocities that excite the soil at different depths. For this work, we used eight vertical polarized geophones at 4.5 Hz, placed at intervals of 2 m each. As suggested by Louie (2001), we used a single geophone sensor at each channel. The first 5 minutes of each acquisition were performed in the passive mode, just acquiring the ambient seismic noise, and the last minute was in the active mode. For the active source, we used the jump of an operator at ~5 m from the first geophone.

The HVSR analysis was carried out at 23 monitoring points (red circles over gray dots, Fig. 8) on May 21, 2015. This method is also known as H/V for "horizontal-to-vertical", and uses a single broadband, three-components seismometer to record ambient seismic noise (Carniel et al., 2008). The method does not require any artificial seismic source. The H/V ratio is directly related to the wave-field characterizing ambient vibrations. For 1D structures (and many 2D structures), the frequency at which the peak occurs is strongly correlated with the fundamental frequency of the soft layer (Arai and Tokimatsu, 1998). For this study, the acquisition time of each HVSR measurement was 4 minutes and the sampling frequency was about 512 Hz.

To define the depth of the basal slip surface, we combined the ReMi-MASW with the HVSR measurements. Specifically, we used the shear-wave velocity (Vs) model obtained from the MASW and ReMi techniques, and the resonance frequency from HVSR to reconstruct the velocity model of the subsoil. We considered the first layer of the soil model as the earth flow material, and the basal slip surface was identified as the depth of change in Vs between the first and the second layer of the model.

For the analysis, we selected for each HVSR measurement the closest ReMi-MASW survey. Figure 9 shows an example for the HSVR at point 15 and the nearest ReMi-MASW profile f (Fig. 8). The results are presented as a dispersion curve from the ReMi-MASW profile (Fig. 9a), and as a H/V plot from the HSVR measurement (Fig. 9b). The red area delimited by the black lines in Figure 9a shows the first fundamental mode, which indicates the maximum propagation velocity of the surface waves. Vs is around 70 m/s in the first few meters and increases with depth reaching the value of 300 m/s at ~2.7 m. The H/V plot shows a peak at 100Hz, corresponding to the fundamental frequency of the earth flow material (Fig. 9b). The absence of major peaks in the low frequency band indicates that the bedrock is fairly homogeneous. Figure 9c shows the Vs model of the subsoil and its uncertainty (dotted blue line). The Vs of the first shallow layers in Figure 9c was estimated by the dispersion curve from the ReMi-MASW profile, and the blue line indicates the Vs value in the middle of the red band (Fig. 9a). The uncertainty in Vs of the shallow layers is small because the red band is narrow here.

During a second field campaign, completed on February 2, 2016, four seismic refraction profiles were acquired using a 24-channel recording system and linear arrays of 10 Hz horizontal-axis geophones with spacing of 2 to 4 m (green lines S1-S4, Fig. 8). The seismic profiles are located at the transition of kinematic zones (Fig. 8). Data were recorded at a rate of 1000 Hz. S-waves were generated by a sledgehammer striking a wood block. On each seismic line, seven sledgehammer shots were recorded: Two at the ends of the line, and five within the array at equal distances. The first-refracted arrivals were visually picked from a display of the shot records (Supplementary material). Once identified, the first S-waves arrivals were used to define space–

time curves for each geophone. A two-dimensional refraction velocity model (i.e. tomography) was developed using these curves and the Rayfract code (Schuster and Quintus-Bosz, 1993). Following Williams and Pratt (1996), we relied on two key assumptions: (i) layers are continuous across the line, and (ii) layers velocities increase with depth. To define the basal slip surface, we assumed that it could be localized within a specific velocity interval. We used the basal slip surface in the boreholes to constrain this velocity interval on the refraction profiles.

3.4 Strain analysis

We used the program SSPX by Cardozo and Allmendinger (2009) to compute strain in the earth flow. SSPX calculates the best-fit strain tensor given displacement vectors at a minimum of three points in 2D or four points in 3D. The program offers several options to compute strain. For our analysis, we used a modified version of the Delaunay routine to compute the strain tensor from the displacement of 3 to 6 monitoring points defining a polygon. The new implementation allows reading a file defining the points of each polygon and their connectivity. Although we monitored displacements in 3D, the distribution of the monitoring points in the vertical is not sufficient to compute 3D strain (for that we would need points on several depth slices). Therefore, we used only the measured horizontal displacements for computing 2D strain in each polygon. Since most polygons have more than 3 points, 2D strain and its associated error can be calculated. We use only polygons for which the absolute value of the strain parameter is larger than its error.

The analysis was completed in two steps: i) for points located in the lower part of the *head*, the *hopper*, and the *toe*, GPS surveys 1 to 8 from April 8 to August 30, 2014 were considered; and ii) for points located along the transport zone (longitudinal profile AA', Fig. 8), and within the *toe*, the GPS surveys 12 to 17 from May 8, 2015 to March 2, 2016 were considered (Table 1). We chose these two periods because of the continuity of the displacement data and because these periods correspond to phases of extraordinary and ordinary movements, respectively. The monitoring points are shown in Figs. 4, 5, 6 and 8, while their connectivity to form the polygons is indicated in Tables 2 and 3. We color the polygons by the amount of dilatation, which assuming no change in thickness of the earth flow in the considered period, gives an idea of increase or decrease of surface area (positive and negative dilatation, respectively). Since the earth flow is longitudinal, dilatation also gives an indication of longitudinal extension (positive dilatation) and shortening (negative dilatation).

3.5 Mechanical modeling

2D Mechanical modeling of the earth flow at the transition of driving and resisting kinematic zone elements was undertaken using FLAC (Itasca). This computer program uses an explicit finite-difference scheme to simulate the plastic flow of rock materials after their yield limit is exceeded. Materials are represented by quadrilateral elements that form a grid fitting the model domain. FLAC is based on a Lagrangian calculation scheme, which is well suited for modeling large deformations such as those occurring on landslides. Furthermore, it allows

modeling interfaces along which sliding or separation can occur, as in the case of the basal slip surface.

The grid used in the analysis contains 360 x 40 elements representing a 45 m x 7 m section of the slope (Fig. 10). The mesh was divided into two sub-grids, an upper finer one for the earth flow, and a lower coarser one for the bedrock, separated by an interface corresponding to the basal slip surface. The thickness of these sub-grids is based on the interpretation of the subsurface data. The earth flow material and the slip surface were assumed to be elasto-plastic with a Mohr-Coulomb constitutive criterion, while the bedrock was treated as a linear elastic material with no failure limit. Since the aim of the analysis is to reproduce the internal deformation of the earth flow caused by basal sliding, we forced plastic flow along the interface. Therefore, we assumed dry conditions to ensure the internal stability of the earth flow and assigned to the interface an "equivalent friction angle" (ϕ'e) ranging from 5 to 10° to simulate different earth flow velocities. These values roughly correspond to an effective friction angle of 10 to 20° for a fully saturated soil with slope-parallel groundwater flow (e.g. Iverson and Reid, 1992; Reid and Iverson, 1992; Iverson, 2005).

Earth flow material properties such as particle size distribution, Atterberg limits, unit weight, water content and residual shear strength were obtained from laboratory tests (e.g. ASTM International Standard D422, D4318, D2937, D2216 and D6467, 2008) completed on samples obtained from 2 pits (0.4 to 0.6 m deep) excavated next to monitoring points 9 and 18 (Fig. 8), while elastic properties for both the earth flow, the bedrock, and the interface were

selected from published data (Table 4). Each sample was taken using a hand-driven cylindrical steel sampler on December 18, 2015.

Two different slope sections were analyzed to investigate the influence of the geometry of the basal slip surface on the resultant structures: i) a transitional slope between a riser and a tread (Fig. 10a) and, ii) a transitional slope between a tread and a riser (Fig. 10b). Surface slope angles (α) correspond to those of the earth flow. According to field observations, compressive structures such as thrust faults and back-tilted surfaces should be generated in the first case, while extensional structures such as normal faults should occur in the second case.

3.6 Sediment discharge estimation

We used velocity data derived from successive sets of GPS surveys and the cross-sectional geometry of the earth flow from the seismic refraction profiles (S1 to S4, Fig. 8), to estimate sediment discharge along the earth flow transport zone. Sediment discharge was calculated considering average velocity of monitoring points moving through the cross sections on different reference periods. Where there was more than one point moving through the section at the same time, we calculated sediment discharge using the surface-weighted velocity of the points. For this calculation, we assume that the cross-sectional geometry of the earth flow remains approximately constant on the short term. This hypothesis is supported by the limited variation of the absolute elevation of monitoring points moving through each section in a specific monitoring period. We used seismic refraction profiles and the mapped distribution of structures on the earth flow surface, to estimate the cross sectional surface associated to each point. Where there was one

point moving successively through a section, we used the arithmetic average of the point velocities.

For our analysis, we considered average velocity calculated on nine periods: i) April 8 to May 9, 2014, ii) May 9 to May 21, 2014, iii) May 21 to June 5, 2014, iv) June 5 to June 17, 2014, v) June 17 to July 17, 2014, vi) July 17 to August 30, 2014, vii) April 8 to August 30, 2014, viii) August 30, 2014 to May 8, 2015 and ix) May 8, 2015 to March 2, 2016. Periods i to vi represent different phases of the surging episode in the spring-summer 2014. Period vii includes all these phases and represent all exceptional movement in the spring-summer 2014. Period viii includes movement during the reactivation of the spring 2015, and period ix includes velocity data after the installation of the complementary monitoring points.

For locations and periods where 2D strain data were available (i.e. within the ***hopper*** from April 8 to August 30, 2014, and along the entire length of the flow between May 8, 2015 and March 2, 2016), we compared sediment entering and outgoing from a kinematic zone, in order to understand if the sediment discharge was constant through the transport zone of the flow, and the effect of strain on the sediment budget of the kinematic zones. It is important to note that a preliminary analysis of the ***hopper*** between May 8 and November 28, 2015 (Guerriero et al., 2016b), indicates that flow material increases its volume moving through the kinematic zones, because the longitudinal extension of the upper part (riser) is not completely balanced by the longitudinal shortening of the lower part (tread).

4. Results

We describe the results in terms of earth flow movement, geometry of the basal slip surface, strain, mechanics at riser and tread transitions, topographic evolution of the source area, and sediment discharge.

4.1 Earth flow movement from GPS surveys

Figure 11 shows the horizontal displacement of the monitoring points installed on April 8, 2014 within the northern (Fig. 11a) and southern (Fig. 11b) branches of the ***head***, ***hopper*** (Fig. 11c), ***neck*** (Fig. 11d), ***body*** (Fig. 11e) and ***toe*** (Fig. 11f). All monitoring points moved between the 1 (April 8, 2014) and the 12 (May 8, 2015) GPS surveys (Fig. 11). Points 24 and 16, moved between the 1 and the 10 and 11 surveys, respectively. Most of the points moved between the 12 and 17 (March 2, 2016) surveys. The monitoring point 0, installed on May 8, 2015, moved between the 14 and the 17 surveys. All complementary monitoring points moved between the 12 (first survey for these points) and the 17 surveys. The total movement of all points was largely dominated by the horizontal component (Figs. 4b, 5b, 6b). The cumulative horizontal displacement of the points over the entire monitoring period ranges between ~97 m for point 20 within the neck, to 0.7 m for point 33 at the toe, and all points moved downward (Fig. 11). The daily velocity averaged on the entire monitoring period ranges between 14 cm/day at point 20 to 0.1 cm/day at point 33.

Table 5 shows the maximum and minimum horizontal and vertical displacements and average horizontal velocity registered in each kinematic zone for the entire monitoring period. We consider the two sub-zones of the ***head*** separately. Overall, the maximum average velocity

was registered at points moving along the middle part of each kinematic zone while the minimum velocity was registered at points moving through the upper part of the driving element (i.e. point 9 of the ***hopper***, 18 of the ***neck*** and 28 of ***toe***) and/or the lower part of the resisting element (i.e. point 4 of the ***head*** and point 27 of the ***body***).

For the monitoring period between April 8 and October 25, 2014, when point 24 was available, the horizontal movement ranged between ~55 m for point 25 and 27.5 m for point 24. The corresponding average daily velocities were 27.5 cm/day and 13.7 cm/day. Between May 2015 and March 2016 i) points 5 to 8 moved in a slow persistent manner, ii) all the points of the ***hopper*** exhibit no movement between January and March 2016, iii) point 23 exhibits no movement between January and March 2016, iv) point 25 exhibits no movement between January and March 2016, and point 26 between November 2015 and January 2016, and v) point 35 exhibits a total displacement larger than points 32, 33 and 34 immediately upslope (Fig. 11).

Displacement and velocity data (Fig. 11 and Supplementary material) indicate four main phases of movement: i) between April 8 and August 30, 2014, the earth flow surged exhibiting exceptional movement with velocity up to 250 cm/day, ii) between August 30 and November 28, 2014, the earth flow was characterized by small and/or localized displacements, iii) between November 28, 2014, and May 8, 2015 most of the earth flow reactivated/accelerated, iv) between May 8, 2015 and March 02, 2016, the earth flow moved in a slow persistent manner. Locally, no movement was observed in this last period, especially between January and March 2016.

At nearly all points most movement occurred between the spring and summer (April to August) 2014 as consequence of the surging acceleration. During this period, the maximum

velocity between two consecutive GPS surveys was registered (red segments, Fig. 11). In the two branches of the *head* and along the *hopper*, the maximum velocity was registered between April 8 and May 9, 2014 (from GPS survey 1 to 2) at points 3, 7 and 13. Within the *neck* and along the *body*, the maximum velocity was registered between May 9 and May 21, 2014 (from GPS survey 2 to 3) at points 20 and 25. At the *toe*, the maximum velocity was registered between May 21 and June 5, 2014 (from GPS survey 3 to 4) at point 28 (Supplementary material).

We use data from GPS surveys 1 to 8 to reconstruct the displacement profile along the transport zone of the flow (longitudinal profile AA', Fig. 8) for the period April to August 2014. The resultant displacement profile (curve a, Fig. 12a) indicates that in this period, the entire length of the flow moved and the displacement ranged between ~85 m at point 20 (curve a, Fig. 12a) to ~0.4 m at points 33 and 34 (Fig. 11f). The displacement profile also indicates several kinematic zones in the transport zone of the flow, each one having an upslope area of acceleration, a downslope area of deceleration, and a displacement peak in the middle (curve a, Fig. 12a). Guerriero et al. (2016c) recognize the same pattern of movement in the same part of the flow over a longer monitoring period (i.e. April 2014 to May 2015). They also indicate that the *head* has the same kinematic characteristics.

Conversely, data from GPS surveys 12 to 17 show that only a small percentage of the total displacement accumulated between May 8, 2015 and March 2, 2016 along the transport zone of the flow (curve b, Fig. 12a). In this second period, the earth flow exhibits "ordinary" activity, mostly with slow movements locally alternating with periods of dormancy. The displacement accumulated during this phase ranges between 2.9 m at point 19** (curve b, Fig. 12a) and 0.15 m at

point 33 (Fig. 11f). For this period, we did not consider point 19 but point 19** (Fig. 8). This is because the inward step up of the strike-slip fault forming the right flank of the flow isolated point 19 from the most active part of the flow. However, similar to the previous surging episode of the spring-summer 2014, the displacement profile of the May 8, 2015-March 2, 2016 period shows several kinematic zones. The geometry of the displacement profile and the distribution of kinematic zones are also similar in these two periods (Fig. 12a). Local differences might be influenced by the number and position of points considered.

4.2 Geometry of the basal- and lateral-slip surfaces

We integrated the information from the boreholes, ReMi-MASW surveys, HVSR measurements, and shallow seismic refraction profiles to determine the geometry of the slip surface along the longitudinal profile AA', and along the seismic refraction profiles S1 to S4 (Figs. 8, 12b).

In total, 24 data points were used, 4 points within the ***head*** (id: 2, 4, S2 and S1), 4 within the ***hopper*** (id: 9, 11, 13, S2), 5 within the ***neck*** (id: 16, 18, 19, 20, S3), 10 within the ***body*** (id: 22, 23, 24, 25, d, 26, S1, c, 27, S4), and 1 within the ***toe*** (id: 28). The depth to the basal slip surface (gray line, Fig. 12b) ranges from a maximum of 7 m within the ***neck***, to a minimum of approximately 2 m in the upper part of the ***head*** and within the ***hopper***. HVSR measurements and ReMi-MASW surveys indicate that the depth to the basal slip surface at the toe reaches almost 6 m at points 33 and 34. Overall the basal slip surface is a repeating series of steeply sloping surfaces (risers) and gently sloping surfaces (treads). Risers and treads correspond to changes in surface slope angle

and longitudinal extension between the *head*, *hopper*, *neck*, and *body*. Within each kinematic zone, the overall shape of the basal slip surface is approximately concave upward, whereas at the transition between zones, the shape is convex upward. Exceptions occur within the *hopper* and *body* where internal risers and treads form small concave and convex surfaces. In general, the thinnest parts of the earth flow are at risers and transition areas, and the thickest parts are at treads (Fig. 12b).

Figure 13 shows the interpretation of the seismic refraction/tomographic profiles S1 to S4. The basal slip surface (red dashed line, Fig. 13) is interpreted within the black band representing the velocity interval locally calibrated with the borehole data. All tomographic profiles show a lenticular-shaped earth flow, with lateral slip surfaces (strike-slip faults) steepening as they approach the topographic surface (red arrows, Fig. 13). Profiles S3 and S4 downslope from the neck reveal the presence of the former drainage creek, which is located towards the right flank of the earth flow in profile S3 and the left flank of the flow in profile S4.

4.3 2D strain from displacement data

For the first step of the strain analysis, we consider the GPS surveys 1 to 8 for the period of extraordinary movement between April 8 and August 30, 2014. For the *head*, *hopper*, and *neck*, we use all eight GPS surveys to compute the evolution of dilatation (polygon 1: *head*, polygons 2-4: *hopper*, polygon 5: *neck*, Fig. 14). For the *toe*, we use only the first and last GPS surveys to compute total dilatation (polygons 6-8, Fig. 15). We do so in the *toe* because our goal is to explore if the deformational style in this zone is consistent with the dilatation for the entire

period. Table 2 summarizes the points' connectivity and the computed dilatation for this first period.

Within the considered kinematic zones, the polygons show both positive dilatation (i.e. longitudinal extension, polygons 2, 3, 5 and 8) and negative dilatation (i.e. longitudinal shortening, polygons 1, 4, 6 and 7; Figs. 14, 15; Table 2). A lower area of negative dilatation (shortening, polygon 1) characterizes the ***head***, while an upper area of positive dilatation (extension, polygons 2 and 3) and a lower area of negative dilatation (shortening, polygon 4) characterize the ***hopper*** (Fig. 14). Similarly, an upper area of positive dilatation (extension, polygon 5) characterizes the ***neck*** (Fig. 14), while an upper area of negative dilatation (shortening, polygons 6 and 7) and a lower area of positive dilatation (extension, polygon 8) characterize the ***toe*** (Fig. 15). Thus, an alternation of regions of longitudinal extension and shortening characterizes the flow. In all eight polygons, the dilatation and principal strain axes orientations (Figs. 14, 15) are consistent with the observed deformational structures (Figs. 4, 5, 6).

For the second part of the analysis, we consider GPS surveys 12 to 17 for the period May 8, 2015 to March 2, 2016 characterized mostly by slow persistent, ordinary movement along the transport zone of the earth flow. Figure 16 shows the dilatation between May 8, 2015 to March 2, 2016 along this area, and Table 3 summarizes the points' connectivity and the evolution of dilatation. Along the transport zone, 21 polygons display both positive (polygons 3, 4, 5, 10, 13, 14, 17, 19, 20 and 21) and negative (polygons 1, 2, 6, 7, 8, 9, 11, 12, 15, and 18) dilatation (longitudinal extension and shortening, respectively; Fig. 16). The largest positive dilatation (and maximum

extension) is in polygon 10 at the beginning of the ***neck***. The lowest negative dilatation (and maximum shortening) is in polygon 12 within the ***neck***.

The lower part of the ***head*** and the transition zone between the ***head*** and the ***hopper*** display negative dilatation (longitudinal shortening) over this period (polygons 1 and 2). The dilatation and principal shortening direction in this area are consistent with the thrusts delineating the lower boundary of the ***head*** (Figs. 4, 16). The ***hopper*** consistently displays an upper area of positive dilatation (extension, polygons 3, 4 and 5), and a lower area of negative dilatation (shortening, polygons 6, 7, 8 and 9). With the exception of polygon 4, the dilatation and principal axes orientations are consistent with the observed structures, which consist of normal faults in the ***hopper***'s upper area and thrusts in the ***hopper***'s lower area (Figs. 4, 16). The ***neck*** shows positive dilatation (extension) at its upper end (polygon 10) and negative dilatation (shortening) in the middle of the zone (polygons 11 and 12). Here, the dilatation and principal axes orientations are also consistent with the observed structures, consisting of normal faults in the ***neck***'s upper area and thrusts in the middle (Figs. 5, 16). The ***body*** displays over the entire period alternating zones of positive dilatation (extension, polygons 13, 14, 17, 19 and 20), and negative dilatation (shortening, polygons 15, 16 and 18). Within these zones, the principal axes orientations are somewhat consistent with the observed structures (Figs. 5, 16), although in this area the distribution of strain and deformational structures is complicated by the presence of several strike-slip faults and pull-apart basins that widen the earth flow (Fig. 5). Polygon 21 containing point 28 at the beginning of the ***toe*** alternates in time between negative dilatation (shortening, GPS surveys 12-13, 12-14 and 12-16), and positive dilatation (extension, GPS surveys

12-15 and 12-17). For the total strain of the period, the principal axes orientations in this polygon (Fig. 16) are consistent with the thrusts observed downslope (points 29-32, Fig. 6), although positive dilatation indicates longitudinal extension at this location.

In the ***toe***, seven polygons display both positive and negative dilatation (longitudinal extension and shortening) throughout the second period (Fig. 17, Table 3). Polygons 22, 24 and 25 show negative dilatation until January 29, 2016 (Fig. 17a-d), but positive dilatation at the end of the period on March 2, 2016 (Fig 17e). Polygon 26 shows positive dilatation over the entire period (Fig. 17a-e). The dilatation in polygons 21, 23 and 27 is more complex. In polygon 27 at the end of the ***toe***, both the lowest dilatation (shortening) in the middle of the period (Fig. 17c), and the largest dilatation (extension) at the end of the period (Fig. 17e) are estimated.

4.4 Structural styles and structures at riser and tread from mechanical modeling

Figures 18 and 19 show the results from the two mechanical models simulating the riser-to-tread and the tread-to-riser transitions, respectively. In both cases, two different values of the equivalent friction angle of the basal slip surface (ϕ'e= 5 and 10°) were used to simulate different relative velocities of the earth flow material with respect to the bedrock. As expected, when the slip surface (and the ground slope) becomes flatter as in the case of the riser-to-tread transition, the earth flow decelerates and compressive structures form at the change in slope to accommodate the decrease in velocity (Fig. 18). Similarly, if the basal slip surface (and the ground slope) becomes steeper as in the case of the tread-to-riser transition, the earth flow accelerates and extensional structures form (Fig. 19).

However, the relative velocity between the riser and the tread controls the geometry of the compressive structures in the riser-to-tread transition (Fig. 18). If the tread is stable and the velocity drop between the riser and tread is large (Fig. 18a-b), a downslope vergent thrust and associated fold with a steep forelimb form at the toe of the riser (Fig. 18c-d). This structure resembles the fault-propagation-folds originated in fold and thrust belts where a thrust steps up from a basal decollement (e.g. Mitra, 1990). On the other hand, if the tread is unstable and the velocity drop between the riser and tread is small (Fig. 18e-f), the longitudinal shortening is accommodated by a smaller, upslope vergent backthrust and associated fold/pressure ridge (Fig. 18g-h). While the first case (Fig. 18a-d) is the typical passive failure observed at the toe of a landslide/earth flow (e.g. Coe et al., 2016; Guerriero et al., 2013; 2016), the backthrust observed in the second case is less frequently reported in the literature. Fleming and Johnson (1989) mapped several backthrusts and folds/pressure ridges within the Aspen Grove landslide in central Utah. Fore and back-thrusts/pressure ridges are also present in the Mount Pizzuto earth flow (Figs. 4-6).

In the case of a tread-to-riser transitional slope, similar extensional structures are generated regardless if the tread is stable or not. Figure 19a shows the case for a stable tread and a large increase in landslide velocity between the tread and riser. Velocity vectors (Fig. 19b), geometry (Fig. 19c), and strain (Fig. 19d) for this case are almost identical to those for the case of an unstable tread and a small velocity increase between tread and riser. It is important to emphasize that these results describe the initial stage of formation of the structures. Multiple

reactivations and long-term creep translate downslope the structures as relatively coherent units, changing their position along the earth flow channel and possibly their geometry.

4.5 Topographic evolution of the earth-flow source area

The earth flow source area comprises the ***head***. Topographic changes within this source area from LiDAR measurements indicate that between September 2014 and February 2015, the northern branch lost material at its upslope end and along its left flank (i.e. along the earth flow scar; Fig. 20a). Conversely, along the longitudinal axis of the northern branch, the earth flow's moving core locally gained material (Fig. 20a). The maximum variations in elevation connected to material lost and gain within the northern branch were -1.2 and +0.95 m, respectively. In the same period, the southern branch lost material along its left flank and at its upslope end (Fig. 20a). Only locally the earth flow's moving core gained material. The maximum variations in elevation connected to material lost and gain within the southern branch were -2.5 and +1 m, respectively. Considering the period of observation and the patchy pattern of the southern branch that lost material (Fig. 20a), we think the negative variation in elevation in this part is due to the presence of dense grassy and shrubby vegetation not removed by the vegetation filter. Field observations on September 2014 confirm the presence of this kind of vegetation.

Between February 2015 and March 2016, topographic changes along the northern branch alternated between material lost and gain and were concentrated along the earth flow's moving core (Fig. 20b). The presence of four zones of coupled depletion and accumulation indicate downslope material transfer in the form of sediment pulses. The maximum variations in

elevation related to material lost and gain within the northern branch were -1.7 and +1.1 m, respectively. The maximum material lost was near the upslope end of the zone while the maximum material gain was at its downslope end (Fig. 20b). In the same period, the southern branch lost material within its middle and lower sectors. The most important topographic change was observed at its downslope end where the subsidence reached 1.3 m (Fig. 20b).

4.6 Sediment discharge along the earth flow transport zone

The earth flow transport zone begins downslope from the source area and comprises the ***hopper***, the ***neck*** and the ***body*** (Fig. 12b). Sections S1 to S4 roughly correspond to the upper and lower ends of these zones (Fig. 8). Figure 21 shows the results from our estimation of the earth flow sediment discharge at these sections. The bar graphs (Fig. 21) show the sediment discharge over periods i) to vi), and the line graphs show the sediment discharge over periods vii) to ix) (for periods, see section 3.7 and legend in Fig. 21). During the surging episode of the spring-summer 2014, the sediment discharge averaged over almost 5 months of activity was approximately constant through the transport zone and varied between 10.4 m^3/day in section S2 to 12.4 m^3/day in section S3 (continuous line, Fig. 21). However, during these 5 months, the sediment discharge consistently decreased in sections S1 and S2 (bars, Fig. 21), varying from 22.9 to 1.6 m^3/day in S1, and 17.3 to 3.4 m^3/day in S2. Conversely, in sections S3 and S4, the discharge first increased between periods i) and ii) and then decreased between periods ii) and vi) (bars, Fig. 21). Interestingly, in the period spring-summer 2014, the maximum values of sediment discharge

occurred at sections S3 and S4, where 67.2 and 60.1 m^3/day of earth flow material passed through these sections, respectively.

After the surging episode of the spring-summer 2014, the earth flow velocity significantly decreased (Fig. 11 and Supplementary material), and at several locations the earth flow movement was below the error of our monitoring system between two or more GPS surveys. Between August 30, 2014 and May 8, 2015 (dashed line, Fig. 21), the sediment discharge calculated at the reference sections decreased from the upper part of the earth flow (section S1) to the earth flow toe (section S4). In the last period between May 8, 2015 and March 2, 2016 (dotted line, Fig. 21), sediment discharge was the lowest calculated in the whole 2014-2016 period and varied between 0.3 m^3/day in section S2 to 0.14 m^3/day in section S4.

5. Discussion

5.1 Movement, propagation and sediment transport mechanisms

Our results indicate that the Mount Pizzuto earth flow has an intermittent nature with periods of ordinary slow movement and/or quiescence alternated with surging events. This complex behavior is typical of earth flows developed in different geologic and climatic settings (e.g. Varnes, 1978; Keefer and Johnson, 1983; Zhang et al., 1991; Baum and Johnson, 1993; Baum et al. 2003; Mackey and Roering, 2011; Bertolini and Pizziolo, 2008; Daehne and Corsini, 2013; Simoni et al., 2013).

The displacement and velocity data indicate that since the installation of the monitoring points, the earth flow movement assumed the characteristics of a surge with velocity up to 250 cm/day. Field observations conducted in March 2014, before the installation of the monitoring points, indicated that new deformational structures were forming along the source area and transport zone, and that the earth flow surface was affected by severe erosion with a major axial gully and a network of rills at its head (e.g. Mackey and Roering, 2011). Deformational structures within the upper part of the earth flow (i.e. the ***head***) were larger and highly developed in comparison to those located within the transport zone (i.e. the ***hopper***, ***neck*** and ***body***). Several new shallow landslides, involving the in-place material, were observed outside the source area, and all ponds in the earth flow contained water and had an outflow channel. Such observations indicate that the earth flow was evolving towards a condition of rejuvenation after suffering extensive erosion (e.g. Mackey and Roering, 2011), caused by intense rainfalls that characterize this region between end of winter and beginning of spring (e.g. Camuffo et al., 2013).

Although this surging phase was possibly already set up at the beginning of the monitoring period, because of the presence of well-developed strike-slip faults and considering that we may have not catch the acceleration commonly preceding surging, our field observations indicate that the surging acceleration (or reactivation) propagated from the source area through the transport zone down to the toe between April and August 2014 (Fig. 11 and Supplementary material). Discharge calculations indicate that during this event, average sediment discharge was nearly constant throughout the earth flow transport zone (Fig. 21). During this episode, the kinematic zones operated in unison to transmit sediment along the transport zone inducing a

short-term cascade effect (e.g. Guerriero et al., 2014). Although the average sediment discharge was nearly constant, sediment discharge at transitional sections between the ***head*** and ***hopper***, and the ***hopper*** and ***neck*** decreased in time, and displayed both an increase and decrease in the transition sections between the ***neck*** and ***body***, and between the ***body*** and ***toe*** (Fig. 21). Additionally, it appears that the source area consistently lost material and the toe of the flow gained material. Such interpretation is consistent with observations at Montaguto by Giordan et al. (2013), works by Bertolini and Pizziolo (2008), and Fleming et al. (1988) indicating that the undrained loading of the upper source area caused by retrogression of the upper flow boundary can be responsible for a surging reactivation that propagates along the earth flow. Even if we did not observe directly the retrogression of the upper flow boundary, our field observations and results seem to be consistent with this kind of triggering mechanism.

Field observations conducted on May 2014 (during the second GPS survey) indicate that the earth flow was bounded by active strike-slip faults. An exception was the central and lower part of the neck where the amount of surface and subsurface water dramatically increased with respect to the upper and lower parts of the flow, and several ponds were located downslope (Fig. 22). In the ***neck***, the amount of displacement accumulated after the second GPS survey varied between less than 10 m at its upper part and more than 80 m next to the neck. Considering the location of active strike-slip faults, the amount of water, and the local variation of velocity (Fig. 11d and Supplementary material), we infer that the earth flow mechanism evolved from a slide in the source area and the upper transport zone to a flow downslope from the neck (e.g. van Asch

and Malet, 2009; Daehne and Corsini, 2013). From the upper part of the ***body*** toward the ***toe***, the movement seems to maintain the characteristics of a slide.

This fluidization of the moving mass can be connected to the development of excess pore water pressures in undrained conditions (van Asch and Malet, 2009), possibly caused by the loss of an efficient drainage pathway (e.g. Iverson, 2005) associated with the compression of earth flow material (van Asch et al., 2006). In our case, this process may be related to the hourglass shape of the earth flow (Fig. 5). Especially, the presence of a well-defined neck could work as a constriction inducing the compression and successive extrusion of the material, as well as the closure of preferential flow paths (e.g. Mackey and Roering, 2011; Handwerger et al., 2013). This might also result in forced circulation of water occurring as an upward secondary flow within the moving mass (e.g. Baum and Johnson, 1993). Iverson (2005) and van Asch et al. (2006) suggest that similar conditions might induce the catastrophic failure of the mass (i.e. fluidization), and the downslope propagation of the kinematic wave triggered by the undrained loading of the lower part of the ***head***. This interpretation might suggest that earth flows having a well-defined neck are more likely to surge with respect to those without, because the transition from slide to flow occurring within the neck allow the propagation of movement toward the lower part of the flow.

The constraining action of the neck and the reduction of the flow cross sectional area in the upper part of this zone, is also indicated by the presence on September 2014 of longitudinal thrusts along the upper part of the ***neck***. Such structures were also observed by Fleming et al. (1999) in the Slumgullion landslide. They indicate a "screw-like motion" along the earth flow

flanks, with material extruded near the flanks and folded along the midline of the earth flow, inducing extensive material reworking. Such reworking action associated with negative dilatation of the flow should also favor the change from slide to flow (e.g. van Asch et al., 2006).

A second phase of (seasonal) acceleration occurred in 2015, approximately between the end of the winter 2014-2015 and the beginning of the spring 2015. This phase occurred after a period of very low activity. Probably, as the propagation of a kinematic wave triggered by undrained loading of the lower part of the ***head*** can connect the successive kinematic zones, a period of dormancy or limited movement can induce their disconnection. The displacement data (Fig. 11) indicate that this seasonal acceleration initiated almost simultaneously within all kinematic zones. It started at the upper end of each kinematic zone and propagated downslope (i.e. through the driving element) while the lower part of the zone was not moving or was moving with a low velocity, creating stress concentration at the resisting element. This interpretation is supported by Fig. 11 and by the observed geometry of thrusts mapped along the flow. As indicated by the mechanical modeling (Fig. 18), downslope verging thrusts in the earth flow form when a large drop in earth flow velocity exists between the driving and resisting elements of a kinematic zone (Fig. 18a-d). Our results indicate that this occurs when the flow exhibits small seasonal acceleration followed by persistent slow movement (i.e. ordinary activity). Under these conditions, the geometry of the basal slip surface should control the movement that, in this part of the kinematic zones, is facilitated by the presence of extensional structures working as preferential flow paths (Baum and Fleming 1991; Krzeminska et al., 2012).

During this phase, the highest values of acceleration were observed within the northern branch of the ***head*** (Fig. 11 and Supplementary material) where they seem to correspond to a surging acceleration. However, this acceleration did not propagate downslope inducing a cascade effect along the following kinematic zones. This can be related to the character of sediment transport along the flow during this phase, occurring as consecutive sediment pulses (Fig. 20b and Results section). It may also be due to the absence of a precursory retrogression of the source area (i.e. lack of new sediment into the flow; e.g. Mackey and Roering, 2011; Mackey et al., 2009), and the lack of connectivity between kinematic zones because of the low amount of material within the source area and the upper part of the transport zone. It is important to remember that the first phase of acceleration and surging reactivation on 2014 removed a large amount of material from the upper part of the earth flow source area. Without constant sediment supply, the earth flow activity decreased on 2015 because of the thinning of the transported material and the lower driving stress (e.g. Mackey and Roering, 2011).

Following this seasonal acceleration, persistent slow movement interrupted by short periods of dormancy (e.g. Keefer and Johnson, 1983) characterized the overall extent of the flow. In this event, as during the seasonal acceleration, the activity of a kinematic zone was independent from adjacent zones upslope and downslope, and sediment discharge calculated at the transition between consecutive kinematic zones was variable along the flow transport zone (May 2015 to March 2016; Fig. 21).

A constant sediment discharge (i.e. steady state) along a slope is often a basic assumption in landslide/earth flow modeling, sediment yield studies, and landscape evolution models of

earth flows (e.g. Mackey et al., 2009; Mackey and Roering, 2011; Booth et al., 2013; Diodato et al., 2015), even if the temporal and spatial scales over which this assumption applies are poorly defined (Sweeney et al., 2012), and the rate of sediment production varies greatly depending on the observation period and the impact of extreme rainfall events (Korup et al., 2010). Our results suggest that in the Mount Pizzuto earth flow, sediment discharge is not constant during ordinary movement.

5.2 Deformation, slip surface geometry and earth flow volume variation

The surface of the Mount Pizzuto earth flow displays structures indicating different structural styles (e.g. Fleming and Johnson, 1989; Guerriero et. al, 2013; 2015a; 2016; Prokešová et al., 2014). Based on the distribution of these structures, five kinematic zones are recognized along the earth flow (Figs. 4-6). Active structures indicating longitudinal extension of earth flow material (i.e. normal faults) characterize the upper part of each kinematic zone (the driving element; Baum and Fleming, 1991) where the earth flow accelerates and a riser makes the slip surface. Structures indicating longitudinal compression outcrop in the lower part of the kinematic zones (resisting element) where the earth flow decelerates and a tread makes the slip surface.

Similarly, 2D strain along the surface of the earth flow indicates the presence of zones of positive and negative dilatation. Positive dilatation occurs where the velocity of the flow increases, while negative dilatation occurs where the velocity decreases (Figs. 11, 12). Surface structures accommodate deformations caused by variations in earth-flow velocity (i.e.,

acceleration and deceleration). This deformation occurs as consequence of variations of longitudinal forces acting within the moving mass and approaching those required for active failure in the longitudinal extension area and passive failure in the longitudinal shortening area (Baum and Fleming, 1991; Savage and Wasowski, 2006). Thus, a change in slope angle of the basal slip surface changes the resulting longitudinal force in the earth flow. This observation is consistent through time and emphasizes the relation between deformation, velocity, and geometry of the slip surface.

The density of structures seems to be independent of the magnitude of the velocity change and related strain. For example, the highest density of extensional structures is in the upper part of the ***hopper***, whereas the peak acceleration of the flow occurs in the upper part of the ***neck*** (Fig. 11 and Supplementary material), where the highest value of longitudinal strain was also calculated. The high density of normal faults in the ***hopper*** corresponds to the highest value of slope in the basal slip surface. From this observation, it appears that the slope angle of the basal slip surface might control the density of structures forming during flow movement. Strain just reflects the structural style. Deformational structures (Figs. 4, 5, 6) are consistent with computed dilatation and principal strain axes orientations (Figs. 14-17).

The displacement profiles of the Mount Pizzuto earth flow (Fig. 12a) indicate that average velocity varies along the earth flow during ordinary and extraordinary movements. In both cases, the maximum displacement/velocity of the Mount Pizzuto earth flow occurred near the neck of the flow. During ordinary movement (Fig. 12a), displacement generally increases from the beginning of the ***hopper*** (i.e., point 9) to the earth-flow ***neck*** (i.e., point 19**, curve b).

Similarly, during extraordinary movement, displacement increases from the beginning of the *hopper* (i.e., point 9) to the earth-flow *neck* (i.e., point 20, curve a). Considering that this part of the flow is characterized by a reduction in the width of the cross section, we infer that displacement/velocity in this part is controlled by the lateral and basal geometry of the slip surface. The presence of risers induces local acceleration of the flow at points 11 and 13. The presence of treads causes local deceleration of the flow around point 13 and 16 (Fig. 12). Thus, in absence of large asperities along the basal slip surface, the earth flow velocity should increase with reduction of cross sectional area, and vice versa. This suggests that the behavior of the earth flow material is similar to an incompressible fluid, especially during surging episodes when the sediment discharge is constant along the flow. Therefore, the use of macro-viscous model for earth flow simulations is not necessarily an oversimplification (e.g. Mackey and Roering, 2011).

Guerriero et al. (2014) underline that the distribution of surface structures can be used to infer the geometry of the basal slip surface, because of the relation between extensional structures and risers and compressional structures and treads. The displacement profile along a kinematic zone appears to have a consistent pattern during both ordinary and extraordinary movement (Fig. 12a). These observations suggest that a relation between the displacement profile of the earth flow (Fig. 12a) and its slip surface geometry (Fig. 12b) does exist and that local variations of flow velocity (i.e. acceleration and deceleration) are controlled by variations in the slope angle of the slip surface. In other words, the lateral and basal geometry of the slip surface controls both the kinematic segmentation of the earth flow and its velocity profile. This relation was also observed by Guerriero et al. (2016c) within the *neck* of the Montaguto earth flow. Additionally,

the velocity of an earth flow can be controlled by its thickness and by the frictional properties of the sliding surface. In the relatively short monitoring period of our study, the GPS data indicate limited variation in elevation and approximately persistent movement with only a few periods of localized no movement. Therefore, we assume that the thickness of the earth flow remains more less constant through time and that the frictional properties of the basal slip surface do not change and are consistently at residual strength.

During both ordinary and extraordinary movements, the earth flow material was subject to longitudinal extension and compression. Strain analysis indicates that all polygons located along driving elements exhibit positive dilatation (i.e. extending flow, Baum et al., 2000; Savage and Wasowski, 2006), while all polygons located along resisting elements show negative dilatation (i.e. compressive flow). Polygons located at transitions between treads and risers exhibit both shortening and extension, since as they move they change from a compressive to an extensional domain. For instance, polygon 1 located at the transition between the ***head*** and the ***hopper***, was subject to negative dilatation between GPS surveys 1 and 3, and to positive dilatation between surveys 3 and 8 (Table 2). This pattern of strain evolution suggests a close relation between longitudinal strain (i.e. dilatation) and the geometry of the basal slip surface (e.g. Savage and Wasowski, 2006), because a change in position of the polygon (i.e. a transition between tread and riser) induces a change in the incremental strain connected to a change in earth flow velocity. Thus, we can use a polygon located between a tread and a riser, and the evolution of its strain to locate the transition between two kinematic zones, as the region where the incremental dilatation changes sign. Also, according to the relation between strain and velocity gradient, we

can reconstruct the spatial and temporal distribution of earth flow velocity. However, to do this we would need a denser monitoring network.

As observed by Guerriero et al. (2016b), during extraordinary movement, the average longitudinal extension of the upper quadrilaterals of the ***hopper*** between GPS surveys 1 and 8 was not completely balanced by the longitudinal shortening of the lower quadrilaterals (Table 2). During ordinary movement, the average longitudinal extension of the upper quadrilaterals of the ***hopper*** between GPS surveys 12 and 17 was overbalanced by the longitudinal shortening of the lower quadrilaterals (Table 3). These data seem to indicate that flow material changes its volume moving through the ***hopper*** kinematic zone. Especially, during extraordinary movement the earth flow volume increases by ~20%, while during slow persistent movement the earth flow volume decreases by ~4%. This change in deformational behavior with respect to the surging episode might be the result of the reduced velocity of the flow and the reduced amount of material moving through the zone (i.e. lower sediment discharge). In other words, the strain rate is controlled by the earth flow velocity. Since deformation at the surface of the flow is representative of deformation at depth, this process might be not exclusive of the ***hopper*** kinematic zone and can be related to the basal slip surface.

At the ***toe***, structures and strain indicate the compressive character of this zone. During the spring/summer 2014, the lower part of the toe was subject to positive dilatation. Our interpretation is that during this period, the distal part of the flow was subject to spreading also indicated by the presence of normal faults, which might be related to persistent erosion of the Ginestra torrent. During ordinary movement, the compressive character of the axial part of the

flow was associated to the lateral extension of the polygons located on the left flank. Our interpretation is that in this period, the toe was subject to lateral spreading possibly connected to the deposition of the material mobilized during the surging acceleration of the spring 2014. Additionally, a change in the overall style of dilatation of the ***toe*** was observed on February 2016 when a small acceleration characterized the kinematics of this zone (Fig. 11 and Table 3). Our interpretation is that this change is connected to a process of reactivation triggered by extensive erosion of the Ginestra torrent. On October 2015, the Benevento province was hit by two large rainfall events (e.g. Valente et al., 2016) that triggered floods, landslides, and were responsible for extensive erosion (Magliulo and Cusano, 2016). Although most of the damages caused by floods were concentrated along the segment of the Calore river valley crossing the Benevento province, the bed of the Ginestra torrent was consistently enlarged by the floods, influencing the stability of the Mount Pizzuto earth flow toe.

Conclusions

The Mount Pizzuto earth flow was active during the monitoring period of April 2014 to March 2016, exhibiting both ordinary and extraordinary activity. The movement was seasonal and characterized by alternation between relatively rapid acceleration/surge in movement and localized and/or relatively slow movement.

A major surging acceleration (i.e. extraordinary movement) occurred in the spring 2014. During this episode, the earth flow acceleration likely started in the source area and propagated downslope inducing a cascade effect between successive kinematic zones. Temporally averaged

sediment discharge computed at four sections located along the transport zone of the flow was nearly constant, and all kinematic zones operated in unison to transmit pulses of sediment along the length of the flow. Under these conditions, the earth flow material behaved similar to an incompressible fluid. A second ordinary acceleration occurred between the end of the winter and the beginning of the spring 2015. Most of the points moved in a slow persistent manner between the spring 2015 and the spring 2016. In this period, sediment discharge was not constant along the flow. In this case the activity of each kinematic zone was independent from zones upslope and downslope. During this second acceleration and associated period of ordinary movement, the earth flow source area transmitted sediment to the transport zone in the form of small pulses. Several points exhibit no movement or movement below the error of our monitoring system in the autumn 2014, indicating a typical seasonal intermittent activity.

Overall, the basal slip surface is a repeating series of steeply sloping surfaces (risers) and gently sloping surfaces (treads) creating discrete kinematic zones. Within each kinematic zone, the overall shape of the slip surface is approximately concave upward, whereas at the transition areas, the shape is convex upward. At risers, where normal faults form on the ground surface, the earth flow accelerates while at treads, where thrusts form on the ground surface, the earth flow decelerates. Our analysis suggests that the velocity profile is controlled by the geometry of the basal slip surface during both ordinary and extraordinary activity. Strain analysis confirms the existence of zones of extension and shortening of the earth flow material, which are consistent with the distribution of structures. In most cases, such zones maintain their position trough time. Moreover, strain analysis indicates that the earth flow material changes its volume moving

through a kinematic zone with volume increase during exceptional movement and volume decrease during ordinary movement. However, while during exceptional movement the increase in volume presumably balances the sediment discharge entering and outgoing the *hopper*, during ordinary movement, the decrease in volume is not sufficient to balance the discharge, indicating a possible dependence of the dilatation with the velocity of the flow.

Implications from our results are: i) earth flows having a well-defined neck are more likely to surge with respect to those not having a neck, ii) it is not always correct to consider the sediment discharge of the earth flow constant, but this assumption should be contextualized as function of the state of flow activity, iii) during surging events, the earth flow behavior might be simulated using macro-viscous models without oversimplifying the problem, and iv) distribution of structures at the surface of an earth flow provide information about the geometry of the basal slip surface and the velocity profile of the earth flow. These implications are important for the characterization and modeling of earth flows in general.

Since the Mount Pizzuto earth flow discharges sediment to the Ginestra torrent, an evaluation of the sediment entering the river network and its impact on the dynamics, morphological evolution, and flooding of the area might be the subject of a forthcoming paper.

Acknowledgements

We thank the Editor Markus Stoffel and two anonymous reviewers for their constructive comments. We thank Alessio Luongo and Neri Mascellaro for their assistance with GPS surveys.

Strain analysis was completed using the program SSPX by Nestor Cardozo and Richard Allmendinger.

References

Ancey, C., 2007. Plasticity and geophysical flows: A review. Journal of Non-Newtonian Fluid Mechanics 142, p. 4-35.

Arai, H., Tokimatsu, K., 1998. Evaluation of local site effects based on microtremor H/V spectra. Proceedings of the second international symposium on the effects of surface geology on seismic motion, Yokohama, Japan.

ASTM, 2008. Standard test method for mechanical cone penetration tests of soil. Book of Standards 04.08

Baum, R. L., Savage, W. Z., Wasowsky, J., 2003. Mechanics of earth flows. Proceedings of the International Conference FLOWS 2003, Sorrento, Italy.

Baum, R. L., Raid M. E., 2000. Ground water isolation by low-permeability clays in landslide shear zone. In: Bromhead, E. N., Dickson N., Ibsen M. L., Landslide in Research, Theory and Practise, Proc. 8th Int. Sym. of landslide, Cardiff, Wales, v. 1, p. 139-144, Tellford, London.

Baum, R.L., Johnson, A.M., 1993. Steady movement of landslide features in fine-grained soils – a model for sliding over an irregular slip surface. U.S. Geological Survey Bulletin 1842, chapter d of landslide processes in Utah - observation and theory.

Baum, R.L., Fleming, R.W., Johnson, A. M., 1993. Kinematics of the Aspen Grove landslide, Ephraim canyon, Central Utah. U.S. Geological Survey Bulletin 1842.

Baum, R.L., Fleming, R.W., 1991. Use of longitudinal strain in identifying driving and resisting elements of landslides. Geological Society of America Bulletin 103, p. 1121-1132.

Baum, R.L., Johnson, A.M., Fleming, R.W., 1988. Measurement of slope deformation using quadrilaterals. US Geological Survey Bulletin 1842, 23 p.

Bertolini, G., Pizziolo, M., 2008. Risk assessment strategies of reactivation of earth flows in Northern Apennines (Italy). Engineering Geology 102, p. 178-192.

Booth, A.M., Roering, J.J., Rempel, A.W., 2013. Topographic signatures and a general transport law for deep-seated landslides in a landscape evolution model. Journal of Geophysical Research: Earth Surface 118, p. 603-624.

Booth, A.M., Roering, J.J., 2011. A 1-D mechanistic model for the evolution of earthflow prone hillslopes. Journal of Geophysical Research 116, p. 1-20.

Bovis, M.J., Jones, P., 1992. Holocene history of earth flow mass movement in south-central British Columbia: the influence of hydroclimatic changes. Canadian Journal of Earth Sciences 29, p. 1746-1755.

Calista, M., Miccadei, E., Pasculli, A., Piacentini, T., Sciarra, M., Sciarra, N., 2016. Geomorphological features of the Montebello sul Sangro large landslide (Abruzzo, Central Italy). Journal of Maps 12, 882 - 891.

Camuffo, D., Bertolin, C., Diodato, N., Cocheo, C., Barriendos, M., Dominguez-Castro, F., Garnier, E., Alcoforado, M.J., Nunes, M.F., 2013. Western Mediterranean precipitation over the last 300 years from instrumental observations. Climatic Change 117, p. 85-101.

Cardozo, N., Allmendinger, R.W., 2009. SSPX: A program to compute strain from displacement/velocity data. Computer and Geoscience 35, p. 1343-1357.

Carniel, R., Melisan, P., Barazza, F., Grimaz, S., 2008. Improvement of HVSR technique by wavelet analysis. Soil Dynamics and Earthquake Engineering 28, p. 321-327.

Castellaro, S., Panzeri, R., Mesiti, F., Bertello, L., 2015. A surface seismic approach to liquefaction. Soil Dynamic and Earthquake Engineering 77, p. 35-46.

Coe, J. A., Baum, R. L., Allstadt, K. E., Kochevar, B. F., Schmitt, R. G., Morgan, M. L., White, J. L., Stratton, B. T., Hayashi, T. A., Kean, J. W., 2016. Rock-avalanche dynamics revealed by large-scale field mapping and seismic signals at a highly mobile avalanche in the West Salt Creek valley, western Colorado. Geosphere 12-2, p. 607-631.

Coe, J. A., McKenna, J. P., Godt, J. W., Baum, R. L., 2009. Basal-topographic control of stationary ponds on a continuously moving landslide: Earth Surface Processes and Landforms 34, p. 264-279.

Coe, J. A., Ellis, W. L., Godt, J. W., Savage, W. Z., Savage, J. E., Michael, J. A., Kibler, J. D., Powers, P. S., Lidke, D. J., Debray, S., 2003. Seasonal movement of the Slumgullion landslide determined from Global Positioning System survey and field instrumentation, July 1998 – March 2002. Engineering Geology 68, p. 67-101.

Coussot, P., Nguyen, Q.D., Huynh, H.T., Bonn, D., 2002. Viscosity bifurcation in thixotropic, yielding fluids. Journal of Rheology 46, p. 573-589.

Daehne, A., Orsini, A., 2013. Kinematics of active earthflows revealed by digital image correlation and DEM subtraction techniques applied to multi-temporal LiDAR data. Earth Surface Processes and Landforms 38, p. 640-654.

Darve, F., Servant, G., Laouafa, F., Khoa, H., 2004. Failure in geomaterials: continuous and discrete analyses. Computer Methods in Applied Mechanics and Engineering 193, 305-308.

Diodato, N., de Vente, J., Bellocchi, G., Guerriero, L., Soriano, M., Fiorillo, F., Revellino, P., Guadagno, F.M., 2015. Estimating long-term sediment export using a seasonal rainfall-dependent hydrological model in the Glonn River basin, Germany. Geomorphology 228, p. 628-636.

Fleming, R. W., Baum, R. L., Giardino, M., 1999. Map and description of the active part of the Slumgullion Landslide, Hinsdale County. Colorado. U.S. Geological Survey Miscellaneous Investigation Series Map I-2672. http://pubs.usgs.gov/imap/i-2672/

Fleming, R. W., Johnson, A. M., 1989. Structures associated with strike-slip faults that bound landslide elements. Engineering Geology 27, p. 39-114.

Fleming, R. W., Johnson, A. M., Schuster, R. L., 1988. The reactivation of the Manti Landslide, Utah. U.S. Geological Survey Professional Paper 1311, p. 1-22.

Gili, J. A., Corominas, & J., Rius, J., 2000. Using global positioning system techniques in landslide monitoring. Engineering Geology 55, p. 167–192.

Giordan, D., Allasia, P., Manconi, A., Baldo, M., Santangelo, M., Cardinali, M., Corazza, A., Albanese, V., Lollino, G., Guzzetti, F., 2013. Morphological and kinematic evolution of a large earth flow. The Montaguto landslide, southern Italy. Geomorphology 187, 61–79.

Gomberg, J., Bodin, P., Savage, W. Z., Jackson, M. E., 1995. Landslide faults and tectonic faults, analogs: the Slumgullion earth-flow, Colorado. Geology 23-1, p. 41-44.

Guerriero, L., Revellino, P., Luongo, A., Focareta, M., Grelle, G., Guadagno, F.M., 2016. The Mount Pizzuto earth flow: deformational pattern and recent thrusting evolution. Journal of Maps 12, p. 1187-1194.

Guerriero, L., Mascellaro, N., Grelle, G., Guadagno, F.M., 2016a. Combined monitoring of earth flow displacement and its environmental drivers. Rendiconti Online della Società Geologica Italiana 41, p. 167-170.

Guerriero, L., Cardozo, N., Revellino., P., 2016b. Earth-flow deformation from GPS surveys, Mount Pizzuto earth flow, southern Italy. Rendiconti Online della Società Geologica Italiana 41, p. 163-166.

Guerriero, L., Revellino, P., Bertello, L., Grelle, G., Berti, M., Guadagno, F.M., 2016c. Kinermatic segmentation and velocity in earth flows: a consequence of complex basdal-slip surfaces. Procedia Earth and Planetary Science 16, p. 146-155.

Guerriero, L., Diodato, N., Fiorillo, F., Revellino, P., Grelle, G., Guadagno, F.M., 2015. Reconstruction of long-term earth-flow activity using a hydro-climatological model. Natural Hazards 77, p. 1-15.

Guerriero, L., Revellino, P., Mottola, A., Grelle, G., Sappa, G., Guadagno, F.M., 2015a. Multi-temporal mapping of the Caforchio earth flow, southern Italy. Rendiconti Online della Società Geologica Italiana, v. 35, p. 166-169.

Guerriero, L., Coe, J.A., Revellino, P., Grelle, G., Pinto, F., Guadagno, F.M., 2014. Influence of slip-surface geometry on earth flow deformation, Montaguto earth flow, southern Italy. Geomorphology 219, p. 285-305.

Guerriero, L., Revellino, P., Coe, J. A., Focareta, M., Grelle, G., Albanese, V., Corazza, A., Guadagno, F. M., 2013. Multi-temporal maps of the Montaguto earth flow in southern Italy from 1954 to 2010. Journal of Maps 9, p. 135–145.

Guerriero, L., Revellino, P., Grelle, G., Fiorillo, F., Guadagno, F. M., 2013a. Landslides and Infrastructures: The case of the Montaguto earth flow in Southern Italy. Italian Journal of Engineering Geology and Environment Book Series, v. 6, International Conference Vajont 1963-2013, p. 447-454.

Handwerger, A. L., J. J. Roering, D. A. Schmidt, Rempel A.W., 2015. Kinematics of earthflows in the Northern California Coast Ranges using satellite interferometry. Geomorphology 246, p. 321-333.

Handwerger, A. L., Roering, J. J., Schmidt, D. A., 2013. Controls on the seasonal deformation of slow-moving landslides. Earth and Planetary Sciences Letters 377-378, p. 239-247.

Hungr, O., Leroueil, S., Picarelli, L., 2014. The Varnes classification of landslide types, an update. Landslide 11, 167-194.

Iverson, R.M., 2005. Regulation of landslide motion by dilatancy and pore pressure feedback. Journal of Geophysical Research–Earth Surface 110-F2, 16 p.

Iverson, R.M., Reid, M.E., 1992. Gravity-driven groundwater flow and slope failure potential; 1, Elastic effective-stress model. Water Resources Research 28, p. 925-938.

Iverson, R.M., Major, J.J., 1987. Rainfall, ground-water flow, and seasonal movement at Minor Creek landslide, northwestern California: physical interpretation of empirical relations. Geological Society of America Bulletin 99, p. 579-594.

James, L.A., Hodgson, M.E., Ghoshal, S., Megison, Latiolais, M., 2012. Geomorphic change detection using historic maps and DEM differencing: the temporal dimension of geospatial analysis. Geomorphology 137, p. 181-198.

Keefer, D.K., Johnson, A.M., 1983. Earthflows: morphology, mobilization and movement. U.S. Geological Survey Professional Paper 1264, 56 p.

Korup, O., Densmore, A.L., Schlunegger, F., 2010. The role of landslides in mountain range evolution. Geomorphology 120, p. 77-90.

Krzeminska, D.M., Bogaard, T.A., van Asch, T.W.J., Van Beek, L.P.H., 2012. A conceptual model of the hydrological influence of fissures on landslide activity. Hydrology and Earth System Sciences 16, 1561-1576.

Louie, J. N., 2001. Faster, Better: Shear-wave velocity to 100 meters depth from refraction microtremor Arrays. Bulletin of the Seismological Society of America 91, p. 347-364.

Mackey, B.H., Roering, J. J., 2011. Sediment yield, spatial characteristics, and the long-term evolution of active earthflows determined from airborne LiDAR and historical aerial photographs, Eel River, California. Geological Society of America Bulletin 123, p. 1560-1576.

Mackey, B.H., Roering, J. J., McKean, J. A., 2009. Long-term kinematics and sediment flux of an active earthflow, Eel River, California. Geology 37-9, p. 803-806.

Magliulo, P., Cusano, A., 2016. Geomorphology of the Calore river alluvial plain. Journal of Maps 12, p. 1119-1127.

Manconi, A., Casu, F., Ardizzone, F., Bonano, M., Cardinali, M., De Luca, C., Gueguen, E., Marchesini, I., Parise, M., Vennari, C., Lenari, R., Guzzetti, F., 2014. Brief communication: rapid mapping of landslide events: the 3 December 2013 Montescaglioso landslide, Italy. Natural Hazards and Earth System Science 14, p. 1835-1841.

Mitra, S., 1990. Fault-propagation folds: Geometry, kinematic evolution, and hydrocarbon traps. American Association of Petroleum Geologists Bulletin 74, p. 921-945.

Mulargia, F., Castellaro, S., 2013. A seismic passive imaging step beyond SPAC and ReMiTM. Geophysics 78, p. 63-72.

Ohori, M., Nobata, A., Wakamatsu, K., 2002. A comparison of ESAC and FK methods of estimating phase velocity using arbitrarily shaped microtremor arrays. Bulletin of the Seismological Society of America 92-6, p. 2323-2332.

Park, C. B., R. D. Miller, and J. Xia, 1999. Multi-channel analysis of surface waves. Geophysics 64, p. 800-808.

Parise, M., 2003. Observation of surface features on an active landslide, and implications for understanding its history of movement. Natural Hazards and Earth System Science 3, p. 569-580.

Pescatore, T., Di Nocera, S., Matano, F., Pinto, F., 2000. L'unità del Fortore nel quadro della geologia del settore orientale dei Monti del Sannio (Appennino meridionale). Bollettino della Società Geologica Italiana 119, p. 587-601.

Pinto, F., Guerriero, L., Revellino, P., Grelle, G., Senatore, M.R., Guadagno, F.M., 2016. Structural and lithostratigraphic controls of earth-flow evolution, Montaguto earth flow, Southern Italy. Journal of the Geological Society 173-4, p. 649-665.

Prokešová, R., Kardoš, M., Tábork, P., Medvedová, A., Stacke, V., Chudy, F., 2014. Kinematic behaviour of a large earthflow defined by surface displacement monitoring, dem differencing, and ert imaging. Geomorphology 224, p. 86-101.

Reid, M.E., Iverson, R.M., 1992. Gravity-driven groundwater flow and slope failure potential; 2, Effects of slope morphology, material properties, and hydraulic heterogeneity. Water Resources Research 28, p. 939-950.

Savage, W., Wasowski, J., 2006. A plastic flow model for the Acquara-Vadoncello landslide in Senerchia, Southern Italy. Engineering Geology 83, p. 4-21.

Schulz, W. H., Mackenna, J. P., Kibler, J. D., Biavati, G, 2009. Relations between hydrology and velocity of a continuously moving landslide – evidence of pore pressure feedback regulating landslide motion? Landslides 6, p. 181-190.

Schuster, G.T., Quintus-Bosz, A., 1993. Wavepath eikonal traveltime inversion: theory. Geophysics 58, p. 1314-1323.

Simoni, A., Ponza, A., Picotti, V., Berti, M., Dinelli, E., 2013. Earthflow sediment production and Holocene sediment record in a large Apennines catchment. Geomorphology 188, p. 42-53.

Sweeney, K.E., Roering, J.J., Almond, P., Reckling, T., 2012. How steady are steady-state landscapes? Using visible–near-infrared soil spectroscopy to quantify erosional variability. Geology 40, p. 807-810.

Valente, A., Iscaro, C., Magliulo, P., Russo, F., 2016. The flood event in Benevento on 14th -15th October 2015: a short report. Rendiconti Online della Società Geologica Italiana 38, p. 105-108.

van Asch, T.W.J., Malet, J.P., 2009. Flow-type failures in fine-grained soils: An important aspect in landslide hazard analysis. Natural Hazard and Earth System Science 9, 1703-1711.

van Asch, T.W.J., Malet, J.P., van Beek, L.P.H., 2006. Influence of landslide geometry and kinematic deformation to describe the liquefaction of landslides: Some theoretical considerations. Engineering Geology 88, p. 59-69.

Varnes, D.J., 1978. Slope movement types and processes. In Schuster, R.L., Krizek, R.J., Landslides Analysis and Control, Transportation Research Board Special Report 176, National Academy Press, Washington, D.C., p. 11-33.

Williams, R.A., Pratt, T.L., 1996. Detection of the base of Slumgullion landslide, Colorado, by seismic reflection and refraction methods. In Varnes, D.J., Savage, W.Z. (Eds.), The Slumgullion

earth flow: a large-scale natural laboratory, U.S. Geological Survey Bulletin 2130, United States Government Printing Office, Washington.

Wood, D. M. (1990), Soil Behavior and Critical State Soil Mechanics, Cambridge University Press, Cambridge.

Zhang, X., Phillips, C., Marden, M., 1991. Internal deformation of a fast-moving earthflow, Raukumura Peninsula, New Zealand. Geomorphology 4, p. 145-154.

Figure captions

Figure 1. Schematic longitudinal profile of a sequence of kinematic zones along an earth flow. The upper part of the figure is modified from Guerriero et al (2014).

Figure 2. The Mount Pizzuto earth flow. The flow is about 1 km long. The photo is taken from the opposite side of the Ginestra torrent valley looking southwest.

Figure 3. Geological map of the Mount Pizzuto earth flow area. Contours are topographic elevation.

Figure 4. a) Structures and hydrologic features in the ***head*** and ***hopper*** of the Mount Pizzuto earth flow. Red dots indicate position of monitoring points installed on April 8, 2014. b) Movement of monitoring stations (black numbers) from April 8, 2014 to March 2, 2016. Color numbers are cumulative vertical displacement (i.e. elevation change).

Figure 5. a) Structures and hydrologic features in the ***neck*** and ***body*** of the Mount Pizzuto earth flow. Red dots indicate position of monitoring points installed on April 8, 2014. b) Displacement of monitoring stations (black numbers) from April 8, 2014 to March 2, 2016. Color numbers are cumulative vertical displacement (i.e. elevation change).

Figure 6. a) Structures and hydrologic features in the ***toe*** of the Mount Pizzuto earth flow. Red dots indicate position of monitoring points installed on April 8, 2014. B) Displacement of monitoring stations (black numbers) from April 8, 2014 to March 2, 2016. Color numbers are cumulative vertical displacement (i.e. elevation change).

Figure 7. The neck of the Mount Pizzuto earth flow exposed after a surging reactivation. The photo is taken looking southwest. The distance between the right and the left flank of the earth flow is approximately 10 m.

Figure 8. Map showing positions in May 2015 of monitoring points installed on April 2014 (grey dots), complementary monitoring points (black dots) and new monitoring point 0 installed on April 2015, HVSR measurements (i.e. red circles over gray points), boreholes (blue dots), Remi/MASW profiles (purple lines), and S-tomography seismic profiles (green lines). AA' is the longitudinal profile used for sediment discharge computation.

Figure 9. Examples of a) dispersion curve of ReMi/MASW profile f (see Fig. 8 for location), b) HVSR measurement at monitoring point 15 (see Fig. 8 for location), and c) reconstructed surface-wave velocity (Vs) vs. depth model of the subsoil from the combination of a and b. In a, the red area delimited by the black lines indicates the maximum Vs. In c, continuous line is

estimated Vs and dotted line is its uncertainty. The first 4 m in c represent the landslide body (low Vs) and the third layer is the bedrock (higher Vs).

Figure 10. Setup of models for mechanical analysis of the earth flow. a) Transition between riser and tread, and b) Transition between tread and riser. The models consist of two sub-grids, a finer one for the landslide and a coarser one for the bedrock, separated by an interface representing the basal slip surface. Dimensions, thicknesses of the grids, and surface slope angles correspond to those of the earth flow.

Figure 11. Cumulative horizontal displacement of monitoring points installed within the a) northern and b) southern branches of the ***head***, c) ***hopper***, d) ***neck***, e) ***body***, and f) ***toe*** of the earth flow. Grey rectangles indicate periods of acceleration. Red segment indicates the period and point (i.e. location) characterized by maximum velocity during two consecutive GPS surveys. Notice that the scale of the displacement axis is different on all plots.

Figure 12. a) Displacement profiles along the transport zone of the earth flow between April 8 and August 30, 2014 (curve a) and between May 8, 2015 and March 2, 2016 (curve b). b) Longitudinal topographic profile (AA') of the earth flow surface and geometry of the longitudinal basal slip surface (grey lines) reconstructed using borehole data, seismic refraction profiles, and HVSR measurements. Monitoring points are shown at locations on April 8 (black dots) and August 30 (grey dots), 2014. Grey dashed lines surrounding basal slip surface are uncertainty envelope. Vertical, thick grey lines crossing a and b show the location of the refraction profiles S1 to S4 (Fig. 8).

Figure 13. Seismic refraction/tomographic profiles S1 to S4 used to reconstruct the geometry of the lateral- and basal slip surfaces of the earth flow. Seismic velocities are in m/s, and the contour interval is 100 m/s. Red-dashed line shows the basal slip surface. Red arrows indicate the position of the strike- slip faults forming earth flow flanks and numbers 1 to 7 on sections are the sledgehammer shots. In each section, the area in square meters of the earth flow material above this surface is reported. For location of profiles see Fig. 8.

Figure 14. Evolution of dilatation in polygons defined by monitoring points within the lower part of the ***head***, ***hopper***, and the upper part of the ***neck***, for the period April 8 to a) May 9, b) May 21, c) June 5, d) June 17, e) July 17, f) July 29, and g) August 30, 2014. White numbers on polygons vertices are monitoring points, and red numbers in a) are polygons ids. Strain ellipses and principal axes of extension and shortening (red and blue ticks, respectively) are shown. Points' connectivity and computed dilatation are included in Table 2.

Figure 15. Dilatation of polygons defined by monitoring points within the ***toe*** of the earth flow, for the period April 8 to August 30, 2014. White numbers are polygons vertices and red numbers are polygons ids. Strain ellipses and principal axes of extension and shortening (red and blue ticks, respectively) are shown. Points' connectivity and computed dilatation are included in Table 2.

Figure 16. Dilatation of polygons defined by monitoring points within the earth flow transport zone (profile A-A', Fig. 8), for the period May 8, 2015 to March 2, 2016. Black numbers are polygons vertices and red numbers are polygons ids. Red and blue ticks are principal axes of

extension and shortening, respectively. Points' connectivity and computed dilatation are included in Table 3.

Figure 17. Evolution of dilatation in polygons defined by monitoring points within the toe, for the period May 8, 2015 to a) July 11, 2015, b) September 6, 2015, c) November 28, 2015, d) January 29, 2016, and e) March 2, 2016. Black numbers are polygons vertices and red numbers in a) are polygons ids. Strain ellipses and principal axes of extension and shortening (red and blue ticks, respectively) are shown. Points' connectivity and computed dilatation are included in Table 3.

Figure 18. Results of mechanical model for riser-to-tread transition (Fig. 10a). a to d show the results obtained by assuming a large velocity drop between the riser and the tread. e to h are for a small velocity drop. First row is finite difference model and initial conditions, second row is displacement vectors, third row is grid distortion, and fourth row is incremental maximum shear strain. b to d and f to h are presented in the zoom areas shown in a and e, respectively.

Figure 19. Results of mechanical model for tread-to-riser transition (Fig. 10b). a) Finite difference model and initial conditions; b) displacement vectors; c) grid distortion; d) incremental maximum shear strain. The model uses a large increase (ϕ'e = 10°) of landslide velocity between the tread and the riser. Results for a small increase of landslide velocity (ϕ'e = 5°) are not presented but they are almost similar. b to d are presented in the zoom area shown in a.

Figure 20. DEM difference maps of the earth flow source area showing elevation variation between a) September 2014 and February 2015 and b) February 2015 and March 2016. Red colors indicate uplift and blue colors subsidence.

Figure 21. Computed sediment discharge at cross sections S1, S2, S3, S4 (Fig. 8). Bars are for periods i to vi. Lines are for periods vii to ix (section 3.7). Labels on line graphs and grey colors on bars indicate these periods. Error bars are included.

Figure 22. The earth flow below the neck after the surging episode of the spring 2014. The width of the earth flow at the neck is around 10 m. Photo taken from the left flank looking to the south on May 2014.

Supplementary data

A. Graphs showing earth flow velocity between 08/04/2014 and 02/03/2016. Each graph shows the evolution of velocity in the monitoring period. Each bar represents the average velocity calculated from two successive GPS surveys. Red bar indicates the maximum velocity registered at that point in the monitoring period. The absence of the bar indicates no movement. Graphs are labeled with the point ID and initial point position is reported in the map. Gray arrows in the graphs background indicate downslope direction along the flow. The map shows also position and extension of the kinematic zones.

B. Example of raw seismic data along section S1 used to reconstruct the cross sectional geometry of the earth flow (see Fig. 8 for position). Each graph contains signals acquired at different shot locations. Red segments indicate picked first arrivals used for the reconstruction of the velocity field. Red star indicates shot position. Black triangles show geophone positions.

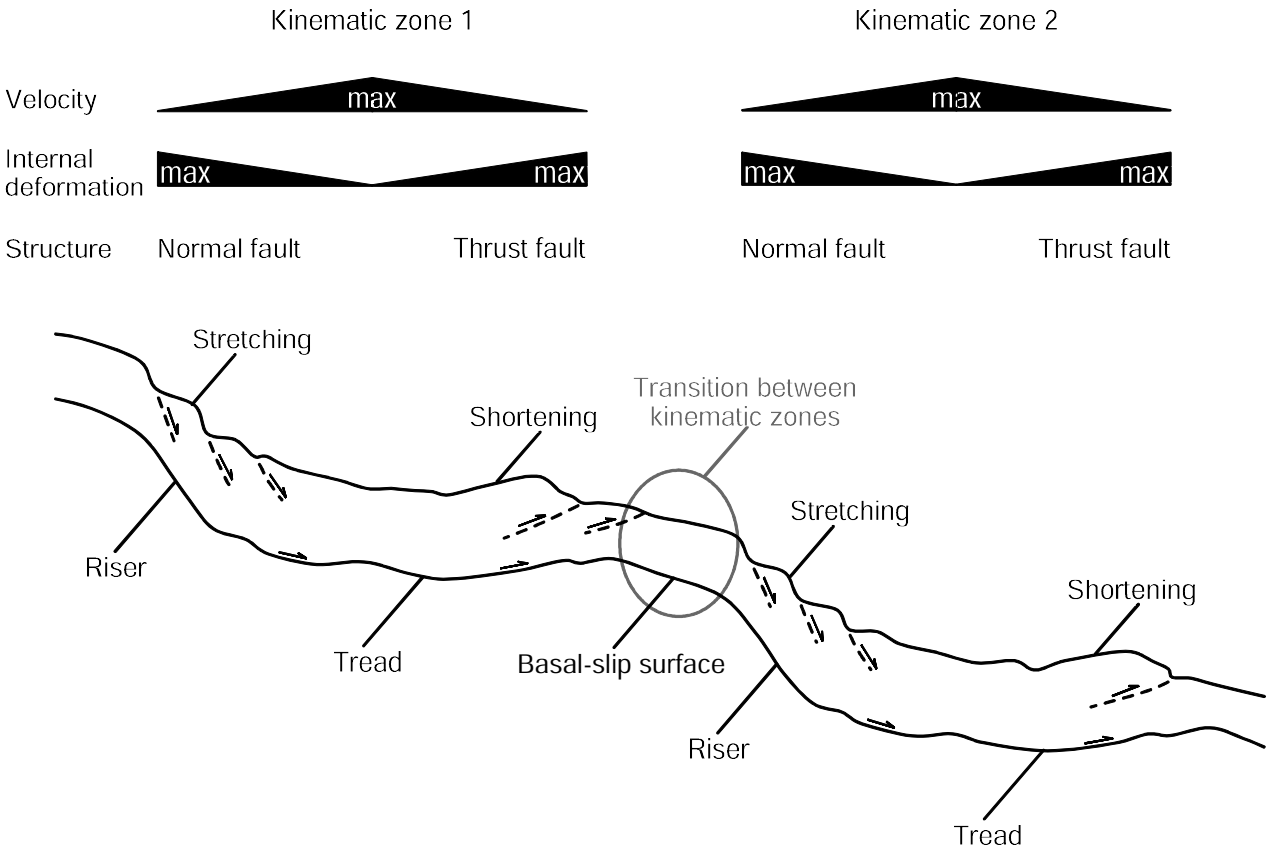
Kinematic zone 1
Kinematic zone 2
Velocity
max
max
Internal deformation
max
max
max
max
Structure
Normal fault
Thrust fault
Normal fault
Thrust fault
Stretching
Shortening
Transition between kinematic zones
Stretching
Shortening
Riser
Tread
Basal-slip surface
Riser
Tread

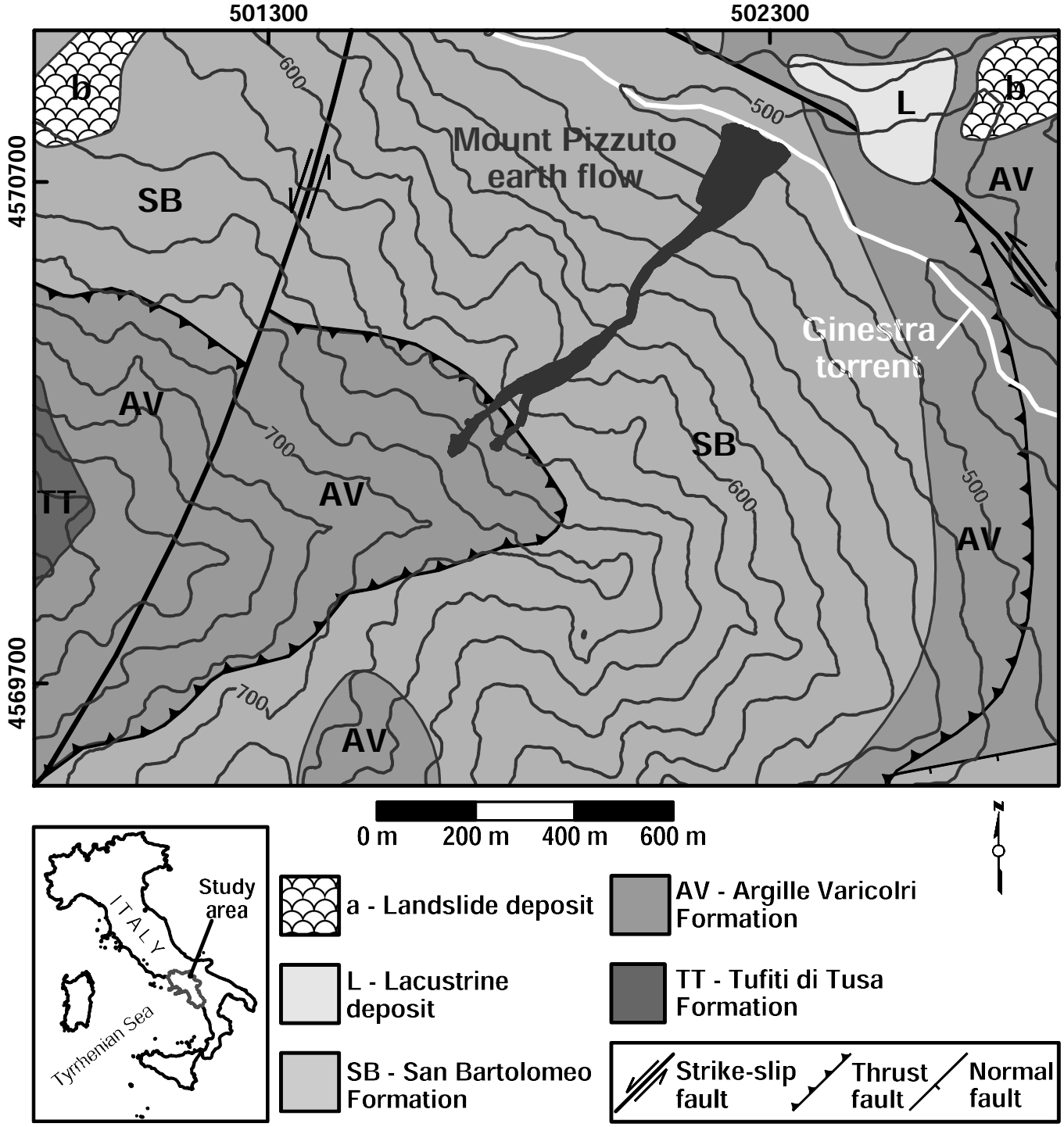
501300
502300
4570700
4569700
600
500
700
700
Mount Pizzuto
earth flow
Ginestra
torrent
SB
AV
TT
AV
SB
AV
AV
L
b
b
0 m
200 m
400 m
600 m
N
Study
area
ITALY
Tyrrhenian Sea
a - Landslide deposit
L - Lacustrine
deposit
SB - San Bartolomeo
Formation
AV - Argille Varicolri
Formation
TT - Tufiti di Tusa
Formation
Strike-slip
fault
Thrust
fault
Normal
fault

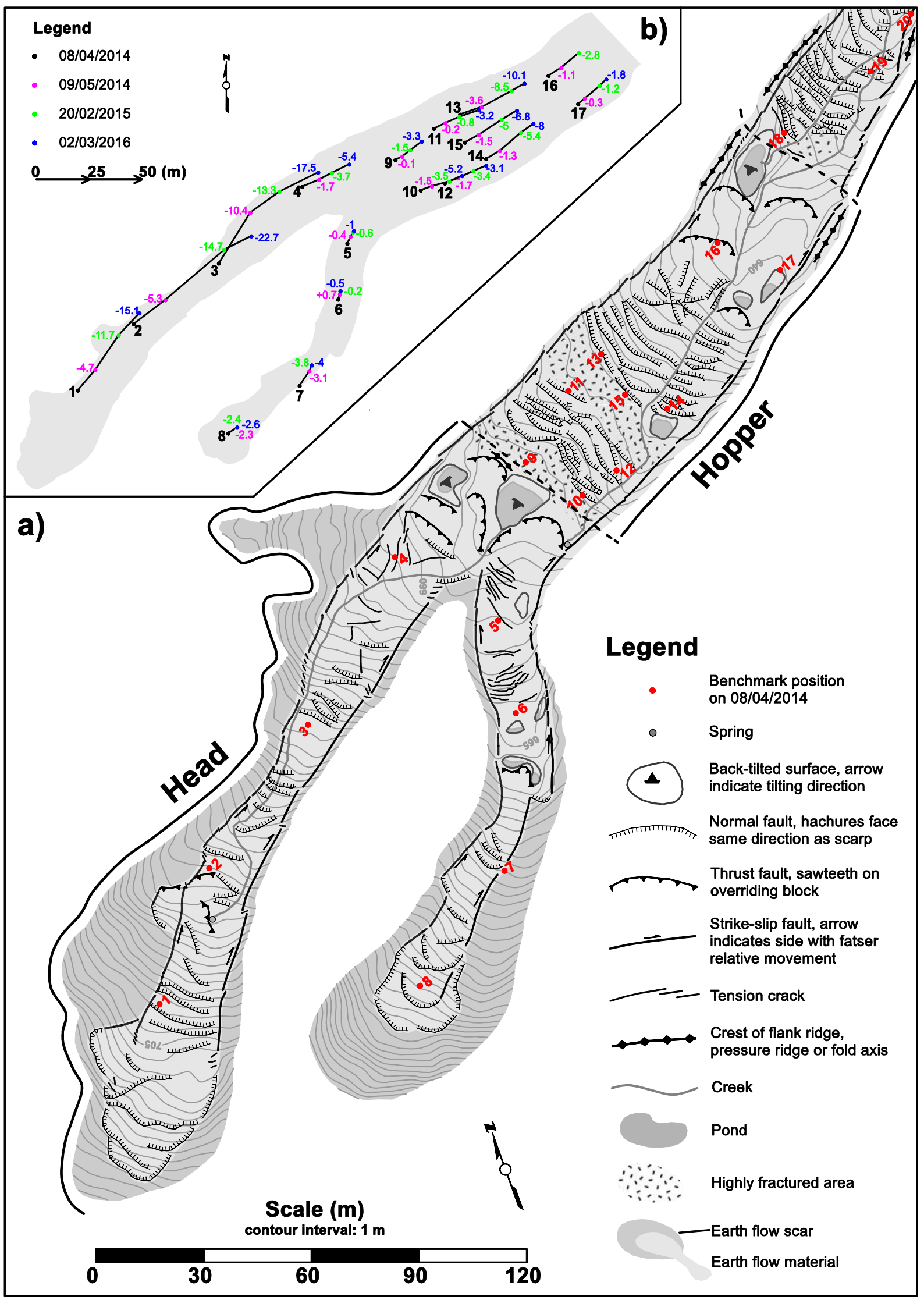
Legend
08/04/2014
09/05/2014
20/02/2015
02/03/2016
0 25 50 (m)
b)
a)
Head
Hopper
Legend
Benchmark position on 08/04/2014
Spring
Back-tilted surface, arrow indicate tilting direction
Normal fault, hachures face same direction as scarp
Thrust fault, sawteeth on overriding block
Strike-slip fault, arrow indicates side with fatser relative movement
Tension crack
Crest of flank ridge, pressure ridge or fold axis
Creek
Pond
Highly fractured area
Earth flow scar
Earth flow material
Scale (m)
contour interval: 1 m
0 30 60 90 120

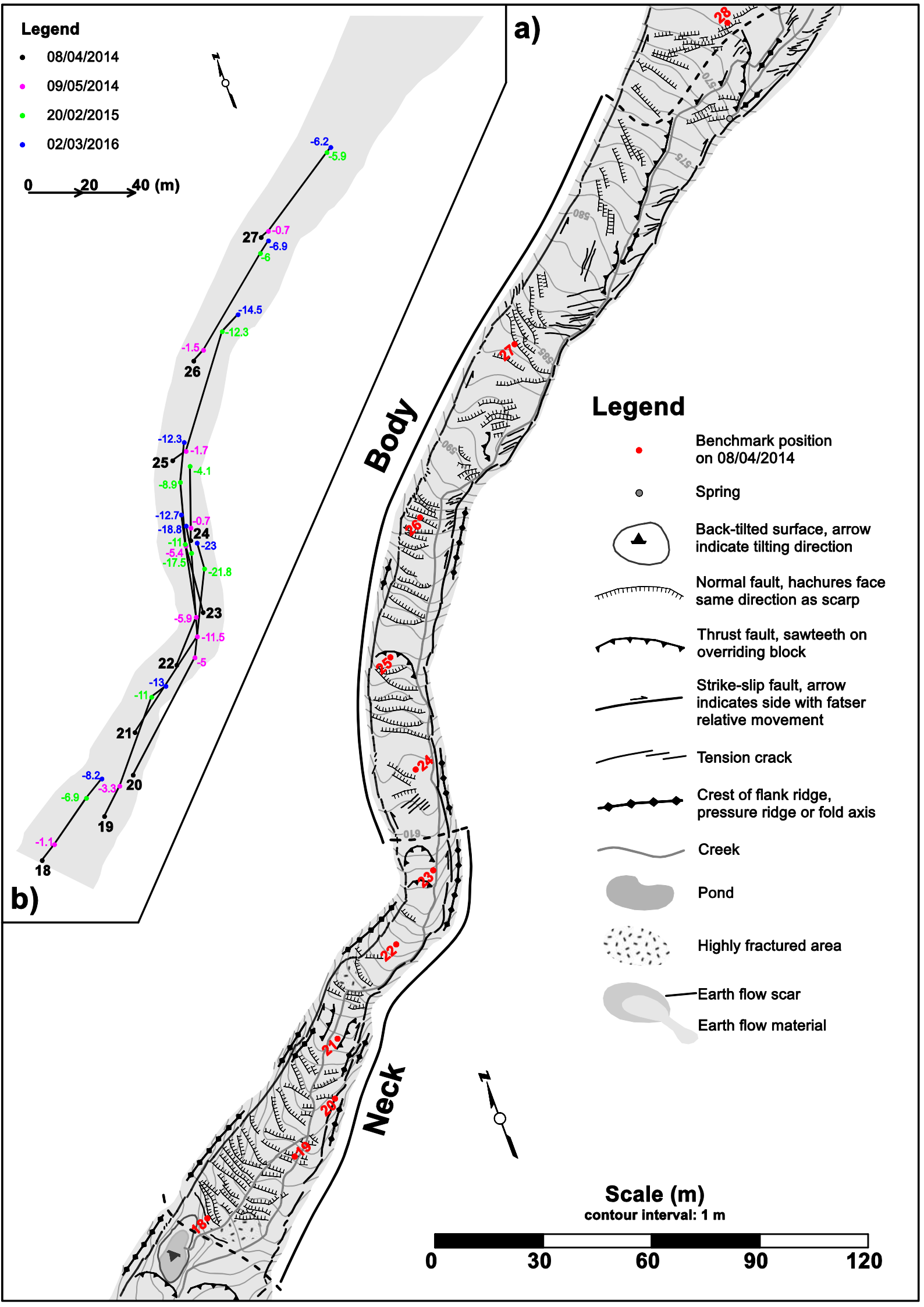
Legend
08/04/2014
09/05/2014
20/02/2015
02/03/2016
0 20 40 (m)
a)
b)
Body
Neck
Legend
Benchmark position on 08/04/2014
Spring
Back-tilted surface, arrow indicate tilting direction
Normal fault, hachures face same direction as scarp
Thrust fault, sawteeth on overriding block
Strike-slip fault, arrow indicates side with fatser relative movement
Tension crack
Crest of flank ridge, pressure ridge or fold axis
Creek
Pond
Highly fractured area
Earth flow scar
Earth flow material
Scale (m)
contour interval: 1 m
0 30 60 90 120

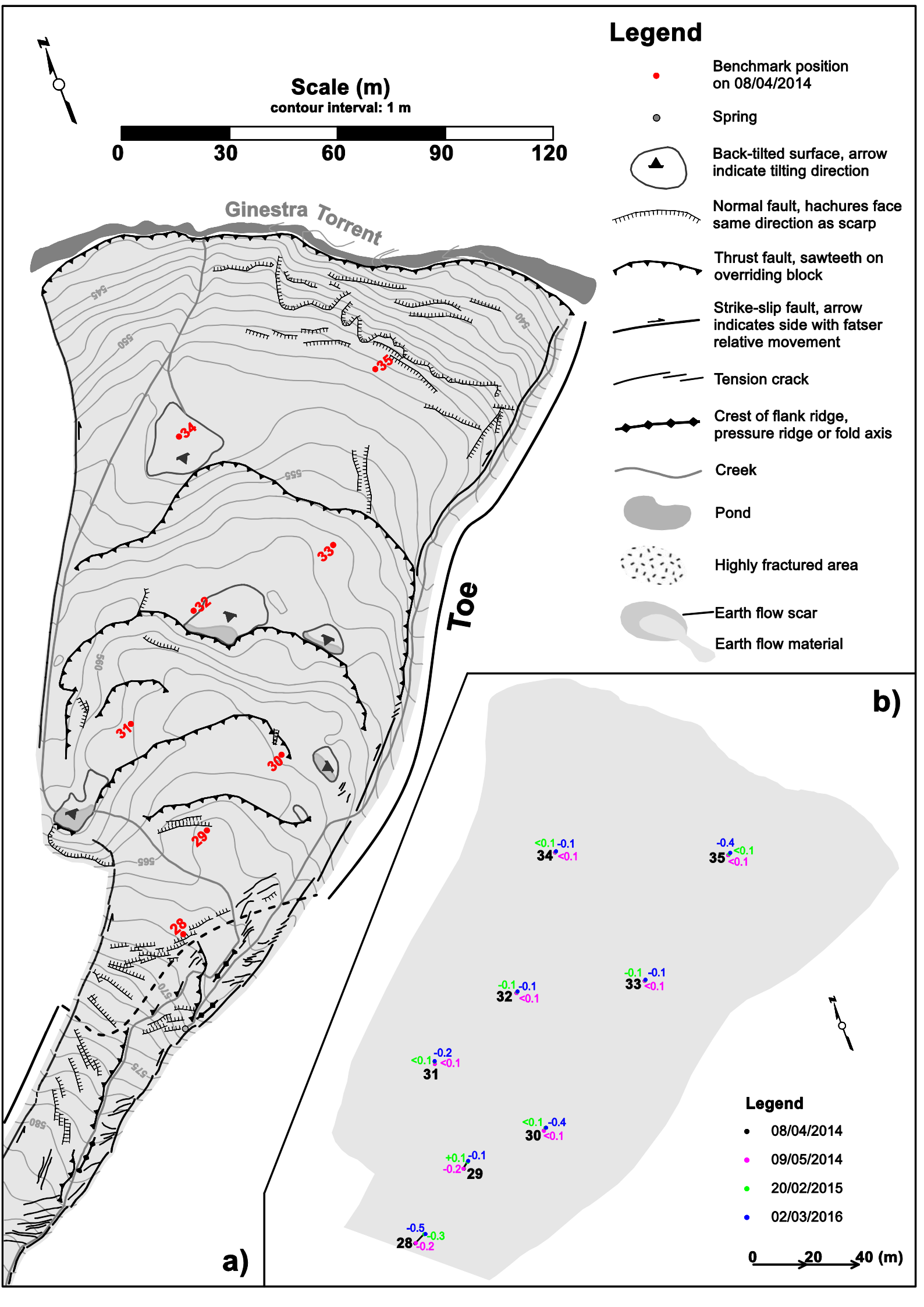
Legend
Benchmark position on 08/04/2014
Spring
Back-tilted surface, arrow indicate tilting direction
Normal fault, hachures face same direction as scarp
Thrust fault, sawteeth on overriding block
Strike-slip fault, arrow indicates side with fatser relative movement
Tension crack
Crest of flank ridge, pressure ridge or fold axis
Creek
Pond
Highly fractured area
Earth flow scar
Earth flow material
Scale (m)
contour interval: 1 m
0
30
60
90
120
Ginestra Torrent
Toe
a)
b)
Legend
08/04/2014
09/05/2014
20/02/2015
02/03/2016
0
20
40 (m)

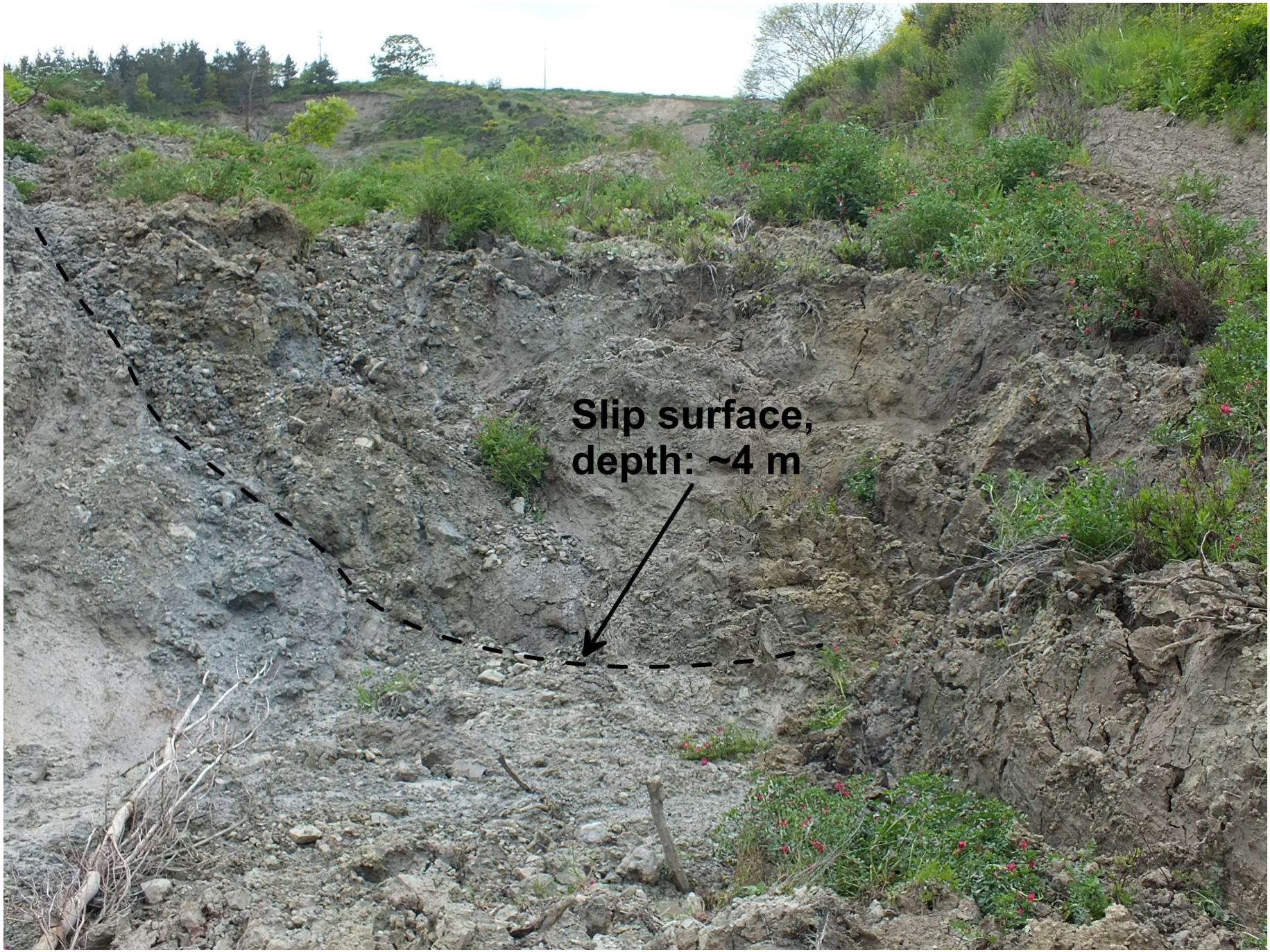
Slip surface,
depth: ~4 m

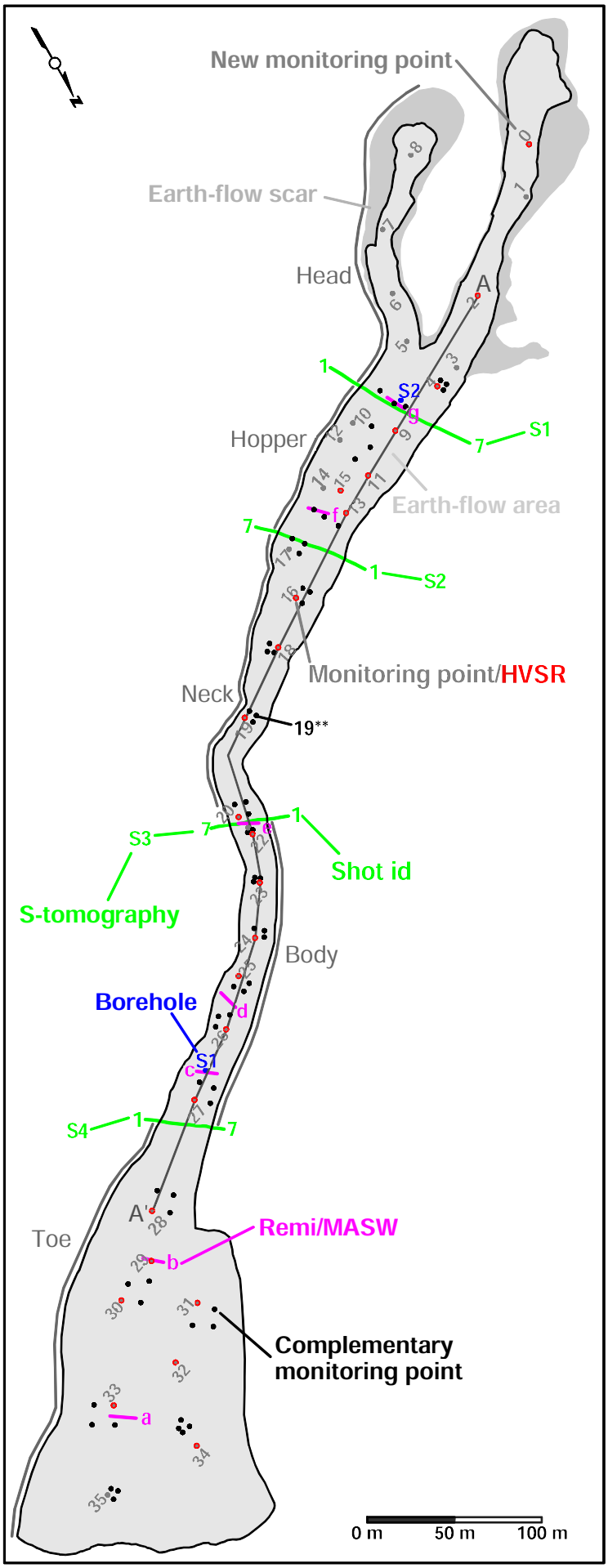
New monitoring point
Earth-flow scar
Head
Hopper
Earth-flow area
Neck
Monitoring point/HVSR
19**
Shot id
S-tomography
S3
S4
S1
S2
Body
Borehole
Toe
Remi/MASW
Complementary monitoring point
A
A'
0 m
50 m
100 m

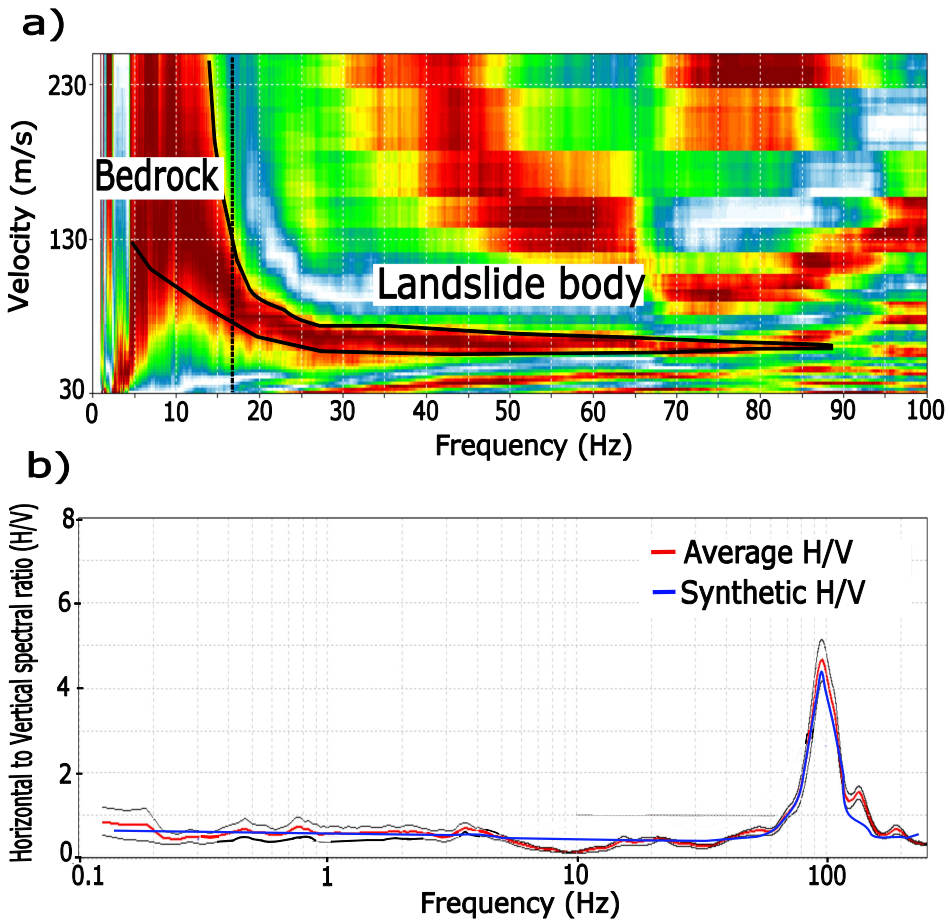
a)
Velocity (m/s)
230
130
30
Bedrock
Landslide body
0
10
20
30
40
50
60
70
80
90
100
Frequency (Hz)

b)
Horizontal to Vertical spectral ratio (H/V)
8
6
4
2
0
Average H/V
Synthetic H/V
0.1
1
10
100
Frequency (Hz)

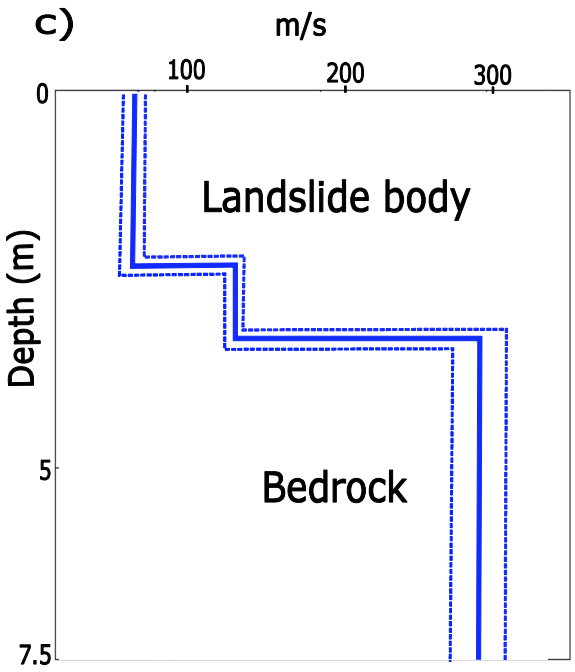
c)
m/s
100
200
300
0
Depth (m)
5
7.5
Landslide body
Bedrock

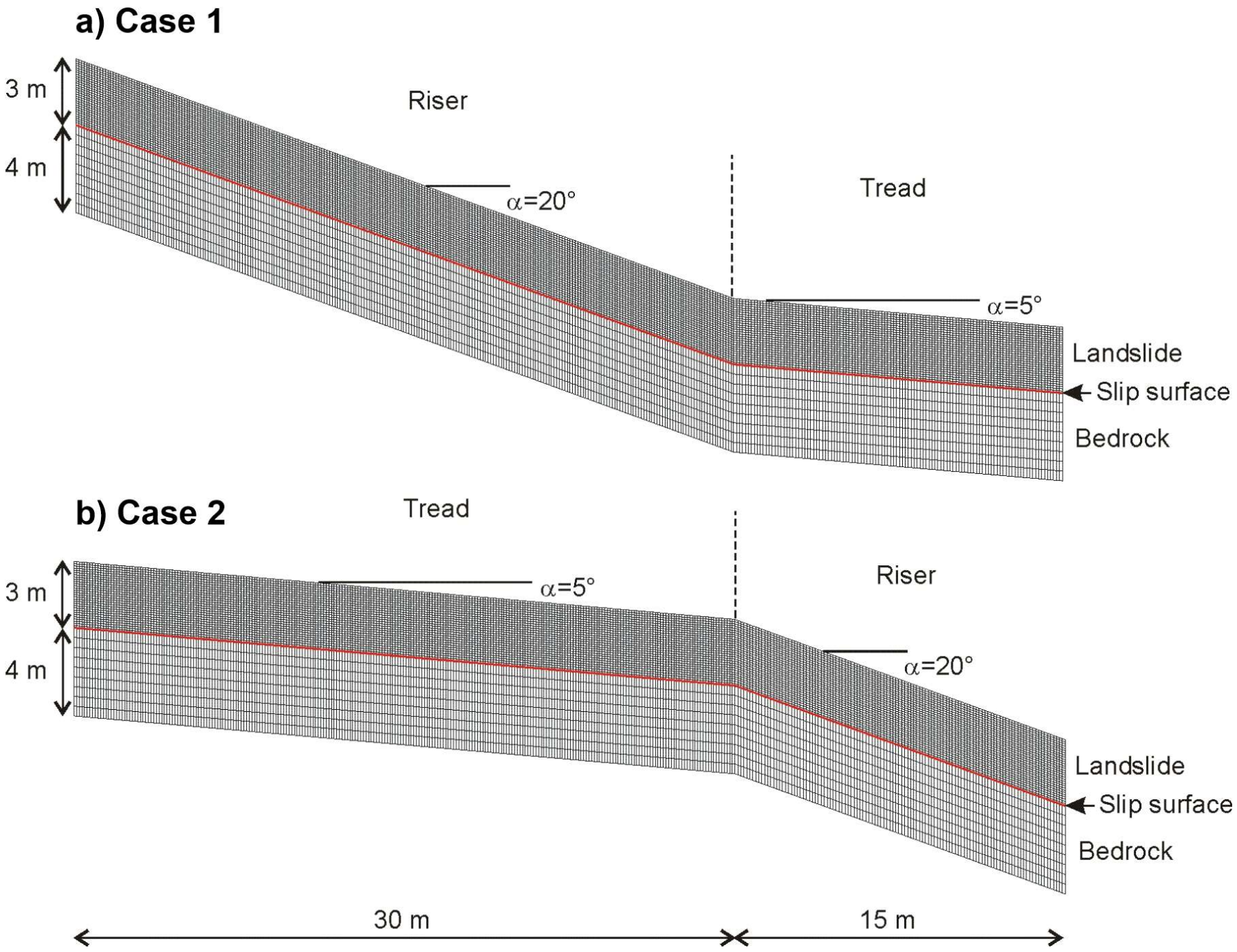
a) Case 1
3 m
4 m
Riser
α=20°
Tread
α=5°
Landslide
Slip surface
Bedrock
b) Case 2
Tread
α=5°
Riser
α=20°
3 m
4 m
Landslide
Slip surface
Bedrock
30 m
15 m

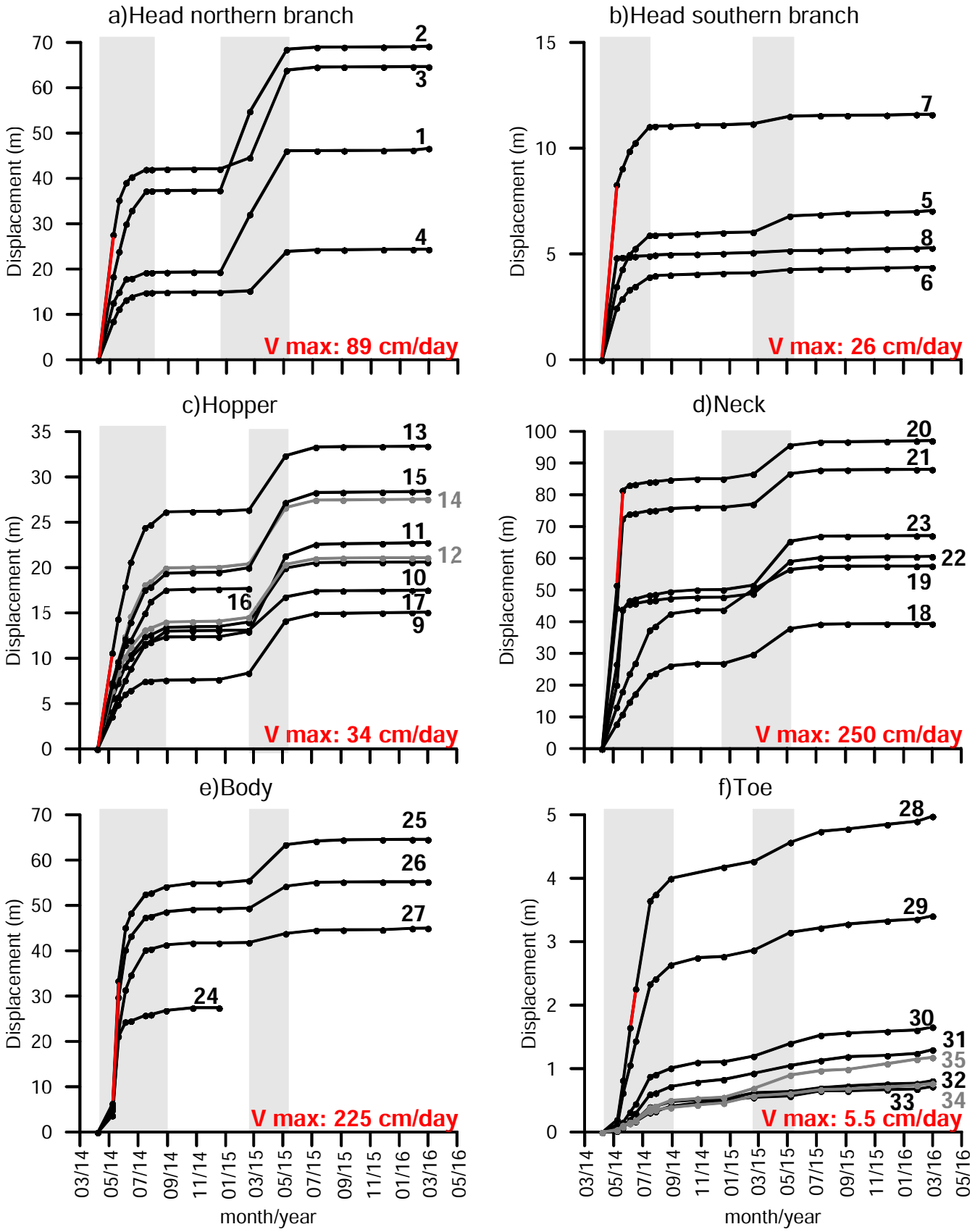
a)Head northern branch
Displacement (m)
V max: 89 cm/day
b)Head southern branch
Displacement (m)
V max: 26 cm/day
c)Hopper
Displacement (m)
V max: 34 cm/day
d)Neck
Displacement (m)
V max: 250 cm/day
e)Body
Displacement (m)
V max: 225 cm/day
f)Toe
Displacement (m)
V max: 5.5 cm/day
03/14
05/14
07/14
09/14
11/14
01/15
03/15
05/15
07/15
09/15
11/15
01/16
03/16
05/16
month/year

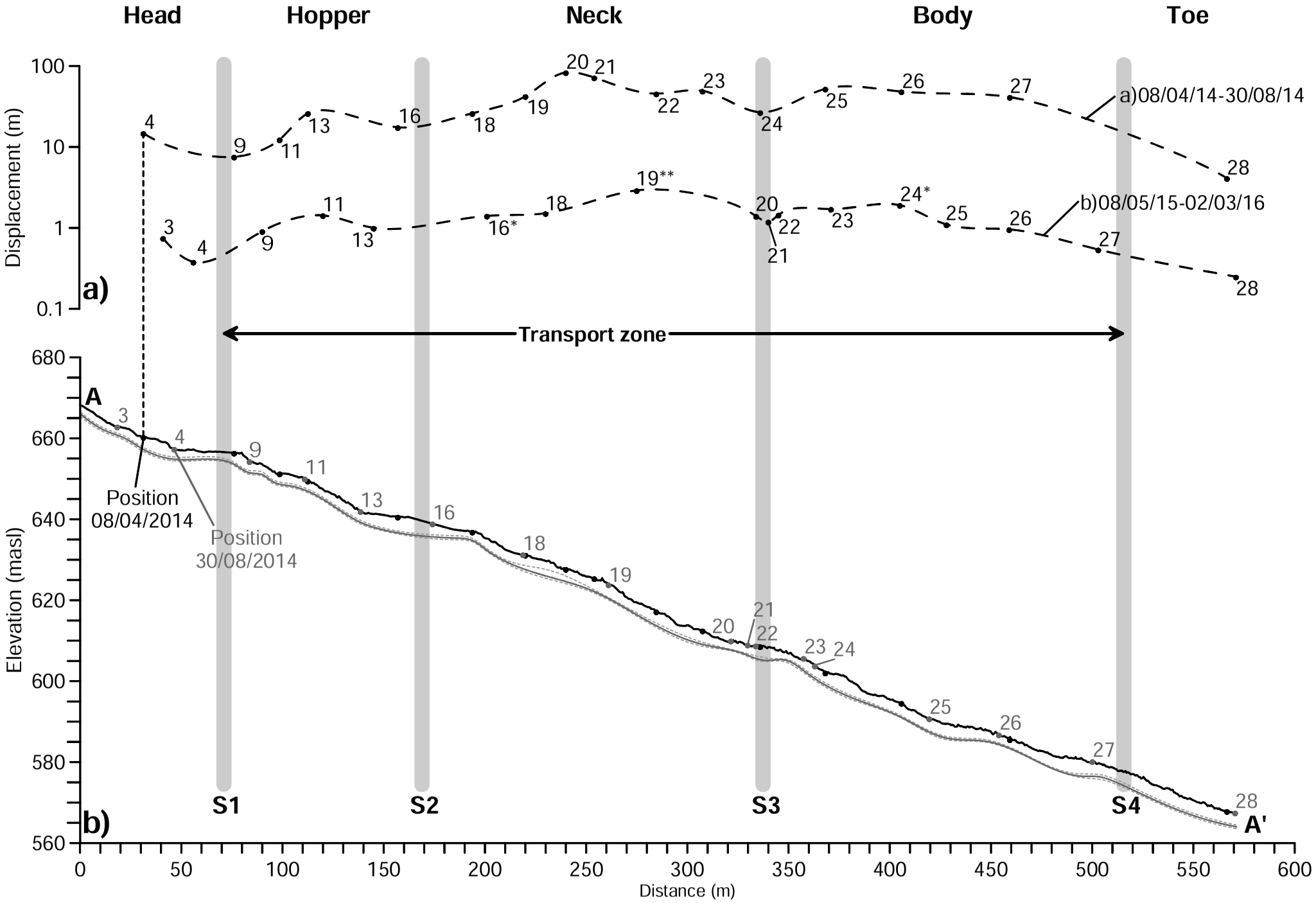
Head
Hopper
Neck
Body
Toe
Displacement (m)
100
10
1
0.1
a)
a)08/04/14-30/08/14
b)08/05/15-02/03/16
Transport zone
Elevation (masl)
680
660
640
620
600
580
560
A
A'
b)
S1
S2
S3
S4
Position
08/04/2014
Position
30/08/2014
0
50
100
150
200
250
300
350
400
450
500
550
600
Distance (m)

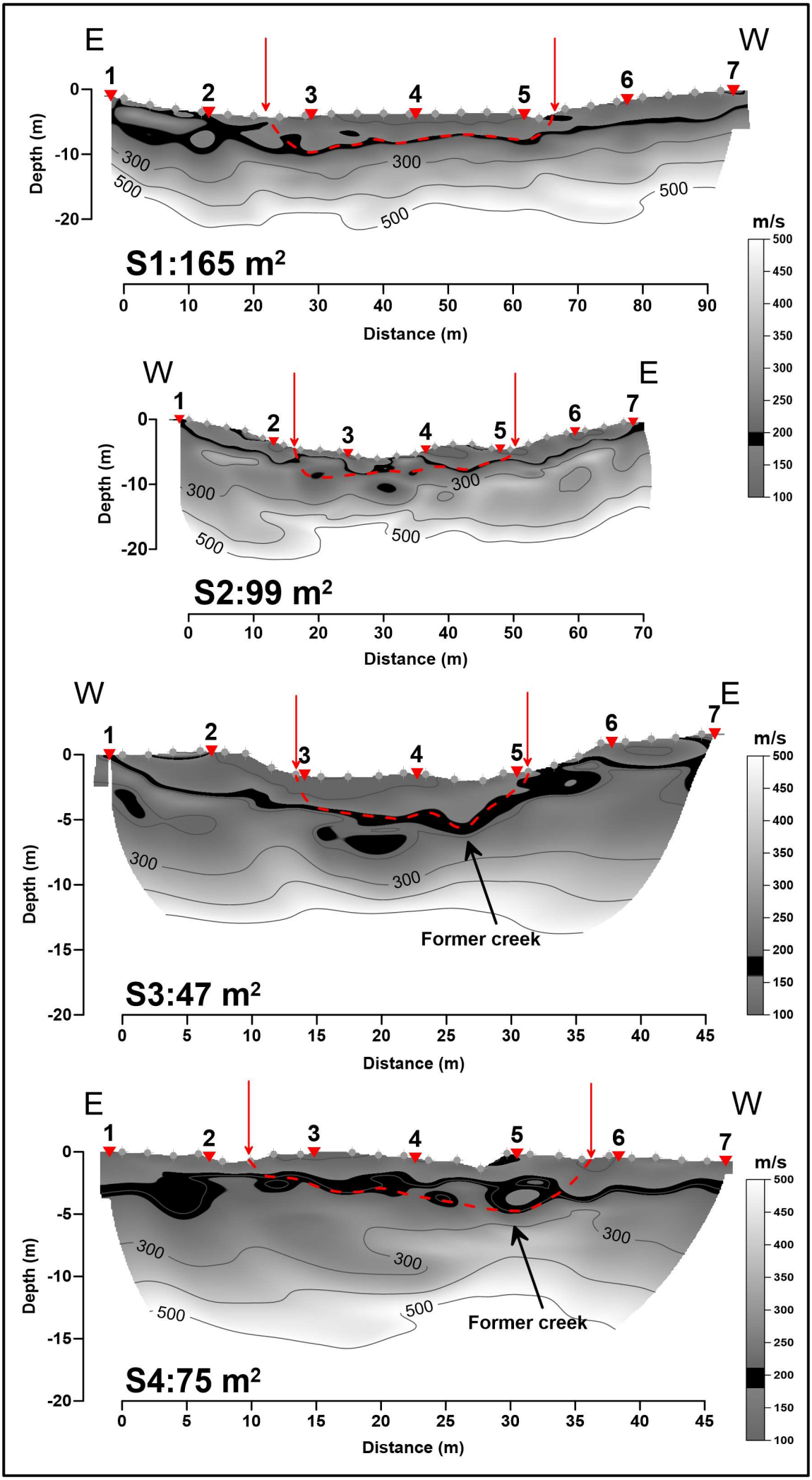
E
W
1
2
3
4
5
6
7
Depth (m)
0
-10
-20
300
500
S1:165 m²
0 10 20 30 40 50 60 70 80 90
Distance (m)
m/s
500
450
400
350
300
250
200
150
100
W
E
S2:99 m²
0 10 20 30 40 50 60 70
Distance (m)
W
E
0
-5
-10
-15
-20
Former creek
S3:47 m²
0 5 10 15 20 25 30 35 40 45
Distance (m)
E
W
S4:75 m²
0 5 10 15 20 25 30 35 40 45
Distance (m)

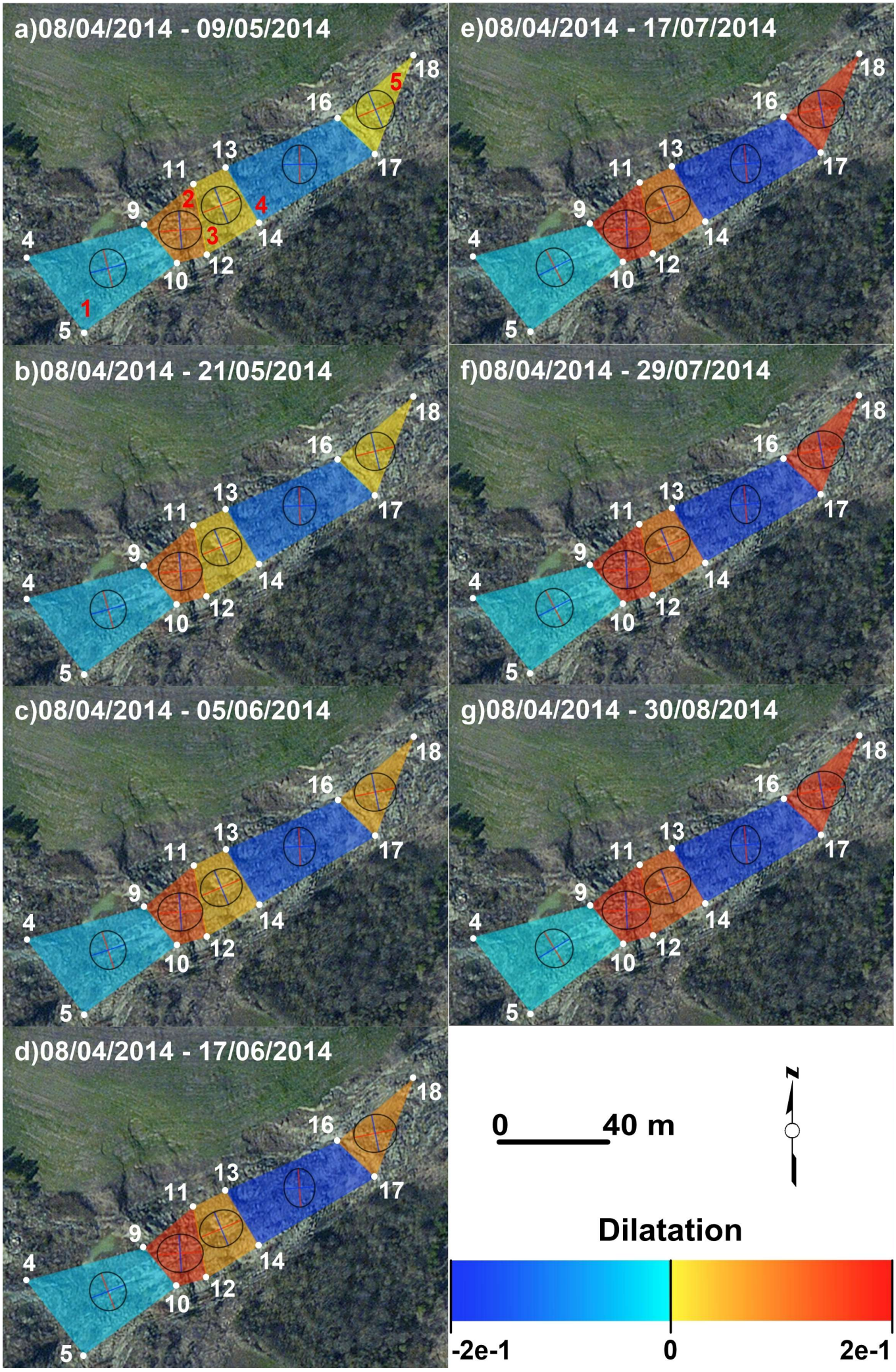
a)08/04/2014 - 09/05/2014
b)08/04/2014 - 21/05/2014
c)08/04/2014 - 05/06/2014
d)08/04/2014 - 17/06/2014
e)08/04/2014 - 17/07/2014
f)08/04/2014 - 29/07/2014
g)08/04/2014 - 30/08/2014
1
2
3
4
5
4
5
9
10
11
12
13
14
16
17
18
0
40 m
N
Dilatation
-2e-1
0
2e-1

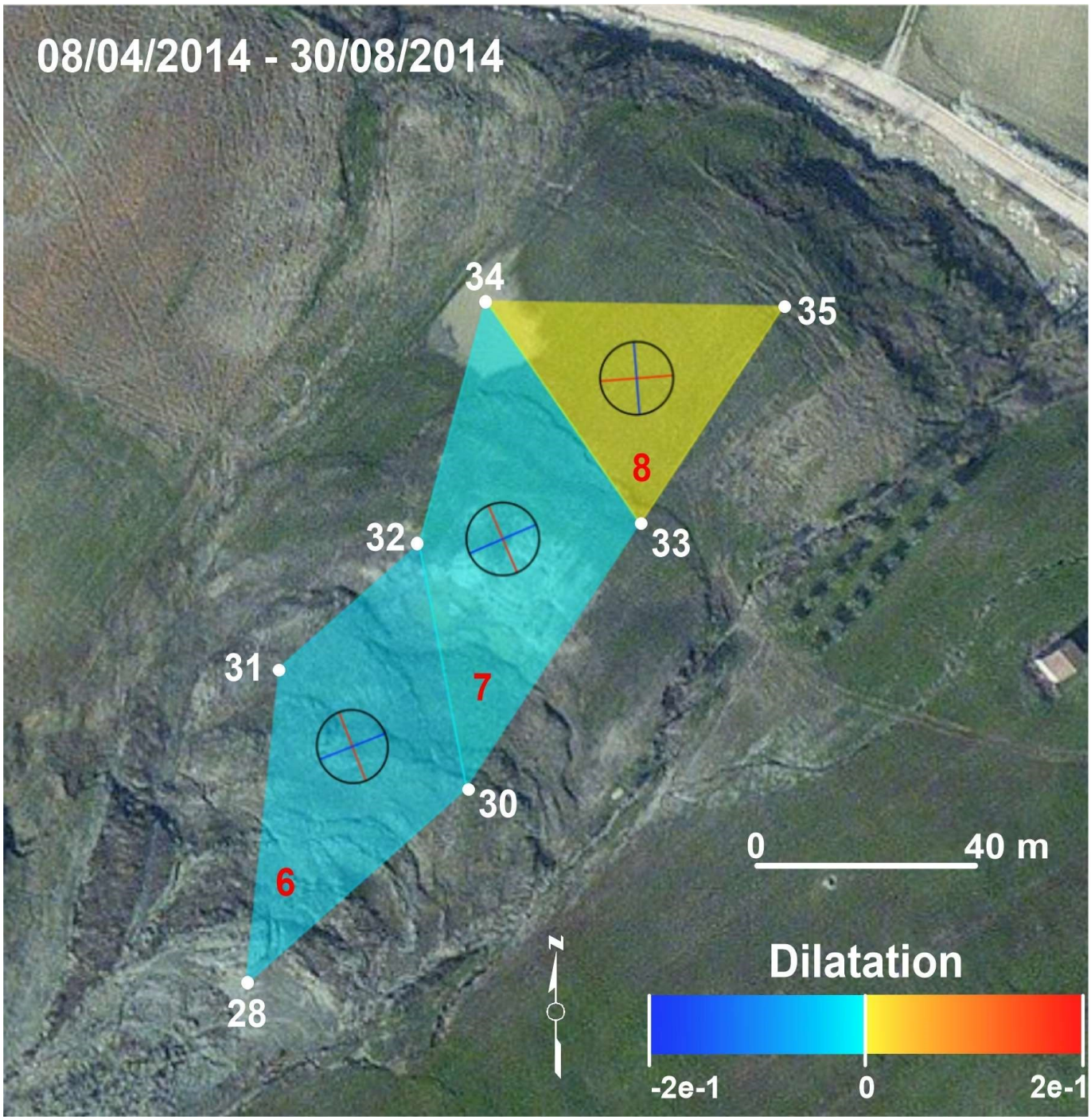
08/04/2014 - 30/08/2014
34
35
8
32
33
31
7
30
6
28
0
40 m
N
Dilatation
-2e-1
0
2e-1

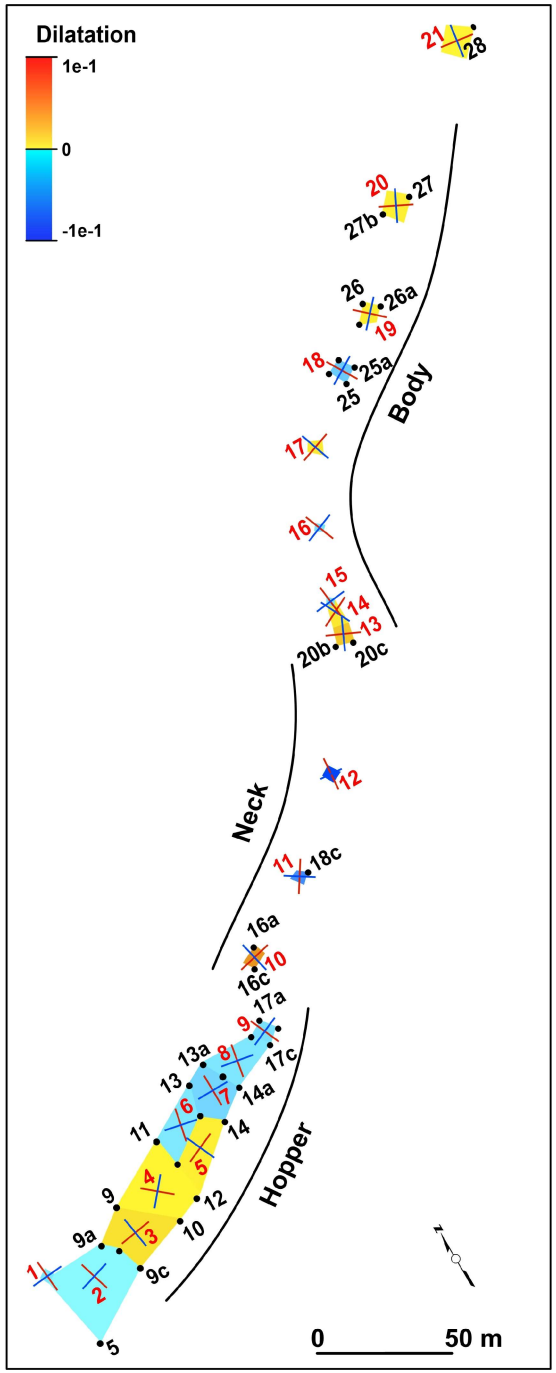
Dilatation
1e-1
0
-1e-1
Body
Neck
Hopper
0
50 m
N

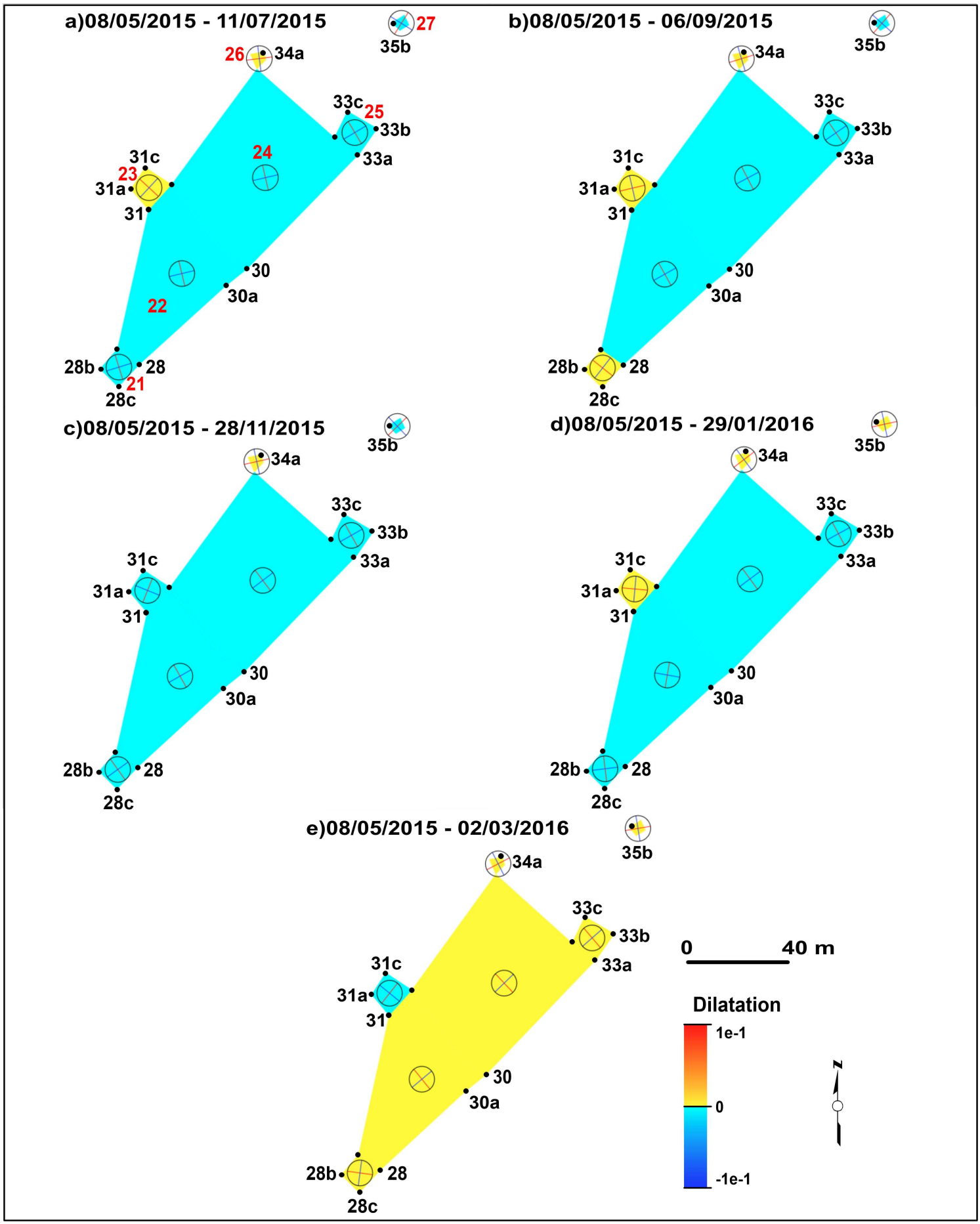
a)08/05/2015 - 11/07/2015
b)08/05/2015 - 06/09/2015
c)08/05/2015 - 28/11/2015
d)08/05/2015 - 29/01/2016
e)08/05/2015 - 02/03/2016
35b
27
26
34a
33c
25
33b
33a
31c
24
23
31a
31
30
30a
22
28b
28
21
28c
0
40 m
Dilatation
1e-1
0
-1e-1
N

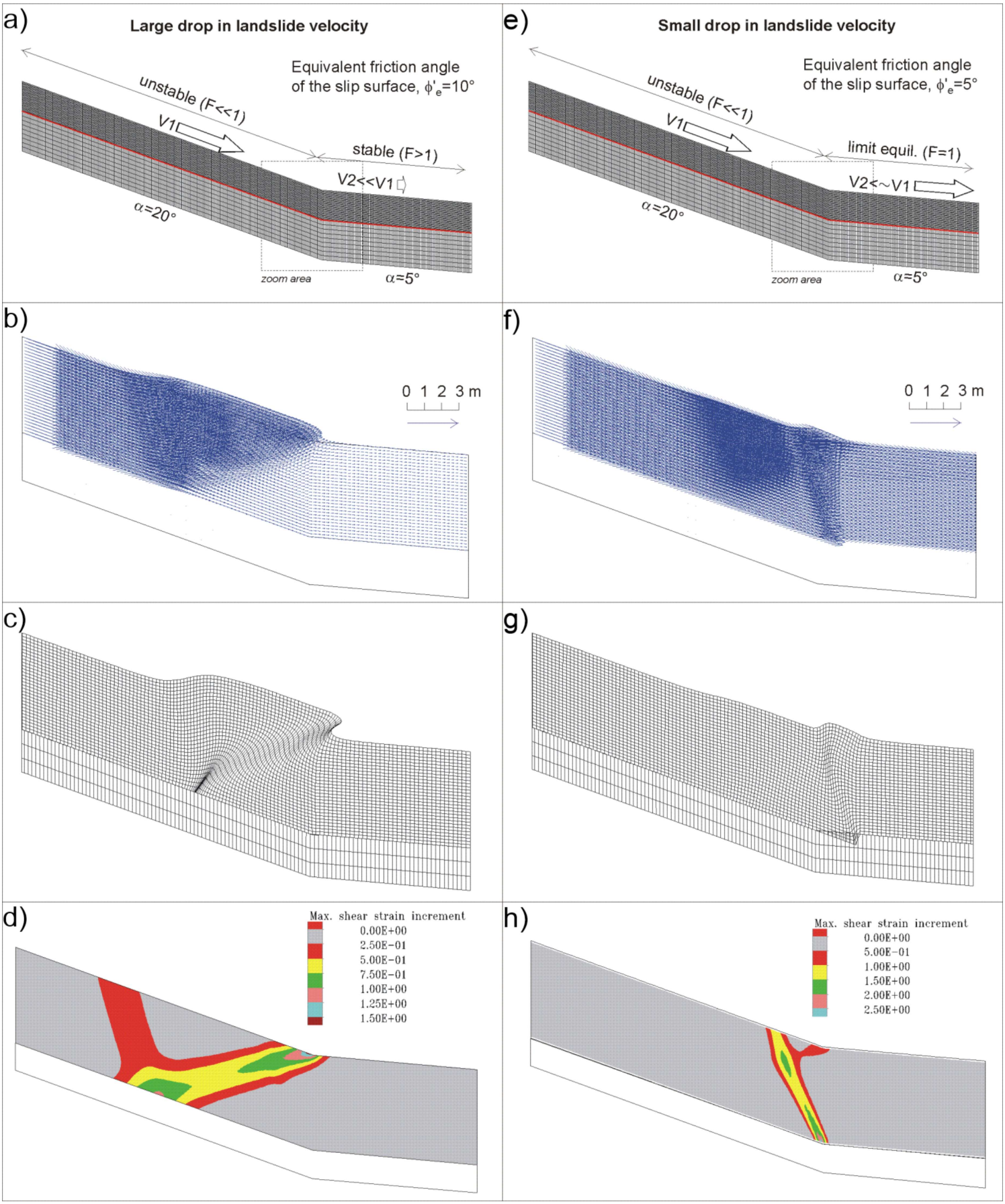
a)
Large drop in landslide velocity
Equivalent friction angle of the slip surface, ϕ'e=10°
unstable (F<<1)
V1
stable (F>1)
V2<<V1
α=20°
zoom area
α=5°
e)
Small drop in landslide velocity
Equivalent friction angle of the slip surface, ϕ'e=5°
unstable (F<<1)
V1
limit equil. (F=1)
V2<~V1
α=20°
zoom area
α=5°
b)
0 1 2 3 m
f)
0 1 2 3 m
c)
g)
d)
Max. shear strain increment
0.00E+00
2.50E-01
5.00E-01
7.50E-01
1.00E+00
1.25E+00
1.50E+00
h)
Max. shear strain increment
0.00E+00
5.00E-01
1.00E+00
1.50E+00
2.00E+00
2.50E+00

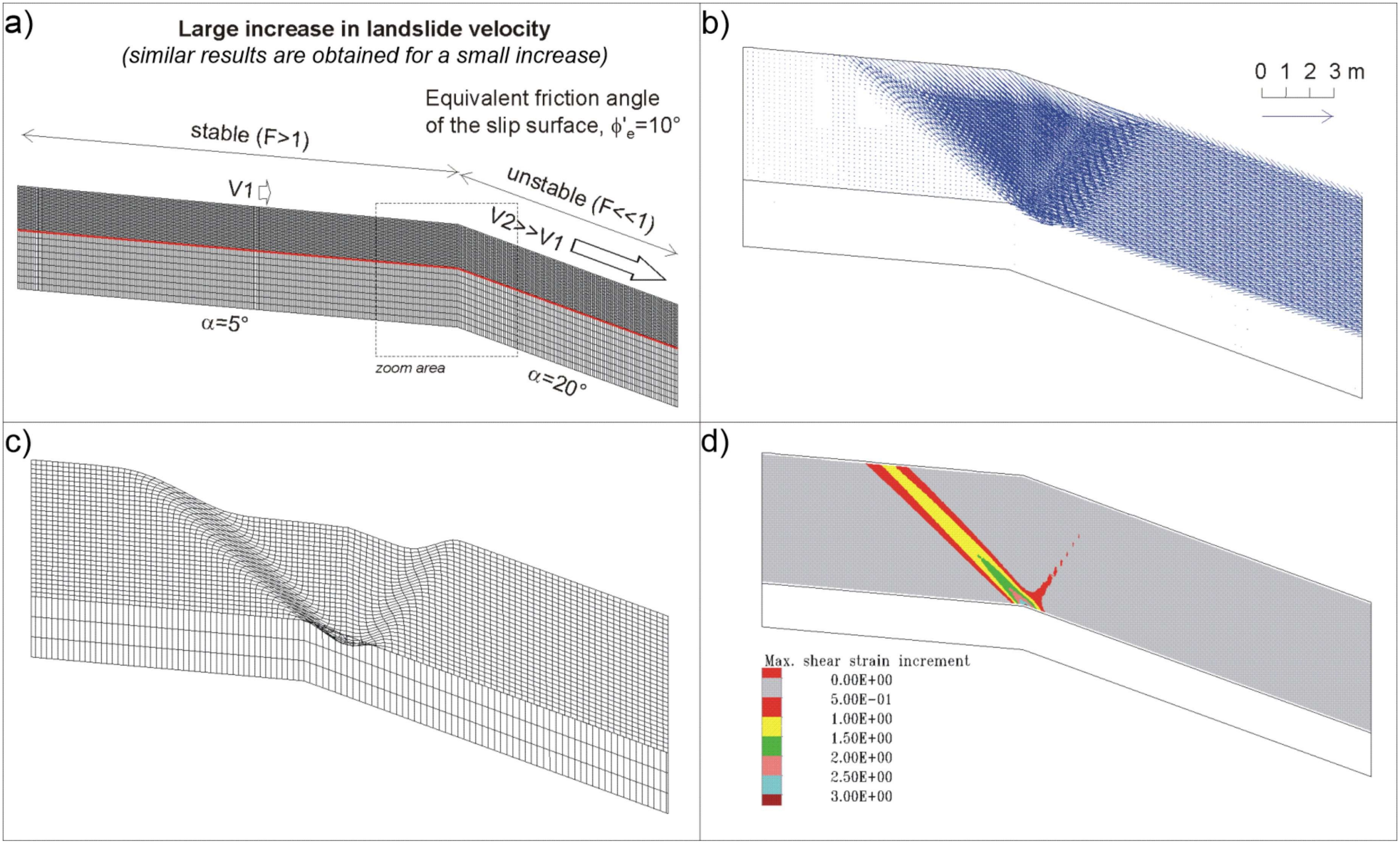
a)
Large increase in landslide velocity
(similar results are obtained for a small increase)
Equivalent friction angle
of the slip surface, ϕ'_e=10°
stable (F>1)
unstable (F<<1)
V1
V2>>V1
α=5°
zoom area
α=20°
b)
0 1 2 3 m
c)
d)
Max. shear strain increment
0.00E+00
5.00E-01
1.00E+00
1.50E+00
2.00E+00
2.50E+00
3.00E+00

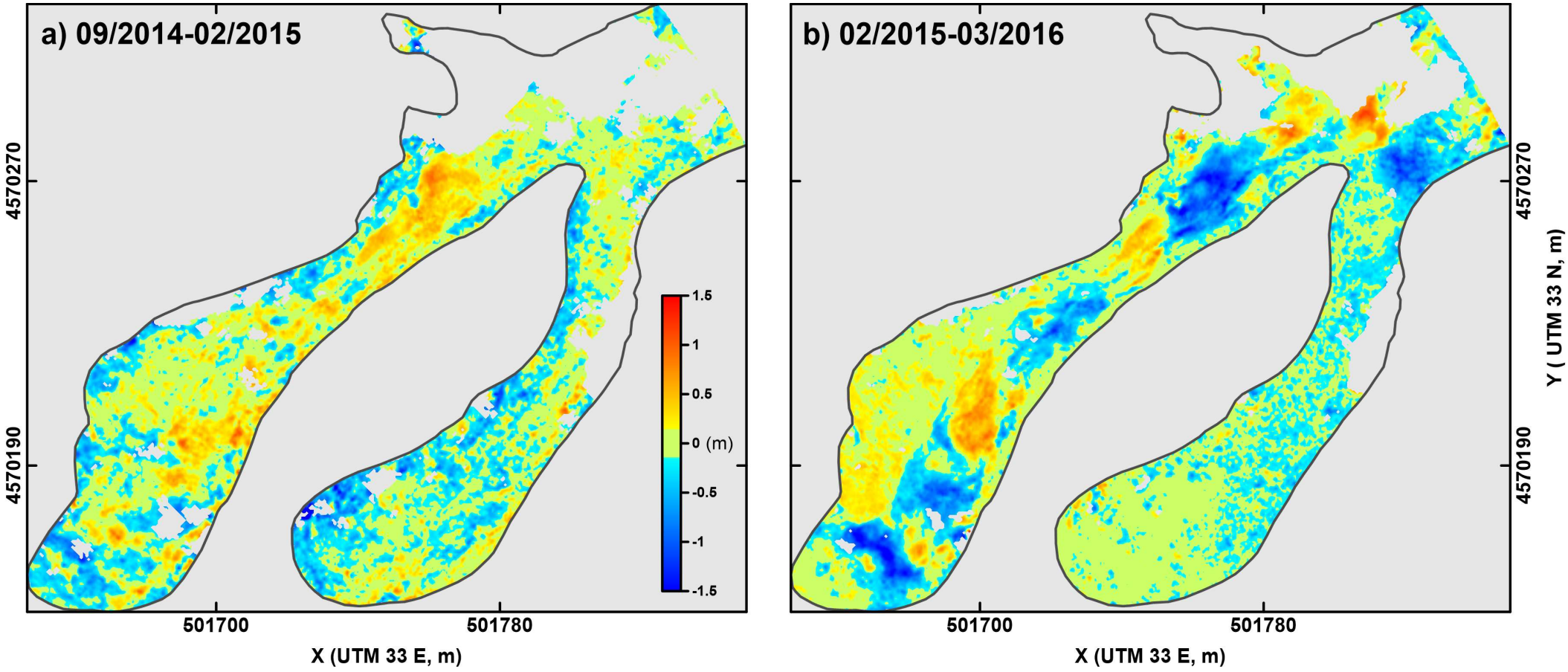
a) 09/2014-02/2015
b) 02/2015-03/2016
4570270
4570190
501700
501780
X (UTM 33 E, m)
Y (UTM 33 N, m)
1.5
1
0.5
0 (m)
-0.5
-1
-1.5

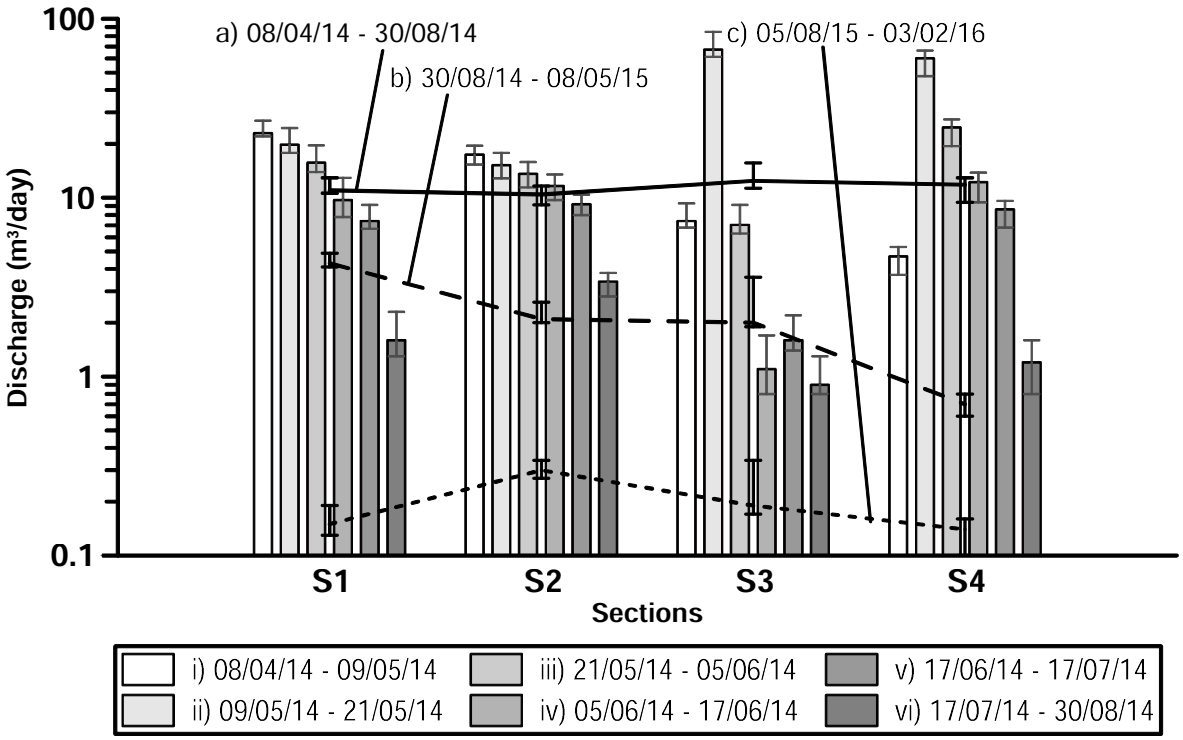
100
10
1
0.1
Discharge (m³/day)
a) 08/04/14 - 30/08/14
b) 30/08/14 - 08/05/15
c) 05/08/15 - 03/02/16
S1
S2
S3
S4
Sections
i) 08/04/14 - 09/05/14
ii) 09/05/14 - 21/05/14
iii) 21/05/14 - 05/06/14
iv) 05/06/14 - 17/06/14
v) 17/06/14 - 17/07/14
vi) 17/07/14 - 30/08/14


4 m

Table 1. RTK-GPS surveys and associated horizontal (h) and 3D root mean square (RMS) errors. Dark grey cells indicate surveys completed with the Leica device. Light grey cells indicate surveys completed with the Geomax device.

ID	Date (d/m/y)	Days	Min h RMS (mm)	Max h RMS (mm)	Avg h RMS (mm)	Min 3D RMS (mm)	Max 3D RMS (mm)	Avg 3D RMS (mm)
1	08/04/14		7	16	12	14	36	26
2	09/05/14	31	20	90	40	30	120	70
3	21/05/14	12	20	90	50	30	160	70
4	05/06/14	15	20	100	40	30	130	70
5	17/06/14	12	20	90	30	30	140	60
6	17/07/14	30	20	80	30	20	110	50
7	29/07/14	12	20	70	40	30	110	60
8	30/08/14	32	20	130	50	30	140	70
9	25/10/14	56	20	60	40	30	90	60
10	19/12/14	55	20	50	40	30	90	70
11	20/02/15	63	20	80	40	30	100	70
12	08/05/15	77	7	16	11	15	32	23
13	11/07/15	64	8	18	11	14	30	22
14	06/09/15	57	10	18	14	21	38	27
15	28/11/15	83	9	19	12	17	36	24
16	29/01/16	62	7	17	11	15	34	23
17	02/03/16	33	8	18	12	16	37	23

Table 2. Connectivity, positions and dilatation of polygons for the period April 8-August 30, 2014.

ID	Connectivity	Position	Dilatation (between Gps surveys, e.g. 1-2 of Table 1)						
			1-2	1-3	1-4	1-5	1-6	1-7	1-8
1	4, 5, 10, 9	He/Hop	-4.25E-2	-5.46E-2	-5.29E-2	-4.29E-2	-2.57E-2	-2.34E-2	-1.30E-2
2	9, 10, 12, 11	Hopper	1.14E-1	1.37E-1	1.62E-1	1.91E-1	2.31E-1	2.38E-1	2.60E-1
3	11, 12, 14, 13	Hopper	3.59E-2	4.77E-2	6.96E-2	9.24E-2	1.26E-1	1.29E-1	1.54E-1
4	13, 14, 17, 16	Hopper	-1.06E-1	-1.40E-1	-1.68E-1	-1.89E-1	-2.09E-1	-2.09E-1	-2.17E-1
5	16, 17, 18	Hop/Ne	7.48E-3	3.53E-2	8.18E-2	1.08E-1	1.93E-1	2.05E-1	2.38E-1
6	28, 30, 32, 31	Toe							-2.44E-2
7	30, 32, 34, 33	Toe							-1.59E-3
8	34, 33, 35	Toe							2.05E-3

Table 3. Connectivity, positions and dilatation of polygons for the period May 8, 2015-March 2, 2016.

ID	Connectivity	Position	Dilatation (between Gps surveys, e.g. 12-13 of Table 1)				
			12-13	12-14	12-15	12-16	12-17
1	4, 4a, 4b, 4c	Head	-1.18E-2	-8.74E-3	-2.56E-2	-1.69E-2	-1.07E-2
2	4a, 4, 9a, 9b, 9c, 5	Head/Hopper	-9.71E-4	-1.37E-3	-9.28E-4	-1.48E-3	-2.02E-3
3	9, 9a, 9b, 9c, 10, 10a	Hopper	1.08E-2	9.96E-3	9.28E-3	9.96E-3	1.03E-2
4	9, 10a, 10, 12, 11a, 11, 9	Hopper	4.12E-3	2.38E-3	2.21E-3	1.21E-3	1.57E-3
5	11a, 12, 14, 15	Hopper	2.60E-3	5.63E-3	4.00E-3	4.43E-3	3.71E-3
6	11, 11a, 15, 13	Hopper	-6.52E-3	-6.13E-3	-7.38E-3	-9.09E-3	-1.06E-2
7	13, 15, 14, 14a, 15a, 13a	Hopper	-1.55E-2	-1.76E-2	-1.76E-2	-1.88E-2	-1.97E-2
8	13a, 15a, 14a, 17c, 17b	Hopper	-1.09E-2	-1.15E-2	-1.17E-2	-1.03E-2	-1.11E-2
9	17c, 17b, 17a, 17	Hopper/Neck	-1.55E-2	-1.52E-2	-1.75E-2	-1.79E-2	-1.48E-2
10	16c, 16b, 16a, 16	Neck	2.26E-2	3.62E-2	4.18E-2	4.49E-2	4.64E-2
11	18, 18a, 18c, 18b	Neck	-4.59E-2	-4.95E-2	-5.45E-2	-5.18E-2	-5.60E-2
12	19c, 19b, 19a, 19	Neck	-2.88E-1	-3.06E-1	-3.02E-1	-3.09E-1	-3.13E-1
13	20c, 20b, 20a, 20	Neck	1.72E-2	1.81E-2	2.84E-2	2.37E-2	2.44E-2
14	20a, 20, 21a, 21, 22a	Neck/Body	3.49E-3	3.52E-3	1.36E-2	9.73E-3	7.26E-3
15	21, 21a, 22, 22a	Body	-4.46E-3	2.12E-3	-2.37E-3	-3.70E-3	-1.58E-2
16	23b, 23c, 23, 23a	Body	-1.19E-2	-1.08E-2	-1.77E-2	-1.40E-2	-1.51E-2
17	24c, 24b, 24a, 24	Body	1.38E-3	4.00E-3	6.98E-3	5.70E-3	6.48E-3
18	25, 25c, 25b, 25a	Body	-1.04E-2	-1.08E-2	-3.72E-3	-1.28E-2	-2.52E-2
19	26b, 26c, 26, 26a	Body	7.24E-3	6.32E-3	1.00E-2	5.89E-3	5.11E-3
20	27c, 27b, 27a, 27	Body	2.01E-2	2.13E-2	1.89E-2	3.95E-3	4.00E-3
21	28c, 28b, 28a, 28	Toe	-9.96E-4	-3.44E-4	7.67E-4	-2.13E-3	1.44E-3
22	28a, 28, 30a, 30, 30c, 31b, 31	Toe	-6.02E-4	-3.16E-4	-4.79E-4	-4.96E-4	2.03E-5
23	31, 31a, 31c, 31b	Toe	4.35E-4	-1.41E-4	1.51E-3	1.21E-3	-2.81E-4
24	31b, 30c, 30, 33a, 33, 34d	Toe	-2.61E-4	-3.30E-5	-3.40E-4	-1.89E-5	1.53E-4
25	33, 33a, 33b, 33c	Toe	-1.05E-3	-1.17E-3	-5.89E-4	-1.11E-3	2.58E-4

26	34d, 34c, 34a, 34b	Toe	2.83E-3	2.52E-3	4.06E-3	1.47E-4	2.75E-3
27	35c, 35b, 35a, 35	Toe	-2.80E-3	-9.85E-4	-1.86E-3	9.66E-4	3.35E-3

Table 4. Material parameters of the mechanical models (Fig. 10) and their values.

Parameter	Earth flow	Bedrock	Slip surface
Plastic limit	20	\	\
Plastic index	20	\	\
Sat. Hydraulic conductivity (m/s)	2.2E-5	\	\
Density, ρ (kg/m³)	2000	2200	\
Young modulus, E (MPa)	5	50	\
Poisson coefficient, ν	0.3	0.3	\
Effective friction angle, ϕ′ (°)	25	\	\
Effective cohesion, c′ (kPa)	0	\	0
Normal stiffness, kn (Pa/m)	\	\	2E8
Shear stiffness, ks (Pa/m)	\	\	2E8
Equivalent friction angle, ϕ'e (°)	\	\	5-10

Table 5. Maximum and minimum horizontal displacement and velocity, and vertical displacement for each kinematic zone (see also Fig. 11 and Supplementary material).

Zone	Max h. disp. (m), point id	Min h. disp. (m), point id	Max h. vel. (cm/day), point id	Min h. vel. (cm/day), point id	Max v. disp. (m), point id	Min v. disp. (m), point id
head (n. b.)	70 @ 2	25 @ 4	10 @ 2	4 @ 4	-22.7 @ 2	-5.4 @ 4
head (s. b.)	11 @ 7	4 @ 6	1.5 @ 7	0.6 @ 6	-4 @ 7	-0.5 @ 6
hopper	34 @ 13	15 @ 9	4.8 @ 13	2.1 @ 9	-10.1 @ 13	-1.8 @ 17
neck	97 @ 20	40 @ 18	14 @ 20	5.7 @ 18	-23 @ 20	-8.2 @ 18

body	65 @ 25	45 @ 27	9.3 @ 25	6.4 @ 27	-14.5 @ 25	6.2 @ 27
toe	5 @ 28	0.7 @ 33	0.7 @ 28	0.1 @ 33	-0.4 @ 35	-0.1 @ 29, 32, 33, 34

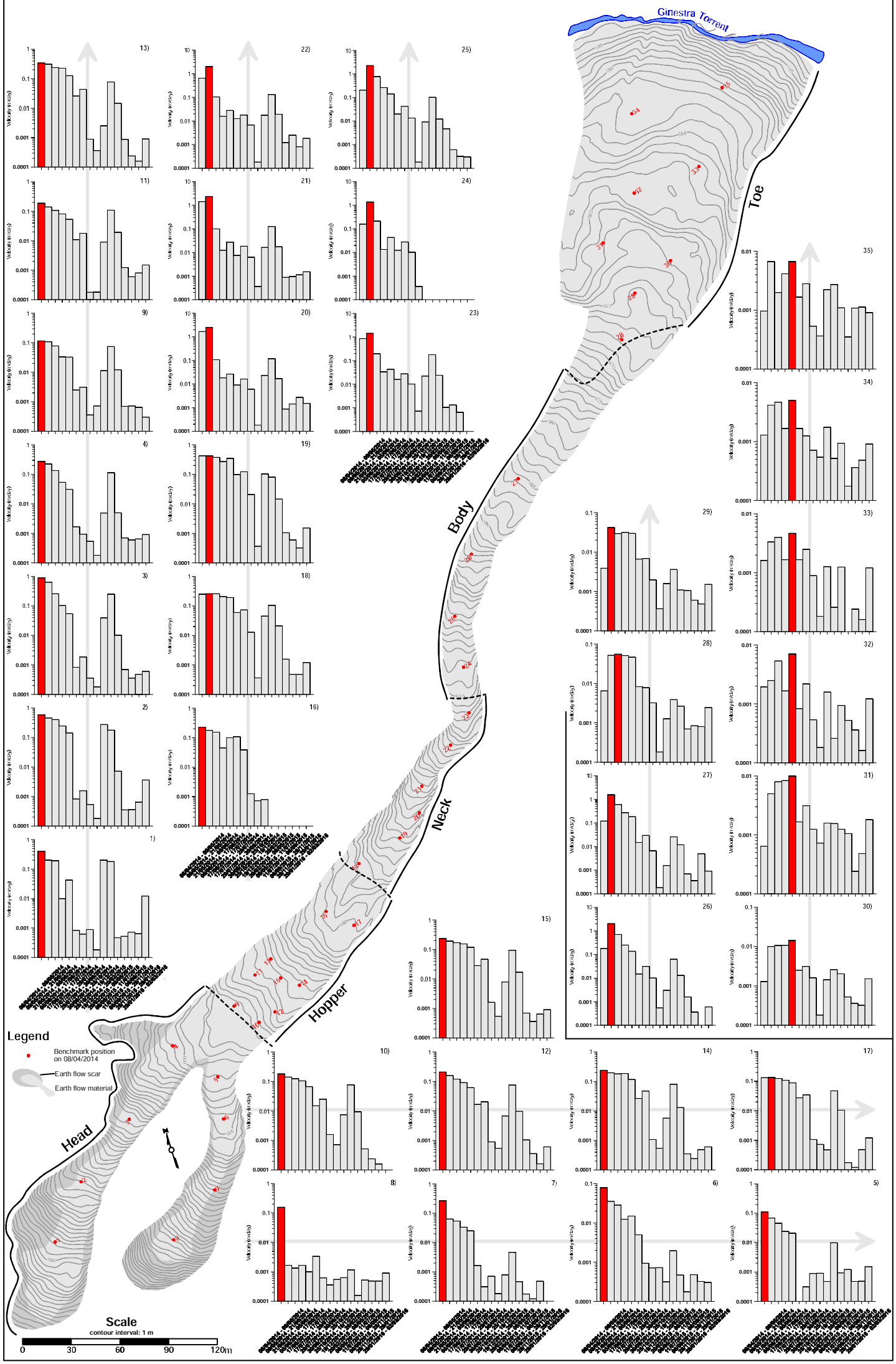
Ginestra Torrent
Toe
Body
Neck
Hopper
Head
Legend
Benchmark position on 08/04/2014
Earth flow scar
Earth flow material
Scale
contour interval: 1 m
0
30
60
90
120m
Velocity (m/day)

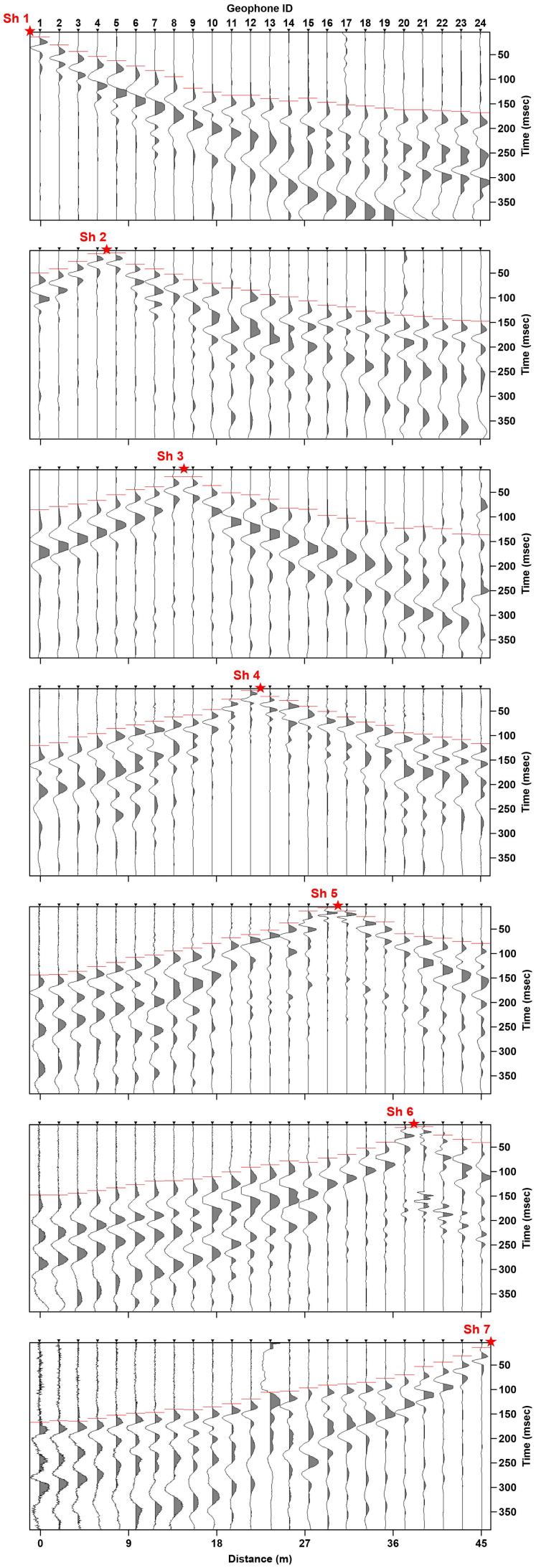
Geophone ID
1 2 3 4 5 6 7 8 9 10 11 12 13 14 15 16 17 18 19 20 21 22 23 24
Sh 1
Sh 2
Sh 3
Sh 4
Sh 5
Sh 6
Sh 7
50 100 150 200 250 300 350
Time (msec)
0 9 18 27 36 45
Distance (m)

PAPER 4

A surface seismic approach to liquefaction

Castellaro S., Panzeri R., Mesiti F., Bertello L.

***published in **Soil Dynamics and Earthquake Engineering,** April 2015

Soil Dynamics and Earthquake Engineering 77 (2015) 35–46

Contents lists available at ScienceDirect

Soil Dynamics and Earthquake Engineering

journal homepage: www.elsevier.com/locate/soildyn

A surface seismic approach to liquefaction

Silvia Castellaro [a,*], Riccardo Panzeri [b], Flaminia Mesiti [b], Lara Bertello [c]

[a] Dipartimento di Fisica e Astronomia, Università di Bologna, viale C.B. Pichat 8, 40127 Bologna, Italy
[b] Geologists in Bologna, Italy
[c] Dipartimento di Biologia, Geologia e Ambiente, Università di Bologna, Italy

ARTICLE INFO

Article history:
Received 26 August 2014
Received in revised form
20 February 2015
Accepted 27 April 2015

ABSTRACT

The liquefaction potential of soils is traditionally assessed through geotechnical approaches based on the calculation of the cyclical stress ratio (CSR) induced by the expected earthquake and the 'resistance' provided by the soil, which is quantified through standard penetration (SPT), cone penetration (CPT), or similar tests. In more recent years, attempts to assess the liquefaction potential have also been made through measurement of shear wave velocity (V_S) in boreholes or from the surface. The latter approach has the advantage of being non-invasive and low cost and of surveying lines rather than single points. However, the resolution of seismic surface techniques is lower than that of borehole techniques and it is still debated whether it is sufficient to assess the liquefaction potential.

In this paper we focus our attention on surface seismic techniques (specifically the popular passive and active seismic techniques based on the correlation of surface waves such as ReMi^{TM}, MASW, ESAC, SSAP, etc.) and explore their performance in assessing the liquefaction susceptibility of soils. The experimental dataset is provided by the two main seismic events of M_L=5.9 and 5.8 (M_W=6.1, M_W=6.0) that struck the Emilia-Romagna region (Northern Italy) on May 20 and 29, 2012, after which extensive liquefaction phenomena were documented in an area of 1200 km^2.

The CPT and drillings available in the area allow us to classify the soils into four classes: A) shallow liquefied sandy soils, B) shallow non-liquefied sandy soils, C) deep non-liquefied sandy soils, and D) clayey–silty soils, and to determine that on average class A soils presented a higher sand content at the depth of 5–8 m compared to class B soils, where sand was dominant in the upper 5 m. Surface wave active–passive surveys were performed at 84 sites, and it was found that they were capable of discriminating among only three soil classes, since class A and B soils showed exactly the same V_S distribution, and it is possible to show both experimentally and theoretically that they appear not to have sufficient resolution to address the seismic liquefaction issue.

As a last step, we applied the state-of-the art CSR–V_S method to assess the liquefaction potential of sandy deposits and we found that it failed in the studied area. This might be due to the insufficient resolution of the surface wave methods in assessing the *Vs* of thin layers and to the fact that *Vs* scales with the square root of the shear modulus, which implies an intrinsic lower sensitivity of *Vs* to the shear resistance of the soil compared to parameters traditionally measured with the penetration tests. However, it also emerged that the pure observation of the surface wave dispersion curves at their simplest level (i.e. in the frequency domain, with no inversion) is still potentially informative and can be used to identify the sites where more detailed surveys to assess the liquefaction potential are recommended.

© 2015 Elsevier Ltd. All rights reserved.

1. Introduction

Assessing the liquefaction potential at a site is a goal traditionally achieved through geotechnical approaches based on the grain size distribution [29] or on CPT and SPT (cone penetration and standard penetration tests), as described by Iwasaki et al. [11] and several other authors (e.g. [30,17,10,25]). These methods are based on the calculation of the cyclical stress ratio (CSR) induced by the expected earthquake at the depth of the potentially liquefiable deposit and the 'resistance' provided by the deposit, quantified through the CPT or SPT. The geotechnical approaches are certainly the most explored, used, and reliable ones since they provide direct quantitative information about some mechanical properties of the soil column. However, they have the disadvantage of

* Corresponding author.
E-mail address: silvia.castellaro@unibo.it (S. Castellaro).

http://dx.doi.org/10.1016/j.soildyn.2015.04.023
0267-7261/© 2015 Elsevier Ltd. All rights reserved.

providing only point information and of being invasive and inapplicable to gravelly soils, where liquefaction has sometimes been documented [15]. Parallel to the geotechnical ones, geophysical approaches have also developed and traditionally exploited the measurement of shear wave velocity V_S (because V_S is linked to the shear modulus of the soil, $\mu = \rho V_S^2$, where ρ is the density) in boreholes [12] or in laboratory samples [31] but at the expense of having the same limitations as CPT and SPT, that is, providing just point information, and being more expensive.

Surface multichannel geophysical methods like those relying on the dispersion of surface waves to retrieve V_S profiles would be ideal in principle, since they are spatially distributed and not invasive and can be used on any soil type. One example of this approach was presented by [15]. Seismic surface methods are however much less sensitive to the stiffness variation of soil with depth compared to the classical geotechnical methods for physical reasons: first, the depth of investigation is proportional to the 'exploring' wavelength but large wavelengths (i.e. large depths of investigation) are sensitive only to reflectors of comparable size; second, while the penetration parameters (sleeve friction or tip resistance) are directly proportional to the soil stiffness μ, V_S is proportional to the square root of μ. Additionally, deriving a V_S profile from the dispersion curve of surface waves is not an easy task and, as the method is indirect and the problem underdetermined, it does not have a unique solution.

Other surface methods like seismic refraction share the same limitations as surface-wave based methods but, additionally, provide biased results in the presence of velocity inversions (i.e. stiffer soils overlying softer soils) and have a much lower penetration, and, since the detection of the arrival time of the S-wave is not straightforward, a degree of inaccuracy in the assessment of the V_S profile is still unavoidable. The results of an 11-year international project to gather new V_S data and develop state-of-the-art probabilistic CSR–V_S correlations for the occurrence of seismic soil liquefaction were presented by Kayen et al. [13]. The new V_S soil profiles, mostly derived from the SASW (Spectral Analysis of Surface Waves) method [20], were collected mainly in Japan (213), with a minority being collected in California (39), China (24), Taiwan (14), Alaska (9), and Greece (2).

In this paper we focus on the 'descendants' of the SASW technique, exploring their applicability within the method proposed by Kayen et al. [13] to the Italian case and examining whether different geophysical approaches are possible to assess the liquefaction susceptibility of a soil.

Our dataset is provided by the May 20 and 29, 2012 earthquakes ($M_L = 5.9$ and $M_L = 5.8$, respectively) that occurred in the Po Plain area (Northern Italy), which caused a large number of liquefaction phenomena over an area extending up to 30 km from the epicenters. Detailed maps of the liquefaction occurrences have been published, for example, by Bertolini and Fioroni [1], Di Manna et al. [6], Papathanassiou et al. [23], and the Emergeo Working Group [7]. All these studies agreed that liquefaction was controlled by paleo-river beds and out-flow channels and fans of the main rivers, thus occurring on terrains characterized by sandy layers in the upper 10 m (Fig. 1).

2. Data collection

2.1. Site selection

In the area struck by the aforementioned seismic events, we focus on 84 sites (Fig. 2). Relying on 121 available penetration tests and drillings (Regional Geological database, http://ambiente.regione.emilia-romagna.it/geologia/), on the evidence from a wide set of aerial pictures (courtesy of G. Bertolini), and on the available geomorphological-depositional maps (Fig. 2), we group the 84 surveyed sites into four classes as described in Table 1 (in all cases the depth of the water table was within 3 m; in the majority of cases, within 1.5 m). These classes can be considered representative of the depositional environments of the entire area affected from the earthquake. Class A and B sites include shallow (< 8 m) sandy soil with liquefaction potential. At sites labeled A, liquefaction occurred during the 2012 events while at sites labeled B there was no surface evidence of liquefaction. Class C sites are those where sand is present at large depth (> 8 m) and did not exhibit liquefaction. Class D sites are composed of clay and silt, with no liquefaction potential. A closer look to the tip resistance q_C and the sleeve friction f_S of the single penetration tests (Appendix A, Fig. 15) and the average f_S/q_C ratio for the four classes (Fig. 3) reveals that a geotechnical difference exists between soils A and B: in the first case a higher sand content is present between 5 and 7 m depth (which is the level that underwent liquefaction), while in the second case sand is dominant in the upper 4 m.

2.2. Site survey

At the 84 sites we combine the active seismic exploration approach of MASW (Multichannel Analysis of Surface Waves, [24]) and the passive approach of ReMi^{TM}-ESAC-SSAP (Refraction Microtemor^{TM} [16]; Extended Spatial Autocorrelation Method, [22]; Statistical Self-Alignment Property, [19]). The former, which relies on mid-to-high frequency artificial sources, usually provides better results in the high frequency domain, that is, shallow depth. The latter, relying on ambient noise, which is ubiquitous and spans a wider frequency interval, has the theoretical potential to perform well in the mid-to-low frequency domain, that is, mid-to-large depths.

This kind of survey exploits the fact that surface waves of different wavelengths, like those produced by common sources, excite the soil at different depths and travel with the specific velocity that characterizes the soil at the different depths: short wavelengths normally propagate slower (due to the low velocity of the shallow layers) while long wavelengths propagate faster. This property, called dispersion, is a phenomenon strictly related to surface waves. From the seismic signal recorded at different positions (a minimum of two) over time (Fig. 4A), slant-stack and FFT procedures produce the so-called phase/group velocity spectra (Fig. 4B), which indicate the most probable velocity of surface waves at each frequency. From this, a forward or inverse modeling procedure makes it possible to reconstruct a possible V_S model for the surveyed soil (Fig. 4C).

The dispersion of surface waves is a multimodal phenomenon. This implies that in the velocity spectra of Fig. 4B several maxima are possible at the same frequency value, corresponding to different propagation modes of the waves. In the case of an ideal source, ideal receiver geometry, and ideal soil (homogeneous and isotropic half-space), the fundamental mode is dominant in terms of energy, but in real cases this does not always occur. Selecting the dispersion curve of the fundamental mode or correctly sorting the higher modes implies a degree of subjectivity and is not always an easy task [9,28].

The 84 surveys performed in this study were conducted by using twelve 4.5 Hz, vertically polarized geophones (Geospace lp), set at intervals of 2.5 m each, connected to a SoilSpy Rosina acquisition system (Micromed spa), and data were processed by using the software Grilla, written by one of the authors (S.C.). Working with vertically polarized geophones implies that we deal with Rayleigh wave phase velocities (Fig. 4B), which are approximately 10–15% lower than V_S, depending on the Poisson's ratio of the materials.

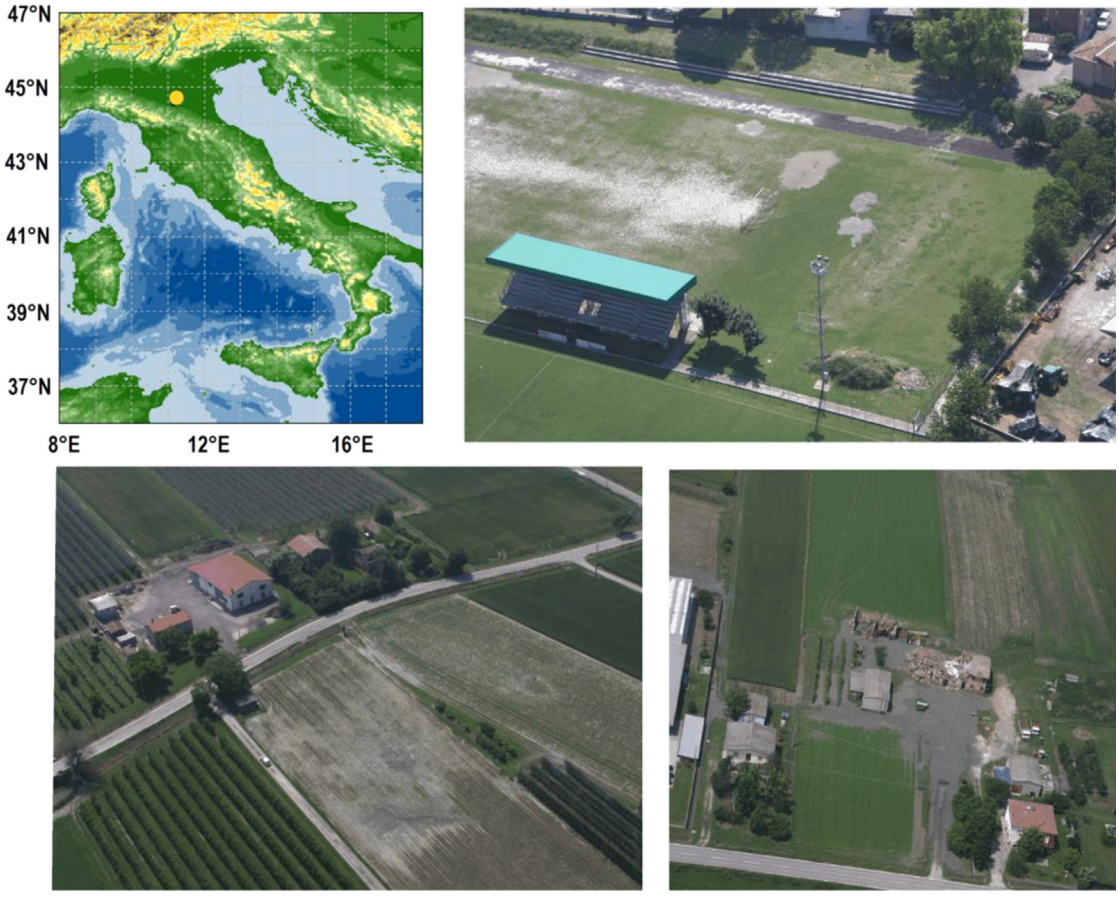

Fig. 1. Examples of soil liquefaction observed after the May 20, 2012, M_L=5.9 earthquake (epicenter indicated by the yellow dot). The aerial pictures are courtesy of G. Bertolini.

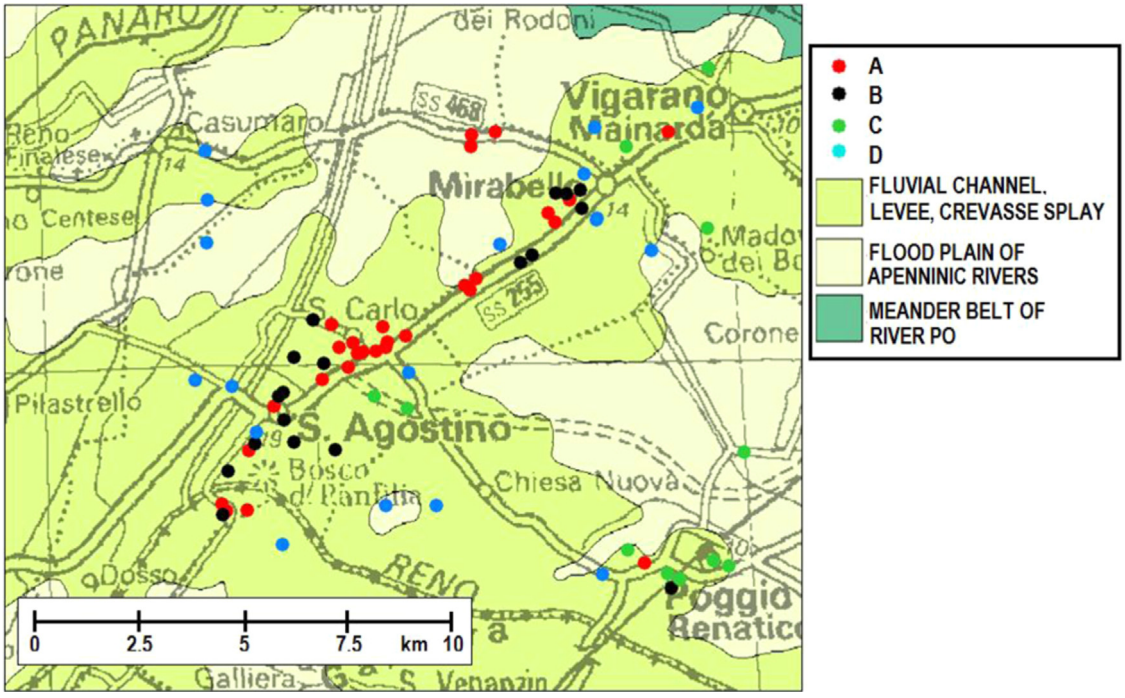

Fig. 2. Location of the seismic surveys performed in the Northern Italian area struck by the 2012 M_L=5.9 and 5.8 earthquakes. The epicenters are located right outside the boundaries of the map, in the northwest direction (Regione Emilia Romagna, geological and topographic regional database).

Table 1
Sedimentological description of the four soil classes.

Soil class	Observed liquefaction	Description [0, 15] m depth	Number of sites
A	Yes	Sands (paleo-river beds, out-flow channels)	28
B	No	Sands (paleo-river beds, out-flow channels)	25
C	No	Shallow clays/silt (<8 m) Deep sands (>8 m)	13
D	No	Clays, silts	18

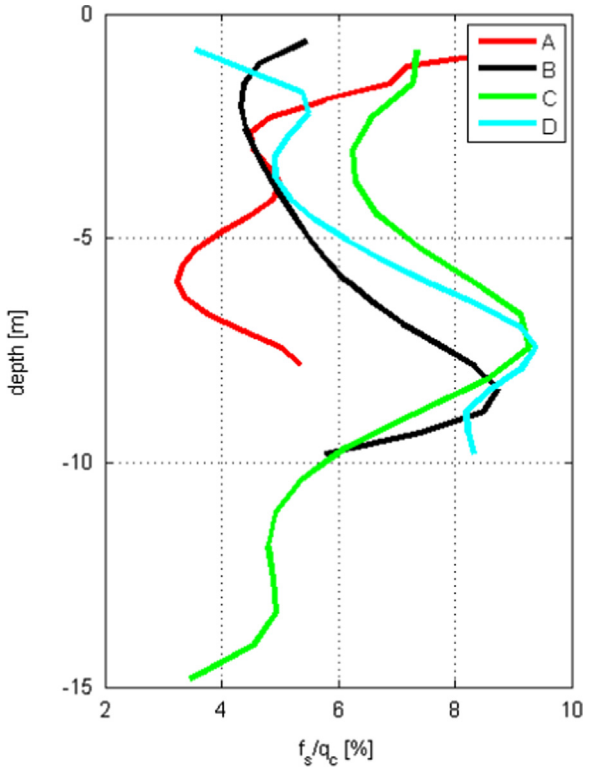

Fig. 3. Average friction ratio (i.e. sleeve friction, f_S, versus tip resistance, q_C) for the four soil classes. The standard deviations can be inferred by looking at the data distribution in the Appendix (Fig. 15). Lower f_S/q_C ratios indicate sandy soils while high ratios indicate silty–clayey soils.

Recalling that a Rayleigh wave induces the maximum displacement at a depth equal to 1/3–1/2 of its wavelength λ (e.g. Chapter 4 in [14,29]), and considering that our surveys show phase velocities V_R ranging between 150 and 250 m/s at $f=4$ Hz (Fig. 5), we get an average wavelength of $\lambda=V_R/f=(150–250)/4=37–62$ m, which stands for a depth of investigation $z_{max}\approx[\lambda/3, \lambda/2]\approx[12, 32]$ m, which is adequate for our task, since liquefaction generally occurs at depths shallower than 15 m and in the present case study it was documented at a depth shallower than 8 m.

The phase velocity spectra collected in this area are all clear and easy to interpret in the [4, 50] Hz frequency range, as can be seen in the examples shown in Fig. 5. This is not always the case. We pick the dispersion curves of the fundamental mode from the phase velocity spectra at the 84 inspected sites, grouping them as per the four soil classes of Table 1. The average dispersion curve plus or minus the standard deviation of each group is shown in Fig. 6. We immediately observe that the geophysical approach is not capable of separating the four soil classes. Class A and B sites, characterized by liquefied and non-liquefied sandy soils, have exactly the same phase velocity distributions, while the CPTs (Fig. 3, Fig. 15 in Appendix A) suggest that some difference exists between these two classes: class A soils are richer in sand between 5 and 7 m depth. This limitation of the adopted seismic surface methods is discussed in the next section.

Class D soils, which are characterized by clay and silt in the first 10 m depth, show significantly lower phase velocity distributions compared to class A and B soils in almost the whole frequency interval considered. Class C soils, characterized by sands at depths larger than 8 m, show phase velocity distributions comparable to class D soils in the high frequency part of the spectra, increasing up to or higher than the distribution of class A and B soils in the low frequency part. This trend is somewhat expected: V_R (and V_S) normally increases from clays to silt to sand in this type of depositional environment. However this is probably the first time that this has been well documented in this part of the Po Plain, to the point that the phase velocity distribution in this geographic area could be used as a proxy for the shallow stratigraphy.

We note that the difference in the V_S values among classes (a few tens of meters per second) appears low compared to the difference in the CPT parameters. This is not surprising if one recalls that that soil stiffness μ is proportional to V_S^2 (and the same relation involving an exponent 2 exists between V_P and other elastic constants and V_R is a function of both V_S and V_P).

The step of moving from the (frequency, V_R) space (Fig. 4B) to the (V_S, depth) space (Fig. 4C), either through forward modeling or inversion procedures, adds uncertainty due to the non-unique inversion process. It is not the aim of this paper to discuss the pitfalls of the inversion procedures, even though a few major points will be highlighted in the following sections. In general we

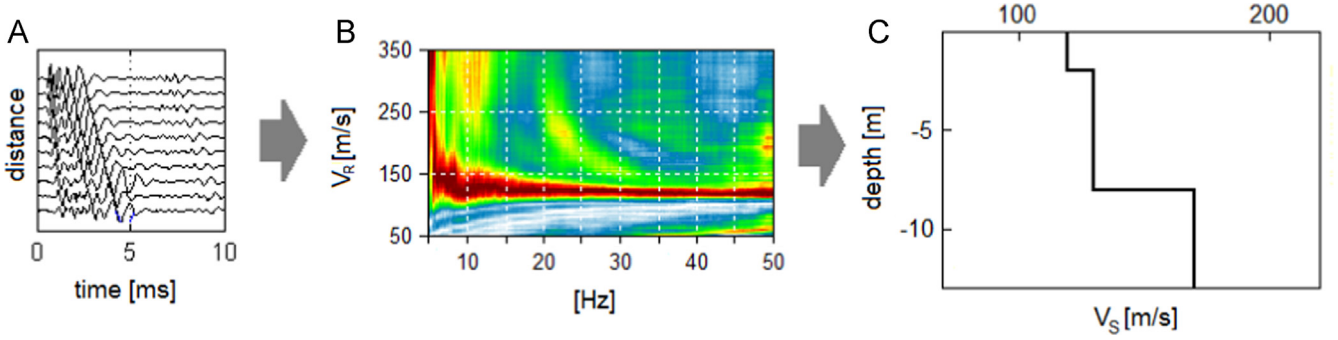

Fig. 4. Workflow of surface-wave based seismic surveys. (A) Time-series recorded from the geophones at increasing distance from the source. The dispersion of surface waves is visible in the enlargement of the 'wave packet'. (B) Rayleigh wave phase velocity spectra. (C) V_S model proposed for the site, whose theoretical dispersion curve fits the dispersion curve properly (i.e. the high energy part of the phase velocity spectra in panel B).

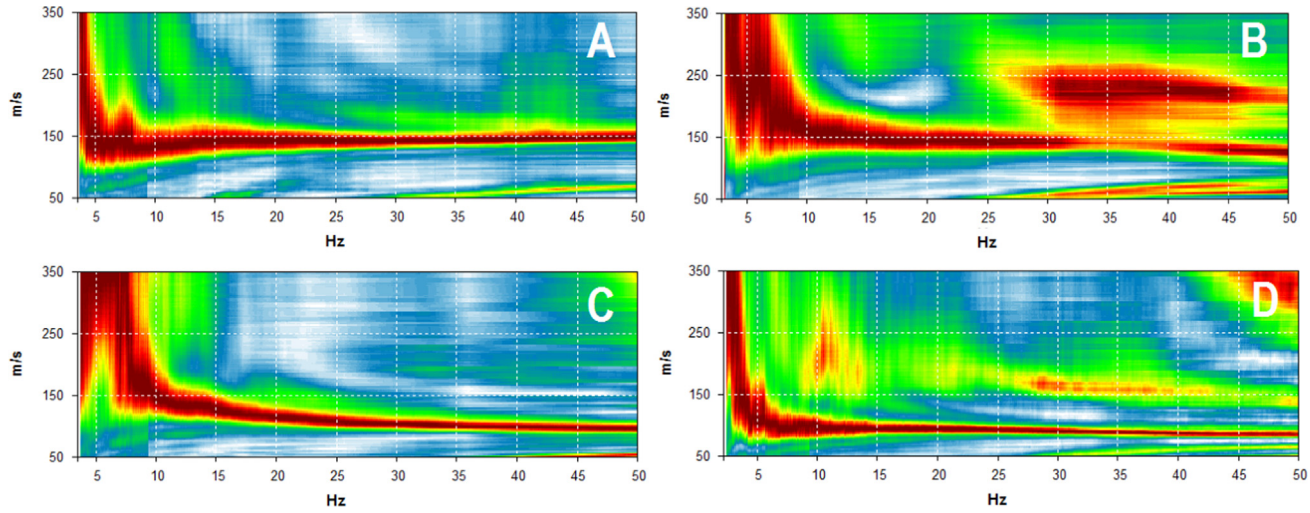

Fig. 5. One example of phase velocity spectra of Rayleigh waves for each soil class in Table 1.

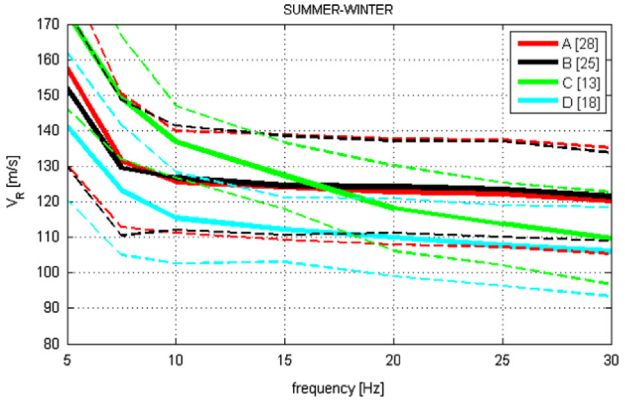

Fig. 6. Dispersion curves (average ± standard deviation) grouped into the four soil classes. The number of curves used to assess the distribution of each soil group is indicated in square brackets in the legend.

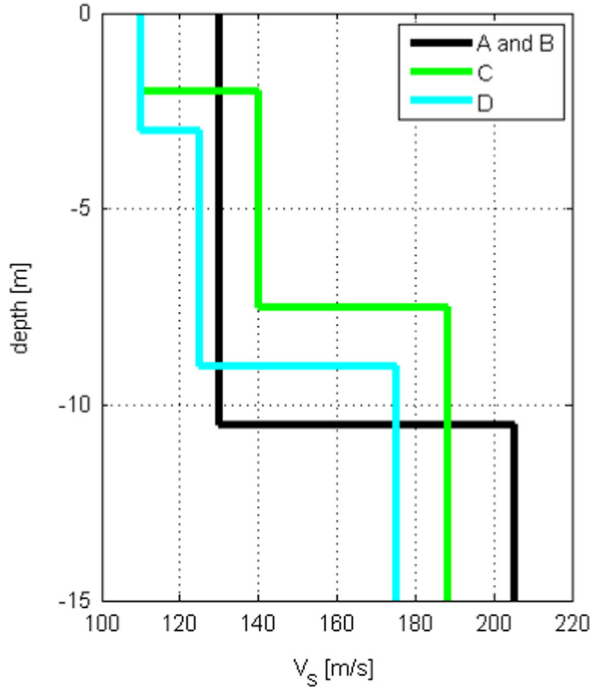

Fig. 7. Typical V_S profiles of each soil class defined in Table 1 as inferred from the average dispersion curve (Fig. 6).

prefer to work directly in the (frequency, V_R) space; however, in Fig. 7 we show the average V_S profiles for the four soil classes derived from the 84 dispersion curves as a general reference.

2.3. Possible biases

Liquefaction is a local phenomenon, linked to buried sand channels and other finite depositional features. Using spatially distributed seismic methods to characterize these geological features, as we did in this study, might introduce some bias. In order to keep this bias to a minimum, we adopted the following precautions:

1) Sites classified as A are sites where liquefaction occurred over large areas (tens of meters). This selection was possible by observing the hundreds of aerial photos (courtesy of G. Bartolini) collected in the first few days after the May 2012 earthquakes.
2) Since the output of any surface-wave based multichannel method (SASW, MASW, ReMi^{TM}, ESAC, SPAC, etc.) is affected by 2D geometries in the subsoil, we kept the array aperture as short as possible in order to ensure the desired depth of investigation (10–15 m) but also to avoid lateral geological heterogeneities. All our arrays are only 27.5 m wide (12 geophones spaced at intervals of 2.5 m each).
3) In active surface-wave based methods (SASW, MASW), a possible way to detect 2D geometries in the subsoil is to compare the dispersion curve obtained by energizing the soil with the same source at the two ends of the array. Even though a difference in the results cannot be unambiguously attributed to heterogeneities in the subsoil (it could be due, for example, to local reflectors/scatterers at one end of the array), obtaining two identical dispersion curves suggests that the subsoil might be treated as a 1D plane–parallel condition. This cross-check was performed at all of the 84 surveyed sites. One example is provided in Fig. 16A and B in Appendix A.
4) A further way to check the 1D plane–parallel assumption for soils is to compare several microtremor H/V recordings acquired along the array line (e.g. [2]). The sensitivity of the H/V technique to stratigraphic layering is discussed in more detail in Section 5 (see also [26]). Here we simply recall that the H/V peaks are proxies for the resonance frequencies of soils, which, in the simplest form, occur at $f = V_S/(4H)$, where H is the thickness of the resonating layer. Since f is also equal to V_S/λ, it follows that the H/V method is more sensitive to the details of

the shallow surface, with the resolution being linked to the wavelength λ, which is directly proportional to H. At all of the 84 surveyed sites we performed three H/V recordings (at ¼, ½, and ¾ of the array line) and compared the H/V curves, checking for possible lateral heterogeneities in the subsoil which would be indicated by peaks (or troughs, [3]) at different frequencies. We applied this method at all of the 84 surveyed sites. One example is provided in Fig. 16 in Appendix A.

When the H/V curves collected at the same site showed significant differences between 4 and 20 Hz (which means at depths shallower that 10 m) and/or did not fulfill the requisites of item 3, we discarded the site and replaced it with a different one.

5) In principle it is possible that liquefaction occurred with no surface evidence at some sites. However, we can exclude liquefaction at sites C and D for sedimentological reasons and the CPT/SPT data available at all sites strongly support the non-occurrence of this phenomenon in class B soils, where sands are too shallow to undergo liquefaction.

A further possible source of bias in this study is the 'time factor'. Liquefaction is a densification process even though the expulsion of solid material from fissures/fractures could generate voids in the subsoil and the accumulation of loose sediment on the surface. The phenomenon is complex and contradictory observations were reported, for example, from the 2010–2011 New Zealand earthquakes where soils re-liquefied [5,8].

The field survey presented in this study was performed from 12 to 18 months after the earthquakes that caused liquefaction. The measurements at class A sites might therefore be biased by having been collected on liquefied (and therefore possibly consolidated) sands. However, Fig. 6 shows that the dispersion curves for class A and B sites are statistically identical in the whole frequency range of interest. This means that they can be traced back to the same V_S profile, even if we know that at 5–7 m depth ([6, 10] Hz), class A soils present liquefied sand while class B soils present clays, which are expected to have a lower V_R–V_S in this depositional environment. This is clearly a limitation of the seismic surface-wave based methods used, as discussed in the next section. In other words, we do not expect the dispersion curves of class A sites to differ significantly from the pre-earthquake conditions, due to the resolution limits of the seismic exploration methods used in this study.

A last possible source of bias is the seasonal variation of the water table depth. This was the reason for repeating the measurements at 25% of the sites, equally distributed between class A and B, in a dry summer (August, 2013) and a rainy winter (February 2014). No significant differences were observed in the V_R values below 10 Hz (i.e., at depths approximately larger than 4 m; see Fig. 17 in Appendix A), which is the depth of interest of the surveyed phenomenon. However the water table depth affects the calculation of the liquefaction potential according to different methods, including the method of Kayen et al. [13] used in this study. The value of this parameter at the time of the earthquakes (May 2012) was known with precision at most surveyed sites from direct data (water wells, drillings). In the few cases in which it could only be extrapolated from water table maps, considering that the earthquakes occurred in spring, which is when the water table is shallow, we used the less conservative values in the calculations.

3. Sensitivity of the dispersion curves

It is intuitively clear that direct methods like cross-hole, down-hole, seismic cone, seismic dilatometer, and so on are potentially capable of providing more accurate V_S profiles (since V_S is physically measured at any desired depth or depth interval) compared to surface methods. However, their accuracy is often overestimated ([18], and references therein) and the fact that they have only point validity is often forgotten.

Surface-wave based methods like those presented in this study are sensitive to the vertical variation of the subsoil in a way which is proportional to the size and depth of the variation. The details of this topic need a separate discussion that will be the subject of a future paper; however, here we outline the main features through some examples.

Let us consider the difference in the sand content between 5 and 7 m depth suggested by the CPT (Fig. 3, Fig. 15 in Appendix A). This makes the difference between class A and B soils from a geotechnical point of view and was responsible for the liquefaction of class A sites. However, this difference cannot be recognized in the surface seismic geophysical tests, which provide exactly the same dispersion curves (Fig. 6).

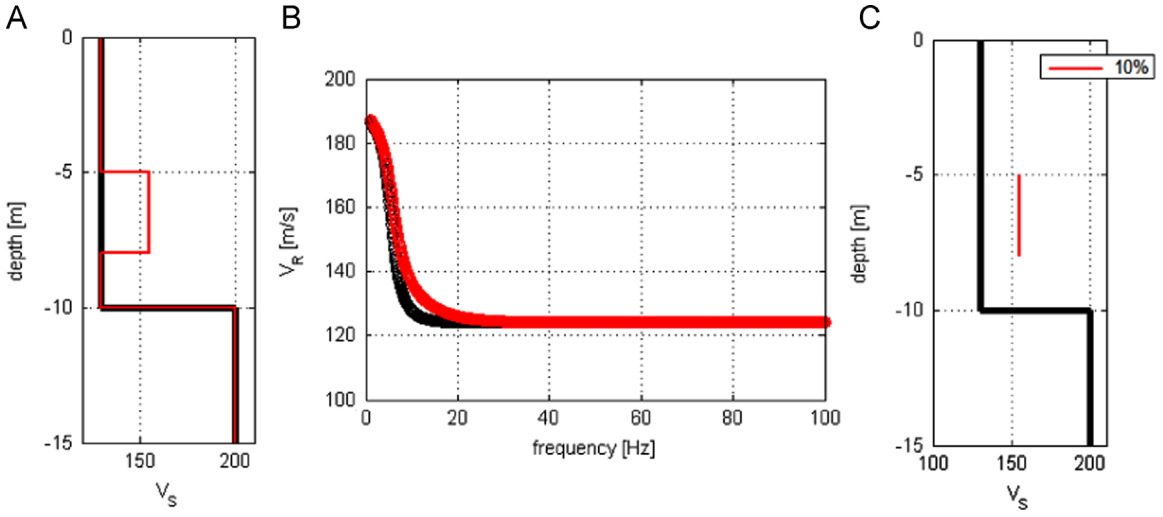

Fig. 8. (A) Initial soil model (black) and modified soil model (red). (B) Theoretical dispersion curves for the two models of panel A. (C) The thickness of the red line is proportional to the maximum percentage change between the dispersion curves of panel B (10% in this case). The position and length of the red line indicate the depth, V_S, and thickness of the layer added to the initial model. (For interpretation of the references to color in this figure legend, the reader is referred to the web version of this article.)

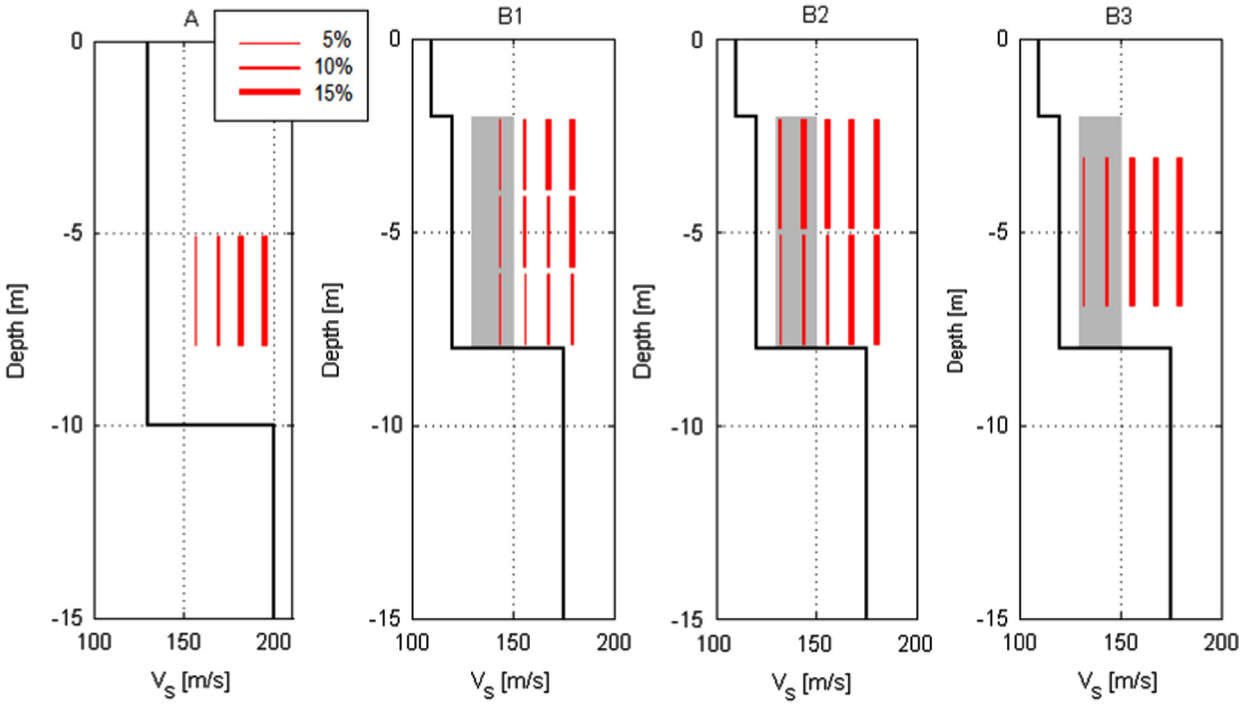

Fig. 9. Let us consider an initial V_S profile (black lines) and its theoretical Rayleigh wave dispersion curve (not shown). The thickness of the vertical red stripes indicates the percentage change introduced in the dispersion curve by the presence of a layer of the thickness, at the depth, and with the V_S represented by the vertical red lines themselves, compared to the initial V_S profile. The gray shaded areas indicate the typical V_S and depth of the liquefied sandy soils encountered in the studied area. (For interpretation of the references to color in this figure legend, the reader is referred to the web version of this article.)

The average V_S profile of class B soils (black in Fig. 8A) gives the theoretical dispersion curve in black in Fig. 8B (we assume Poisson's ratios equal to 0.49 and density equal to $1.7 \cdot 10^3$ kg/m^3 for all layers). Let us now add a 3-m-thick sand layer at the depth of 5 m, with $V_S = 155$ m/s (typical V_S value for sand in this area, red in Fig. 8A), as suggested by the CPT for class A sites. The dispersion curve of the modified soil profile is shown in red in Fig. 8B. This differs from the initial case by at most 10% and is indicated by the thickness of the red line in Fig. 8C. We note that dispersion curves differing by less than 10% can hardly be distinguished in practice.

In Fig. 9 we provide more examples to illustrate the extent to which the presence of a stiffer layer (e.g., sand) in a V_S profile can be recognized in the surface wave seismic data. The data are presented as in Fig. 8C, where the thickness of the vertical red stripes is proportional to the maximum percentage of change introduced in the dispersion curve by the presence of the stiff layer.

Fig. 9A, in practice, shows that starting from a V_S profile as the black one, the addition of a stiffer layer along the profile can be recognized only if it implies a V_S increase larger than 30% (from 130 to 170 m/s), otherwise the dispersion curves will not differ significantly.

In panels B1–B3 we repeat the experiment starting from different V_S profiles (e.g. the average non-liquefiable clayey–silty soil of class D) and imagining the presence of a layer of potentially liquefiable sand (2, 3, and 4 m thickness) at different depths (from 2 to 8 m depth). The vertical red stripes suggest that: a 1-m-thick layer at 2 m depth with $V_S = 175$ m/s (i.e. a V_S value 50% higher than that of the surrounding clay) would generate a local change in the dispersion curve of about 15%. The same sandy layer at 6 m depth would introduce a difference of less than 5% in the dispersion curve, which means it is practically undetectable.

By following the thickness of the red stripes in Fig. 9 we observe an intuitive fact: that in order for a layer to be recognized in a predefined profile, it has to become thicker and to have a stronger V_S variation as its depth increases. The picture also shows that thin and 'deep' layers can be completely invisible to the method.

The gray shaded areas in Fig. 9 indicate the typical V_S and depth of the liquefied sandy soils encountered in the studied area. Setting the detection threshold at a 5% change in the dispersion curve (which is very optimistic), as can be seen in panel B1, a sand layer of 2 m thickness would not be identified by the method at any depth of interest for liquefaction. A sand layer of 3 m thickness starts showing its presence with a very modest 5 to 10% change in the dispersion curve (panel B2) and a 4-m-thick layer at 3 m depth changes the dispersion curve by only 5% (panel B3).

4. Results

The first relations between V_S values and liquefaction potential described in the literature were based on laboratory or direct (in hole) measurements. More recent attempts [13] introduced, together with direct measurements, a number of V_S estimated from Spectral Analysis of Surface Waves (SASW), which is an ancestor of MASW. These methods consist in the calculation of the corrected seismic demand (cyclic stress ratio, CSR*) and the corrected soil capacity (V_{S1}) to be used as entry values in plots where the liquefaction and non-liquefaction areas are divided by curves representing different probability levels (Fig. 10).

The critical stress ratio (CSR) is the ratio between the average shear and vertical stresses, τ_{avg}/σ_{avg}. This can be rewritten as $CSR = 0.65\ a_{max}/g\ \sigma_V/\sigma'_V\ r_d$, where a_{max} is the peak ground acceleration at the surface, σ_V is the total overburden stress, σ'_V is the effective vertical overburden stress, and r_d is a non-linear mass participation factor, which depends on a number of factors including the soil depth, the average V_S of soil, the peak ground acceleration, and the earthquake magnitude. We use Eq. 4 in Kayen et al. [13] to calculate r_d, by setting $a_{max} = 0.31$ g and $M_W = 6.1$, which are the values of the 2012 main shock. The other parameters (depth of the sand layer on which to perform the calculations and depth of the water, average V_s of the overlying

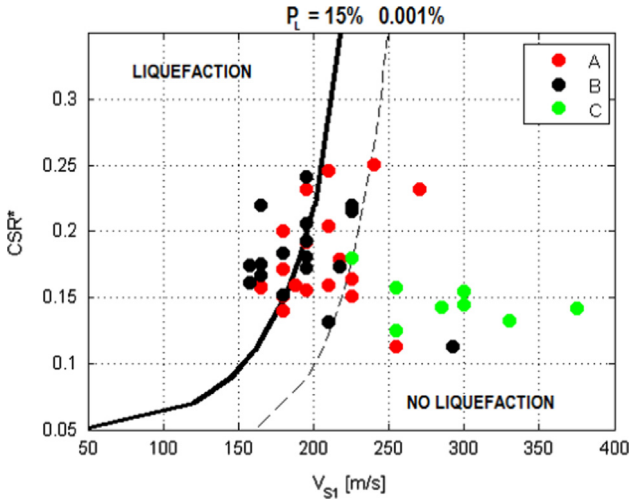

Fig. 10. Corrected cyclic stress ratio (CSR*) versus corrected shear wave velocity (V_{S1}) for the sand layer at the inspected sites. The thick black line corresponds to the 15% liquefaction probability level proposed by Kayen et al. [13].

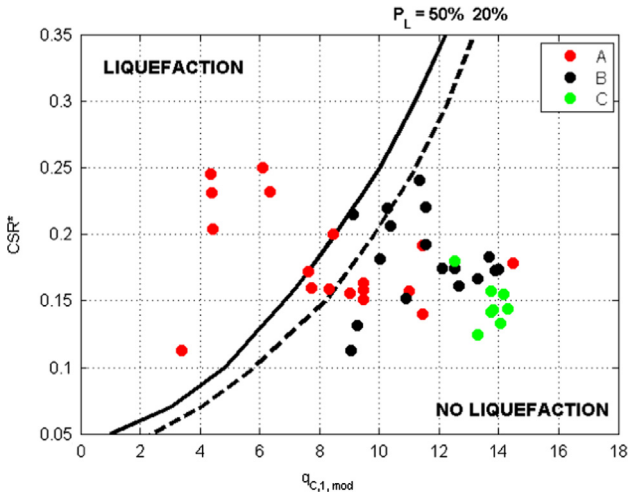

Fig. 11. Corrected cyclic stress ratio (CSR*) versus corrected and fines-modified CPT tip resistance ($q_{c1,mod}$) for the sand layer at the inspected sites. The black lines represent the contours of 50 and 20% probability of liquefaction [17]. Data are normalized with respect to $M_W=7.5$ and $\sigma'_V=1$ atm.

soil) are known at all sites from the penetration test, drillings, water wells, and the geophysical surveys performed ad hoc.

The adjustment of CSR to CSR* is done by scaling the computed CSR to compensate for the duration of shaking (duration weighting factor, DWF) relative to an equivalent $M_W=7.5$ event, so that CSR*=CSR/(DWF K_σ), where $K_\sigma=1$, following the recommendations in Kayen et al. [13] and DWF$=15\cdot M_W^{-1.342}$ (Eq. 17 in ibid.).

The results are plotted in Fig. 10 and show that our class A and B data (liquefied and non-liquefied sandy soils) are randomly distributed around the $P_L=15\%$ line (this value is recommended in [13], and corresponds to a safety factor of 1.2), while the class C data (deep sands) are well separated and fall in the non-liquefaction zone.

We also note that if we wish to include both the A and B sites in the liquefaction area, we need to operate according to $P_L=10^{-5}$, which represents a huge factor of safety (dashed line in Fig. 10).

We observe that the phase velocity spectra/dispersion curves (Fig. 6) are just experimental data with little subjective interpretation. Transforming these data into V_S profiles and calculating the CSR*–V_{S1} values requires a large number of assumptions and corrections (earthquake DWFs, adjustment for the influence of fines, calculation of effective stress, etc.) and is not a unique process (inversion of the data to get V_S profiles). All this effort does not seem to be warranted in the case of the present study and, besides the points above, there can be two further reasons for such a failure: 1) surface wave methods do not have sufficient sensitivity to characterize appropriately the V_S of the 2–4 m thick sandy layers potentially involved in the liquefaction phenomenon, and/or 2) the sandy deposits in this part of the Po Plain area have features that make them different from the sands studied worldwide by Kayen et al. [13].

In order to better discriminate between the last two hypotheses, we calculated the liquefaction potential of the same sand layers through the fines-modified CPT tip resistance approach, $q_{c1,mod}$ [17]. Results in terms of CSR*–$q_{c1,mod}$ are shown in Fig. 11 and suggest that the geotechnical method provides a better prediction of the liquefaction potential (a failure rate of less than 20% is achieved by adopting the 20% liquefaction probability curve) compared to the seismic-surface wave based method, thus making the first hypothesis more credible.

We observe that the surface wave dispersion curves alone (Fig. 6), prior to any inversion, can still be very informative. On the basis of the 84 surveys, for this area of the Po Plain we propose a soil classification scheme based on the Rayleigh wave dispersion curves (Fig. 12), which indicates the degree (high, intermediate, or low) of caution recommended in assessing the liquefaction potential of the soil under the typical design earthquake ($M_W\approx6.1$) imposed by the national building code [21] in this part of Italy for standard constructions. The class boundaries – high, intermediate, and low – mean that 50, 30, and $<5\%$, respectively, of the sites presenting a dispersion curve completely falling within them experienced liquefaction during the 2012 $M_W\approx6.1$ events (near field condition).

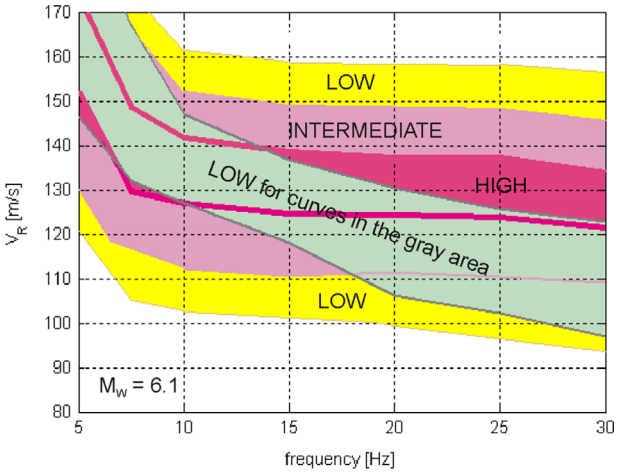

Fig. 12. Soil classification scheme based on the Rayleigh wave dispersion curves for the surveyed area. The adjectives "high", "intermediate", and "low" indicate the degree of caution recommended in assessing the liquefaction potential of the soil. In general, low V_R values in this plot indicate clays, while the sand content increases the V_R values. A dispersion curve falling completely within the gray area indicates with high probability a site with clay at shallow depth and sand at large depth (>8 m); this configuration represents a low liquefaction disposition under the typical $M_W\approx6.1$ earthquakes used as design earthquakes in this area [21]. A curve falling completely within the magenta area indicates with high probability a site with sand which could undergo liquefaction. Further investigations are recommended at these sites, for example by using CPT–STP, to assess the liquefaction potential. A curve falling completely within the lower yellow area indicates with high probability a clayey soil with low liquefaction potential. A curve falling completely within the upper yellow area indicates a site with dense sand in the upper 15 m, which would be less prone to liquefaction under the reference earthquake.

Generally speaking, low V_R values in this plot correspond to clays, while sand content increases the V_R values. A dispersion

curve falling completely within the gray area of Fig. 12 indicates with high probability a site with clays followed by sand at a depth greater than approximately 8 m. This configuration represents a low liquefaction susceptibility under a typical $M_W \approx 6.1$ earthquake.

A curve falling completely within the magenta area indicates a site with sand which can potentially undergo liquefaction. Further investigations are recommended at these sites, for example, by using CPT–STP, to better assess the liquefaction potential.

A curve falling completely within the lower yellow area ($V_R < 110$ m/s in the 10–30 Hz interval) indicates with high probability a clayey soil with low liquefaction potential. A curve falling completely within the upper yellow area ($V_R > 150$ m/s in the 10–30 Hz interval) indicates a site with dense sand in the upper 15 m, which would be less prone to liquefaction under the reference earthquake.

The above discussion applies also to the case of sites with a stiff crust, such as a dessicated clay layer or manmade fill, overlying loose saturated sand. In these cases there would be a 'kink' in the dispersion curve (not normally dispersive) which would not closely match the dispersion curve shapes discussed above but would still represent a potentially liquefiable soil. The most part of the dispersion curve is however expected to lay within the boundaries of Fig. 12, excluding the high frequency part which might lay above these limits.

Such a scheme appears to be more effective (and less demanding) in identifying the soils where further study is recommended compared to the CSR*–V_{S1} approach, in which V_{s1} is computed from surface-wave based seismic approaches. We emphasize that even though the V_R-frequency plot of Fig. 12 represents the result of this study, before applying it to different geographical and geological settings, specific tuning and verification are needed.

5. Further considerations

For each of the surveyed sites, we performed two microtremor H/V recordings in order to verify the homogeneity of the soil under the array. As is widely known, plane–parallel layering is a mandatory condition for the active–passive surface-wave array inversion. Since the H/V curves have point validity at the high frequencies (i.e. shallow depths) considered in this study, by taking at least two recordings along the array one can get an idea of the lateral continuity of the reflectors (which show up as peaks in the H/V) along the array (see also Fig. 16 in Appendix A). We grouped the 168 recorded H/V curves into the four soil classes to look for possible systematic differences but, as shown in Fig. 13, we just found that the H/V curves completely overlap in the whole experimental frequency range. This results from the fact that the impedance contrast among layers (clay–silt–sand) in this part of the Po Plain is too moderate to show up as H/V peaks (this was expected in advance since theoretical modeling shows that an impedance contrast of approximately 1.5 is needed to produce visible H/V peaks, [4]).

At 25% of the sites, the array and H/V recordings were performed both in summer 2013 and in winter 2014 in order to check for significant seasonal variations that might compromise the significance of the scheme proposed in Fig. 12. The conditions in summer were extremely dry and geophone penetration was difficult, thus requiring soil wetting to facilitate the penetration. The conditions in winter were the opposite: the soil was completely saturated with water.

In about half of these cases (i.e. 1/8 of the total number), the dispersion curves recorded in winter showed values of V_R that were 10 m/s lower than those recorded in summer and the difference particularly involved clays (i.e. class C and D sites). This might be due to the desiccation and consolidation of shallow clayey deposits that follows the water-table drop in summer and that is only partly released in winter (a complete recovery of the initial state can never be reached, [27]). However, considering the summer and winter measurements separately does not modify Fig. 12 in a significant way (see also Fig. 17 in Appendix A).

As a last consideration, we performed an extensive search of the regional databases for seismic arrays collected before the 2012 earthquakes, at sites that underwent liquefaction, to inspect for possible variations in the V_S of the sandy deposits after liquefaction. Unfortunately, despite the large number of liquefaction phenomena observed, we found only one site where the conditions were met: at the Sant'Agostino Cemetery a ReMi^{TM} survey was recorded in 2010 (solid line in Fig. 14), and it is compared to a survey recorded in 2012 in the frame of the present study (dotted line in Fig. 14). As can be seen, both dispersion curves fall completely in the high caution area of Fig. 12, and after the liquefaction, V_R appears to be on average 15 m/s higher than before the earthquake. The 2010 survey was fully passive and a 1D passive array might provide biased V_R–V_S estimates but only in excess [16,19]. The 2014 curve was instead derived from active–passive surveys, and therefore no bias is expected due to the unknown position of the sources with respect to the 1D array. This means that under unfavorable circumstances, the 2010 curve might be even lower than what is shown in Fig. 14. In conclusion, liquefaction at this site has apparently increased the V_R–V_S values of the deposit. However we cannot clearly derive general conclusions from this single case.

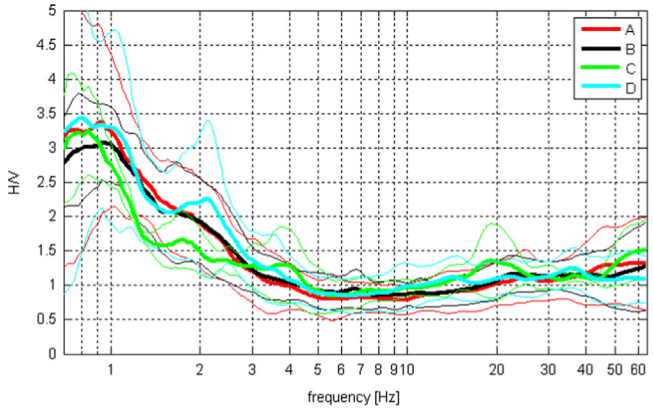

Fig. 13. Average H/V curves ± standard deviations grouped into the four soil classes.

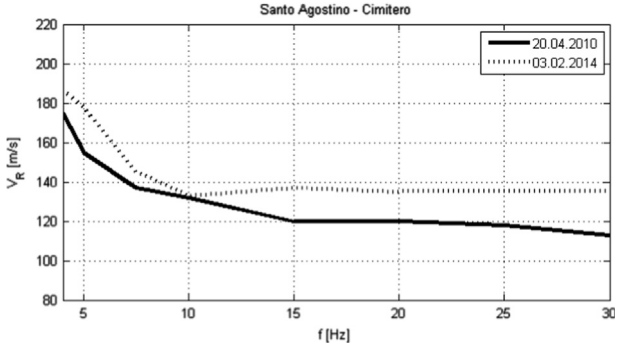

Fig. 14. Comparison between the dispersion curves recorded before (solid line) and after (dotted line) the 2012 earthquake at Sant'Agostino cemetery, a site which underwent extensive liquefaction phenomena.

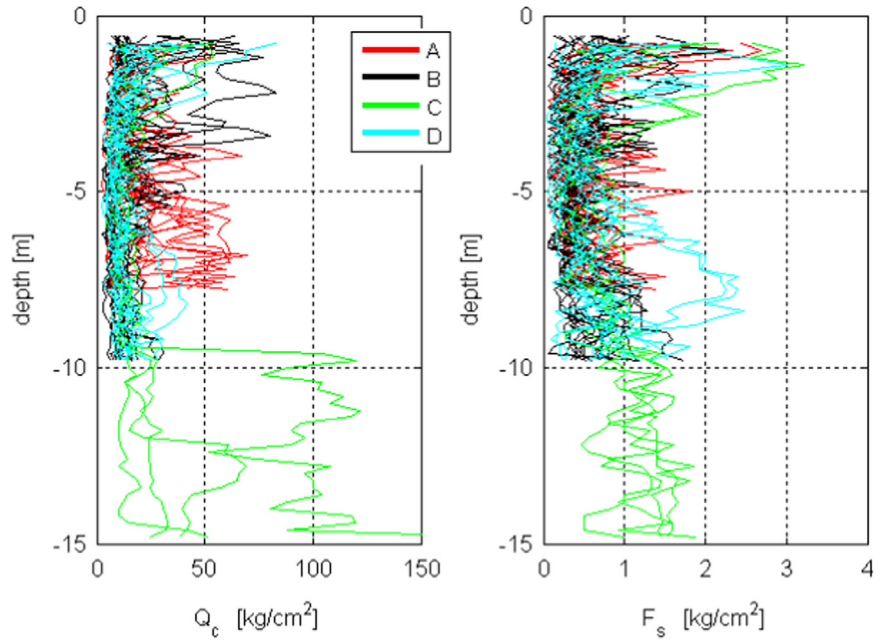

Fig. 15. Tip resistance (q_C, left) and sleeve friction (f_S, right) from CPT tests at the inspected sites. Only a few tests reached depths greater than 10 m .

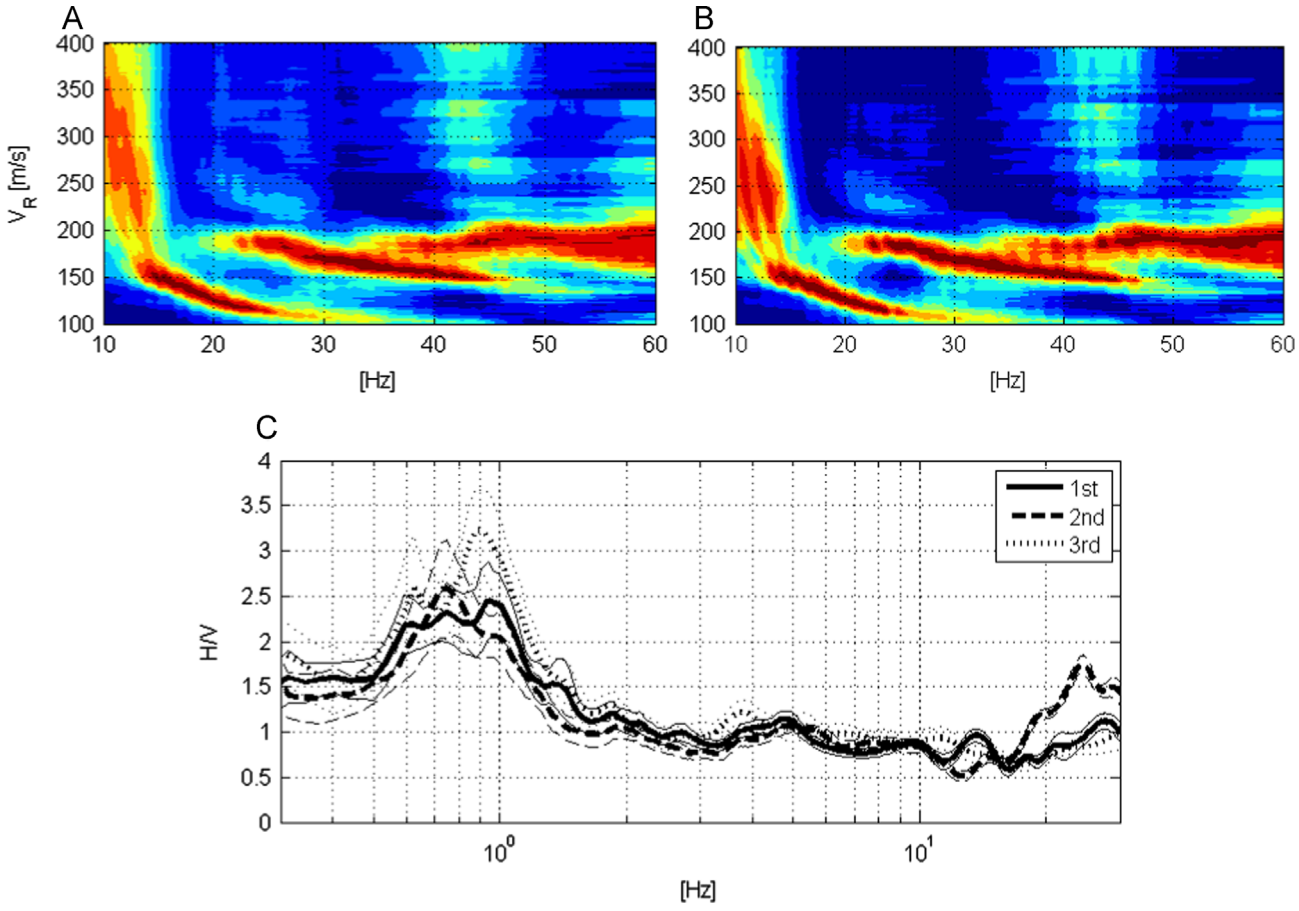

Fig. 16. Rayleigh wave phase velocity spectra obtained from the correlation of waves generated by an active source at 10 m distance from the first (A) and the last (B) geophone of the array line. (C) Comparison of the H/V curves recorded at ¼, ½, and ¾ of the array line. This example refers to a class D site .

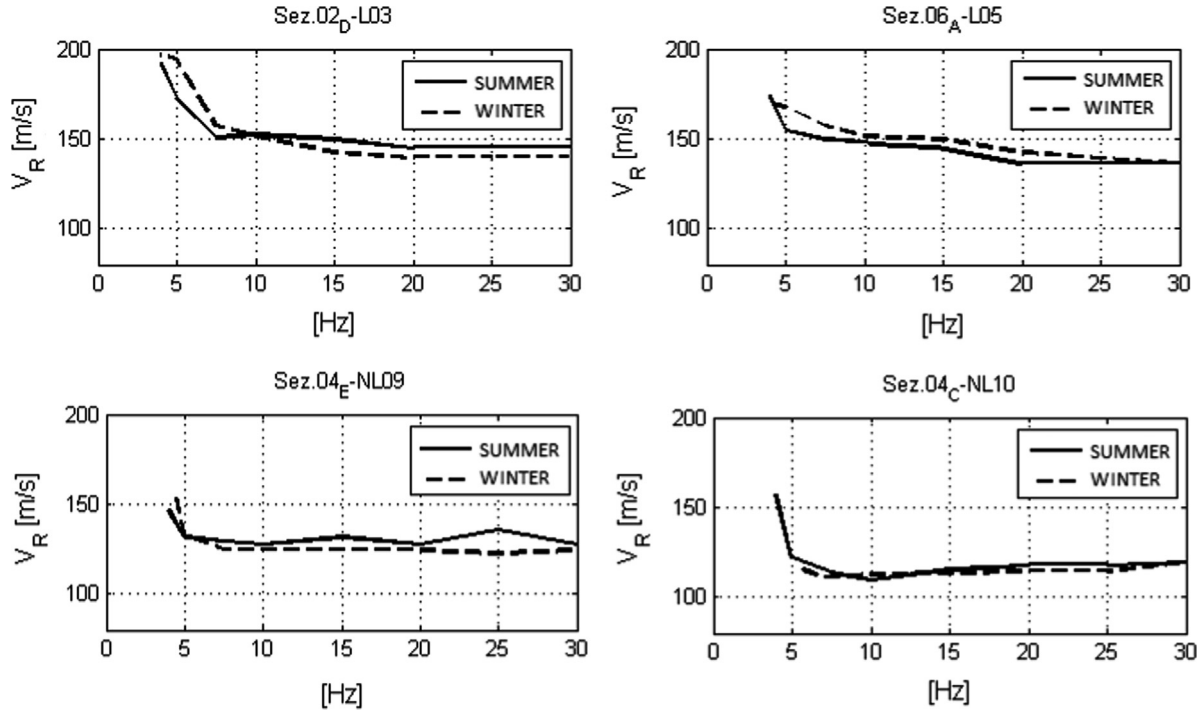

Fig. 17. No significant difference is observed, as an effect of the water table change, in the dispersion curves of class A and B soils collected in summer 2013 and winter 2014 below 10 Hz (i.e. at depths greater than approximately 4 m), which is the interval where liquefaction phenomena were observed .

6. Discussion and conclusions

The liquefaction potential of soils is commonly assessed through geotechnical methods (CPT, SPT, etc.) but some attempts to estimate it through geophysical parameters, such as the shear wave velocity, V_S, of soils, have also been developed. Measuring V_S in boreholes or in the laboratory (when the collection of undisturbed samples is possible) has the advantage of providing more accurate values at the specific depth of interest but at the expense of higher costs and invasiveness compared to the geotechnical methods and of the same point validity. Being able to measure V_S from the surface and over wider areas therefore appears to be a desirable solution. In 2013, Kayen et al. proposed a probabilistic and deterministic method to assess the liquefaction potential of sands through V_S measurements. The dataset used also included a number of V_S estimates from surface-wave based methods, specifically SASW.

In this work we verified the applicability of seismic active and passive multichannel modern surface wave techniques in the prediction of liquefaction potential. The opportunity was provided by the two earthquakes that occurred in the Po Plain (Northern Italy) in 2012, causing extensive liquefaction. Using the above mentioned seismic surface techniques, we surveyed 84 sites where geological information was available from direct geotechnical methods (penetration test, drilling, etc.).

Based on the geotechnical information, the sites were grouped into four classes: A) liquefied sandy soils; B) non-liquefied sandy soils; C) deep sands; D) clayey–silty soils. The penetration tests suggested that on average in class A soils, sand was dominant at 5–7 m depth (and was in practice the liquefied layer) while in class B soils, sand was dominant at shallower depths. However, the geophysical surveys showed that the Rayleigh wave phase velocity spectra were clusterized into three groups only: classes A and B were found to be indistinguishable from a seismic point of view. Through a set of theoretical models we showed that this is due to the resolution of the adopted seismic methods, which is a function of the 'exploring wavelength', and which makes seismic layers such as the sands under investigation – which are just 2–4 m thick and have V_S just a few ten of meters higher than the surrounding clay–silt – practically invisible at depths greater than 4–5 m.

We then applied the probabilistic and deterministic methods to assess the liquefaction potential of sands through the V_S measurement proposed by Kayen et al. [13], but we found that this approach failed in the case of the present study since class A and B soils were found to be randomly distributed between the liquefaction and non-liquefaction zones, while predictive power exists for class C soils, which, as they represent deep sands, fall in the non-liquefaction zone.

The geotechnical approach based on the tip resistance in the CPT to assess the liquefaction potential was found to be more successful.

The reason for the failure of the surface geophysical method seems to be linked, therefore, not to the specific features of the sands in this area but to the insensitivity of the seismic surface-wave based methods used to the details of stratigraphy for this specific goal.

In conclusion, based on this study (i.e. in the region of $V_{S1}=[150, 250]$ m/s), it seems that surface-wave methods (MASW, ReMi, ESAC, SPAC, and many others), which are extremely useful in a wide range of applications, do not have sufficient sensitivity to be used as predictors of liquefaction in the classic frame of seismic demand versus soil capacity scheme.

However, at least in this specific depositional environment, it also seems that the simple analysis of the Rayleigh wave phase velocity spectra – before any inversion procedure (Fig. 6) – can be used since it suggests the presence of sand or clay. On the basis of the experimental results we built the 'caution against liquefaction' graph shown in Fig. 12, which can however only be used in the studied area. Nonetheless, the procedure – after specific tuning for different geological settings – could probably also be applied at different sites.

Acknowledgments

We thank Matteo Berti for proposing the case study and for the useful discussions, Giuseppe Bertolini for the aerial photos, Francesco Mulargia for the discussions, Giovanni Santarato and Nasser Abu-Zeid for the ReMi™ array at the Sant'Agostino Cemetery performed in 2010 ("Convenzione tra l'Università di Ferrara, la Provincia di Ferrara, i Comuni di Ferrara, Argenta, Bondeno, Comacchio ed Hera Ferrara S.r.l., per attività di ricerca finalizzata alla valutazione del rischio sismico locale nel territorio della Provincia di Ferrara"). We thank the two anonymous reviewers, whose constructive criticism helped us improve the first version of the manuscript. This work was partly funded with a DPC-INGV-S2-2014 Constraining observations into seismic hazard grant.

Appendix A

See Figs. 15–17 here.

References

[1] Bertolini G, Fioroni C. Aerial inventory of surficial geological effects induces by the recent Emilia earthquake (Italy): preliminary report. Ann Geophys 2012;55:705–11.
[2] Castellaro S, Mulargia F. Vs30 estimates using constrained *H*/*V* measurements. Bull Seismol Soc Am 2009;99:761–73.
[3] Castellaro S, Mulargia F. The effect of velocity inversions on *H*/*V*. Pure Appl Geophys 2009;166:567–92.
[4] Castellaro S, Mulargia F. Simplified seismic soil classification: the VfZ matrix. Bull Earthq Eng 2014;12:735–54.
[5] Cubrinovski M, Bradley B, Wotherspoon L, Green R, Bray J, Wood C, et al. Geotechnical aspects of the 22 February 2011 christchurch earthquake. Bull N Z Soc Earthq Eng 2011;44:205–26.
[6] Di Manna P, Guerrieri L, Piccardi L, Vittori E, Castaldini D, Berlusconi A, et al. Ground effects induced by the 2012 seismic sequence in Emilia: implications for seismic hazard assessment in the Po Plain. Ann Geophys 2012;55:697–703.
[7] Emergeo Working Group. Liquefaction phenomena associated with the Emilia earthquake sequence of May-June 2012 (Northern Italy). Nat Hazards 2013;13:1–13.
[8] Green RA, Wood C, Cox B, Cubrinovski M, Wotherspoon L, Bradley B, et al. Use of DPC and SASW tests to evaluate liquefaction potential: predictions vs. observations during the recent New Zealand earthquakes. Seismol Res Lett 2011;82:927–38.
[9] Gucunski N, Woods RD. Numerical simulation of the SASW test. Soil Dyn Earthq Eng 1992;11:213–27.
[10] Idriss IM, Boulanger RW. Soil liquefaction during earthquakes. Oakland, CA: Monograph MNO-12, Earthquake Engineering Research Institute; 2008. p. 261.
[11] Iwasaki T, Tokida K, Tatsuoka F, Watanabe S, Yasuda S, Sato H. Microzonation for soil liquefaction potential using simplified methods. In: Proceedings of the 3rd international earthquake microzonation conference. Seattle; 1982. p. 1319–30.
[12] Kaybali K. Soil liquefaction evaluation using shear wave velocity. Eng Geol 1996;44:121–7.
[13] Kayen R, Moss RES, Thompson EM, Seed RB, Cetin KO, Der Kiureghian A, et al. Shear-wave velocity-based probabilistic and deterministic assessment of seismic soil liquefaction potential. J Geotech Geoenviron Eng 2013;139:407–19.
[14] Lay Wallace. Modern global seismology. New York: Academic Press; 1995. p. 517.
[15] Lin PS, Chang CW, Chang WJ. Characterization of liquefaction resistance in gravelly soil: large hammer penetration test and shear wave velocity approach. Soil Dyn Earthq Eng 2004;24:675–87.
[16] Louie J. Faster, better: Shear-wave velocity to 100 m depth from refraction microtremor arrays. Bull Seismol Soc Am 2001;91:347–64.
[17] Moss RES, Seed RB, Kayen RE, Stewart JP, Der Kiureghian Cetin, KO. CPT-based probabilistic and deterministic Assessment of in situ seismic soil liquefaction potential. J Geotech Geoenviron Eng 2006;132:1032–51.
[18] Mulargia F, Castellaro S. Experimental uncertainty on the *Vs*(z) profile and seismic soil classification. Seismol Res Lett 2008;80:985–8.
[19] Mulargia F, Castellaro S. A seismic passive imaging step beyond SPAC and ReMi™. Geophysics 2013;78:KS63–72.
[20] Nazarian S, Stokoe KH. In situ shear wave velocities from spectral analysis of surface waves. In: Proceedings of the 8th world conference on earthquake engineering. vol. 3, Prentice-Hall, Englewood Cliffs, NJ; 1984. p. 31–38.
[21] NTC. Norme Tecniche sulle Costruzioni, D.M., 14/01/2008, Ministero delle Infrastrutture Italy; 2008.
[22] Ohori M, Nobata A, Wakamatsu K. A comparison of ESAC and FK methods of estimating phase velocity using arbitrarily shaped microtremor arrays. Bull Seismol Soc Am 2002;92:2323–32.
[23] Papathanassiou G, Caputo R, Rapti-Caputo D. Liquefaction phenomena along the paleo-Reno river caused by the May 20, 2012, Emilia (northern Italy) earthquake. Ann Geophys 2012;55:735–42.
[24] Park CB, Miller RD, Xia J. Multichannel analysis of surface waves. Geophysics 1999;64:800–8.
[25] Robertson PK. Interpretation of cone penetration tests—a unified approach. Can Geotech J 2009;46:1337–55.
[26] SESAME Project. Guidelines for the implementation of the *H*/*V* spectral ratio technique on ambient vibrations: measurements, processing and interpretation, SESAME European Research Project WP12, deliverable no. D23.12, ⟨http://sesame-fp5.obs.ujf-grenoble.fr/Papers/HV_User_Guidelines.pdf⟩; 2004 [last accessed 11.05.12].
[27] Terzaghi K. Theoretical soil mechanics. John Wiley&Sons, Inc.; 1943. p. 265.
[28] Tokimatsu K, Tamura S, Kojima H. Effects of multiple modes on Rayleigh wave dispersion characteristics. J Geotech Eng 1992;118:1529–43.
[29] Tsuchida H. Prediction and countermeasure against the liquefaction in sand deposits. Abstract of the seminar in the Port and Harbor Research Institute; 1970 (in Japanese).
[30] Youd TL, Idriss IM, Andrus RD, Arango I, Castro G, Christian JT, et al. Liquefaction resistance of soils: Summary report from the 1996 NCEER and 1998 NCEER/NSF workshops on evaluation of liquefaction resistance of soils. J Geotech Geoenviron Eng 2001;127:817–33.
[31] Zhou YG, Chen YM. Laboratory investigation on assessing liquefaction resistance of sandy soils by shear wave velocity. J Geotech Geoenviron Eng 2007;133:959–72.

4. CONCLUSIONS

Results from this research represent an improvement in the state of the art of earthflows study, in particular as far as the solid-to-fluid transition of the involved material, the geomorphological characteristics and the calculations of sediment discharge. Moreover an attempt in the use of geophysical methods in the study of the liquefaction susceptibility was carried out.
The results of this three years project can be summarized as follows:

1. The results obtained from the rheological tests showed a thixotropic behavior (Mainsant et al., 2012b) of the investigated clayey soils, i.e. a yield-stress fluid behavior associated with bifurcation in viscosity. Results also showed a decrease in critical shear stress and an increase in viscosity bifurcation with higher water content. All yield-stress soils, despite coming from landslides with very different geomorphologies, obey to a common exponential law relating τ_c and the deviation w-LL. Finally, a link has been made between morphological characteristics and rheometric properties, as high mobility earthflows studied in this paper (Hollin-Hill, Harmalière and Montevecchio) seem to exhibit the strongest fluidization. The field investigations on the Montevecchio landslide indicate that the trend of the surface wave are related to the displacement rate, in particular high seismic velocity was found while the landslide was not moving or slow moving (in the order of cm/months), and low seismic values were found during the fast moving of the earthflow. The increase of surface wave velocity after failure can be explained by the progressive decrease of soil porosity associated with the consolidation of the landslide mass and this process can continue for weeks or months and may be interrupted by a new reactivation. These studies open up promising prospects for flow-like landslide monitoring and suggests that w measurements could be used to assess the stress at which a clayey soil of known LL fluidizes. Moreover, it is possible to highlights the potential value of geophysical monitoring on active landslides to bring some insight in the rheological change in clayey soils.

2. From the geomorphological point of view, field investigations and observations on the Monte Pizzuto earthflow indicated that i) earthflows having a well-defined neck are more likely to surge with respect to those not having a neck, ii) it is not always correct to consider the sediment discharge of the earth flow constant, but this assumption should be contextualized as function of the state of flow activity, iii) during surging events, the earth flow behavior might be simulated using macro-viscous models without oversimplifying the problem, and iv) distribution of structures at the surface of an earth flow provide information about the geometry of the basal slip surface and the velocity profile of the earth flow.

3. Geophysical methods as ReMi-MASW surveys and HVSR acquisitions seem to be not useful in the assess of the liquefaction susceptibility. This might be due to the insufficient resolution of the surface wave methods to identify the V_s of thin layers and to the fact that V_s scales with the square root of the shear modulus, which implies an intrinsic lower sensitivity of V_s to the shear resistance of the soil (compared to parameters traditionally measured with the penetration tests). However, it also came out that the pure observation of the surface wave dispersion curves at their simplest level (i.e. in the frequency domain, with

no inversion) is still potentially informative and can be used to identify the sites where more detailed surveys to assess the liquefaction potential are recommended. In fact we made up a ‘caution against liquefaction’ graph, in which you can identify the degree (high, intermediate or low) of caution recommended in assessing the liquefaction potential of the soils under the typical designed earthquake imposed by the national building code in this part of Italy for standard constructions.

A possible future progress could be developed in laboratory tests. With the rheometric tests we focused on the behavior of the clayey samples with a water content over the Liquid Limit (LL) and we calculated the variations of the shear modulus (G) and the critical shear stress (τ_c). In the field, these conditions are representative just for the paroxysmal phase of an earthflow (velocity of movement in the range of several meters/hour). It is possible to study the mechanical properties of the material, in the range between the LL and the average water content in the field, using bender elements on a triaxial cell (Mitaritonna et al., 2010). As originally reported by Dyvik et al., (1985) piezo-ceramic bender elements are electromechanical transducers capable of converting mechanical energy (movement) either to or from electrical energy. A bender element typically consists of two thin conductive piezo-ceramic plates rigidly bonded to a central metallic plate. When a driving voltage is applied to the element, one plate elongates and the other shortens resulting in the bending of the system (Brignoli et al., 1996). The bender elements have to be powered by a waveform signal generator. The output signal is converted into digital and transmitted to PC via an interface and processed with the virtual oscilloscope software. The travel time of the shear wave from the transmitter to the receiver is determined via a specific software that allows the user to quickly and easily calculate the shear wave velocity. Preparing the clayey sample in the cell and inserting a bender element at the base and the other one at the top, it is possible to directly measure the surface wave velocity of remolded samples at different void ratio. As $G=\rho.Vs$ (where ρ is the density and V_s is the shear wave velocity), the different value of measured V_s directly correlated to the changes in G. That could allow us to have complete information of the variation of G for all the possible water content in a clay sample.

REFERENCES

Baliva F., 2006. Profilo di velocità delle onde S dallo studio dei microtremori. PhD thesis, University of Siena.

Baum R. L., Johnson A. M., 1993. Steady Movement of Landslide Features in Fine-Grained Soils – a Model for Sliding Over an Irregular Slip Surface. Chapter D of Landslide Processes in Utah – Observation and Theory. U.S. Geological Survey Bulletin 1842, Reston, VA, D1-D28.

Baum R. L., Savage W. Z., Wasowsky J., 2003. Mechanics of earth flows. Proceedings of the 133 International Conference FLOWS 2003. Sorrento, Italy.

Beekman A. N., 2008. A comparison of experimental ReMi measuraments with various source, array, and site condition. Master thesis of Sciences in Civil Engineering, University of Arkansas.

Bertolini G., Fioroni C., 2012. Aerial inventory of surficial geological effects induces by the recent Emilia earthquake (Italy):preliminary report. Ann Geophys., **55**, 705–11.

Booth A.M., Roering J.J., Rempel A.W., 2013. Topographic signatures and a general transport law for deep-seated landslides in a landscape evolution model. Journal of Geophysical Research: Earth Surface, **118**, 603-624.

Bovis M.J., Jones P., 1992. Holocene history of earth flow mass movement in south-central British Columbia: the influence of hydroclimatic changes. Canadian Journal of Earth Sciences, **29**, 1746-1755.

Brignoli E.G., Gotti M., Stokoe K.H., 1996. Measurement of Shear Waves in Laboratory Specimens by Means of Piezoelectric Transducers. Geotechnical Testing Journal, ASTM, 19, **4**, 384-397.

Carriere S.R, Jongmans D., Chambon G., Bievre G., Lanson B., Bertello L., Berti M., Chambers L.E., Jaboyedoff M., Malet J.P., 2016. Rheomteric properties of clayey soils originating from flow-like landslide. Journal of Geophysical Research: Earth Surface. In review.

Casson N., 1959. Rheology of disperse systems. Ed. C.C. Mill, Pergamon Press, Oxford.

Castellaro, S., Panzeri, R., Mesiti, F., Bertello, L., 2015. A surface seismic approach to liquefaction. Soil Dynamic and Earthquake Engineering, **77**, 35-46.

Coe J. A., McKenna J. P., Godt J. W., Baum R. L., 2009. Basal-topographic control of stationary ponds on a continuously moving landslide. Earth Surface Processes and Landforms, **34**, 264-279.

Coussot P., Nguyen Q. D, Huynh H. T., Bonn D., 2002. Viscosity bifurcation in thixotropic, yielding fluids. Journal of Rheology, **46(3)**, 573–589.

Cruden D. M., Varnes D. J., 1996. Landslide types and processes. Landslide, Investigation and Mitigation. Special Report 247. Transportation Research Board. Washington 36–75.

Daehne A., Corsini A., (2012). Kinematics of active earthflows revealed by digital image correlation and DEM subtraction techniques applied to multi-temporal LiDAR data. *Earth Surf. Process. Landforms*, **38**, 640-654.

D'Elia B., 1975. Aspetti meccanici delle frane tipo "colata". Rivista Italiana di Geotenica, **9**, 32-42.

Di Manna P., Guerrieri L., Piccardi L., Vittori E., Castaldini D., Berlusconi A., et al., 2012. Ground effects induced by the 2012seismic sequence in Emilia :implications for seismic hazard assessment in the Po Plain. Ann Geophys., **55**, 697–703.

Dyvik R., Madshus C., 1985. Laboratory measurements of Gmax using bender elements. Proc. of the ASCE Annual Convention: advances in the art of testing soils under cyclic conditions, Detroit, Michigan, 186-196.

Emergeo Working Group, 2013. Liquefaction phenomena associated with the Emilia earthquake sequence of May-June 2012 (Northern Italy). Nat Hazards, **13**, 1–13.

Hungr O., Evans S. G., Bovis M. J., Hutchinson J. N., 2001. A review of the classification of the landslide of the flow type. Environmental and Engineering Geosciences 7, 221-238.

Hungr O., Leroueil S., Picarelli L., 2014. Varnes classification of landslide types, an update. Landslides **11**, 167-194.

Hutchinson J. N., Bhandari R. K., 1971. Undrained loading, a fundamental mechanism of mudflows and other mass movements. Geotechnique **21**, 353-358.

Hutchinson J. N., 1988. General report: morphological and geotechnical parameters of landslides in relation to geology and hydrogeology. In: Proceedings of the 5th International Symposium on Landslides. Lausanne **1**, 3–35.

Khaldoun A., Moller P., Fall A., Wegdam G., De Leeuw B., Meheust Y., Fossum J. O., Bonn D., 2009. Quick clays and Landslides of clayey soils, Phys. Rev. Lett., **103**, 188301.

Iverson R. M., 1986. Unsteady, non-uniform landslide motion: 1.Theoretical dynamics and the steady datum stat. The Journal of Geology **94**, 1–15.

Iverson R. M., Major J. J., 1987. Rainfall, groundwater flow, and seasonal movement at Minor Creek landslide, northwestern California – physical interpretation of empirical relations. Geological society of America Bulletin **99**, 579-594

Iverson R. M., 2000. Landslide triggering by rain infiltration. Water Resource research **36**, 1897-1910.a.

Jongmans, D., Garambois, S., 2007. Geophysical investigation of landslide: a review. Bull. Soc. géol. Fr., **2**, 101-112.

Jongmans D., Baillet L., Larose E., Bottelin P., Mainsant G., Chambon G., Jaboyedoff M., (2015). Application of ambient vibration techniques for monitoring the triggering of rapid landslides. Engineering Geology for Society and Territory, **2**, 371-374.

Kayen R., Moss R.E.S., Thompson E.M., Seed R.B., Cetin K.O., Der Kiureghian A., et al., 2013. Shear-wave velocity-based probabilistic and deterministic assessment of seismic soil liquefaction potential. J Geotech Geoenviron Eng., **139**,407–19.

Keefer D.K., Johnson A.M., 1983. Earthflows: morphology, mobilization and movement. U.S. Geological Survey Professional Paper, **1264**, 56.

Louie J. 2001. Faster, better: Shear-wave velocity to100 m depth from refraction microtremor arrays. Bull. Seismol. Soc. Am., **91**, 347–64.

Mainsant G., Larose E., Bronnima C., Jongmans D., Michoud C., Jaboyedoff M. (2012a). Ambient seismic noise monitoring of a clay landslide: toward failure prediction. Geophisical Research Letters, **117**, F01030.

Mainsant G., Jongmans D., Chambon D., Larose E., Baillet L., (2012b) – Shear wave velocity as an indicator fo rheological changes in clay materials: Lessons from laboratory experiments. Geophisical Research Letters, **39**, L19301.

McMechan G. A., Yedlin M. J., 1981. Analysis of dispersive waves by wave field transformation. Geophysics, 46, **6**, 869-874.

Mitaritonna G, Amorosi A., Cotecchia F., 2010. Multidirectional bender element measuraments in the triaxial cell: equipment set-up and signal interpretation. Rivista Italiana di Geotecnica, 1/2010, 50-69.

Mitsoulis E., 2007. Flows of viscoplastic materials: models and computations. The British Society of Rheology, 135-178.

Mucciarelli M., Masi A., Vona M., Gallipoli M. R., Harabaglia P., Caputo R., Piscitelli S., Rizzo E., Picozzi M., Albarello D., 2003. Quick survey of the possible causes of damage enhancement observed in San Giuliano after the 2002 Molise, Italy seismic sequence. European Geophys. Society, **4**, 599-614.

Nakamura Y., 1989. A method for dynamic characteristics estimations of subsurface using microtremors on the ground surface. Q. Rept. Railway Technical Research Institute Japan, 30, 25–33

Park C.B., Miller R D., Xia J., 1999. Multichannel analysis of surface waves: Geophysics, **64**, 800–808.

Pastor M., Blanc T., Pastor M.J., (2009). A depth integrated viscoplastic model for dilatant saturated cohesive-frictional fluidized mixitures: Application to fast catastrophic landslides. Journal of non-Newtonian fluid mechanics, **158**, 142-153.

Pastor M., Manzanal D., Fernandez Merodo J.A., Mira P., Blanc T., Drempetic V., Pastor M.J., Haddad B., Sanchez M., (2010). From solids to fluidized soils: diffuse failure mechanisms in geostructureswith applications to fast catastrophic landslides. Granular Matter, **12**, 211-228.

Papathanassiou G., Caputo R., Rapti-Caputo D., 2012. Liquefaction phenomena along the paleo-Reno river caused by the May 20, 2012, Emilia (Northern Italy) earthquake. Ann Geophys., **55**,735–42.

Picarelli L., Urciuoli L., Ramondini G., Comegna L., 2005. Main features of mudslides in tectonised highly fissured clay shales. Landslides, **2(1)**, 15–30.

Pullammanappallil S., Honjas J., Louie J. N., Siemens J. A., Miura H., 2003. Comparative Study of the Refraction Microtremor (ReMi) Method: Using Seismic noise and standard P-wave refraction equipment for deriving 1-D S-wave profiles. 6th international SEG-J conference, Tokyo, Japan.

Renalier F., Bièvre G., Jongmans D., Campillo M., Bard P.Y., 2010. Clayey landslide investigations using active and passive Vs measurements, in Advances in Near-Surface Seismology and Ground-Penetrating Radar. Geophys. Dev. Ser., **15**, 397–414.

Reynolds J. M., 1997. An Introduction to Applied and Environmental Geophysics, 796 pp., John Wiley, Chichester, U. K.

Schulz W. H., Lidke D. J., Godt J. W., 2008. Modeling the spatial distribution of landslide-prone colluvium and shallow groundwater on hillslopes of Seattle, WA. Earth Surface Processes and Landforms **33**, 123–141.

Schulz W. H., Kean J. W., Wang G., 2009. Landslide movement in southwestern Colorado triggered by atmospheric tides. Nature Gosciences, **2**, 863-866.

Thorson J. R., Claerbout J. F., 1985. Velocity-stack and slant-stack stochastic inversion. Geophysics, **50**, 2727-2741.

Tokimatsu K., Tamura S., Kojima H., (1992). Effects of multiple modes on Rayleigh wave dispersion. J. Geotech. Eng. **118**, 1529–1543.

Tokimatsu K. (1997). Geotechnical site characterization using surface waves. Proc. 1st Intl. Conf. Earthquake Geotechnical Engineering, **3**, 1333–1368.

Van Asch T. W. J., Van Beek T. A., Bogaard L. P. H., 2007. Problems in predicting the mobility of slow-moving landslides. Eng. Geol. Amsterdam, **91**, 46–55.

Varnes D.J., 1978. Slope movement types and processes. In: *Special Report 176:* Landslides*: Analysis* and *Control* (Eds: Schuster, R. L. & Krizek, R. J.). Transportation and Road Research Board, National Academy of Science, Washington D. C., 11-33.

Weitz D., Wyss H., Larsen R., 2007. Oscillatory Rheology - Measuring the Viscoelastic Behaviour of Soft Materials. Harvard University G.I.T. Laboratory Journal **3-4**, 68-70.

Manual and book

Manual of rheotec, Introduction to rheology. Messtechnik GmbH Ottendorf-Okrilla. Volume 2.1

Barnes H.A., Hutton J.F., Walters K., An introduction of rheology. Netherlands, Amsterdam. 1989. Print.

Bingham E.C., Fluidity and plasticity. McGraw-Hill, New York. 1922. Print

Malkin A., Isayev A. I., Rheology: Concepts, Methods, and Applications (Second Edition), 2012. Print.

APPENDIX

During the three years PhD project, I participated at some international conference

1) **European Geosciences Union in Vienna (2015).** Title: Study of the dynamic behavior of earthflows through the analysis of shear wave velocity in the landslide body.
   Type of presentation: **poster**;

2) **Fourth Italian Workshop on Landslides in Naples (2015).** Title: Kinematic segmentation and velocity in earth flows: a consequence of a complex basal-slip surface. Type of presentation: **oral** (held by the first author);

3) **European Geosciences Union in Vienna (2016).** Title: Continuous monitoring of surface wave velocity at the Montevecchio earthflow (Forlì-Cesena Province, Northern Apennines). Type of presentation: **oral**;

4) **Società Geologica Italiana in Naples (2016).** Title: Monitoring of a fast moving landslide in a weak cemented sandstone in Northern Apennines. Type of presentation: **oral**;

Geophysical Research Abstracts
Vol. 17, EGU2015-15393, 2015
EGU General Assembly 2015
© Author(s) 2015. CC Attribution 3.0 License.

Study of the dynamic behavior of earthflows through the analysis of shear wave velocity in the landslide's body

Lara Bertello
Geology at the University of Bologna

Over the first year of my PhD, I carried out a literature search about earthflows features and dynamics and conducted periodic ReMi-MASW campaigns to assess the temporal variation of shear velocity for several landslides that were recently reactivated. Literature search was conducted to review recent works related to shear wave velocity as an indicator for rheological changes in clay materials (Mainsant et al., 2012). From January to August 2014 I carried out numerous ReMi-MASW surveys to characterize several active earthflows in the Emilia-Romagna Apennines. I did these measures both inside and outside the landslide's bodies, usually during the first ten days after the reactivation. At first, these measures indicate low shear waves velocity inside the landslide and high velocity outside. This is due to the different consistence of the materials, to the different water content and to the void index. Then I repeated the measures over time in the same places on the same landslide, in order to detect the variability of Vs over time in correlations with the landslide's movements.
Periodic ReMi-MASW survey were conducted on the following landslides:
• The Montevecchio (FC) earthflow was reactivated the 1th of February 2014 (estimated volume of 240.000 m^3) and increased the movement's velocity around the 7th of February 2014, after intense precipitations. Analyzing the data collected inside the landslide's body, I observed an increase of Vs over time, due to the decrease of landslide velocity;
• The Silla (BO) complex landslide reactivated the 10th of February 2014 (estimated volume of 900.000 m^3), and moved downslope with a maximum velocity in the order of several m/hour. Studying the data, it is possible to notice how the Vs increase over time only in the lower portion of the landslide. In fact the upper portion is still active, so the Vs remained unchanged over time.
• the Puzzola-Grizzana Morandi (BO) complex landslide. This landslide was reactivated the 10th of February 2014 involving about 5000 m^3 of materials. Analyzing the data collected inside the landslide's body, I observed an increase of Vs over time, due to the decrease of landslide velocity and, probability, to the remedial works carried out after the reactivation;
• The Mozuno (BO) rotational landslide. This landslide was reactivated around the first day of March 2014. The data collected show a decrease of Vs variability, due to an increase of fractures near the main scarp;
• The Borgo Val di Taro (PR) complex landslide. This landslide was reactivated during the night between the 9th and the 10th of February 2014 with a maximum velocity around 40m/d. The data collected show an increase of Vs, due to the slowing of the movements and the consolidation of landslide material;
• The Camugnano (BO) transitional landslide. The reactivation of this landslide was around the 15th of March 2014. Analyzing the data collected inside the landslide's body, I noted an increase of Vs over time, due to the slowing of the movements;
• The Zattaglia-Poggio Zampiroli (BO) transitional landslide. The reactivation of the landslide occurred on the 9th of February 2014. The data show really different values of Vs in relation to the landslide's portion investigated and show an increase of Vs over time.
In all these cases, the measures taken outside the landslide's body do not show a significant Vs variability, because the material are not involved in the landslide's movements.
Preliminary results from field data clearly show that the variation of the shear wave velocity with time is related to the movements of the landslides and to the different consistence of the materials.

Available online at www.sciencedirect.com

ScienceDirect

Procedia Earth and Planetary Science 00 (2016) 000–000

Procedia
Earth and Planetary Science

www.elsevier.com/locate/procedia

The Fourth Italian Workshop on Landslides

Kinematic segmentation and velocity in earth flows: a consequence of a complex basal-slip surface

Luigi Guerriero[a]*, Paola Revellino[a], Lara Bertello[b], Gerardo Grelle[a], Matteo Berti[b], Jeffrey A Coe[c], Francesco Maria Guadagno[c]

[a]*Department of Science and Technology, University of Sannio, Benevento, Italy*
[b]*Department of Biological, Geologic and Environmental Sciences, University of Bologna, Bologna, Italy*
[c]*U.S. Geological Survey, MS 966, Denver Federal Center, Denver, Colorado, USA*

Abstract

We investigated the relation between structures, velocity distribution and basal-slip surface geometry within individual kinematic domains of two large earth flows in the Apennine Mountains of southern Italy: the "Montaguto" earth flow and the "Mount Pizzuto" earth flow. Our analyses indicated that earth flows can be composed of distinct kinematic zones characterized by a specific deformational pattern and longitudinal velocity profile. Velocity variation along a kinematic zone is controlled by the geometry of the basal slip surface and in particular by local variation of the slope angle. Such geometry seems to control also the density of the forming extensional structures at driving earth flow elements (i.e. riser).
© 2016 The Authors. Published by Elsevier B.V.
Peer-review under responsibility of the organizing committee of IWL 2015

Keywords: earth flow; velocity; basal-slip surface; structure; kinematic zone; GPS; southern Italy

1. Introduction

Periodic movement of large, thick landslides on a discrete basal-slip surface produces modifications of the topographic surface, creates deformational structures (i.e. faults and folds), and influences the location of hydrologic features like springs, ponds, and streams[5]. Earth-flow movement alternates between long periods of relatively slow movement and relatively rapid surges in movement[21]. Slow movement could persist for days, months, or years[4]. Surges in earth-flow movement are less common and earth flows capable of surging move in a slow persistent

* Corresponding author. Tel.: +39-333-9760824.
E-mail address: Luigi.guerriero@unisannio.it

1878-5220 © 2016 The Authors. Published by Elsevier B.V.
Peer-review under responsibility of the organizing committee of IWL 2015.

manner most of the time[21]. Velocity of earth flow during slow, persistent, movement range from less than 1 mm/d to several meters per day[21]. The highest localized earth-flow surge speed documented in the literature is 0.13 m/s[20].

Velocity profiles in earth flow generally show the existence of well-defined basal and lateral shear-surfaces normally associated with sliding movement[19,21,7,3,12]. In spite of their flow-like morphology, the dominant mechanism of earth-flow movement is sliding at residual strength[21,7,2,3].

The geometry of the basal-slip surface, that can be controlled by geologic structures and ancient earth-flow deposits[15,25] can control the position of deformational structures and the spatial variation in the rate of displacement, both of which are responsible for kinematic segmentation of the landslide body[2,15]. Thus, large earth flows are often composed of several distinct kinematic zones[2,15,16,18] characterized by stretching (extension; i.e. driving element) of the upper part of the zone and shortening (compression; i.e. resisting element) of the lower part[2].

On the basis of this knowledge, we investigated the relation between structures, velocity distribution and basal-slip surface geometry within individual kinematic domains of two large earth flows in the Apennine Mountains of southern Italy: the "Montaguto" earth flow and the "Mount Pizzuto" earth flow. Both earth flows involved structurally complex slopes. Especially, at Montaguto, we considered the mapped distribution of structures and hydrologic features from Guerriero et al.[15], the geometry of the basal-slip surface beneath individual domains reconstructed by Guerriero et al.[15] and used successive sets of orthorectified aerial-photos to determine the velocity distribution of 25 natural objects within the "neck domain". At Mount Pizzuto we considered the mapped distribution of structures and hydrologic features from Guerriero et al.[18], used 2 hand-excavated boreholes, 7 shallow-seismic profiles and 27 ambient seismic noise acquisitions (HVSR) to define the geometry of the basal-slip surface, and used RTK-GPS surveys of a network of 35 benchmarks to determine the distribution of average flow velocities.

2. The Montaguto earth flow

2.1. Earth flow description

The Montaguto earth flow affects the southern slope of La Montagna Mt. in Southern Italy. It is located along the northern side of the Cervaro River valley at approximately 4566000 N and 518000 E (UTM coordinates). The earth flow is approximately 3 km long and involves between 4 to 6 millions of m^3 [11,13]. Its width ranges from 75 m at the earth-flow neck to 450 m in the upper part of the earth-flow source area. Total elevation difference from the toe, adjacent to the Cervaro River, to the top of the 90 m high headscarp, is approximately 440 m. The average slope angle, excluding the headscarp, is approximately 7.2°.

Earth-flow displacement occurs mainly along lateral strike-slip faults and shear zones. Lateral strike-slip faults are better expressed in the lower part of the source area, where they are commonly associated with flank ridges and along the earth-flow transport zone where fault segments reached a length of few hundreds of meters. Shear zones are distributed along earth-flow boundary between fault segments and locally between active lateral strike-slip faults and between active lateral strike-slip fault and the earth-flow margin. The earth-flow travel path is complex and is strongly influenced by inactive earth-flow deposits and geologic structures[25].

The earth-flow deposit derives from the Miocene Flysch of the Faeto formation and the Pliocene Villamaina formation that widely outcrops in the upper and lower zone of the slope, respectively[11]. The Flysh of the Faeto formation and the Villamaina formation are lithologically complex[11]. This geological complexity influences groundwater flow and many springs are present from 600 m above the sea level to the top of the La Montagna Mountain[6]. Several spring groups are located along the western flank of the earth-flow Body and within the earth-flow Head feeding the earth-flow creek.

Historical information collected by Guerriero et al.[13] and Guerriero et al.[17] showed that the Montaguto earth flow has been periodically active during the last decades and it is approximately 100 years old. In particular, the 1958 and the 2006 reactivations were the largest in terms of mobilized volume and changes in earth flow extension and morphology. Both reactivations followed an exceptional hydrologic year in terms of total rainfall amount[14].

2.2. Deformational structures and segmentation

Guerriero et al.[13] mapped deformational structures and hydrologic features of the Montaguto earth flow in May 2010. Structures were mapped using real-time kinematic (RTK) Global Positioning System (GPS) technique[10], with a dual-frequency GPS receiver. Horizontal accuracy during field mapping ranged between ±1.5 and ±7.2 cm; 3D accuracy ranged between ±3 and ±11.2 cm. Describing structures, they used terminology and classifications from structural geology because they accurately depicted the geometry and relative sense of displacements for the structures that were observed[13]. Mapped distribution of the structures was used to identify kinematic zones formed by major paired driving and resisting earth-flow elements[2].

Map of figure 1a shows the configuration of the Montaguto earth flow in 2010. Deformational structures within the flow comprises normal faults and tension cracks, indicating earth-flow stretching, thrust faults, back-tilted surfaces, flank ridges and, fold structures and /pressure ridges, indicating earth-flow shortening, back-tilted surfaces indicating backward rotation and strike-slip fault bounding the earth-flow moving core. Five active kinematic zones containing structures indicating both stretching and shortening were recognized along the earth flow: the Head, the Hopper, the Neck, the Body and the Active Toe. The source area was formed by two zones of paired extension and shortening. The upper zone, the Head, consisted of the headscarp, internal landslides, back-tilted surfaces with associated ponds and a cluster of thrust faults. The lower zone, the Hopper, which started immediately downslope from a cluster of thrust faults, consisted (in upslope to downslope progression) of a cluster of normal faults, flank ridges bounded by strike-slip faults, and two thrust faults. Downslope from the Hopper, the earth-flow Neck was delineated at its upslope end by a group of normal faults (shown as a single fault because of scale limitations) and at its downslope end by a thrust fault and a back-tilted surface. As the earth flow emerged from the earth-flow neck, it changed direction and moved to the southeast, instead of to the southwest. The active earth-flow Body, downslope from the neck, contained paired normal faults and thrust faults and discontinuous strike-slip faults that were associated with flank ridges toward the downslope end of the zone. Downslope from the Body, the Active Toe was defined by normal faults at its upslope end and thrust faults at its downslope end. Strike-slip faults periodically formed at the advancing front of the Active Toe through 2010, as it continued to advance downslope and spread laterally. For further detail about the evolution of structures and kinematic zones refer to Guerriero et al.[15].

2.3. Balsal-slip surface geometry

Guerriero et al.[15] used data from boreholes, pit excavations, static cone penetration tests, seismic profiles, and difference DEMs to reconstruct the geometry of the basal-slip surface. In total, they used 26 data points to constrain the geometry of the basal-slip surface along the longitudinal profile of the flow: 1 point within the Head zone, 5 within the Hopper, 3 within the Neck, 6 within the Body, and 11 within the Active Toe (Fig. 2). The depth of the basal-slip surface ranged from 14 m within the Active Toe to about 4 m in the Neck (Fig. 2). Overall, the basal-slip surface (Fig. 2) is a repeating series of steeply sloping surfaces (risers) and gently sloping surfaces (treads). The upslope ends of each kinematic zone are at risers and the downslope ends are at treads. Normal faults occur at risers and thrust faults occur at treads. Within each kinematic zone, the overall shape of the slip surface is concave upward, whereas at the transition areas between zones, the shape is convex upward. In general, the thinnest parts of the earth flow are at risers and transition areas, and the thickest parts are at treads. Individual pairs of risers and treads formed quasi-discrete kinematic zones that operated in unison to transmit pulses of sediment along the length of the flow[15] (Fig. 2).

3. The Mount Pizzuto earth flow

3.1. Earth flow description

The Mount Pizzuto earth flow[18] is among the most active earth flows of the Benevento province (Revellino at al., 2010). It affects the northeastern side of the Pizzuto Mount. from about 720 m above sea level (a.s.l.) to about 550 m

(a.s.l.), and involves an estimated volume of 300,000 m3 of fine-grained flyshoid material. From a geological viewpoint, the Mount Pizzuto earth flow is located at the overthrust fault between i) the Argille Varicolori formation forming the upper part of the slope, where the flow source area is located, and ii) the Flysh of San Bartolomeo formation outcropping in the middle and lower parts of the slope[24]. The tectonic contact between such formations materializes a WNW-ESE trending thrust fault that constitute a weak zone where several landslide source-area are localized[24]. The Mount Pizzuto earth flow has been periodically active in the last decades and, as stated by local people, early in 2006 it surged damming the Ginestra torrent at its toe. The earth-flow dam induced episodic floods that periodically damaged a segment of a local road and power and telephone service lines. In 2008, a man-made ditch was excavated along the torrent course and a large diameter drain was installed. It worked until early 2011, when a new flood destroyed the drain, the local road and the service lines.

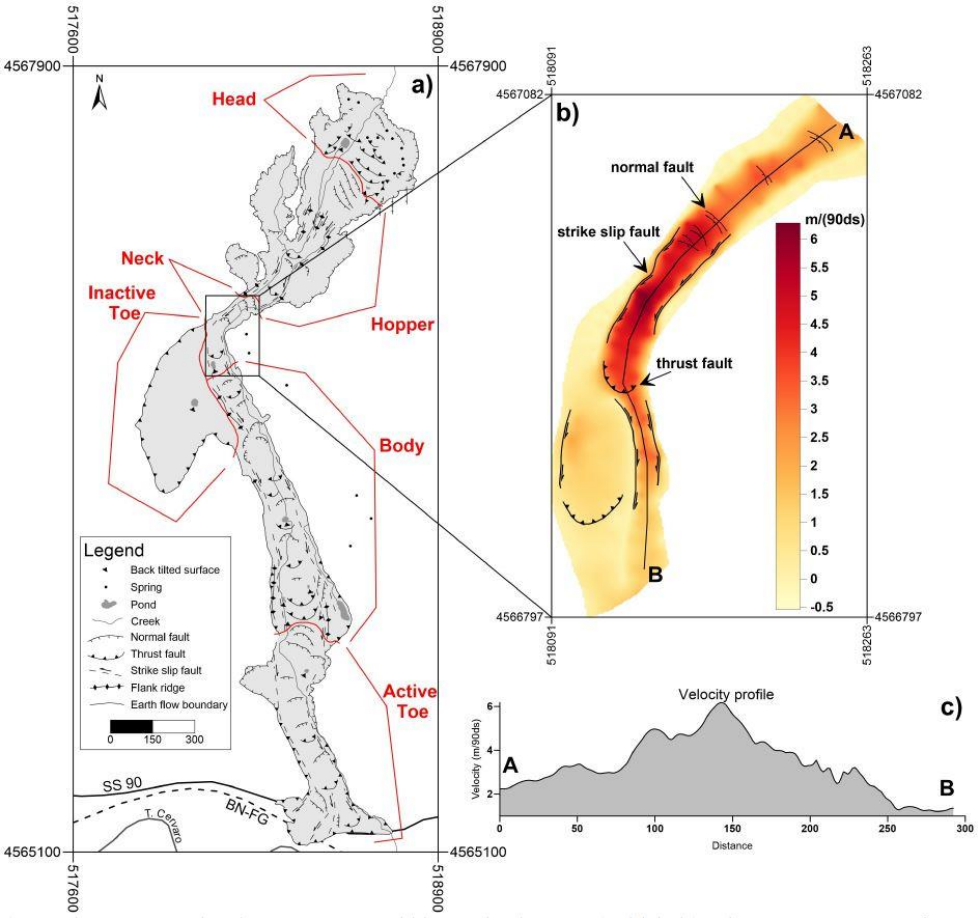

Fig. 1. Maps showing a) structures and kinematic zones of the Montaguto earth flow and b) structures and velocity within the earth flow Neck. C) Velocity profile of the earth flow Neck, see b) for profile position.

3.2. Deformational structures and segmentation

Guerriero et al.[18] mapped deformational structures and hydrologic features of the Mount Pizzuto earth flow in September 2014. Structures were mapped using real-time kinematic (RTK) Global Positioning System (GPS) technique[10], with a dual-frequency GPS receiver. Horizontal accuracy ranged between ±1.5 and ±7.2 cm and 3D

accuracy ranged between ±3 and ±11.2 cm. GPS data were exported in form of vector features as point, line, and polygon, and were processed onto a GIS environment. Describing structures, they used terminology and classifications from structural geology because they accurately depicted the geometry and relative sense of displacements for the structures that were observed[13]. Mapped distribution of the structures was used to identify kinematic zones formed by major paired driving and resisting earth-flow elements[2]. Map of figure 1a, simplified from the highly detailed map of Guerriero et al.[18], shows the configuration of the Mount Pizzuto earth flow in 2014.

Deformational structures within the flow comprises normal faults and tension cracks, indicating earth-flow stretching, thrust faults, back tilted surface, flank ridges and, fold structures and /pressure ridges, indicating earth-flow shortening, back-tilted surfaces indicating backward rotation and strike-slip fault bounding the earth-flow moving core. Five kinematic zones were recognized along the earth flow: the Head, the Hopper, the Neck, the Body, and the Toe. The Head of the earth flow (Fig. 3) consists of two coalescent branches containing both extensional and compressional structures. The northern branch began with a group of normal faults delineating a natural amphitheater. Downslope from this first set of normal faults the earth-flow moving core is bounded by discontinuous strike slip faults and contains both normal faults, tension cracks and thrust faults. Segments of strike-slip faults are arranged as left- or right-stepping en echelon arrays and stepping direction controls the width of the earth flow. Segments length ranges from 4 to 30 meters. Tension-crack opening direction ranges from 30° counterclockwise to 30° clockwise from the direction of the strike-slip faults forming the left flank of the flow. The southern branch began with a group of normal faults forming the main headscarp (from 2 to 4 m high) and structure distribution is similar to the northern branch. The northern and the southern branches join where thrust faults are associated with back-tilted surfaces and ponds. Downslope from the Head zone, a highly fractured area marks the beginning of the Hopper kinematic zone (Fig. 3). This kinematic zone is laterally bounded by inward-stepping segments of strike-slip faults accommodating earth-flow narrowing. The earth-flow Hopper can be divided into three major deformational zones: i) an upper zone characterized by normal faults and tension cracks, ii) a middle zone contains a group of normal faults that face downslope in its upper part and tends to face toward the flanks in the lower part and, iii) a lower zone is characterized by thrust faults associated with back-tilted surfaces containing ponds. The Neck kinematic zone contains the narrowest section of the earth flow. Along the Neck, the moving core is bounded on both flanks by discontinuous strike-slip faults that step inward upslope from the neck and outward downslope. It begins with a highly fractured area that evolves downslope into a cluster of downslope-facing normal faults. The Neck kinematic zone ends in correspondence of thrust faults. Downslope from the Neck is the Body kinematic zone. It is bounded by segments of strike-slip faults, locally alternated with en-echelon sets of tension cracks. The upper part of the Body is characterized by a group of extensional features (i.e. normal faults and tension cracks) and a thrust fault. Downslope, pull-apart basin delineated by extensional and compressional structures are present at steps of strike slip faults forming the right flank of the flow. Toward the longitudinal axis of the flow, longitudinal segments of thrust fault form the suture line between the material remobilized in April 2014 and the material outgoing from the structural basin. Thrust faults in this part of the earth flow mark the end of the Body kinematic zone. The earth flow Toe consists of a smaller, upper, extensional zone with a group of normal faults and a larger compressional zone with large thrust faults associated with back-tilted surfaces. Most of these back-tilted surfaces contains ponds.

4. Methods

4.1. Measuring earth-flow displacement from successive sets of orthoimages at Montaguto

We measured the displacement of 25 natural and artificial objects (i.e. large rock fragments, draining pipes etc…) on the surface of the Neck kinematic zone of the Montaguto earth flow, visible in successive sets of satellite orthoimages. The orthoimages were Eros-B digital orthorectified images taken on 25/05/2010 and 25/08/2010, respectively. EROS-B satellite acquire panchromatic images with a nadiral Ground Sampling Distance (GSD; i.e. spatial resolution) of 0.7 m (single sided pixel dimension) and the radiometric resolution is within a spectral range of 0.5 to 0.9 μm. Objects consisting of groups of pixels were recognized on the basis of their geometry and color (i.e.

Digital Number) distribution. Corners of object were visually picked from a display and displacement was manually measured into a GIS. Irregularly distributed displacement values were interpolated to produce a displacement map. Interpolation was completed using Inverse power to a distance method and deformational structures were used as breaklines. The error in displacement was assigned on the basis of the computed east-west and north-south root mean square errors in position of 16 stable ground control points (corner of pixel on stable ground). The 2× xRMS values ranged from ±0.04 to ±0.12 m, but averaged about 0.08 m. The 2× yRMS values ranged from ±0.02 to ±0.18 m, but averaged about 0.06 m. Considering that xRMS ≠ yRMS, the error in displacement module depends on the direction of the displacement vector and xRMS and yRMS are the maximum and the minimum, respectively.

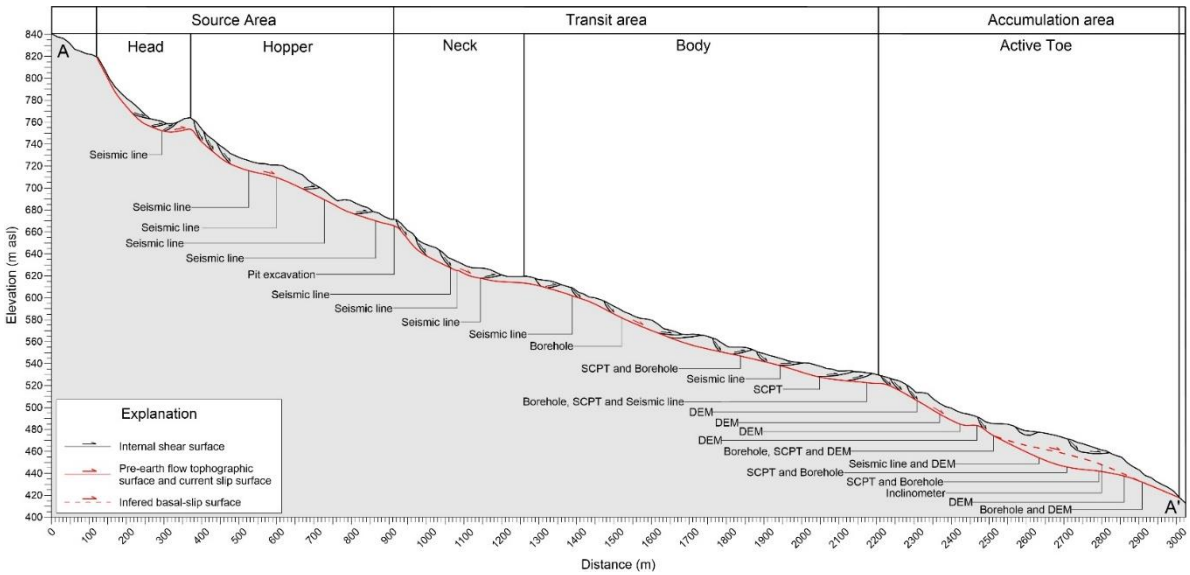

Fig. 2. Longitudinal profile of the Montaguto earth flow showing the geometry of the basal-slip surface. Types of data used to control the position of the basal-slip surface are shown (e.g., seismic line and pit excavation). SCPT is static cone penetration test.

4.2. Subsurface exploration of the Mount Pizzuto earth flow

We used 2 boreholes, 7 shallow-seismic profiles (i.e. ReMi-MASW) and 27 ambient seismic noise acquisitions (i.e. HVSR) to detect the depth of the basal slip-surface along the Mount Pizzuto earth flow (Gerriero et al., in review; Fig. 4). The boreholes were hand-excavated using a helicoidal auger. Shallow seismic profiles were carried out using MASW method (Multichannel Analysis of Surface Waves; add reference) and the Soilspy equipment (Micromed). The acquisitions were completed using 8 vertical geophones (4.5 Hz) with 2 meters spacing, in both passive (ReMi) and active (MASW) mode. In order to produce a signal characterized by a low noise at high frequency, we jump 5 meters apart the first geophone. The surveys were interpreted with Grilla (Micromed Software) with a manual procedure. The HVR[22,23] analysis were carried out with Tromino (Micromed).

4.3. Installation, distribution and monitoring of points at Mount Pizzuto

We installed, in April 2014, 35 monitoring points inside the Mount Pizzuto earth flow. Monitoring points were placed inside the earth flow approximately along its longitudinal axis. Exceptions were the monitoring points from 9 to 19 that were installed within the Hopper and the upper part of the Neck (Fig. 3). Monitoring points were distributed along the earth flow on the basis of field observations used to identify major kinematic zones. In each kinematic zone we installed from 4 to 9 points. The points, placed with a clear view of the sky, were surveyed using Real Time Kinematic GPS technique using a Leica Viva-Net rover equipped with a Leica GS08 dual-frequency

antenna. Real time correction for high-accuracy measurement was obtained through the ItalPos network. The horizontal RMS and the 3D RMS in positioning, calculated during all surveying sessions, ranged from 0.7 and 3.2 cm and from 1.6 and 5 cm, respectively. All of the points were surveyed during 2 GPS campaigns of 1 day over a period of 395 days. The first survey was in April 08, 2014. Earth-flow displacement and direction were measured onto a GIS environment.

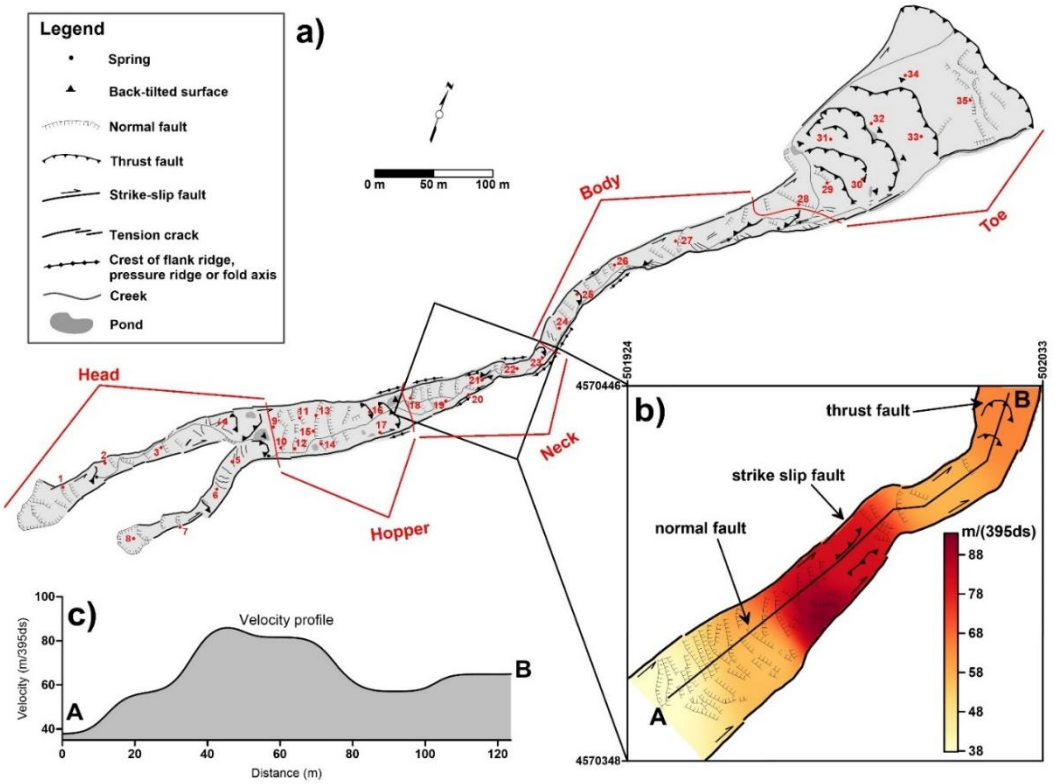

Fig. 3. Maps showing a) structures, kinematic zones and monitoring points of the Mount Pizzuto earth flow and b) structures and velocity within the earth flow Neck. C) Velocity profile of the earth flow Neck, see b) for profile position.

5. Results

5.1. Displacement, velocity and structures within the Neck of the Montaguto earth flow

The Neck of the earth flow was actively moving between May and August 2010 (90 days). The average earth-flow velocity over the entire monitoring period ranges from 0.016 m/d of the upper and lower parts of the kinematic zone to 0.066 m/d of its middle part. Variation of earth-flow velocity along the longitudinal axis of the kinematic zone is shown in the velocity profile of figure 1c. It is characterized by a peak of approximately 6 m/395ds in the middle part of the kinematic zone toward the right flank of the flow and an upper and a lower parts where velocity increase and decrease, respectively. Distribution of displacement and average velocity, shown in figures 1b underline the existence of three sectors characterized by i) few normal faults and a linear increase of flow velocity; ii) a group of normal faults in the upper part of the sector, an irregular variation of earth-flow velocity and a peak in velocity where the flow moving core is bounded by segments of strike slip faults; iii) a negative variation of earth-flow velocity associated with the existence of thrust faults and a rapid narrowing of the section of the active flow.

5.2. Slip surface geometry of the Mount Pizzuto earth flow

We used data from 2 boreholes, 7 seismic profiles (i.e. ReMi-MASW), and 27 ambient seismic noise acquisitions (i.e. HVSR) to reconstruct the geometry of the basal-slip surface of the Mount Pizzuto earth flow (Fig. 4a). In total, we used 29 data points to constrain the basal-slip surface geometry along the longitudinal profile of the flow: 4 points within the Head zone, 6 within the Hopper, 4 within the Neck, 8 within the Body, and 6 within the Active Toe (Fig. 4). Position of boreholes and ReMi-MASW is reported in figure 4a using red symbols. HVSR measurement were completed in correspondence of monitoring points installed along the flow (Fig. 4). Their position can be seen in figure 4a plotting the position of blue symbols on the black line indicating the earth flow ground surface. The depth of the basal-slip surface ranged from 6 m within the Active Toe to about 2 m in the Neck (Fig. 4). Overall, the basal-slip surface (Fig. 4) is a repeating series of steeply sloping surfaces (risers) and gently sloping surfaces (treads). The upslope ends of each kinematic zone are at risers and the downslope ends are at treads. Risers and thread are better expressed in terms of longitudinal extension and change in slope angle in the Head, the Hopper and the Neck.

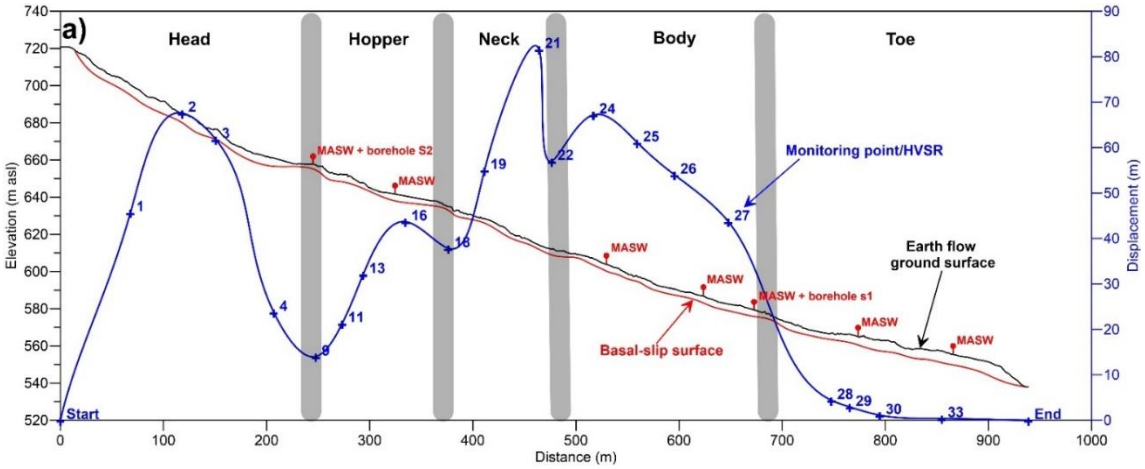

Fig. 4. Longitudinal profile of the Mount Pizzuto earth flow showing the geometry of the basal-slip surface and displacement profile.

5.3. Displacement and velocity of the Mount Pizzuto earth flow from April 2014 to May 2015

All of the monitoring points moved between April, 2014 and May, 2015 (395 days) and total movement was largely dominated by the horizontal component. Cumulative displacement of moving points ranged from 92 m of monitoring point 20 within the Neck of the earth flow to 0.4 m of monitoring point 33 and 34 at the Toe of the earth flow and all of the points moved downward. Displacement of monitoring points showed in figure 4 (blue symbols) ranged from 81 m of monitoring point 21 within the Neck of the earth flow to 0.4 m of monitoring point 33 at the Toe of the earth flow. The blue line of figure 4a shows how the module of displacement vectors corresponding to monitoring points variate along the flow. Especially, each kinematic zone is characterized by an upslope area of acceleration and a downslope area of deceleration with a peak of displacement localized in the middle. An exception from this statement is the earth flow Toe where the module of the displacement vectors linearly decreases toward the toe of the flow. The average daily velocity at the Head of the earth flow ranged from 6 cm/d of the point 4 to 17 cm/d of the point 2. At the Hopper of the earth flow, the peak of daily velocity is of 4 cm/d and occurs at the monitoring point 9. Within the Neck, the average daily velocity ranged from 10 cm/d of the point 18 to 20 cm/d of the point 21, while it ranged from 17 cm/d of the point 24 to 11 cm/d of the point 27 within the Body. At the Toe of the earth flow, the average daily velocity ranged from 1 cm/d of the point 28 to 0.1 cm/d of the points 33 and 34.

5.4. Displacement, velocity and structures within the Neck of the Mount Pizzuto earth flow

The Neck of the earth flow was actively moving between April 2014 and May 2015 (395 days). The average earth flow velocity over the entire monitoring period ranges from 0.1 m/d to 0.22 m/d. Variation of earth-flow velocity along the longitudinal axis of the kinematic zone is shown in the map of figure 3b and in the velocity profile of figure 3c. It is characterized by a peak of approximately 90 m/395 days in the middle part of the kinematic zone toward the right flank of the flow and an upper and a lower parts where velocity increase and decrease, respectively. Where earth-flow material accelerates, normal faults accommodate flow stretching while where earth-flow velocity decrease thrust faults accommodate earth-flow shortening. This is the case of a sector located immediately downslope from the area where the maximum velocity is reached where thrust faults accommodate earth-flow deceleration. This area is located between the peak of velocity and the sector where velocity linearly decrease (Fig. 3c).

6. Discussion

Our results, combined with data from Guerriero et al.[15] and data from Guerriero et al.[18] indicates that the ground surface of the Montaguto and of the Mount Pizzuto earth flow are disseminated of structures indicating different styles of deformation of the earth flow material. Guerriero et al.[15] underline that structure distribution can be used to infer the geometry of the basal-slip surface, because of the relation existing between extensional structures and raiser in the basal slip surface and compressional structures and thread, and is the basis to understand if an earth flow is formed by distinct kinematic zones. Such structures accommodate deformation caused by spatial variation of earth-flow velocity (i.e. acceleration and deceleration) and from our analysis appears that their density on the ground is independent by the magnitude of the velocity change. The highest density of extensional structure along the Mount Pizzuto earth flow can be observable in the upper part of the Hopper kinematic zone where a highly fractured area was mapped by Guerriero et al.[18] while, the highest acceleration of the flow occurs in the upper part of the Neck (Fig. 4). This highly fractured area corresponds to the riser of the Hopper that is characterized by the highest value of the slope angle of the basal-slip surface. Our interpretation is that the slope angle of the basal-slip surface might control the density of deformational structures forming during flow movement.

The displacement profile of the Mount Pizzuto earth flow (Fig. 4) indicates that average velocity (displacement / 395 days) variate along the earth flow showing several sectors of acceleration and deceleration. The existence of these sectors was also observed within the neck of the Montaguto earth flow. Such sectors roughly correspond to driving and resisting elements forming kinematic zones. The maximum displacement of the Mount Pizzuto earth flow occurred at point 21 near the neck of the flow. Excluding point 18, displacement increases linearly from the upper end of the Hopper (i.e. point 9) to the earth-flow neck (i.e. point 21). Considering that this part of the flow is characterized by a consistent reduction of the earth-flow section and that field observation confirm a constant activity of the flow in terms of sediment supply, we might infer that the module of the displacement is controlled by both the width of its section and the geometry of the basal-slip surface. Especially, the presence of thread induces a deceleration of the flow around point 18 while the presence of a riser induces an acceleration of the flow.

In this context, velocity profile along kinematic zones has a consistent pattern as described in the result section for the Neck of the Montaguto earth flow and the Neck of the Mount Pizzuto earth flow. These observations indicate that a relation between velocity profile of an active earth flow and its slip surface geometry does exist. Especially, local variation of earth flow velocity (i.e. local acceleration and deceleration) are controlled by variation of the slope angle along the slip surface. In other words, the geometry of the basal slip surface controls both the kinematic segmentation of an earth flow and the geometry its velocity profile.

7. Conclusion

Our work shows that earth flows involving structurally complex slopes can be composed of distinct kinematic zones characterized by a specific longitudinal velocity profile. Velocity variation along a kinematic zone is

consistence with the distribution of structures disseminated on the ground surface of the flows that accommodates deformation of material during movement. Such variation is controlled by the geometry of the basal slip surface and in particular by local variation of the slope angle. Such geometry seems to control also the density of the forming extensional structures at driving earth flow elements (i.e. riser).

Acknowledgements

Reference

1. Baum RL, Messerich J, Fleming RW, 1998. Surface deformation as a guide to kinematics and three-dimensional shape of slow-moving, clay-rich landslides, Honolulu, Hawaii. Env Eng Geos 1998:4:283–306.
2. Baum RL, Fleming RW. Use of longitudinal strain in identifying driving and resisting elements of landslides. *Geol Soc Am Bull* 1991:**103**:1121–1132.
3. Baum RL, Johnson AM. Steady Movement of Landslide Features in Fine-Grained Soils – a Model for Sliding Over an Irregular Slip Surface. Chapter D of Landslide Processes in Utah – Observation and Theory. *US Geol Surv Bull* 1993:**1842**:D1-D28.
4. Coe JA, Ellis WL, Godt JW, Savage WZ, Savage JE, Michael JA, Kibler JD, Powers PS, Lidke DJ, Debray S. Seasonal movement of the Slumgullion landslide determined from Global Positioning System survey and field instrumentation, July 1998 – March 2002. *Eng Geol* 2003:**68**:67-101.
5. Coe JA, McKenna JP, Godt JW, Baum RL. Basal-topographic control of stationary ponds on a continuously moving landslide. *Ear Surf Proc Lan* 2009:**34**:264 – 279.
6. Diodato N, Guerriero L, Fiorillo F, Esposito L, Revellino P, Grelle G, Guadagno FM. Predicting monthly spring discharge using a simple statistical model. *Wat Res Man* 2014:**28**:969-978.
7. Fleming RW, Johnson RB, Schuster RL. The reactivation of the Manti landslide. Utah. *US Geol Surv Prof Pap* 1988:**1311**.
8. Fleming RW, Johnson AM. Structures associated with strike slip faults that bound landslide elements. *Eng Geol* 1989:**27**:39–114.
9. Fleming RW, Baum RL, Giardino M. Map and description of the active part of the Slumgullion landslide, Hinsdale County, Colorado. *US Geol Surv Misc Inv Ser* Map I-2672, 1999:**1**:1000-scale. http://pubs.usgs.gov/imap/i-2672/
10. Gili JA, Corominas J, Rius J. Using Global Positioning System techniques in landslide monitoring. *Eng Geol* 2000:**55**:167–192.
11. Giordan D, Allasia P, Manconi A, Baldo M, Santangelo M, Cardinali M, Corazza A, Albanese V, Lollino G, Guzzetti F. Morphological and kinematic evolution of a large earth flow. The Montaguto landslide, southern Italy. *Geom* 2013:**187**:61–79.
12. Gomberg J, Bodin P, Savage WZ, Jackson ME. Land- slide faults and tectonic faults, analogs: the Slumgullion earth- flow. Colorado. *Geol* 1995:**23**:41–44.
13. Guerriero L, Revellino P, Coe JA, Focareta M, Grelle G, Albanese V, Corazza A, Guadagno FM. Multi-temporal maps of the Montaguto earth flow in southern Italy from 1954 to 2010. *J Maps* 2013:**9**:135–145.
14. Guerriero L, Revellino P, Grelle G, Fiorillo F, Guadagno FM. Landslides and Infrastructures: The case of the Montaguto earth flow in Southern Italy. *It J Eng Geol Env*, International Conference Vajont 1963-2013, 2013:447–454.
15. Guerriero L, Coe JA, Revellino P, Grelle G, Pinto F, Guadagno FM. Influence of slip-surface geometry on earth flow deformation, Montaguto earth flow, southern Italy. *Geom* 2014:**219**:285-305.
16. Guerriero L, Revellino P, Mottola A, Grelle G, Sappa G, Guadagno FM. Multi-temporal mapping of the Caforchio earth flow, southern Italy. *Rend On Soc Geol It* 2015:**35**:166 – 169.
17. Guerriero L, Diodato N, Fiorillo F, Revellino P, Grelle G, Guadagno FM. Reconstruction of long-term earth-flow activity using a hydro-climatological model. *Nat Haz* 2015:**77**:1-15.
18. Guerriero L, Revellino P, Luongo A, Focareta M, Grelle G, Guadagno FM. The Mount Pizzuto earth flow: deformational pattern and recent thrusting evolution. *J Maps* in review.
19. Hutchinson JN. A coastal mudflow on the Londay clay cliffs at Beltinge, North Kent (England). *Géot* 1970:**20**:412–438.
20. Hutchinson JN, Prior DB, Stephens N. Potentially dangerous surges in an Antrim [Ireland] mudslide. *Qu J Eng Geol* 1974:**7**:363-376.
21. Keefer DK, Johnson AM. Earthflows: Morphology, mobilization and movement. *US Geol Surv Prof P* 1983:**1264**.
22. Nakamura Y. A method for dynamic characteristics estimation of subsurface using microtremor on the ground surface. Railway Technical Research Institute, *Qu Rep* 1989:**30**.
23. Nogoshi M, Igarashi T. On the amplitude characteristics of microtremor (part 2). *Zisin = Jishin* 1971:**24**:26-40.
24. Pescatore T, Di Nocera S, Matano F, Pinto F. L'unità del Fortore nel quadro della geologia del settore orientale dei Monti del Sannio (Appennino meridionale). *Boll Soc Geol Ital* 2000:**119**:587-601.
25. Pinto F, Guerriero L, Revellino P, Grelle G, Senatore MR, Guadagno FM. Structural and lithostratigraphic control of earth-flow evolution, Montaguto earth flow, southern Italy. *J Geol Soc Lon* in review.

Geophysical Research Abstracts
Vol. 18, EGU2016-2538, 2016
EGU General Assembly 2016
© Author(s) 2016. CC Attribution 3.0 License.

Continuous monitoring of shear wave velocity at the Montevecchio earthflow (Forlì-Cesena Province, Northern Apennines)

Lara Bertello (1), Matteo Berti (1), and Silvia Castellaro (2)

(1) Department of Earth Sciences, University of Bologna, Via Zamboni, 67, 40127, Bologna, Italy. E-mail: lara.bertello@studio.unibo.it, (2) Department of Physics and Astronomy, University of Bologna, Viale Berti Pichat, 6/2, 40127, Bologna, Italy.

The Montevecchio landslide is located about 20 km to the south - west of Cesena (Northern Italy). The landslide has a length of nearly 700 m, a maximum width of 50 m in the accumulation zone and the depth of the slip surface is around 10 m. This landslide was triggered several times in the last few years. At first on the 1th of February 2014 and at the end of February 2014 some remedial works started. From February to May 2014, the velocity of the landslide was around meters/day. At the end of May 2014, two monitoring systems were installed in the main track of the earthflow channel. The System 1 consists of a rain gauge, a pressure sensor at the depth of 1 meter, a time-lapse camera Brinno (taking photos every 30 minutes), a laser system and four geophones at 4.5Hz with a spacing of 2 meters. The System 2 consists of three GPS rover placed in the earthflow channel and the master station outside the landslide. During the 2015, the Montevecchio earth flow reactivated three times. The last reactivation was during the night between the 24th and the 25th of May. Analyzing the data acquired from the geophones, the trend of the shear wave velocity over time was detected. The data correspond to an acquisition of the ambient seismic noise (passive mode) with a sampling frequency of 300 Hz for 2min every hours and all them are collected in a Flash Memory Drive. A drop in Vs is found from the 21th-22th of May, in correspondence with a rainfall event. The video collected by the time-lapse camera shows that the landslide started to move downslope with a velocity of about 10 cm/d. Before this rainfall, the landslide was moving at a very low speed (less than 1 cm/day) and shear wave velocities were relatively high. The displacement rate increased on the 27th of May after the second rainfall event (30 mm/d) and reached the value of 10 m/day. The velocity remained apparently constant for several days, but we should consider that the data collected from the 27th of May to the 1th of June are not significant because the geophones were buried and moved downslope of about 50 meters. On the 1st of June the monitoring system was retrieved e reinstalled in its original position. From the first week of June to the 25th of July, the landslide slowed down and reached a velocity of 1 cm/d and accordingly, the Vs shows an increasing trend, except for the drop on the 22th-23th of June. Observing the video, the landslide did not accelerate; maybe the drop in shear wave velocity is a direct consequence of a rainfall event that occurred on the 22th, but we are still working on this aspect. A preliminary interpretation of the observed relationship between the displacement rate of the landslide and the shear wave velocity of the moving mass relies on the changes in the consistence of the material. During the phase of fast moving, the soil probably increases the void ratio and loses its stiffness, so Vs are low. At the contrary, during the phase of slow moving, the void ratio is relatively low and Vs are higher.

Monitoring of a fast moving landslide in a weak cemented sandstones in the Northern Apennines

Landslides of the flow type are known to cause severe damages to houses and infrastructure (e.g. Hungr et al., 2001). Despite numerous documented cases of landslides that evolved from moderately to fast moving flow like landslides, the mechanics involved in this transition remains still uninvestigated (van Asch and Malet, 2009). This is also due to the difficulties in designing a monitoring system that registers this transition with high frequency data. We present in this work a case study of a first time failure in a bedded sandstone in the Northern Apennines of Italy. The landslide is referred to throughout the work as Ronco-Puzzola landslide, which is located in the municipality of Grizzana Morandi, approximately 30km S of Bologna in the Northern Apennines of Italy. The landslide evolved in two distinct stages: the initial failure took place on April 2013 and the catastrophic reactivation occurred on 10th February 2014. In according to Cruden and Varnes (1996), the Ronco-Puzzola landslide can be classified as composite rock-earth slide in the upper part of the slope with flow like cinematic in the lower portion. Surface geophysical analyses were carried out in order to define the consistence and volumes of the involved material. In detail, periodic ReMi-MASW surveys and HVSR acquisitions were performed both inside and outside the landslide body to define the pre and post-event slope condition. A monitoring system was installed on October 2013 in the upper portion of the landslide and it consisted of 2 piezometers equipped with electric pressure transducers, 3 inclinometers, 3 wire extensometers and 12 visual targets mounted on steel rods. At the time of slope failure (Feb. 10th, 2014), only the visual targets, the pluviometer and a piezometer were active. According to the extensometer data, the upper part of the landslide started to move steadily by 1mm/day since the beginning of December 2013. On January 19th, 2014 all the visual targets started to move : the highest velocities were recorder from the lower and central targets (1800mm/day), whose data are available only until Feb. 2nd, because the landslide swamped one of the target. Sudden increases in displacement rates were observed between Jan. 30th and Feb. 1st (500 mm/day) and at the catastrophic failure (400mm/day). Although different parts of the landslide mass moved synchronically, at this stage the velocities are slightly higher for the targets placed in the upper part. Rapid increases of displacement rates are closely associated with short precipitation inputs. The second stage of the monitoring system activity began on July 2nd 2014: the rate of displacement recorded after mitigation measures were undertaken, indicates that the landslide is substantially stable and the water table level lies on average at 4.5m below the ground level.